# Assessing Raman spectroscopy to determine the thermal maturity of organic matter: application to hydrocarbon exploration

Delano Gerardo Henry

BSc, MSc, DIC

This thesis is submitted in accordance with the

requirement of Kingston University London

For the degree of

Doctor of Philosophy

Department of Geography, Geology and the Environment

Submission date: October 2019

Word Count: 52,267

**Supervisors**

Prof. Ian Jarvis, Kingston University London

Prof. Gavin Gillmore, Kingston University London

Prof. Michael Stephenson, British Geological Survey

# Abstract

Determining the thermal alteration (maturity) of organic matter (OM) in sedimentary rocks is vital for predicting hydrocarbon (HC) generation and to calibrate basin models that help petroleum geologists delineate areas of interest for HC exploration. Vitrinite reflectance (VR) is the 'gold standard', however uncertainty can arise in certain circumstances, such as in rocks with sparse vitrinite particles, hydrogen-rich OM and from overpressured basins, plus issues relating to sample preparation and operator inexperience. VR is also limited to post-Silurian rocks. It is therefore essential to have a wide range of maturity methods available that an operator can call upon depending on the circumstances.

This study demonstrates that Raman spectroscopy is a viable rapid and non-destructive technique to determine OM maturity that requires minimal sample preparation for coals and mudrocks. A new standard acquisition and processing method is described that is rapid and introduces less bias than previous methodologies, as spectral deconvolution is not performed. The method includes performing a Savitzky-Golay smoothing filter using a 21-point quadratic polynomial algorithm, a 3$^{rd}$-order polynomial baseline correction, followed by normalizing all spectra to a maximum G-band height of 2000 au. An automated spreadsheet is presented that automatically calculates the most commonly used Raman parameters including the G-band full-width at half-maximum (G-FWHM), Raman band separation (RBS), R1 (height ratio of the D1- and G-band) and a new parameter termed the scaled spectrum area (SSA; total area between 1100–1700 cm$^{-1}$).

The method has been tested successfully on a suite of prospective shale gas Carboniferous rocks from the UK with a wide maturity range and has been calibrated with VR. The G-FWHM is the most reliable Raman parameter with a strong correlation with VR ($R^2$ 0.96), followed by the SSA ($R^2$ 0.88); R1 ($R^2$ 0.73) and RBS ($R^2$ 0.65). The method has been extended to characterise a suite of shale gas geological reference materials from the United States Geological Survey (USGS) and Jurassic–Cretaceous mudrock samples from the UK and Norwegian continental shelf. It is shown that isolating the organic matter using mineral acids alters the Raman parameters by reducing/removing background fluorescence caused by the non-organic components of the rock. This reduces the bias associated with background subtraction, improving precision and accuracy. Results on samples with known VR retardation due to overpressure demonstrate that Raman may be insensitive to the retardation effect.

A portable Raman instrument has also been tested on a set of coal and shale rock-chips samples. The results demonstrate that the portable Raman is more suited to coal samples, as the shale samples have considerable background fluorescence which obscures the OM Raman bands, as well as increasing the bias associated with the background subtraction.

A comparison of maturity results from Raman, VR, Rock-Eval ($T_{max}$ and production index) and illite crystallinity, illustrate that discrepancies can occur due to technical, methodological and theoretical issues and further supports the consensus that multiple maturity parameters should be used in order reduce the risk in estimating the maturity of source rocks.

Raman is a viable alternative method to determine the maturity of OM for HC exploration, but this study highlights the pitfalls and advantages of differing Raman methodologies. It is essential that the analytical community develops a standard approach for the method to be more widely adopted in the future.

*"The man on top of the mountain didn't fall there."*

**Vince Lombardi**

# Table of Contents

## Acknowledgements

This project has been financially supported by Kingston University London and the University Alliance Doctoral Training Alliance (DTA) Energy programme.

I am extremely thankful to my first supervisor Prof. Ian Jarvis (Kingston University), who has given me exceptional support throughout my studies and significantly increased the quality of this thesis. His hard work, dedication, high standards and efficiency is exceptional. My sincere gratitude also goes to my secondary supervisors Prof. Gavin Gillmore (Kingston University) and Prof. Michael Stephenson (British Geological Survey) who have added important contributions and have always been accessible.

Ian Gill (Kingston University) has been of great help in assisting and teaching me how to prepare samples for vitrinite reflectance analysis. My gratitude goes to Simon Crust (Kingston University), who has always been an important point of contact for anything related to my PhD. Dr Chris Vane (British Geological Survey) who performed Rock-Eval pyrolysis and his organic geochemistry input is greatly appreciated, as well as Dr Jenny Huggett (Petroclays) and Prof. David Wray (University of Greenwich) for assisting in the preparation and analyses for illite crystallinity.

I am also extremely thankful to the International Committee for Coal and Organic Petrology (ICCP) for sponsoring my travel and accommodation to attend an organic petrology short course in Potsdam (Berlin, Germany). CoreLab (Redhill, London) was extremely kind in allowing me to use their vitrinite reflectance microscope. My gratitude also goes to B&WTek who allowed me to test their portable Raman instrument at Kingston University and at their office in High Wycombe.

I am extremely grateful to the people who played a role in acquiring samples for this thesis, and I again thank Prof. Ian Jarvis for making the necessary contacts. I would like to thank Dr Joe Emmings (British Geological Survey), Dr Holly Turner (University of Portsmouth), Dr Manuel Vieira (Shell, UK) and Dr Aaron Jubb (United States Geological Survey).

I would also like to thank my family for their constant support. A special acknowledgement goes to Michela, my closest friend and partner, for always being there.

# Tables

# Figures

# Dissemination

## Published papers in peer reviewed journals

**Henry, D.G.,** Jarvis, I., Gillmore, G., Stephenson, M., Emmings, J., 2018. Assessing low-maturity organic matter in shales using Raman spectroscopy: Effects of sample preparation and operating procedure. Int. J. Coal Geol. 191, 135–151.

**Henry, D.G.,** Jarvis, I., Gillmore, G., Stephenson, M., 2019. A rapid method for determining organic matter maturity using Raman spectroscopy: Application to Carboniferous organic-rich mudstones and coals. Int. J. Coal Geol. 203, 87–98.

**Henry, D.G.,** Jarvis, I., Gillmore, G., Stephenson, M., 2019. Raman spectroscopy as a tool to determine the thermal maturity of organic matter: application to sedimentary, metamorphic and structural geology. Earth-Science Reviews, 198, doi: 10.1016/j.earscirev.2019.102936.

## Papers in review

**Henry, D.G.,** Jarvis, I., Gillmore, G., Stephenson, M., Vane, C.H., Huggett, J., Wray, D., in review. Raman spectroscopy, vitrinite reflectance, Rock-Eval pyrolysis and illite crystallinity maturity indices: a critical comparison for Carboniferous shale gas exploration. Submitted to J. Mar. Petrol. Geol. Short comm. Paper.

## Conference poster presentations

The abstracts for the conference presentations are provided in Appendix G.

## Thesis Layout

The thesis is presented as a compilation of published papers, manuscripts that have been sent for review and manuscripts that are in preparation.

**Chapter 1:** The aims and objectives of the thesis will be outlined.

**Chapter 2:** A general introduction on the theory of the most important aspects of this thesis will be introduced, such as: organic matter accumulation and maturation; traditionally used palaeo-geothermometers and their advantages and limitations and the theory of Raman spectroscopy.

**Chapter 3:** This chapter reviews the geological application of Raman spectroscopy to assess the thermal maturity of organic matter. The chapter is based on: **Henry, D.G.,** Jarvis, I., Gillmore, G., Stephenson, M., 2019. Raman spectroscopy as a tool to determine the thermal maturity of organic matter: application to sedimentary, metamorphic and structural geology. Earth-Sci. Rev. 198, doi: 10.1016/j.earscirev.2019.102936.

**Authors' Contribution:** D.G.H. proposed the idea of a review article and was encouraged by I.J. to pursue it. D.G.H. performed the literature review and analysis. I.J. contributed in enhancing the quality of the review paper and revised several drafts. G.G. and M.S contributed to the final version of the manuscript.

**Chapter 4:** This chapter assesses and compares different types of sample preparation and processing methods. A rapid, simple and novel method that minimises bias is presented. This chapter is from the publication: **Henry, D.G.,** Jarvis, I., Gillmore, G., Stephenson, M., Emmings, J., 2018. Assessing low-maturity organic matter in shales using Raman spectroscopy: Effects of sample preparation and operating procedure. *Int. J. Coal Geol.* 191, 135–151.

**Authors' Contribution:** D.G.H. carried out the necessary literature review, experiments and development of the new Raman processing method. I.J. verified the analytical methods that was developed by D.G.H. and supervised the results. I.J. revised several draft manuscripts and greatly improved the quality of the research. G.G. and M.S contributed to the final version of the manuscript.

**Chapter 5:** The method developed in Henry et al. (2018) is applied to Carboniferous rock-chip samples from several sites in the UK and several Raman parameters vs. vitrinite reflectance (VR) calibration curves are constructed. A blind test is then performed to test the calibration curves, to assess which Raman parameter is best suited to estimate the thermal maturity of organic matter. This chapter demonstrates that Raman parameters have a strong correlation with VR and that the best Raman parameter is the G-FWHM, followed by the RBS and SSA. This chapter is from the publication: **Henry, D.G.,** Jarvis, I., Gillmore, G., Stephenson, M., 2019. A rapid method for determining organic matter maturity using Raman spectroscopy: Application to Carboniferous organic-rich mudstones and coals. *Int. J. Coal Geol.* 203, 87–98.

**Authors Contribution:** D.G.H. carried out all the experiments. I.J. supervised D.G.H.'s results and interpretations and gave feedback on how to improve the strength of the manuscript. G.G. and M.S contributed to the final version of the manuscript.

**Chapter 6:** The Raman results from the UK Carboniferous samples obtained using a bench top instrument have been compared with those from a portable Raman instrument, together with results from vitrinite reflectance, Rock-Eval pyrolysis and illite crystallinity. The advantages of using multiple thermal maturity methods and their similarities and discrepancies are discussed. This chapter is based on a manuscript that is in revision for publication in *Marine and Petroleum Geology*: **Henry, D.G.,** Jarvis, I., Gillmore, G., Stephenson, M., Vane, C.H., Huggett, J., Wray, D. Raman spectroscopy, vitrinite reflectance, Rock-Eval pyrolysis and illite crystallinity maturity indices: a critical comparison for Carboniferous shale gas exploration.

**Authors Contribution:** I.J. conceived of the idea to carry out Rock-Eval pyrolysis and illite crystallinity. D.G.H. contacted C.H.V. to perform Rock-Eval pyrolysis. I.J. contacted J.H and D.W. for illite crystallinity sample preparation and analysis. D.G.H. performed the illite crystallinity preparation with the help of J.H. The samples were sent to D.W. who performed the illite crystalilnity analysis. I.J. helped revise several draft manuscripts improving the scientific quality of the manuscript. G.G., M.S., J.H and D.W. all contributed to the final manuscript.

**Chapter 7:** Candidate shale gas reference samples from the United States Geological Survey (USGS) are analysed to further test the applicability of Henry et al.'s (2018) method on a wider range of material of different ages and from different basins. Results are compared with previously acquired Raman and vitrinite reflectance data from Jubb et al. (2018). Results from rock-chips and strew slides are compared using Henry et al.'s (2018, 2019) method.

**Chapter 8:** Here, Henry et al.'s (2018, 2019) method is applied to Upper Jurassic Kimmeridge Clay and equivalent samples from the UK and Norwegian continental shelves, to test samples of different ages and from different geological basins. Samples with known vitrinite reflectance (VR) retardation are tested, to see whether Raman spectroscopy is also affected by this phenomenon.

**Chapter 9:** Concluding statements and summary of the main findings, followed by recommendations for future work.

# *Chapter 1* Introduction

## 1.1 Introduction

Measuring the thermal alteration (maturity) of organic matter (OM) in sedimentary source rocks is extremely important for petroleum geologists. Data are used to calibrate basin models which can help determine the timing and location of oil and gas generation and expulsion, as well as quantifying missing lithostratigraphic units, and constraining poroperm-critical diagenetic reactions such as quartz and carbonate cementation and illitization (Susanne et al., 2008; Allen and Allen, 2013; Andrews, 2013). Although this study focuses on determining the thermal maturity of OM for hydrocarbon exploration, it is also routinely applied for metamorphic studies and frictional heating in fault zones during earthquakes.

Vitrinite reflectance (VR) is considered to be the gold standard for quantitively assessing the maturity of source rocks (Hackley et al., 2015). It measures the reflective properties of a highly polished scratch-free, relief-free and clean surface of vitrinite particles, which are the major constituent in coals and occur as dispersed OM particles in sedimentary rocks. However, it has long been recognized that VR can produce unreliable results for dispersed OM in shales. This is attributed to misidentification of primary indigenous vitrinite particles and the suppression and/or retardation of VR values, caused by rocks having high hydrogen contents (e.g. liptinites, amorphous organic matter and hydrogen-rich vitrinites), contrasting organic matter composition and behaviour in different lithologies, and overpressuring in basins (Price and Baker, 1985; Durand et al. 1986; Teichmüller, 1987; Mukhopadhyay and Dow, 1994; Car, 2000; Suárez-Ruiz et al, 2012; Hackley and Cardott, 2016; Schito et al., 2017).

In order to reduce the risk in maturity assessment, several methods are often implemented together, such as: spore colouration index, thermal alteration index of various organic matter components, fluorescence microscopy and spectroscopy, Rock-Eval™ pyrolysis, and biomarker analysis (Hartkopf-Fröder et al., 2015). All of these methods analyse organic matter (OM) in sedimentary rocks, as OM is the most

temperature-sensitive component and undergoes irreversible physical and chemical changes as it is exposed to higher temperatures (Tissot and Welte, 1984). However, non-OM methods are also used, such as: apatite fission tracking, fluid inclusion thermometry, illitization (illite crystallinity), standard oxygen isotopes and clumped isotopes.

All OM maturity methods contain technical, methodological and theoretical problems (Espitalie et al., 1977; Merriman and Kemp, 1996; Wilkins, 1999; Hartkopf-Fröder et al., 2015). It is therefore advised that multiple methods are combined in order to help minimize the risk by cross-checking the results, as no single maturity method is universally reliable (Nuccio, 1991; Whelan and Thompson-Rizer, 1993; Wilkins, 1999). Having a wide selection of methods also allows petroleum geoscientists to optimize their analysis based on the quantity, composition and age of the sample, maturity grade, operator expertise, equipment availability, and time and money constraints.

Raman spectroscopy (RS) is now emerging as a commonly used method to determine the maturity of OM in sedimentary rocks (Schito et al., 2019; Goryl et al., 2019; Henry et al., 2018, 2019; Hou et al., 2019; Khatibi et al., 2019; Lupoi et al., 2019; Rantitsch et al., 2019; Wang et al., 2019). It is also increasingly being used to estimate the metamorphic temperatures of rocks (Wopenka and Pasteris, 1993; Beyssac et al., 2002; Jehlička et al., 2003; Rahl et al., 2005; Aoya et al., 2010; Lahfid et al., 2010; Endo et al., 2012; Mathew et al., 2013; Kouketsu et al., 2014; Muirhead et al., 2016; Chen et al., 2017; Fomina et al., 2019; Kouketsu et al., 2019; Yu et al., 2019) and temperatures reached in fault zones after an earthquake (Furuichi et al., 2015; Kaneki et al., 2016; Liu et al., 2016; Kouketsu et al., 2017; Kuo et al., 2017, 2018; Kaneki and Hirono, 2018, 2019; Mukoyoshi et al., 2018).

The novelty of Raman spectroscopy is that it is a fast, non-destructive method that requires minimal sample preparation (Henry et al. 2019; Lupoi et al., 2019), depending on the methodology used. Developing an automated objective methodology is an ongoing issue and has been a major research topic in recent years (Kouketsu et al. 2014; Lünsdorf and Lünsdorf, 2016; Henry et al., 2018; Lupoi et al., 2018; Schito and Corrado, 2018). However, the applicability and reliability of Raman spectroscopy for

59 OM samples that have not been exposed to metamorphic temperatures has been
60 questioned (Quirico et al., 2005; Jubb et al., 2018).

61

## 62 1.2 Aims and objectives

63 The application of Raman spectroscopy as a tool to quantitatively measure the
64 maturity of organic matter in sedimentary rocks will be assessed for hydrocarbon
65 exploration. A multidisciplinary approach will be implemented in order to achieve this
66 aim, by comparing the laser Raman spectra and parameters with organic petrology,
67 vitrinite reflectance, Rock-Eval pyrolysis, illite crystallinity and sedimentology. The
68 main aim is to be able to calculate equivalent vitrinite reflectance values using Raman
69 spectroscopy and to determine the best Raman parameter to quantify OM maturity
70 in rocks.

71 The study will first develop a methodology based on the analysis of a preliminary set
72 of Carboniferous core and outcrop samples, which will be used throughout the
73 project. The methodology will then be calibrated on a set of Carboniferous coals and
74 shales with a wide maturity range, which will be extended and tested on a wider set
75 of Carboniferous rocks with a wide range of maturities in the UK. Samples of different
76 ages and from different geological basins from United States of America and the UK
77 and Norwegian continental shelves will also be analysed to test whether the
78 calibration curves can be applied universally. The objectives are listed below:

79 1. Compare how different sample preparation techniques and operational
80 procedures affect the Raman spectrum; followed by developing a rapid and
81 simple methodology that will be used throughout the thesis.
82 2. Investigate the correlation between Raman parameters with conventional
83 maturity tools including vitrinite reflectance, Rock-Eval pyrolysis and illite
84 crystallinity.
85 3. Construct calibrations curves using various Raman parameters with vitrinite
86 reflectance, in order to estimate equivalent vitrinite reflectance values. From

this, the best Raman parameter to provide an OM maturity proxy will be determined.

4. Determine the reproducibility and validity of the methodology and calibration curves on a wider set of Carboniferous rocks from the UK.
5. Further test the reproducibility of the calibration curves and confirm the application of Raman spectroscopy on samples of different ages and basins.
6. Understand how Raman measurements might be performed on a rig site applied to cuttings and/or core samples.

The aim is to more fully assess the viability of using Raman spectroscopy as a routine tool for the determination of OM maturity in rocks, and to suggest how to progress the wider adoption of the technique.

# *Chapter 2* Background

This chapter will introduce the theory of the most important aspects that are relevant to this thesis, such as: organic matter accumulation and maturation; traditionally used palaeo-geothermometers and their advantages and limitations; and the theory of Raman spectroscopy. The relevance of these topics and their inclusion in this chapter will highlight controlling factors that govern the deposition and preservation of OM and how different kerogen types in OM have different thermal evolution pathways, which have implications for the maturity method that is used.

A review of the different thermal maturity methods is included, as this thesis will explore whether Raman spectroscopy can be used as a reliable thermal maturity tool. Understanding the limitations and advantages of the other methods can help in determining the potential advantages or limitations that may be expected when using Raman spectroscopy. The theory of Raman spectroscopy is introduced, to demonstrate how the technique can be applied to OM.

## 2.1 Organic matter

Total organic carbon (TOC) is the measurement of organic richness of a sedimentary rock and includes both kerogen and bitumen, and typically makes up c. 2 wt% of shale gas source rocks (Fig. 2.1; Barker, 1979; Jarvie, 1991). Kerogen is described as the fraction of organic matter (OM) that is insoluble in organic solvents and it is formed during the later stages of diagenesis. Bitumen (hydrocarbons, resins, asphaltenes) is the soluble fraction of organic matter and consists of two forms: inherited and secondary bitumen. Inherited bitumen comes from the alteration of lipids that are not incorporated in fulvic or humic acids, and secondary bitumen is derived from the breakdown of kerogen and/or oil in source rocks. Kerogen typically makes up c. 90 % of the total TOC in shales (Fig. 2.1, Barker, 1979).

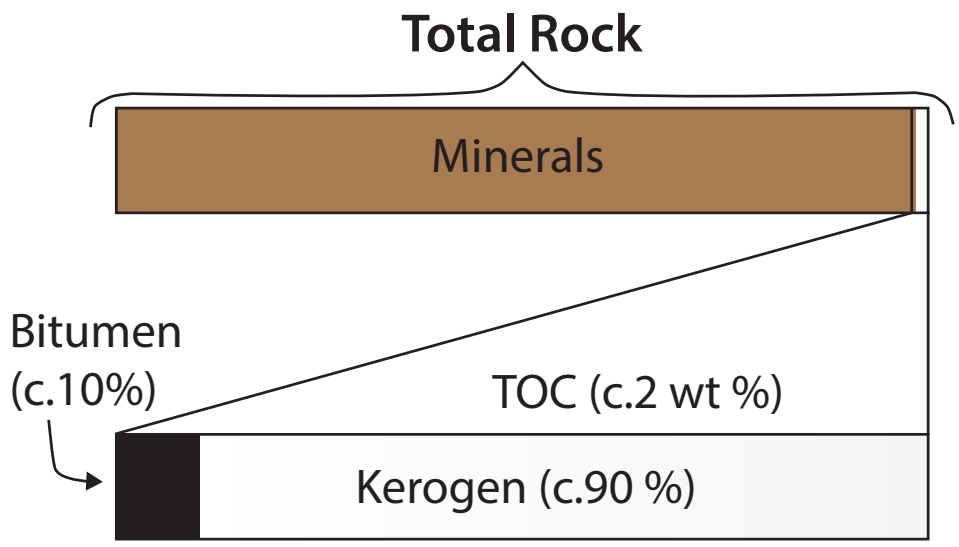


**Figure 2.1.** Average total organic matter from a shale source rock. From Barker (1979).

Figure 2.2 shows typical TOC values for a petroleum source rock. The minimum TOC value for a conventional petroleum system is 0.5 % for shales and 0.2 % for carbonates. Carbonates have a lower minimum TOC threshold as they expel hydrocarbons more efficiently than shales. The minimum TOC values for unconventional shale oil and shale gas is considerably higher at c. 1 % and c. 2 % respectively. The quantity of TOC is proportional to gas yields, expulsion efficiency and porosity in shale gas plays (Jarvie, 2012). However, TOC values can be misleading, and many geologists believe that '*If I have high TOC, I have a good source rock*'. Although TOC does play an important role, this is not always true, as the quality of the source rock is also determined by the kerogen type and thermal maturity, and the thickness and areal extent of the unit also need to be taken into consideration (Dembicki, 2009).

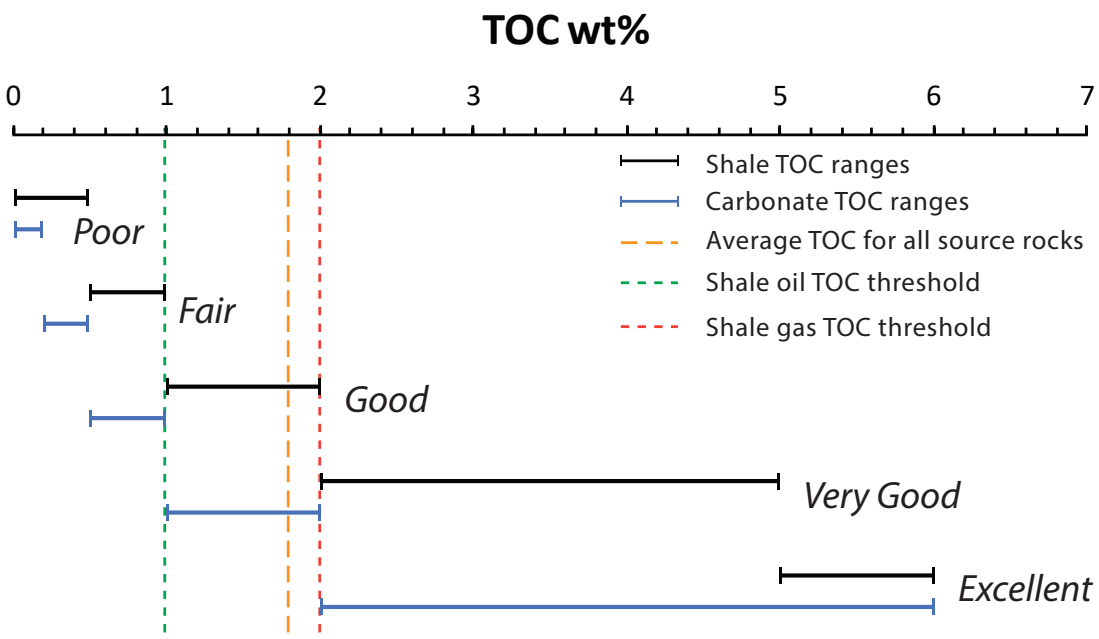


139

140 **Figure 2.2.** Typical TOC values for a conventional petroleum source rocks and their quality. The vertical
141 stippled green and red line represents the minimum TOC values for unconventional shale oil and shale
142 gas respectively. The orange stippled line represents the average TOC for all source rocks. Values taken
143 from Peters and Cassa (1994) and Andrews (2013).

144

145 The accumulation and preservation of OM in the sedimentary record occurs in special
146 circumstances. At present, <1.0 % of organic matter escapes the surface carbon cycle
147 and is trapped in sedimentary rocks (Allen and Allen, 2013). The preservation of OM
148 is controlled by three main factors, the: (1) production of OM; (2) destruction of OM;
149 and (3) dilution of OM. Understanding these three processes can be used to predict
150 the quantity and quality of OM in a source rock (Bohacs et al., 2005).

151 The production of organic matter in the oceans and lakes is primarily a function of the
152 supply of nutrients such as phosphates, nitrates and silicates (Bohacs et al., 2005;
153 Sigman and Hain, 2012). The major source of nutrients is from the continental
154 margins, where rivers and winds transport nutrients from terrestrial environments
155 into the ocean, such as the mouth of the Amazon River and the west coast of Africa,
156 respectively (Fig. 2.3a-b; Sigman and Hain, 2012; Allen and Allen, 2013). Upwelling
157 zones along continental shelves are also a major source of nutrients to the surface
158 ocean, as they bring up cold oxygenated and nutrient-rich waters to the surface, hence

increasing ocean surface productivity (Sigman and Hain, 2012; Meyer et al., 2016). A modern-day example of an upwelling zone is along the western coast of South America, which brings up the nutrient-rich Humboldt Current to the ocean surface (Fig. 2.3c). Both of these processes lead to high levels of biological productivity.

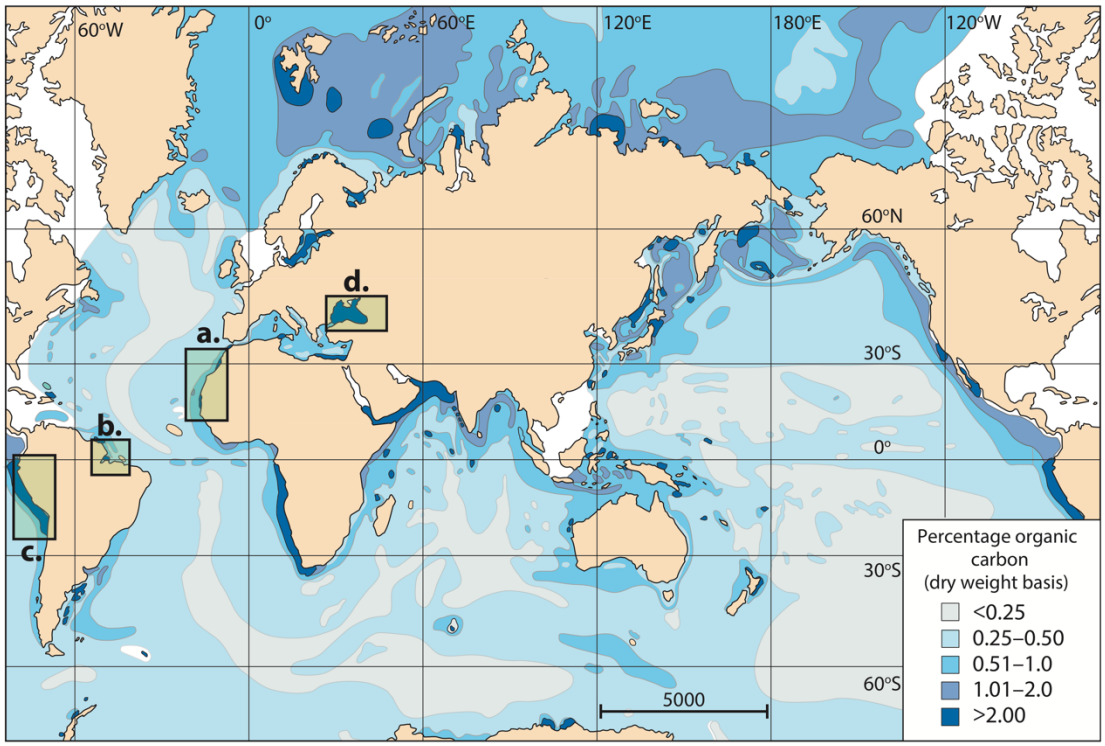


**Figure 2.3**. Map of the distribution of organic carbon in the oceans and seas. **(a)** West Coast of Africa. **(b)** Amazon river mouth flowing into the Atlantic Ocean. **(c)** Humboldt Current. **(d)** Black Sea. Adapted from Allen and Allen (2013) which was reproduced from Romankevich (1984).

Destruction of OM is a function of exposure time to oxygen and oxygen levels. Reducing the exposure time to oxygen can be achieved in several ways: (i) OM depositing in a shallow basin reducing the transit time of OM in the water column to the seabed (Suess, 1980; Trabucho-Alexandre, 2015). (ii) Flocculation of OM with clay particles increasing the weight and size of the aggregate, therefore increasing the speed of descent (Trabucho-Alexandre, 2015). (iii) The rapid deposition of sediments, such as debris flows and turbidites that rapidly bury the OM on the seabed, inhibiting the diffusion of oxidants exposed to the OM, as well as reducing the amount of bioturbation (Dow, 1978; Müller and Suess, 1979; Ibach, 1982). The movement of local

and regional tectonics can lead to the formation of regional seaways and isolate sea basin, which can encourage thermal and saline stratification and hence limit the vertical circulation of oxygen, leading to stagnant oxygen deprived anoxic bottom waters. A modern-day example is the Black Sea (Fig. 2.3d; Murray et al., 1989; Stanev et al., 2018).

Areas of high productivity increase the demand for oxygen, as oxygen-hungry bacteria decompose the dead organisms that fall through the water column (Dow, 1978). Once the oxygen demand is equal to, or greater than the oxygen supply, an anoxic environment can develop (Pedersen and Calvert, 1990). Anoxia will reduce the amount of OM destruction as it limits oxidation, aerobic bacteria, scavenging and bioturbation that would otherwise destroy the OM (Allen and Allen, 2013). Furthermore, global processes can also control the supply of oxygen and hence preservation of OM. The Mesozoic Era is a good example, as the preservation of OM was enhanced due to both global tectonic and climatic forces; as high sea floor spreading rates increased $CO_2$ production, which led to global warming and higher sea surface temperatures inhibiting the solubility of oxygen in the oceans (Kendall et al., 2009); as well as low pole-to-equator thermal gradients due to the absent polar ice caps (Huber et al., 1995), in turn reducing the strength of ocean circulation and encouraging the stratification of oceans.

Dilution of OM can have a positive or negative effect, depending on the sedimentation rate. Ibach (1982) proposed that the optimum dilution rates vary with different lithologies (Fig. 2.4). Rapid sedimentation is often needed in order to reduce the OM exposure time to oxygen at the sea floor, however very high sedimentation rates can lead to dilution of OM, in turn reducing the overall TOC in a sedimentary rock (Fig. 2.4).

Therefore, by understanding these special circumstances and their spatial occurrence, geologists can predict the distribution and concentration of potential source rocks regionally around the world and locally in geological sedimentary basins.

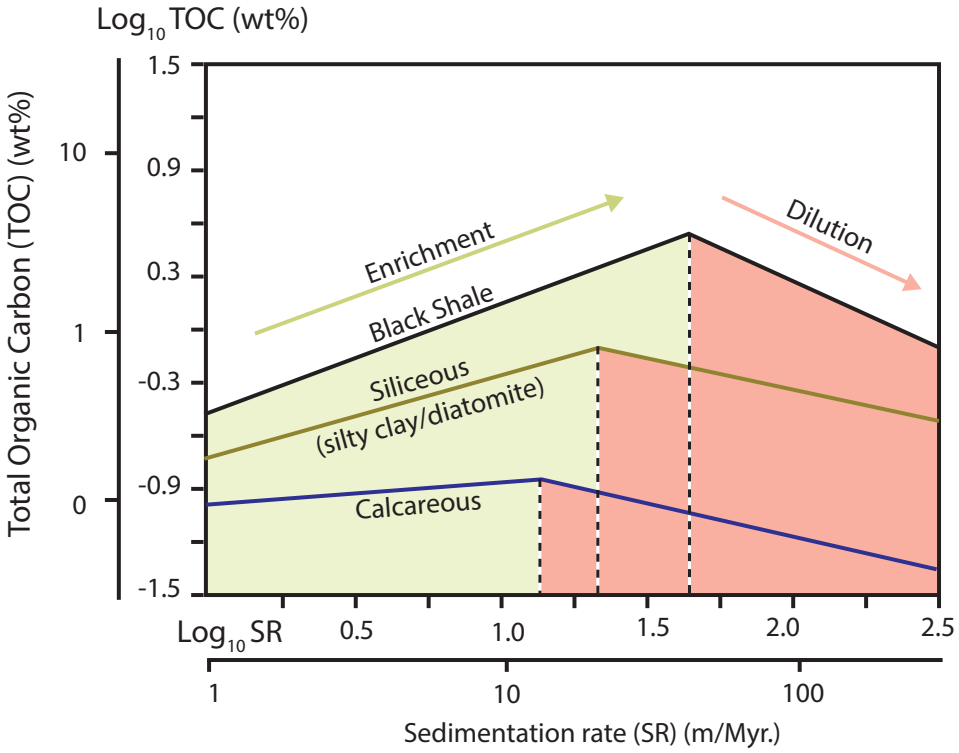


206

207 **Figure 2.4.** Relationship between sedimentation rates and TOC for various marine rocks (adapted from
208 Ibach, 1982).

209

210 ### *2.1.1 Kerogen types*

211 Kerogen is divided into four main types: Type I, Type II, Type III and Type IV. Types I-III
212 are hydrocarbon-producing, whereas Type IV has exhausted all of its potential to
213 produce hydrocarbons. The kerogen types can be determined by their hydrogen and
214 carbon (H/C) and oxygen and carbon (O/C) ratios using the van Krevelen diagram (Fig.
215 2.5a, Tissot and Welte, 1984). The atomic H:C and O:C ratios evolve with increasing
216 thermal maturation, as the hydrogen and oxygen content decreases with increasing
217 maturation, leading to the relative enrichment of carbon.

218 A modified van Krevelen diagram using the hydrogen index (HI) and oxygen index (OI)
219 from Rock-Eval™ pyrolysis can be used in a similar way to the H/C vs. O/C van Krevelen
220 diagram (Fig. 2.5b). The van Krevelen diagram demonstrates that different kerogen
221 types start with different hydrogen and carbon concentrations, therefore they follow

different evolutionary paths, producing different types and quantities of hydrocarbons at the same maturity (Fig. 2.5a and 2.6). When the hydrogen content is depleted, the source rock has exhausted all of its potential to produce oil and/or gas, regardless of the kerogen type.

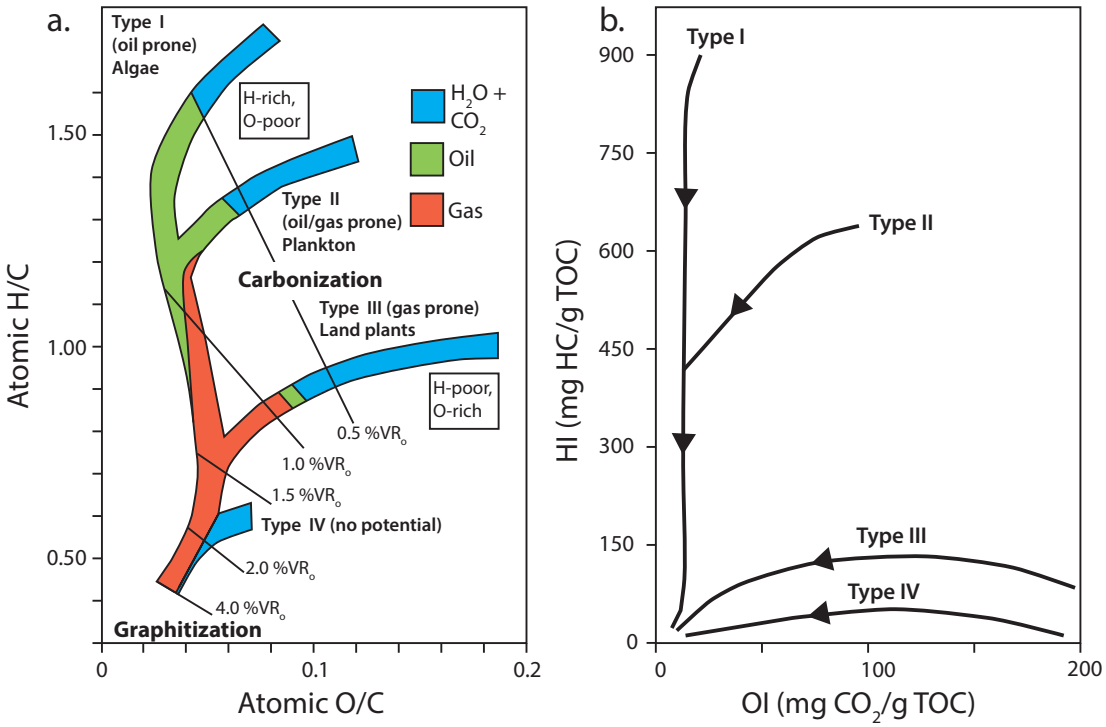


**Figure 2.5.** The van Krevelen and modified van Krevelen plots, showing the thermal evolution pathway of Type I, II, II and IV organic matter. **(a)** A van Krevelen diagram of H/C vs. O/C, superimposed with vitrinite reflectance zonations and the principal product produced from the kerogen types. Adapted from Waples (1985). **(b)** Modified van Krevelen diagram using the hydrogen index (HI) and oxygen index (OI) from Rock-Eval pyrolysis. Adapted from Tissot and Welte (1978).

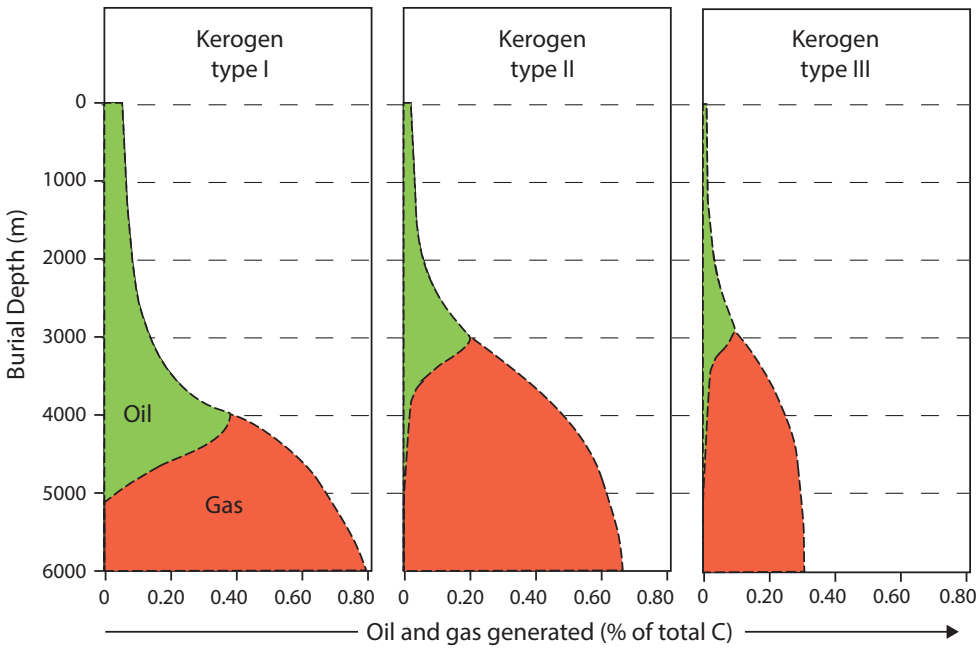


232

233 **Figure 2.6**. Hydrocarbon generation potential for the three kerogen types, at a constant burial of 60
234 metres per million years and a geothermal gradient of 35°C per km. From Vandenbroucke, (2003),
235 adapted from Tissot and Espitalié (1975).

236

237 Type I source rocks are composed of liptinite macerals found mostly in lacustrine
238 environments, but they can occur in marine settings. They are mainly composed of
239 the remains of planktonic algae that are enriched in aliphatic lipids with high hydrogen
240 concentrations, indicating a high potential to generate liquid hydrocarbons, although
241 they can also produce gas at high maturities (Fig. 2.6). The majority of the organic
242 matter is structureless and unrecognizable due to bacterial reworking and is termed
243 amorphous organic matter (AOM) (Pacton et al., 2011). The lacustrine alga
244 *Botryococcus braunii* and marine equivalents *Tasmanites* spp. are other examples of
245 sources of Type I organic matter. Type I source rocks tend to transform hydrocarbons
246 at lower temperatures (Tissot and Welte, 1984), which is shown in the van Krevelen
247 diagram (Fig. 2.5). The Eocene-aged Green River Formation of western USA is a well-
248 known Type I source rock (Katz, 1995).

249 Type II source rocks are composed of liptinite macerals that originate from marine
250 algae, zooplankton and phytoplankton cysts (organic-walled dinoflagellates and

acritarchs) and some terrestrial components including pollen and spores, leaf waxes and fossil resin. Similar to Type I, the majority of the organic matter components are AOM. Despite the wide origins of Type II kerogens, they are grouped together as they generate mostly liquid hydrocarbons, due to their high hydrogen contents (Tissot and Welte, 1984). With progressive maturation, Type II kerogens can also generate substantial gas (Fig. 2.6). The majority of shale gas targets are overmature oil prone Type II source rocks, where residual gas has remained trapped in the source rock (Jarvie et al., 2007; Passey et al., 2010). The high gas content is related to both the primary formation of gas from kerogen and the secondary cracking of liquid hydrocarbons (Jarvie et al., 2007). The Kimmeridge Clay is a well-known proven Type II source rock in the North Sea (Barnard and Cooper, 1981; Gautier, 2005). Type II-S is a variety of Type II kerogen and occurs when sulphur is incorporated into the chemical structure of the kerogen during diagenesis. The significance of this is that oil generation starts earlier than expected, because the sulphur and hydrogen bonds are weaker than the hydrogen and carbon bonds, which leads to thermal cracking occurring at lower temperatures, ultimately yielding more oil at lower maturities (Baskin and Peters, 1992; Yan et al., 2004); but of lower quality due to the presence of sulphur (Jarvie and Lundell, 2001).

Type III source rocks originate from terrestrial plants and are dominated by vitrinite macerals that lack fatty or waxy components and are mostly composed of lignin and cellulose (Waples, 1985). They are typically deposited in paralic settings along delta plains and abandoned river channels. Turbidites and debris flows are also able to transport Type III kerogen into marine basins, where a mixture of Type II/III can be found. However, they are usually rare or absent in distal deeper water settings. Type III kerogens generate dry gas and relatively smaller quantities of liquid hydrocarbons. Overall, Type III produces a lower total amount of hydrocarbons due to their low hydrogen concentrations (Fig. 2.6). Type IV kerogen is a highly aromatic carbonized version of Type III kerogen that is poor in hydrogen with no hydrocarbon generation potential and is dominated by inertinite macerals.

Heteroatoms are also present and vary with kerogen type and maturity, the most common are nitrogen, sulphur and oxygen (Petkovic, 2017). Type I and Type II

kerogens contain less oxygen atoms as they originate from oxygen-poor lipids, whereas Type III kerogens consist of oxygen-rich lignin, cellulose, phenols and carbohydrates (Waples, 1985). Type IV kerogens are highly oxidized and will therefore be enriched in oxygen within their molecular structure. Lignin Type III kerogen contain lower concentrations of nitrogen and phosphorus than algal Type I and II kerogens. Algae is therefore of higher nutritional value and is preferentially decomposed by bacteria in the early stages of diagenesis leading to the formation of amorphous organic matter (AOM). Type III kerogens have phenolic components that are toxic to many organisms and this is another reason why they are preferentially preserved (Waples, 1985). Sulphur in kerogen is mainly derived from the reduction of sulphate from anaerobic bacteria and is more commonly found in marine environments. Sulphur is only incorporated into the kerogen structures when sulphate reduction is extensive and $Fe^{+2}$ ions are absent; otherwise the sulphur and $Fe^{+2}$ can react to from iron sulphides, principally pyrite ($FeS_2$). High pyrite concentrations are often correlated with high TOC in marine Type II kerogens (Berner and Raiswell, 1983).

### *2.1.2 Kerogen maturation*

Organic matter (OM) is the most temperature sensitive component in a sedimentary rock, as it undergoes irreversible physical and chemical changes when subject to increasing temperatures. OM can therefore be used to track the hydrocarbon generation potential of source rocks (Tissot and Welte, 1984). Tissot and Welte (1984) described three main stages of burial evolution for sedimentary rocks: (1) diagenesis; (2) catagenesis; (3) metagenesis. During diagenesis most of the OM transformation is associated with biological activity, whereas catagenesis and metagenesis is dependent on thermal transformations as a result of increasing temperatures (Fig. 2.7). Although temperature is the most important factor during thermal maturation, the degree of transformation is also time dependent, as stated by the Arrhenius equation (Arrhenius, 1889).

$$K = Ae^{-Ea/RT(t)} \qquad \textbf{Equation 2.1}$$

Where, *K* is the reaction rate; *A* is a pre-exponent factor constant; $Ea$ is the activation energy; *T* is the absolute temperature in kelvin; *R* is the universal gas constant; *t* is time.

The kinetic parameters differ between kerogens, which explains why different kerogens produce oil and gas at different stages. The Arrhenius equation explains that a rock that has been subject to 80°C for 60 million years will be more mature than a rock that has been subject to the same temperature but for only 40 million years. Additionally, Le Chatelier's rule implies that increasing pressure slows down the thermal kinetic reactions, however this is thought to play a minor role during normal burial conditions and is ignored in most studies. Nevertheless, rocks that have been exposed to extreme pressures have retarded vitrinite reflectance values (Carr, 2000).

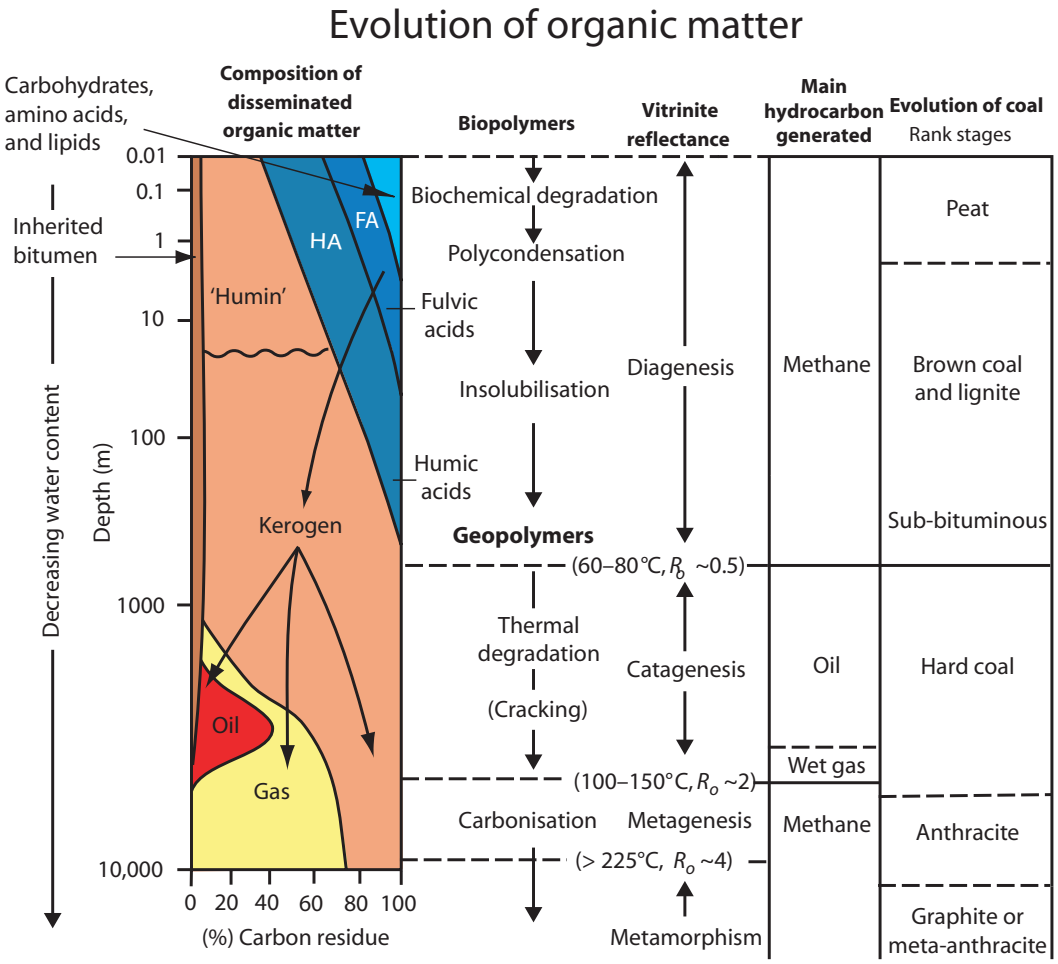


**Figure 2.7.** General evolution of organic matter during diagenesis, catagenesis and metagenesis, correlated with the timing and type of hydrocarbon generation. FA: fulvic acids; HA: humic acids. From Allen and Allen (2013), adapted from Tissot and Espitalié (1975).

### *2.1.2.1 Diagenesis (0 - 60 ℃)*

Microbial activity is the main mediator for the transformation of OM during diagenesis (Deming and Baross, 1993). Aerobic microbial activity occurs in the uppermost portion of loose sediments where free oxygen is present in the pores, whereas anaerobic microbial activity occurs in deeper sediments where free oxygen is unavailable forming anoxic conditions. Anaerobic microorganisms obtain oxygen sequentially via reducing nitrates, manganese oxides, iron oxides and sulphates. As mentioned earlier, the liberation of $Fe^{+2}$ and S via the reduction of ferric oxides and sulphate respectively, leads to the formation of iron sulphides such as pyrite ($FeS_2$) (Berner and Raiswell,

1983). If $Fe^{+2}$ is absent, then S can be incorporated into the kerogen structure producing sulphur-rich hydrocarbons during catagenesis (Type II-S). However, this mostly occurs in marine rocks as sulphur is depleted in terrestrial environments. It also typically occurs in organic-rich rocks where there is enough OM for the bacteria to feed on for energy, so that the microbes are able to reach the sulphate-reduction stage. Importantly, following the exhaustion of sulphate, biogenic methane is produced via fermentation reactions of methanogenesis (Thiel et al. 2019).

Aerobic and anaerobic microbes scavenge biopolymers such as proteins and carbohydrates for proteins and sugars respectively, and the remaining more resistant organic matter starts to coalesce (polycondensate) to form fulvic acids, humic acids and the precursor of kerogen, humin (Fig. 2.7, Tissot and Welte, 1984). Lipids and lignin are more resistant and are preserved with little alteration and can often be recognized under the microscope as algae, spores, pollens cuticles and woody components. In addition to biogenic methane, $CO_2$, $H_2O$, $H_2S$ are also produced, whilst the residual organic matter becomes more insoluble as it transforms to kerogen (Tissot and Welte, 1984).

#### *2.1.2.2 Catagenesis (60 - 150 ℃)*

The continuous supply of sediment in a basin will bury the sediments deeper into the subsurface, ultimately increasing the temperature and pressure. The catagenesis stage occurs between temperatures 50 – 150°C, which correspond to c. 0.5 – 2.0 $\%VR_o$ (Fig. 2.7). As a result, kerogens will start to breakdown, producing firstly longer chained liquid hydrocarbons followed by shorter chained gaseous hydrocarbons at higher temperatures. The H/C ratio will decrease as hydrogen is depleted during the formation of hydrocarbons, as shown in the van Krevelen diagram. Non-carbon atoms in functional groups, as well as aliphatic units are also being driven off, which leads to the enrichment of carbon in the OM. As temperature increases and dehydrogenization continues, the resulting benzene rings will begin to fuse together and stack due to aromatization, forming better ordered OM. Towards the end of catagenesis, aliphatic carbon chains disappear and the carbon in kerogen begins to become more aromatized and ordered with increasing maturation. This aromatization and ordering

of the molecular structure is what increases the reflective properties of vitrinite particles (Hackley and Lewan, 2018).

#### *2.1.2.3 Metagenesis (150 - 225 ℃)*

Metagenesis is the last stage prior to metamorphism. Here, the organic matter will continue to be thermally altered and become more ordered as it produces primary gas from kerogen, as well as secondary gas from the cracking of longer chained hydrocarbons into $CH_4$. The remaining kerogen is further enriched in carbon, as the little hydrogen that is left, is used up to produce the remaining methane. The residual kerogen will undergo graphitization and may eventually transform into a perfectly ordered graphite as it undergoes metamorphism (Fig. 2.7; Buseck and Beyssac, 2014).

Overall, during these stages, the kerogen increases in mass as it undergoes carbonization and condenses as it loses volatile elements such as N, S, O and H. Therefore, the kerogen transforms from a poorly ordered carbon with high concentrations of volatile elements and structural and chemical defects, to a more ordered carbon with lower volatile matter and less structural and chemical defects as illustrated in Fig. 2.8.

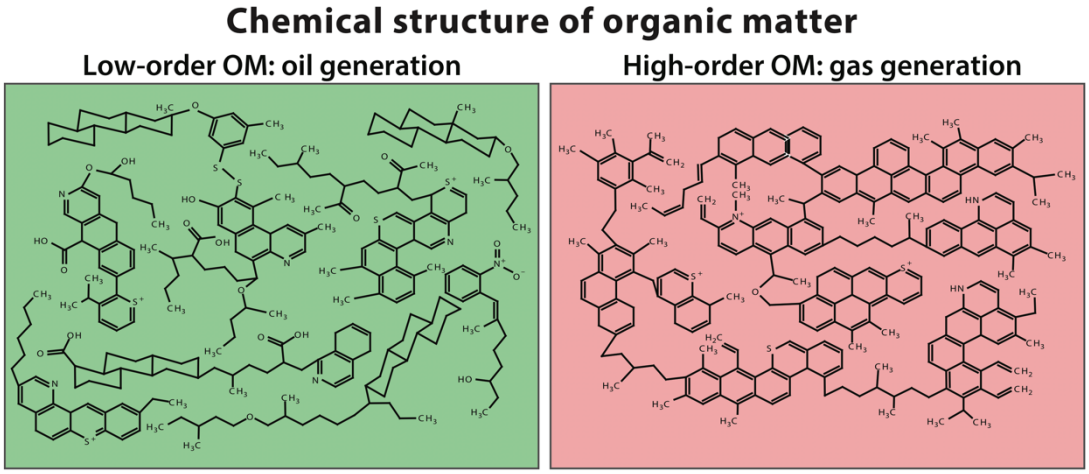


**Figure 2.8.** The chemical and structural changes of kerogen from early catagenesis to late catagenesis/early metagenesis. Note how the O, N and S elements disappear along with the reduction of longer chain aliphatic units, carboxyl and hydroxyl groups. With increasing maturity, the kerogen undergoes aromatization and the formation of more planar structure. Figure modified from Behar and Vandenbroucke (1987).

## 2.2 Traditional palaeo-geothermometers

There are many organic and non-organic methods used to determine the thermal maturity of sedimentary rocks (Harkopf-Fröder et al., 2015). All methods have advantages and limitations but having multiple methods that can be called upon to determine the maturity of sedimentary rocks, enables geologists to optimize their analysis based on the composition and age of the sample, maturity grade, equipment availability, operator expertise and time and money constraints.

Organic methods include petrographic (vitrinite reflectance, thermal alteration/spore colouration index and fluorescence) and geochemical methods such Rock-Eval pyrolysis and biomarker analysis. Whereas, the most widely used non-organic methods include illite crystallinity determination and fission track analysis.

### *2.2.1 Organic methods*

#### *2.2.1.1 Petrographic methods*

Optical maturity methods require skill and experience in order to distinguish different macerals, as well differentiating between autochthonous (primary) and allochthonous (reworked/secondary) material. Misidentification of macerals and their origin may result in unreliable results. Although difficult, optical methods do have an advantage over bulk analysis, as the colour and/or reflectance of a selected group of macerals are systematically measured to investigate the thermal evolution, which provides more reliable results. As discussed earlier, rocks can contain a mixture of various different organic matter particles that yield oil and gas at different temperatures, therefore a bulk analysis like Rock-Eval pyrolysis may give unreliable maturity results, especially if the rock contains substantial inertinite Type IV kerogen.

**Vitrinite Reflectance**

Vitrinite reflectance (VR) has a long history as a thermal maturity tool that dates back to the early 1950s and later became widely used by industries and research

organizations in the 1960s (Mukhopadhyay and Dow, 1994). VR measures the percentage of incident light reflected from a polished surface of a vitrinite particle under oil immersion. The percentage of light that is reflected back is presented as $\%VR_O$. The polished surface must be scratch-free, relief-free, and clean, otherwise VR measurements can produce unreliable results. The reflective properties of vitrinite particles increases with increasing thermal maturity, as the vitrinite particles become more ordered, as it undergoes carbonization and aromatization (Hackley and Cardott, 2016). Less ordered vitrinite would have low reflectance, as more of the light will be scattered due to the poorly ordered structure.

Vitrinite is derived from higher land-plant communities, which only began to develop during the Devonian (Peters et al., 2005), hence VR cannot be applied on rocks older than the Devonian. Nevertheless, VR is now the most commonly used thermal maturity indicator in petroleum exploration (Allen and Allen, 2013). The thermal maturity of vitrinite is divided into four classes (Table 2.1): (1) Under-mature/immature (<0.5% $VR_o$), no potential for thermal generation of oil or gas; (2) Oil-window, which starts at c. 0.5 – 0.6 $\%VR_o$ and terminates at c. 0.85 – 1.1 $\%VR_o$, depending on the kerogen type; (3) Gas-window, starting at c. 1 – 1.5 $\%VR_o$ and ending at c. 3.0 $\%VR_o$; (4) Over-mature (>3 $\%VR_o$), when the source rock has exhausted all of its potential to generate hydrocarbons.

**Table 2-1.** Vitrinite reflectance values indicating the onset and termination of the four classes: under-mature, oil-window, gas-window and over-mature.

| Class | Hydrocarbon zone | Onset ($\%VR_o$) | Terminates ($\%VR_o$) |
|---|---|---|---|
| Under-mature | The source rocks have not been exposed to high enough temperatures to generate oil and gas. | <0.5 | |
| Oil-window | Generation of oil. | 0.5 – 0.6 | 0.85 – 1.1 |
| Gas-window | Generation of gas | 1.0 – 1.3 | ~3 |
| Over-mature | No more potential for hydrocarbon generation | > ~3 | |

Depending on the sample type, whether it is from core or cuttings from a borehole, or from outcrop, different risks are present. Understanding the risks for each sample type is crucial. Cuttings from a borehole are most problematic, as rock samples can be contaminated by cavings that originate from higher up the stratigraphy, which will give maturity values of younger rocks. Typically, maturity measurements from cavings are lower, and when the results are plotted in a histogram, they can be seen as a separate population and can be disregarded at the operator's discretion. In cuttings, core and outcrop samples, secondary allochthonous vitrinite, which represents either inertinite or reworked material from older rocks, may be present in the sample and will have higher reflectance values than primary vitrinite. Again, this population with higher than expected reflectance values can be disregarded. Bitumen may be present in all the samples and is often mistakenly interpreted as primary vitrinite particles, which can give lower than expected maturity results.

Figure 2.9 is an idealized histogram of vitrinite reflectance values taken from a suite of vitrinite particles showing a trimodal distribution as a result of measuring cavings, primary vitrinite and secondary vitrinite. Different populations can be recognized and disregarded at the operator's digression, although this method can be highly subjective (Engel and Macko, 1993; Toxopeus, 1983). Differentiating primary vitrinite from secondary vitrinite using optical microscopy can be challenging, however secondary vitrinite grains can often have different angularity and size, bright rims and micro-fractures, which are typically due to weathering and transportation. Inertinite can also be misinterpreted as primary vitrinite, although grains are typically more angular and brighter than primary vitrinite grains. Bitumen often fills pores and may have peculiar structures; it is also duller compared to primary vitrinite particles.

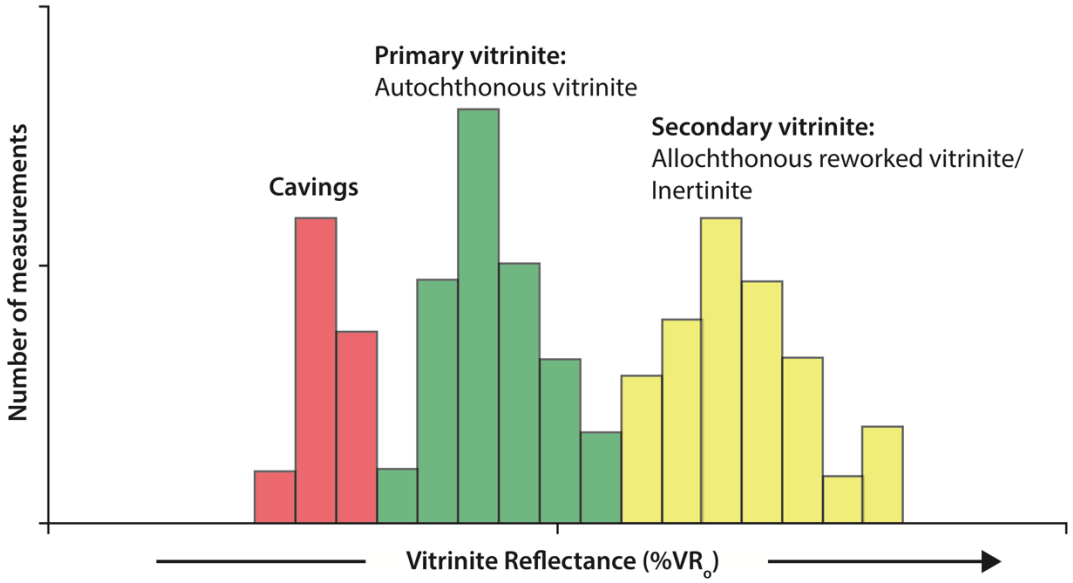


462

463 **Figure 2.9.** Theoretical idealised trimodal histogram of vitrinite reflectance values from borehole rock
464 cuttings, which includes younger less mature caving material, primary vitrinite representing the true
465 thermal maturity and more mature secondary reworked vitrinite and/or inertinite.

466

467 In the absence of faults, unconformities and igneous intrusions, VR increases
468 systematically with burial (Carr, 2000). However, primary VR values can also be
469 effected by suppression and/or retardation; typically brought on by the presence of
470 macerals with high hydrogen concentration (i.e. liptinites, AOM and hydrogen-rich
471 vitrinites), lithology type (e.g. coal, shale, siltstone, sands) and overpressured basins
472 (Carr, 2000; Suárez-Ruiz et al., 2012; Hackley and Cardott, 2016). Macerals with
473 suppressed reflectance are correlated with abundant hydrogen-rich macerals and the
474 type of lithology. For example, the presence of hydrogen-rich vitrinites or an abundant
475 amount of AOM will reduce the vitrinite reflectance values; and sandstones lithologies
476 will typically have more suppressed values in comparison to shales, and shales will
477 generally have suppressed values in comparison with coal, which may be due to
478 differences in clay mineralogy which may aid maturation (Wu et al. 2012) and poro-
479 perm properties which may assist or inhibit the interaction of oxidizing fluids (Hackley
480 and Cardott, 2016). Basins that suffer from overpressures retard VR values and can
481 again underestimate the maturity of source rocks, as the increased pressure reduces
482 the thermochemical reaction rate of OM (Carr, 2000).

Carr (2000) developed a flow chart to determine the source of low vitrinite reflectance, whether suppression or retardation (Fig. 2.10). Conditions that are associated with suppression and/or retardation of VR values are commonly encountered in shale gas exploration, as the shale targets are typically composed of Type II kerogens with abundant hydrogen-rich amorphous organic matter (AOM), as well as being generally composed of >50 m thick impermeable shales that have been deeply buried creating slightly to highly overpressured conditions (Jarvie, 2012). This leads to uncertainty when measuring the maturity of organic matter in shale gas targets, in addition to the fact that primary vitrinite particles are often small and sparse to absent in marine Type II shales and that there is an increased likelihood of vitrinite particles being altered by physical and chemical weathering during transport to marine basins.

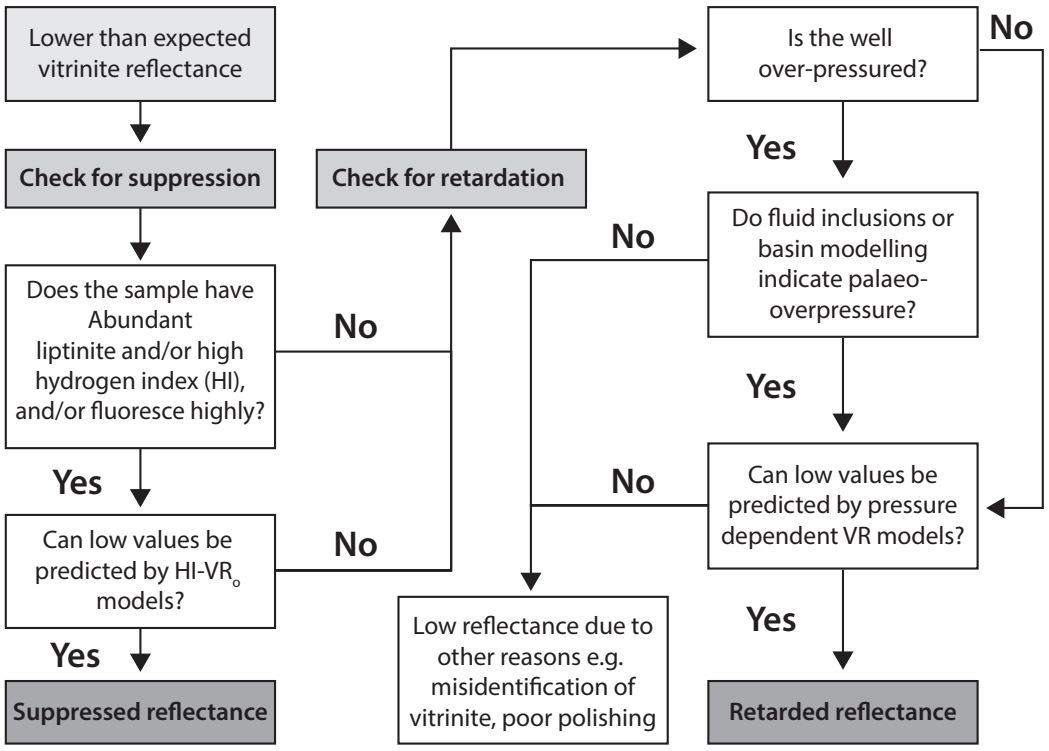


**Figure 2.10.** Flow chart of the steps for determining vitrinite reflectance suppression and/or retardation in sedimentary rocks. Adapted from Carr (2000).

VR is performed on highly polished blocks, which can also lead to additional sources of error, as improper polishing can lead to relief and scratches on the vitrinite grains, which will impact the reflective properties (ISO 7404-2, 2009). The polished sections also need to be kept in a desiccator overnight prior to the analysis to remove moisture in the pores, which could dilute the refractive index of the immersion oil. While conducting VR, the size of the measuring spot should be significantly smaller than the vitrinite grain, as a larger spot size will record a larger surface area that may include more surface imperfections, which may result in lower reflectance values. Measurements should also avoid vitrinite grains close to pyrite grains, as these are highly reflective.

Hackley et al. (2015) conducted a round-robin exercise to understand the interlaboratory reproducibility of VR. They showed that the reproducibility of the same sample in different laboratories ranged from 0.12 – 0.54 % from the absolute reflectance value and the reproducibility of the VR decreased consistently with increasing maturity. Organic-lean shales with high maturities had the poorest reproducibility between different laboratories and analysts. This is because high maturity vitrinite grains show substantial anisotropy, which results in high bireflectance (the difference between maximum and minimum reflectance values acquired using a rotating polarizer). The bireflectance can be as much as 2.5 – 4.0 % for high maturity samples (Teichmüller, 1987; Houseknecht and Weesner, 1997; Spötl, 1998; Liu et al., 2013). Shales containing proximal terrestrial material showed better levels of reproducibility, due to the higher concentration of primary vitrinite grains that can be easily identified; this is consistent with the earlier results of DeVanney and Stanton (1994).

Reflectance microscopy is also performed on other OM matter components that have been calibrated with vitrinite reflectance such as: graptolites (Volk et al., 2002; Wang et al., 2018), scolecodonts (Bertrand, 1990; Bertrand and Malo, 2012) and bitumen (Mählmann and Le Bayon, 2016; Hacley and Lewan, 2018). These alternative reflective microscopy methods are widely used when vitrinite particles are absent due to either the depositional setting or age of the sample.

529

530

531 **Transmitted Microscopy: Spore colouration index and thermal alteration index**

532 Spore colouration (SCI) and thermal alteration indices (TAI) are both studied using
533 strew slides under transmitted light. They assess the irreversible colour
534 transformation that happens to OM components as they undergo thermal alteration;
535 from a pale-yellow to a red/brown, to darker colour tones (Fig. 2.11, Harkopf -Fröder
536 et al., 2015). SCI assess the colour change of spores, while the TAI assesses most, if
537 not all organic components including: spores and pollen, conodonts, foraminifera,
538 ostracods, dinoflagellate cysts, acritarchs and AOM (Legall et al., 1981; Marshall, 1990;
539 Dean and Turner, 1994; Harkopf -Fröder et al., 2015; Schito et al. 2019). The scales
540 used for SCI and TAI are calibrated with vitrinite reflectance values and differ from
541 laboratory to laboratory (Fig. 2.11). The colours are usually assessed visually by
542 comparing the colours to a known colour standard that has been standardized and
543 correlated with vitrinite reflectance values, however this is very subjective.

544 A more quantitative approach has been applied by Duggan and Clayton (2008) by
545 measuring the RGB intensities. However, discrepancies using RGB intensities can be
546 caused by microscope and camera settings (Harkopf -Fröder et al., 2015). The
547 variation of colour measurements can also vary due to the thickness of the OM
548 components (Batten, 1996; Harkopf -Fröder et al., 2015). Nevertheless, being able to
549 use all the organic matter assemblages in a rock is very advantageous and therefore,
550 SCI and TAI can be used when vitrinite particles are rare and/or absent. Sporomorphs
551 (spores and pollen) date back to the late Silurian when the earliest signs of terrestrial
552 plant life were established, similar to vitrinite macerals. However, spores are more
553 ubiquitous in terrestrial and marine environments than vitrinite particles, as they are
554 transported to distal environments more easily (Richardson, 1996).

555

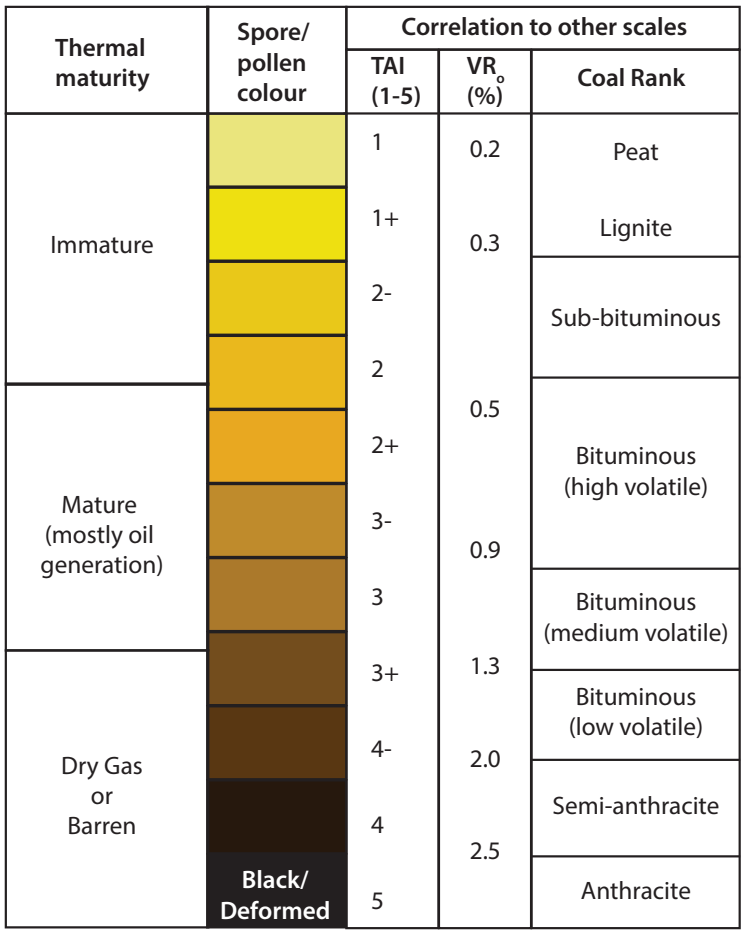


**Figure 2.11.** Pearson's (1984) colour chart for organic thermal maturity determination correlated with thermal alteration index (TAI) and vitrinite reflectance. Adapted from Traverse (1998).

## Fluorescence

Fluorescence microscopy is typically performed on liptinite materials. With increasing maturation, the fluorescence qualitatively evolves from yellow, orange-red to dark brown colours and then extinguishes at corresponding VR values of ~1.2 – 1.3 %VR$_o$ (Hackley et al., 2013; Harkopf -Fröder et al., 2015). Each fluorescent maceral will have their own threshold that determines different stages of thermal maturity and are calibrated with VR. A more quantitative approach is the fluorescence alteration of multiple macerals (FAMM) method that is able to estimate the maturation of dispersed organic matter (DOM), as well as the hydrogen-richness of macerals (Wilkins, et al., 1995; Lo et al., 1997; Kalkreuth et al., 2004).

Figure 2.12 is a fluorescence alteration diagram where the fluorescence intensity after 700 seconds of excitation from a fluorescent light, is plotted against the fluorescence alteration ratio, which is the final fluorescence intensity divided by the initial fluorescence intensity. The 'normal' vitrinite particle trend is plotted (Wilkins et al., 1995). The fluorescence alteration ratio is related to the thermal maturity, whereas the final fluorescence at 700 s is associated to the concentration of hydrogen. This can be used to identify and differentiate between inertinite, liptinites and sybhydrous or peryhydrous vitrinite grains, depending on which side of the 'normal' vitrinite trend line the data plots on. The major disadvantage of fluorescence is that it can only be used on samples with maturities between 0.4 – 1.2 %$VR_o$, so it has limited use for shale gas exploration where VR values of > 1.4 %$VR_o$ are recommended (Jarvie et al., 2007).

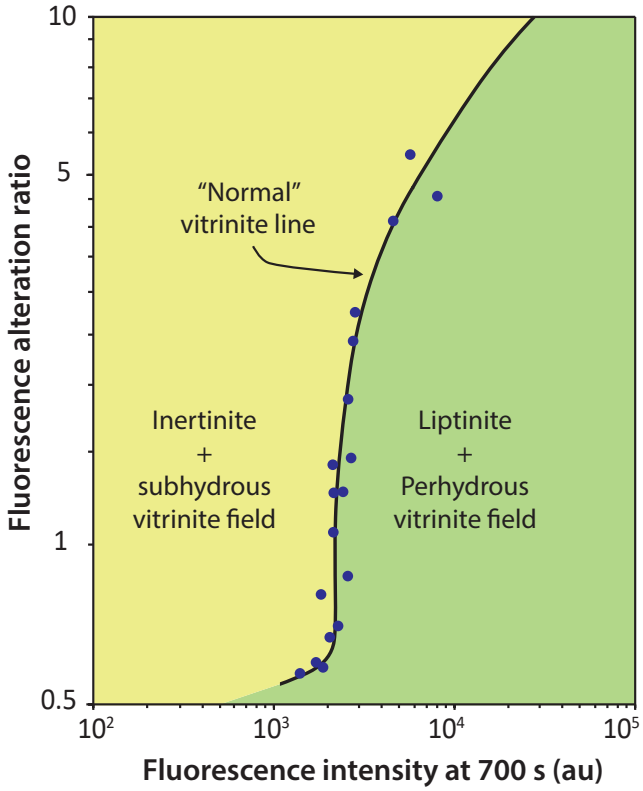


**Figure 2.12.** A fluorescence alteration diagram from Wilkins et al. (1995). The line represents a normal vitrinite path from Australian Permian and Triassic coals and divides the diagram into two fields: inertinite and/or subhydrous vitrinite (left/yellow field) and liptinites and/or peryhydrous vitrinite (right/green field). The fluorescence alteration ratio reflects the maturity and the fluorescence intensity at 700 seconds represents the hydrogen concentration.

#### *2.2.1.2 Geochemical methods*

**Rock-Eval Pyrolysis**

Rock-Eval pyrolysis is used to measure both the richness and maturity of a source rock (Tissot and Welte, 1984; Espitalié et al., 1997). Figure 2.33 shows how an experiment is run for Rock-Eval pyrolysis. A rock will be exposed to 300 °C for a set amount of time and the free hydrocarbons already present in the rock will be volatized, followed by progressively heating the sample up to 650 °C in an inert atmosphere; the rock is then allowed to cool down. During this heating process the quantities of hydrocarbons and $CO_2$ are measured using a flame ionisation detector (FID) and an infrared cell respectively.

The S1 peak (mg hydrocarbons/g rock) is the amount of free hydrocarbons that was already present in the rock; the S2 peak (mg hydrocarbons/g rock) is the amount of hydrocarbons than has been generated by pyrolysis and the S3 peak (mg $CO_2$/g rock) is the quantity of $CO_2$ produced by pyrolysis. The S4 (mg carbon/g rock) is also measured and is the residual carbon content in the rock. The temperature at which the S2 peak occurs is known as the $T_{max}$ and is an indicator of the maturity, particularly for immature and highly matured samples. The higher the $T_{max}$ values the more mature the rock is (Table 2.2).

With increasing thermal maturity, the S2 peak becomes less intense (Fig. 2.13) and therefore the $T_{max}$ parameter becomes less reliable for high maturity samples, as the S2 peak becomes less discernible. The disadvantages in using the S2 peak, is that it can be modified due to non-indigenous hydrocarbons, such as drilling additives, migrated hydrocarbons and/or heavy free hydrocarbons that have not been volatized. In organic-lean or high-maturity samples, the S2 peak is often flat and it is difficult to determine the $T_{max}$ temperature.

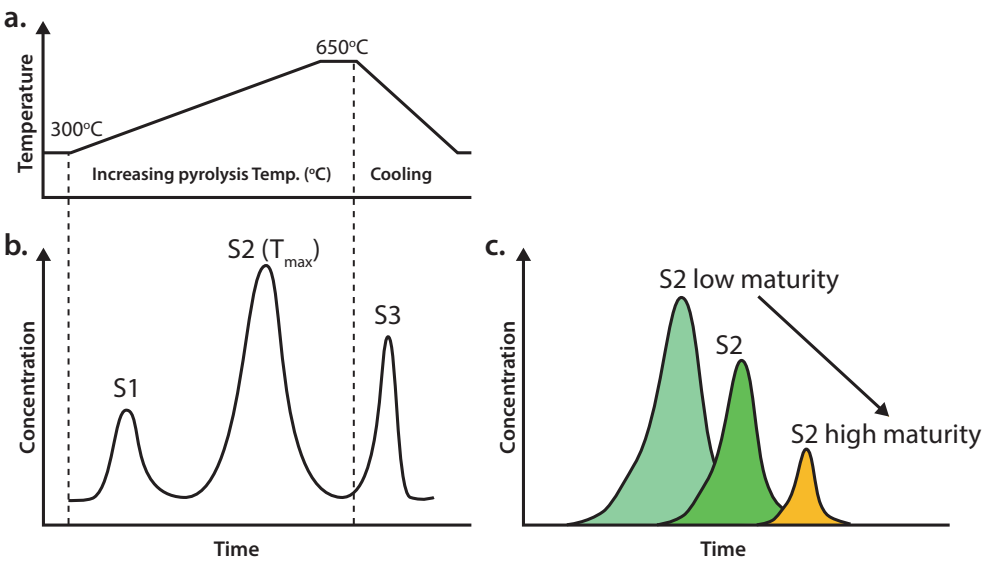


**Figure 2.13.** Idealised Rock-Eval pyrolysis analysis and results. **(a)** A rock will be progressively heated from 300 °C to 650 °C and then the rock will be allowed to cool down. **(b)** during the pyrolysis, free (S1) and generated hydrocarbons (S2) and $CO_2$ (S3) will be released and the concentrations are measured. **(c)** The S2 is related to the maturity of the rock. With increasing maturity, the S2 peak will shift to the right (at higher temperatures) and become smaller. Adapted from Espitalié et al. (1977).

**Table 2-2.** $T_{max}$ values and their associated maturity for oil generation. From Peters and Cassa (1994).

| **Maturity** | **$T_{max}$ (°C)** |
|---|---|
| Immature | < 435 |
| Early Maturity | 435 to 445 |
| Peak Maturity | 445 to 450 |
| Late Maturity | 450 to 470 |
| Post-mature | > 470 |

The production index (PI) is another measure of maturity (Table 2.2) and can be calculated using the Rock-Eval parameters in Equation 2.4. The hydrogen index and oxygen index can also be calculated using the Rock-Eval parameters using Equations 2.5 and 2.6, which can also be used to estimate the maturity of a source rock on a

626 modified van Krevelen diagram. Rock-Eval pyrolysis can also be used to determine the
627 total organic carbon (TOC) in a sedimentary rock using Equation 2.7.

628 $$PI = \frac{S_1}{S_1+S_2}$$ **Equation 2.4**

629 $$HI = \frac{S_2}{TOC \times 100}$$ **Equation 2.5**

630 $$OI = \frac{S_3}{TOC \times 100}$$ **Equation 2.6**

631 $$TOC\ (\%) = \frac{[0.082(S_1+S_2)+ S_4]}{10}$$ **Equation 2.7**

632

633 **Table 2.6.** Production index values with their associated hydrocarbon generation zone. Values from
634 Espitalie et al. (1977).

| Generation Class | Production Index (PI) |
|---|---|
| Immature | < 0.10 |
| Oil generation | 0.10 – 0.40 |
| Gas generation/oil cracking | > 0.40 |

635

636 The limitation of using $T_{max}$ and PI is that rocks can contain a heterogeneous
637 assemblage of kerogens types, which can produce unreliable results, as different
638 kerogen types yield oil and gas at different temperatures. Therefore mono-maceral
639 kerogen assemblages (a rock containing one type of kerogen greater than or equal to
640 95% by volume) are better suited. Contamination from oil-based mud, lignite and free
641 heavy hydrocarbons that were not totally volatized can also cause discrepancies in the
642 results, as well as the presence of other types of non-indigenous hydrocarbons.

643 **Biomarkers**

644 Biomarkers are organic molecules that have been preserved in sedimentary rocks.
645 Biomarker analyses is performed using a gas chromatography mass spectrometer (GC-
646 MS), which can measure the relative abundances of biomarkers such as alkanes,
647 steranes, hopanes and trisnorhopane, that can be used to estimate the source rock

maturity, as well as the depositional environment and the origin of organic matter. The basic theory for maturity assessment is to obtain the relative abundances and/or ratios of biomarkers that are either stable or unstable at high temperatures.

The Carbon Preference Index is the relative concentrations of n-alkanes in the $C_{14}$ to $C_{36}$ range. High concentrations of odd-dominant alkanes in this range indicate immature OM, whereas a reduction of the odd-dominant alkanes reveals that the oil window has been reached. The Methyl-Phenantrene Index is the relative concentration of thermodynamically stable 2 and 3 methylphenantherene and the less stable 1 and 9 methylphenantherenes. Hopanes are also used, where the more stable $C_{31}$ hopane 22S and $C_{30}$ hopane $\alpha\beta$ increases with maturity (Hartkopf-Fröder et al., 2015). This is the same for steranes, as the biological 22R form converts to the thermodynamically more stable 22S form, and the ratio of the two can be used to estimate the maturity of the source rock.

The limitations of biomarkers are that they are only applicable in specific maturity ranges and that the concentration of biomarkers reduce with increasing maturity, hence they cannot be used for high-maturity samples (Peters and Moldowan, 1993; Hartkopf-Fröder et al., 2015). The bulk analysis and contamination problems mentioned for Rock-Eval pyrolysis are also applicable for biomarkers.

### *2.2.2 Non-organic methods*

Non-organic methods are useful for determining the thermal maturity of sedimentary rocks where there is a lack of OM present.

**Illite Crystallinity**

Illite crystallinity, also known as the Kübler Index (Kübler, 1964), is a technique that determines the half-height width of the illite peak at 10 Å using an X-ray diffractometer (XRD) on the < 2 µm clay fraction. The illite crystallinity values decrease with increasing temperatures (Fig. 2.14). The properties of illite are dependent on the temperature, thermal gradient, chemical environment, time and surrounding tectonic stress of the rock, which means that it has the potential to track the thermal evolution;

676 however, it should be used with caution and may not have a direct relationship with
677 VR, as it follows a more complex and different kinetic reaction. However, it can be
678 particularly useful when used in conjunction with organic matter maturation data.
679 Ferreiro Mählmann et al. (2012) showed that for high heat flows, organic matter
680 matures faster than the clay mineral reaction, and for low heat flow clay mineral
681 reactions are faster than OM maturation. Therefore, by using the two methods
682 simultaneously, the changes in thermal gradient between wells can be qualitatively
683 assessed. The operator will also need to be aware that allochthonous and
684 autochthonous mineral assemblages may have substantially different maturity results
685 depending on the detrital bulk analysis origin of illite, similar to VR, however, unlike
686 VR, they cannot be distinguished as illite crystallinity is measured by performing a bulk
687 analysis (Arostegul et al., 2019).

688

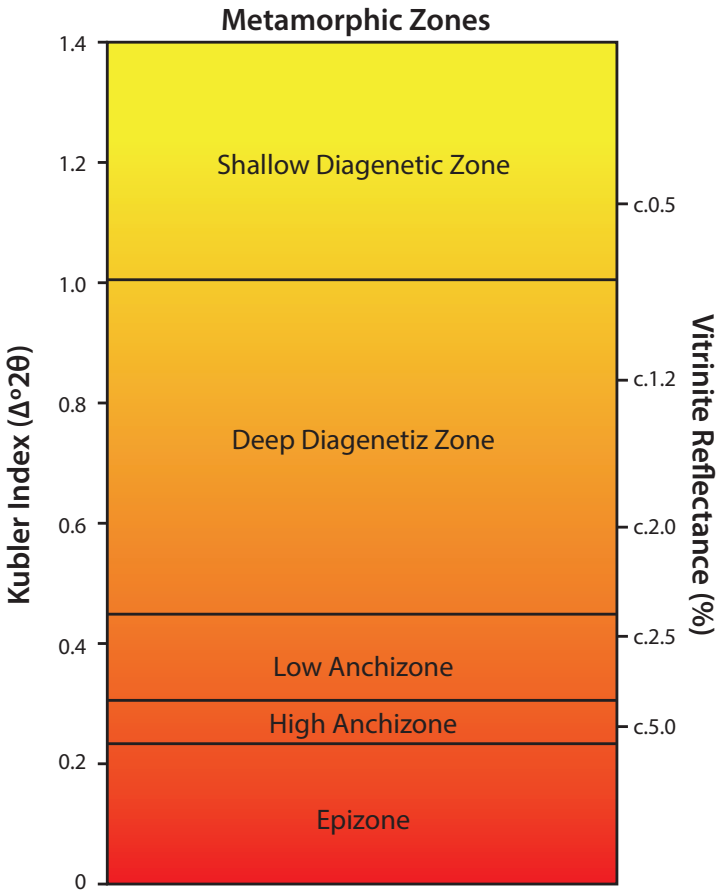


689

690 **Figure 2.14.** Comparison of the illite crystallinity, metamorphic zone, temperature and vitrinite
691 reflectance. Adapted from Verdel et al. (2011).

692

693 **Fission Track Analysis**

694 Apatite fission tracking is unique as it can estimate the cooling rates, as well as the
695 maximum temperatures reached in a sedimentary rock. It is therefore used to study
696 how the temperature varies during burial and uplift (Naeser, 1979; Allen and Allen,
697 2013; Hartkopf-Fröder et al., 2015; Malusà and Fitzgerald, 2019 and references
698 therein). The spontaneous fission decay of $^{238}U$ in an apatite or zircon grain creates
699 what is known as a 'track', that needs to be polished and chemically etched (nitric
700 acid) before it can be seen under a microscope. The lengths of the fission tracks are in
701 equilibrium with the maximum temperature at a specific time. Longer tracks are
702 associated with lower temperatures and shorter tracks are associated with higher
703 temperatures. Spontaneous fission occurs continuously, therefore measuring the

distribution of track lengths enables operators to understand the timing and variations of maximum temperatures experience by each set of fission tracks (Fig. 2.15).

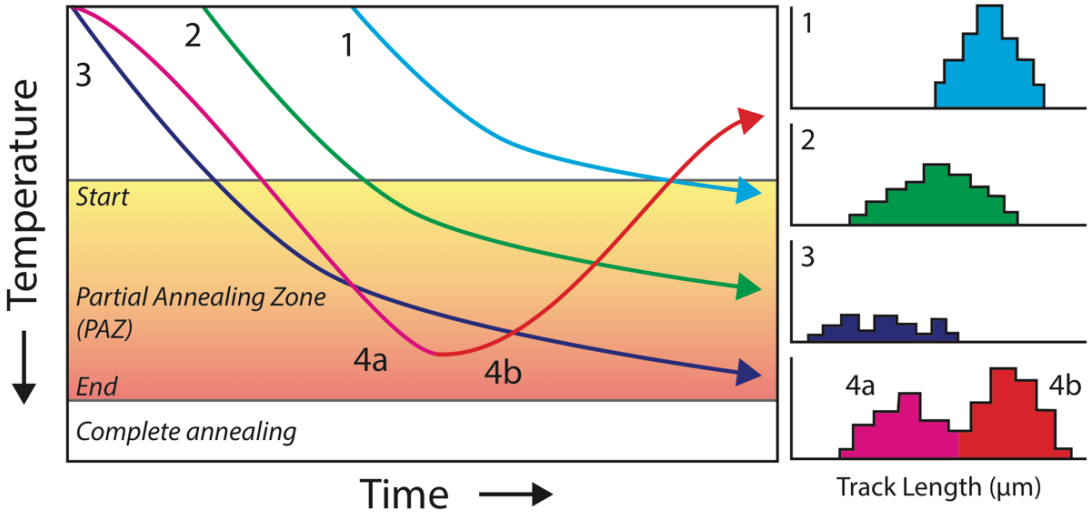


**Figure 2.15.** Theoretical time-temperature paths, with idealised illustrations of the distribution of fission track lengths for each path. Adapted from Ravenhurst and Donelick (1992).

However, the tracks undergo partial annealing and complete annealing of the tracks occurs at c. 120 °C (c. 1.2 %$VR_o$) for apatite (Corrigan, 1993) and c. 240 ± 40 °C (c. 4.0 %$VR_o$) for zircon (Hurford, 1986). Therefore, apatite fission track analysis has a limited temperature range which would not be suitable for estimating the maturity of rocks for conventional thermogenic gas or shale gas exploration. Zircon fission track analysis has a much wider range that is applicable for samples from the oil and gas generation windows. Nevertheless, the annealing and resetting of the fission tracks can still play an important role in understanding the thermal history of the area, especially when the data are combined with other maturity parameters.

## 2.3 Laser Raman spectroscopy theory

The Austrian physicist A. Smekal theoretically predicted the inelastic scattering of light in 1923 (Smekal, 1923); however, it was not until 1928, when C.V. Raman first observed this phenomenon and later published the article “A new type of secondary radiation” in Nature (Raman and Krishnan, 1928) that the concept was proven. This

new secondary radiation was later known as the Raman effect. Shortly after, C.V. Raman was awarded the Nobel Prize for Physics in 1930. Raman is now a widely used tool in molecular spectroscopy and has many applications in all branches of natural sciences (Lewis and Edwards, 2001 and references therein). Its popularity has grown, as it is a rapid, non-destructive method, that requires little or no sample preparation, and analysis can be achieved on a micrometre scale depending on the laser spot size (2 – 100 μm) (Smith and Dent, 2005 and references therein).

Spectroscopy is the study of how light interacts with a material. The most common methods of spectroscopy include fluorescence, infrared and Raman. Infrared and Raman belong to vibration spectroscopy, as it measures the vibrational energy levels of a material when it interacts with an incident light (Ferraro et al., 2003 and references therein). Infrared spectroscopy studies how much of the light is absorbed, whereas Raman spectroscopy measures how much light is scattered due to molecular vibrations. In order for a vibration to be infrared active, the molecular dipole moment must change during the vibration. For it to be Raman active, there must be a change in polarizability during vibration. Polarization is when the cloud of electrons around the nuclei deforms to form a short-lived state known as a 'virtual state' (Fig. 2.16. This state is highly unstable, and instantaneously decays to the final state, as shown in the energy level diagram in Figure 2.16. In general, polar groups with antisymmetric vibrational modes tend to be stronger in IR spectroscopy, whereas symmetric vibrational modes are stronger in Raman spectroscopy. Figure 2.16 also shows the main difference between IR absorption and Raman scattering; infrared absorption depends on the direct excitation of a molecule from a ground state to a vibrational state.

There are two types of scattered light, inelastic and elastic, which can be explained using the energy level diagram (Fig. 2.16). The elastic scattering of light is known as Rayleigh scattering, and is when the frequency of the scattered light is unchanged, as the electron decays back to the same energy state of the incident light (Fig. 2.16). No information regarding the molecular vibration is eluded. The inelastic scattering of light is known as the Raman effect, and it is associated with a change in frequency of

754 the incident light, as the cloud of electrons decays back to a different energy state (Fig.
755 2.16).

756 Raman scattering is a lot less common than Rayleigh scattering, as only one Raman
757 photon is produced for every $10^6$ to $10^9$ photons that are scattered (Ewen and Dent,
758 2005). During Raman scattering, if the frequency is lower (hence longer wavelength)
759 than the incident light a red shift is observed, known as Stokes scattering and the
760 energy state is promoted to a higher energy state (Fig. 2.16c). When the frequency is
761 greater (hence shorter wavelength) than the incident light a blue shift occurs known
762 as Anti-Stokes scattering and the energy state drops to a lower energy state (Fig.
763 2.16c). Stokes scattering occurs when the sample is originally at a ground vibration
764 state and Anti-Stokes occurs when the sample is already in an excited vibrational state
765 (which is less common at room temperature) and therefore the incident light gains
766 energy from the already vibrating molecule and hence why there is an increase in
767 frequency.

768

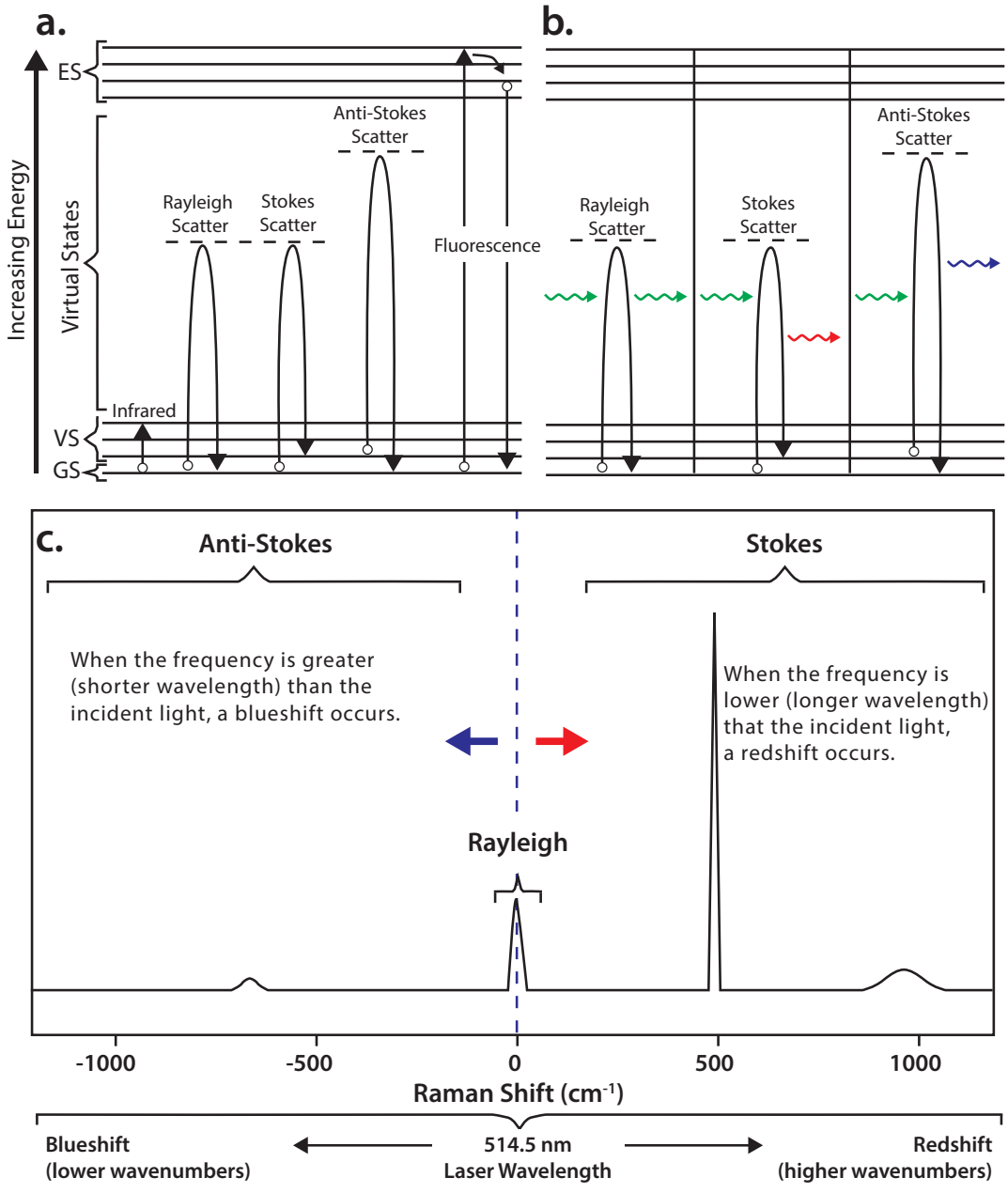


769

770 **Figure 2.16.** Diagram highlighting the difference between Stokes Raman scattering and the other
771 vibration spectroscopy techniques. **(a)** Vibrational excitation diagram, showing the different types of
772 vibrational spectroscopy and fluorescence spectroscopy. GS: ground state; VS: vibrational state; ES:
773 electronic state. The dashed lines represent the virtual states. **(b)** Frequencies of scattered light
774 compared to the incident light. The change in frequency is due to the interaction of the molecular
775 vibrations within the sample, which may lead to a change in scattered frequency. Most of the scattered
776 light frequency is unchanged (Rayleigh). Stokes is when there is an increase in frequency and Anti-
777 Stokes is when there is a decrease in frequency. **(c)** Illustration of a Raman spectrum of silicon using a
778 laser wavelength of 514.5 nm, which corresponds with the Rayleigh band. Stokes and anti-Stokes
779 scattering occur when the wavelength of the incident light becomes longer and shorter respectively. In
780 Raman spectroscopy, the Stokes region is used.

The energy difference between the initial and final state is known as the Raman shift ($\Delta v$, **Equation 2.2**) and is characteristic of the molecular structure and the lattice vibration of a molecule.

$$\Delta v = \frac{\mathbf{1}}{\lambda\ incident} - \frac{\mathbf{1}}{\lambda\ scattered} \qquad \textbf{Equation 2.2}$$

Where, $\boldsymbol{\lambda}$ is the wavelength in $cm^{-1}$ of the incident light and the scattered light. When the frequency difference is equal to the energy at which a molecule will vibrate, then a peak will be present at the corresponding wavenumber on a spectrum. Therefore, the Raman shift can be used as a means of molecular fingerprinting. For example, diamonds which are composed of purely carbon molecules with the same structural configuration, will have one peak that occurs at a Raman shift of c. 1332 $cm^{-1}$. A more complex material, with various molecules and structures, will have a unique combination of several peaks each corresponding to a particular molecular structure. When the value of $\Delta v$ is 0 $cm^{-1}$ then there is no loss or gain in energy (Rayleigh scatter); when there is a negative $\Delta v$, then it is known as anti-Stokes scattering; and when there is a positive $\Delta v$, then it is known as Stokes scattering (Fig. 2.16c and Equation 2.2).

The intensity of the Raman signal is directly proportional to the incident laser wavelength:

$$\boldsymbol{I} \propto \frac{1}{\lambda^4} \qquad \textbf{Equation 2.3}$$

Where, $I$ is the intensity and $\lambda$ is the excitation wavelength. Therefore, the Raman signal using a 514 nm laser will be ~2.3 times stronger than using a 633 nm laser. Hence, using a shorter wavelength will produce more scattering. This is because shorter wavelengths have a higher frequency and will interact with the object more often than a longer wavelength would (Fig. 2.17).

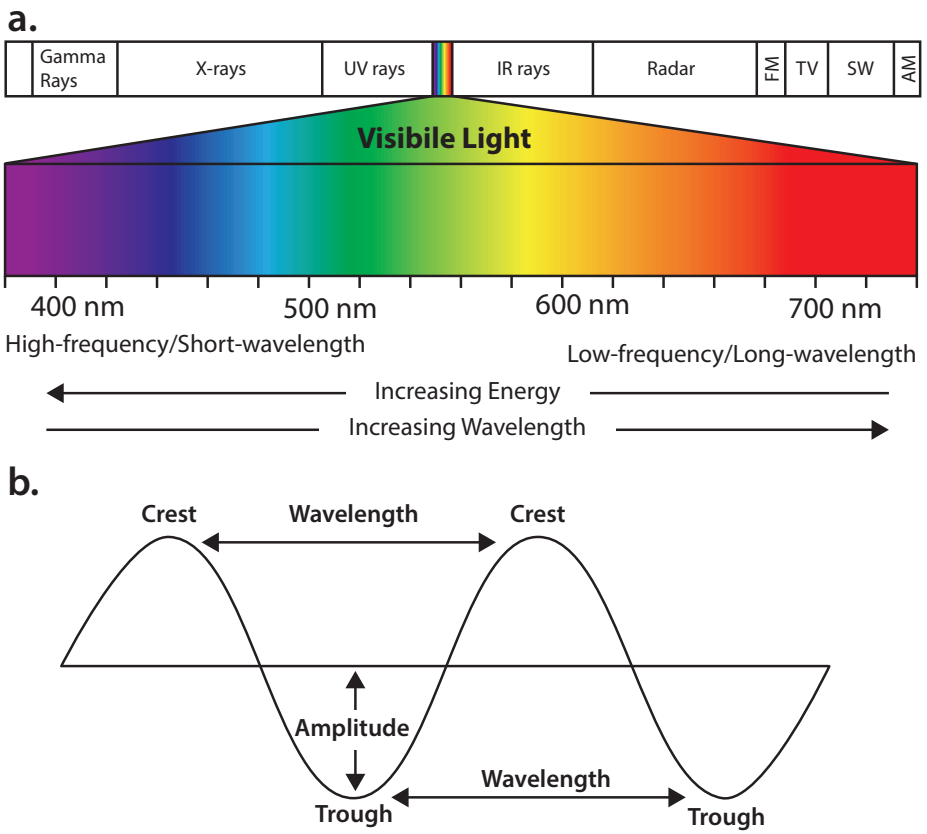


806

807 **Figure 2.17.** The electromagnetic spectrum of visible light along with the associated wavelengths. **(a)**
808 Visible light spectrum showing that with increasing wavelength there is a decrease in energy and vice
809 versa. **(b)** Anatomy of a wave showing the wavelength, amplitude, crest and trough. With decreasing
810 wavelength, the light has a higher frequency and thus interacts with a material more times than a lower
811 frequency light.

812

813 Since Raman spectroscopy is vibrational spectroscopy, it is a good idea to understand
814 what controls molecular vibrations. A molecule is composed of atoms that are joined
815 together by chemical bonds. When the molecule is excited, the atoms and bonds
816 experience a periodic motion. The frequency of this motion is dependent on the
817 atomic mass of the molecules and the type of bonding. For example, heavy atoms that
818 have a weak bond will vibrate at a lower frequency and will therefore produce a peak
819 with a low Raman shift. This is because the difference between the incident and
820 scattered wavelength has not changed significantly (Equation 2.2). Whereas, lighter
821 atoms with a strong bond will vibrate at a higher frequency, as a result, the Raman

band will have a higher Raman shift. This is because the difference between the incident and scattered wavelength is greater (Equation 2.2).

Consider the molecules C–C and C=C. Both the molecules have the same mass but have different bonds: the C=C has a stronger double bond that vibrates at a frequency of ~1580 – 1650 $cm^{-1}$ and C–C has a weaker bond and vibrates at a lower frequency of ~700 – 1250 $cm^{-1}$. Now consider the C=C and C=S molecules. Both have double bonds, but because S has a higher mass it will vibrate at a lower frequency and thus it will have a lower Raman shift between ~1000 – 1200 $cm^{-1}$. Using this information, the Raman spectrum can reveal important chemical and structural information. For example, the major elements that are common in kerogen are carbon, hydrogen, oxygen, nitrogen and sulphur (Table 2.3), although the relative concentrations are highly variable depending on the original precursor composition and maturity. Using the theory discussed above we can expect that heavy molecules with weak bonds will have a low Raman shift and light molecules with double bonds, such as C=H bonds, will occur at higher Raman shifts.

**Table 2-3.** Major elements in kerogen and their atomic weights.

| **Element** | Carbon | Hydrogen | Oxygen | Nitrogen | Sulphur |
|---|---|---|---|---|---|
| **Atomic weight** | 12 | 1 | 16 | 14 | 32 |

The Raman spectrum has the Raman shift ($\Delta v$) on the x-axis (in $cm^{-1}$) and the relative intensity of the Raman bands on the y-axis. The key features used to analyse a spectrum are the position of the Raman bands (Raman shift), the relative shifting of individual bands, their relative intensities (y-axis) and the narrowing or broadening of individual bands (Fig. 2.18). The positions of the bands can be used to identify the composition of the material; the shift of individual bands can be related to the potential stress/strain brought on by pressure and/or temperature; the relative intensity of different peaks alludes to their concentrations; and the narrowing or

broadening of the bands indicate the crystalline quality, the narrower it is, the more ordered the crystal lattice is.

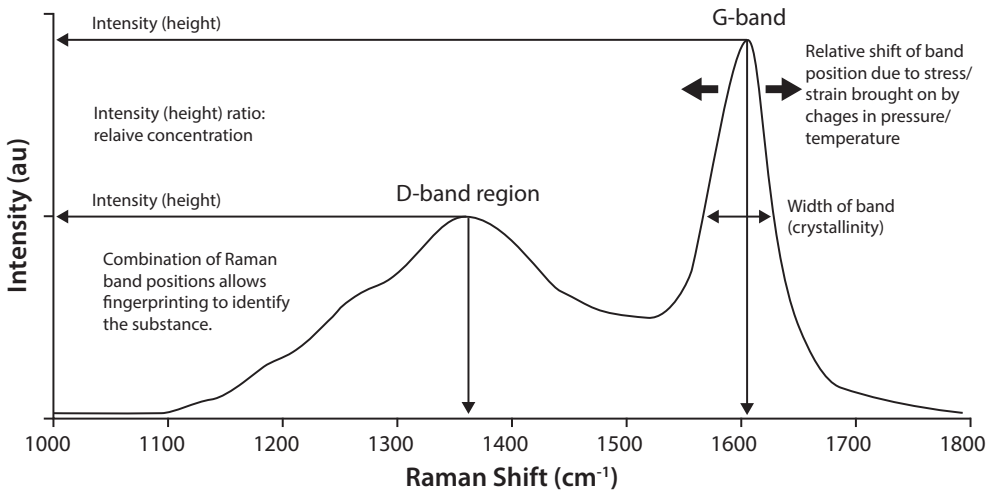


**Figure 2.18.** Analytical results for a carbon sample illustrating the different ways to interpret a Raman spectrum: band intensity; peak position; the width of a band; and the shifting of a band. The Raman shift is on the x-axis and the intensity of the bands are measured on the y-axis.

## 2.4 Summary

This chapter has dealt with important aspects that we consider operators should have prior knowledge of, when using Raman spectroscopy as a thermal maturity tool on organic matter (OM). A review of the traditional thermal maturity methods highlights that not one method can be universally applied to all organic matter particles and rock-types. There is therefore a need to have a wide selection of thermal maturity tools that can be called upon depending on the kerogen type, rock type, thermal maturity grade and the presence of specific organic matter particles, as well as other factors such as time, money and expertise constraints.

The following chapter will provide an in-depth review of the geological application of Raman spectroscopy, which will highlight some of the current issues that the community need to solve, as well as the advantages and limitations of the method.

# *Chapter 3* Raman spectroscopy as a tool to determine the thermal maturity of organic matter: reviewing the application to sedimentary, metamorphic and structural geology studies

This chapter is based on a paper published in *Earth-Science Reviews*: Henry, D.G., Jarvis, I., Gillmore, G., Stephenson, M., 2019. *Raman spectroscopy as a tool to determine the thermal maturity of organic matter: reviewing the application to sedimentary, metamorphic and structural geology studies. Earth-Sci. Rev. 198, doi: 10.1016/j.earscirev.2019.102936.*

## 3.1 Abstract

Raman spectrometry is a rapid, non-destructive alternative to conventional tools used to assess the thermal alteration of organic matter (OM). Raman may be used to determine vitrinite reflectance equivalent OM maturity values for petroleum exploration, to provide temperature data for metamorphic studies, and to determine the maximum temperatures reached in fault zones. To achieve the wider utilisation of Raman, the spectrum processing method, the positions and nomenclature of Raman bands and parameters, all need to be standardized. We assess the most widely used Raman parameters as well as the best analytical practices that have been proposed. Raman band separation and G-band full-width at half-maximum are the best parameters to estimate the maturity for rocks following diagenesis–metagenesis. For metamorphic studies, the ratios of band areas after performing deconvolution are generally used. Further work is needed on the second-order region, as well as assessing the potential of using integrated areas on the whole spectrum, to increase the calibrated temperature range of Raman parameters. Applying Raman

spectroscopy on faults has potential to be able to infer both temperature and deformation processes. We propose a unified terminology for OM Raman bands and parameters that should be adopted in the future. The popular method of fitting several functions to a spectrum is generally unnecessary, as Raman parameters determined from an un-deconvoluted spectrum can track the maturity of OM. To progress the Raman application as a geothermometer a standardized approach must be developed and tested by means of an interlaboratory calibration exercise using reference materials.

## 3.2 Introduction

Raman spectroscopy is increasingly being used to determine the thermal alteration (maturity) of organic matter (OM). The novelty of Raman spectroscopy is that it is a rapid and non-destructive technique that can be used to complement other methods or it can be employed independently, and it offers a means to screen samples before more expensive and destructive analysis (Sauerer et al., 2017; Schmidt et al., 2017; Henry et al., 2018, 2019; Khatibi et al., 2018b; Schito and Corrado, 2018; Wilkins et al., 2018). Raman spectroscopy is now part of a wide selection of tools that can be used to track the thermal maturity of OM. These include: vitrinite reflectance ($VR_o$); bitumen reflectance; graptolite reflectance; chitinozoan reflectance; spore colouration index; OM fluorescence; organic geochemistry, including Rock-Eval™ pyrolysis and biomarker analysis (Hartkopf-Fröder et al., 2015). Having a selection of methods to determine OM maturity allows geoscientists to optimize their analysis based on the quantity, composition and age of the sample, maturity grade, operator expertise, equipment availability, and time and money constraints.

Tuinstra and Koenig (1970) published the first paper showing two distinct Raman bands in graphite: the disordered (D) and graphite (G) bands. Beny-Bassez and Rouzaud (1985) highlighted the first use of Raman spectroscopy to determine the coalification and graphitization stages of OM by studying samples that had been artificially heated; they were also the first authors to construct an empirical relationship with $VR_o$. Pasteris and Wopenka (1991) then applied Raman spectroscopy in a study of naturally metamorphosed carbonaceous metapelites in order to assess

923 the metamorphic grade by conducting visual comparisons. Wopenka and Pasteris
924 (1993) later demonstrated that the area ratio of the D and G bands are effective in
925 determining the metamorphic grade of metamorphic rocks. Following this, Spötl et al.
926 (1998) used natural samples to demonstrate that Raman spectroscopy may be used
927 to determine equivalent $VR_o$ values for a wide maturity range (0.38–6.10 $\%VR_o$).
928 Beyssac et al. (2002) derived the first temperature dependent empirical equation, in
929 order to quantitively determine the peak temperature between 330–650 °C during
930 metamorphism. This was a turning point, and the study encouraged the wider use of
931 Raman spectroscopy as a geothermometer for geological samples, with an
932 exponential increase in papers being published over the last 25 years (Fig. 3.1).

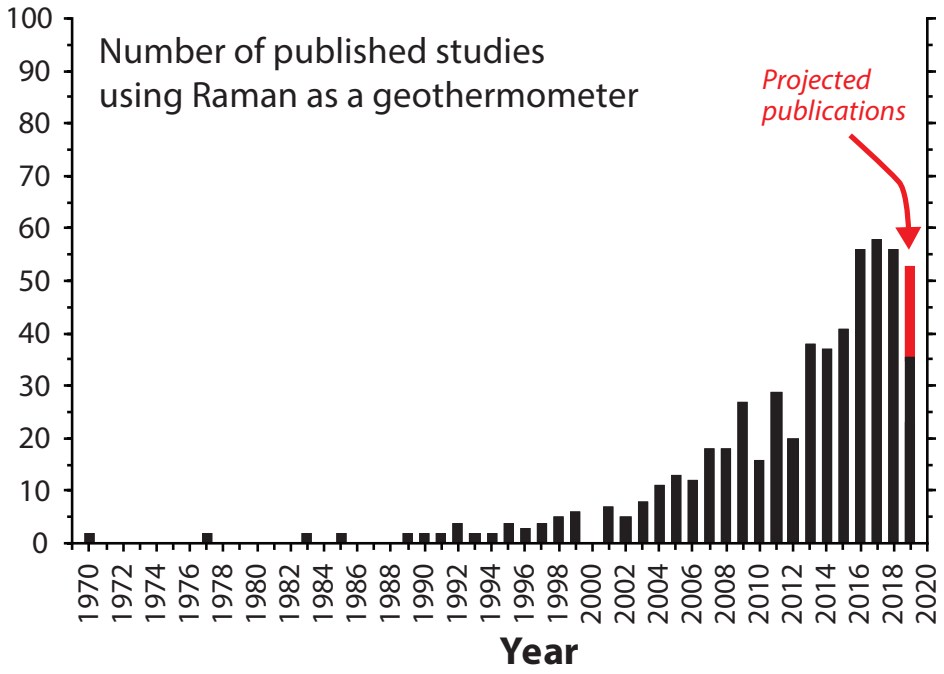


933

934 **Figure 3.1.** Bar chart showing the exponential increase in studies that have used Raman
935 spectroscopy as a geothermometer. The data were acquired from the Web of Science
936 bibliography database and is by no means an exhaustive data set. Projected publications for
937 2019 is based on the number papers that were published during the same period for 2018.

938

939 Raman spectroscopy has been used in three main applications as a geothermometer,
940 to determine: (1) source rock maturity for hydrocarbon exploration (Liu et al., 2013;

941 Sauerer et al., 2017; Schito et al., 2017. 2019; Schito and Corrado, 2018; Wilkins et al.,
942 2018; Henry et al., 2019; Hou et al., 2019; Khatibi et al., 2019; Lupoi et al., 2019; Mi et
943 al., 2019; Wang et al., 2019); (2) the maximum temperature reached during regional
944 and contact metamorphism (Wopenka and Pasteris, 1993; Beyssac et al., 2002;
945 Jehlička et al., 2003; Rahl et al., 2005; Aoya et al., 2010; Lahfid et al., 2010; Endo et al.,
946 2012; Mathew et al., 2013; Nakamura and Akai, 2013; Hilchie and Jamieson, 2014;
947 Kouketsu et al., 2014; Muirhead et al., 2017a, b; Chen et al., 2017; Beyssac et al., 2019;
948 Fomina et al., 2019; Kouketsu et al., 2019; Yu et al., 2019; Zhang and Santosh, 2019);
949 (3) the maximum temperature reached during frictional heating along fault planes
950 after an earthquake (Furuichi et al., 2015; Kaneki et al., 2016; Liu et al., 2016; Kouketsu
951 et al., 2017; Kuo et al., 2017, 2018; Kaneki and Hirono, 2018, 2019; Mukoyoshi et al.,
952 2018). Studies have had various degrees of success, and due to widely varying
953 methodologies, comparison of the results remains difficult. Here, we review the most
954 commonly used and suitable Raman parameters for each application, as well as assess
955 the best practices that have been proposed, in an attempt to encourage a
956 standardised approach. We will also provide recommendations for future progress.

## 957 3.3 Thermal maturation of organic matter

958 Determining the maturity of OM is essential to confirm the presence of a working
959 petroleum system and to establish the time-temperature history of geological events.
960 When OM is exposed to high temperatures, it undergoes an irreversible chemical and
961 structural evolution (Tissot and Welte, 1984), which makes it an ideal component to
962 determine the maximum temperature reached in a sedimentary or metamorphic rock.
963 This is in contrast to mineral assemblages, where temperature records may be reset
964 by subsequent dissolution and recrystallization. However, different types of organic
965 matter in a sedimentary rock respond differently to increased temperatures. This
966 needs to be taken into consideration, as it has been shown to impact the Raman
967 spectrum (Guedes et al., 2005, 2010).

968 Tissot and Welte (1984) determined four different stages of thermal maturation
969 during burial: diagenesis, catagenesis, metagenesis, and metamorphism. Diagenesis
970 occurs as soon as deposition has taken place, and stops when temperatures reach 60–

971 80 °C (0–0.5 %$VR_o$; Tissot and Welte, 1984). Here microbial degradation and low-
972 temperature reactions destroy proteins and carbohydrate biopolymers, and the
973 remaining more resistant constituents polycondense to form geopolymers and
974 subsequently kerogen. By-products of diagenesis include $CO_2$, $H_2O$, $H_2S$, $SO_2$, $N_2$ and
975 biogenic $CH_4$. Catagenesis ranges from c. 60–150 °C (0.6–2.0 %$VR_o$) and the kerogen
976 is subject to thermal decomposition reactions that break up large kerogen molecules
977 to smaller kerogen molecules (Tissot and Welte, 1984). During early catagenesis oil is
978 mostly produced (0.5–1.3 %$VR_o$), followed by the production of wet gas (1.3–2.0
979 %$VR_o$; Tissot and Welte, 1984). Catagenesis is also associated with increased ordering
980 of the OM. Metagenesis occurs at temperatures c. 150–200 °C (2.0–4.0 %$VR_o$) and
981 produces primary dry gas directly from the remaining kerogen and secondary gas from
982 the cracking of longer chained hydrocarbons (Tissot and Welte, 1984). At the end of
983 this stage, heteroatoms and hydrogen have all been depleted by carbonisation, and
984 the residual carbon becomes disordered graphite that will undergo progressive
985 graphitization during metamorphism, eventually becoming a perfectly ordered
986 graphite with increasing temperatures and pressures (Landis, 1971; Buseck and
987 Beyssac, 2014).

988 Alternative mechanisms that can thermally mature OM include: the emplacement of
989 igneous intrusions (contact metamorphism); and frictional heating along fault planes
990 (Buseck and Beyssac, 2014). What differs here, is the way in which the OM is heated.
991 For burial, as described above, the OM is typically heated due to the geothermal
992 gradient and radiogenic heat production (Tissot and Welte, 1984; Allen and Allen,
993 2013). Diagenesis, catagenesis and metagenesis occur over long-time scales at
994 relatively low temperatures (<200 °C) and impact a whole basin; similarly, regional
995 metamorphism occurs over long-time scales with wide ranging effects, but at
996 significantly higher temperatures (200–1000 °C; Hoinkes et al., 2005). Contact
997 metamorphism may generate similar temperatures to regional metamorphism (200–
998 1000°C) but takes place over shorter time scales ($10^3$–$10^6$ years) and only matures OM
999 locally within the thermal aureole (Hoinkes et al., 2005). Maturation of organic matter
1000 due to frictional heating along fault zones is associated with rapid heating rates of tens
1001 to hundreds of °C $s^{-1}$, along with substantial shearing, deformation and pulverization

of the OM (Nakamura et al., 2015; Kaneki et al., 2016). There is no remnant heat that 'cooks' the country rock, unlike igneous intrusions; however, movement may occur multiple times along the same fault, thereby generating multiple episodes of heating.

It is widely acknowledged that temperature and time are the most important factors in the maturation process of OM (Beyssac et al., 2002; Allen and Allen, 2013); however, it is also crucial to understand how different heating rates, pressures and shearing/deformation impact the Raman spectra of OM. In order to get the most out of Raman spectroscopy as a geothermometer we must assess: (1) which parameters are best suited for each application; (2) whether different thermal and pressure conditions can be determined from OM Raman parameters or the visual appearance of the spectrum; (3) the extent to which shearing and pulverization of OM may impact the Raman spectrum; (4) whether different calibration curves are needed for OM that has experienced different time-temperature-pressure histories. Some of these questions have been asked and answered in different ways in the literature and will be addressed in this review.

## 3.4 Organic matter Raman bands and nomenclature

The Raman spectrum of OM is composed of a first-order region (1000–1800 $cm^{-1}$) and a second-order region (2400–3500 $cm^{-1}$). The first-order region comprises two main peaks; the disordered (D) band (c. 1340–1360 $cm^{-1}$) and the graphite (G) band (c. 1580 $cm^{-1}$) (Fig. 3.2a). The G-band is related to the in-plane vibration of carbon atoms in graphene sheets with $E_{2g2}$ symmetry (Tunistra and Koenig, 1970; Jehlička and Beny, 1999). In graphite, this is the only major band in the first-order region.

The D-band occurs at c. 1340–1360 $cm^{-1}$ in disordered amorphous OM and is associated with structural defects and heteroatoms (Beny-Bassez and Rouzaud, 1985). It has been described as the breathing motion of the sp2 atoms in an aromatic ring with a $A_{1g}$ symmetry mode vibration (Tunistra and Koenig, 1970). In disordered OM, additional bands are identifiable as small bumps and asymmetric bands, however, the number, nomenclature and origin of these bands are often conflicting when deconvolution is performed (Beyssac et al., 2002; Li et al., 2006; Romero-Sarmiento et

al., 2014; Ferralis et al., 2016; Schito et al., 2017; Henry et al., 2018). The occurrence of the most common additional bands (Fig. 3.2b) are as follows: D2-band (c. 1610 $cm^{-1}$); D3-band (c. 1500 $cm^{-1}$); D4-band (1200 $cm^{-1}$); D5-band (c. 1260 $cm^{-1}$) and D6-band (c. 1440 $cm^{-1}$). The D2-band has been related to the disorder inside the graphitic lattice with $E_{2g2}$ symmetry (Allwood et al., 2006) and is merged with the G-band for low-ordered OM. With increasing maturity, the D2-band evolves, firstly appearing as a small bump on the red-shift shoulder of the G-band until it eventually splits from the G-band and disappears (Buseck and Beyssac, 2014). The D3-band results from the out-of-plane vibration due to defects and heteroatoms, which eventually disappear during graphitization (Wopenka and Pasteris, 1993; Beyssac et al., 2002; Baludikay et al., 2018). The D4- and D5-bands were related to the CH species in aliphatic hydrocarbon chains by Ferralis et al. (2016), as they demonstrated a strong correlation between the atomic H:C ratio and the band properties. The D6-band at c.1440 $cm^{-1}$ was recognised by Romero-Sarmiento et al. (2014), which in their study was termed the D5-band. They proposed that the D6-band is related to the hydrocarbons trapped within the micropores of organic matter. From now on, when we refer to fitted bands after performing deconvolution, they will be followed by the suffix 'function', for example D4-function.

The second-order region (2200–3400 $cm^{-1}$) has mostly been used for samples that have undergone metamorphism, as the bands are not clearly distinguished for lower maturity samples (Fig. 3.3). The region has a total of five bands with different evolutionary paths from disordered to ordered OM, and they begin to become identifiable at the anthracite stage (>2 $\%VR_o$; Pasteris and Wopenka, 1991; Wopenka and Pasteris, 1993; Cuesta et al., 1994; Spötl et al., 1998; Jehlička and Beny, 1999; Beyssac et al., 2002; Jehlička et al., 2003; Rantitsch et al., 2004; Zeng and Wu, 2007; Liu et al., 2013; Yuman et al., 2018). The most common interpretation of these bands is that they are mixture of overtones and combinations of different inelastic scattering of the bands in the first-order region (Wopenka and Pasteris, 1993; Beyssac et al., 2002; Childress and Jacobsen, 2017). For example, the S2-band at c. 2700 $cm^{-1}$ is an overtone of the D1-band at c. 1340$cm^{-1}$ (1340 x 2 = 2680 $cm^{-1}$), whereas the S3-band at c. 2950 $cm^{-1}$ is a combination of the D1 and G-bands (1350 + 1580 = 2930 $cm^{-1}$).

There is considerable inconsistency in the nomenclature and positions of the Raman bands used by different authors, and the number of bands used for analysis in both the first- and second-order regions; this leads to confusion when comparing results from different studies, which has inhibited the development of a standardized method. To avoid confusion in future publications, we propose to use the nomenclature described in Fig. 3.2 and Table 3.1 for the first-order region and Fig. 3.3 and Table 3.2 for the second-order region. The recommended number of bands to include during deconvolution is discussed in Section 3.6.1.

In the first-order region, the G-band has been referred to the "O" band, which stands for "ordered" (Wopenka and Pasteris, 1993; Spötl et al., 1998; Jehlička and Beny, 1999; Zeng and Wu, 2007; Schiffbauer et al., 2012; Liu et al., 2016) or the "G" band (Cuesta et al., 1994; Kelemen and Fang, 2001; Beyssac et al., 2002), which stands for "graphite", and the latter is a ubiquitous term used in most recent literature. However, Kouketsu et al. (2014) argued that it is not possible to determine the G-band at c. 1580 $cm^{-1}$ for low-grade OM, and therefore called the band at c. 1580 $cm^{-1}$ the "D2" band. Ito et al. (2017) used the D2-band abbreviation to be synonymous with the G-band; other studies have used "G-band" to be a combination of the G- and D2-bands (Henry et al., 2018, 2019). It is noted that the D2-band has been referred to as the D'-band (Marshall et al., 2005; Ammar and Rouzaud, 2012). By contrast, Jubb et al. (2018) located the D2-band position at c. 1520 $cm^{-1}$, where the D3-band is commonly placed, whereas Song et al. (2019) fitted the D2-band at c. 1700 $cm^{-1}$, where there is a known carbonyl group (C=O) vibration (Li et al., 2006).

The D1-band at 1350 $cm^{-1}$ was termed the "A" band by Kelemen and Fang (2001), as it represents the "amorphous" structure of the OM. Hu et al. (2015) also used unconventional nomenclature, calling the fitted function at 1336 $cm^{-1}$, the "D" band (instead of the D1-band) and the function at c.1200 $cm^{-1}$ band the "D1" band (instead of the D4-band). Ferralis et al.'s (2016) D5-band classification was previously used by Romero-Sarmiento et al. (2014), however their D5-band was located at c. 1440 $cm^{-1}$, rather than c. 1260 $cm^{-1}$. Ferralis et al. (2016) unconventionally named two bands in the same spectrum, the "D3" band. This lack of consistency is detrimental to the wider use of Raman and creates considerable confusion.

1093 We propose that the terminology outlined in Fig. 3.2 and Table 3.1 should be adopted
1094 for the first-order region of Raman spectra. The general term "D-band" is used for
1095 non-deconvoluted spectra; where deconvolution is performed individual D1 – D6
1096 'bands' (functions) can potentially be distinguished (Fig. 2).

1097

1098 **Table 3-1.** The proposed nomenclature for the Raman spectrum in the first-order region.

| Method | Proposed band nomenclature | Position ($cm^{-1}$) | Alternative nomenclatures | Notes |
|---|---|---|---|---|
| No deconvolution | D-band | c.1580 | A | |
| | G-band | c.1350 | O | |
| Deconvolution | G-function | c.1580 | $G_L$, O, D2 | If D2 is not fitted, assume that the band is a combination of G and D2. |
| | D1-function | c.1340 | D | |
| | D2-function | c.1610 | $G_L$, O, D2, G | |
| | D3-function | c.1500 | D2 | |
| | D4-function | c.1200 | | If D4 is fitted, and D5 is not, assume that they are combined. |
| | D5-function | c.1260 | | This band is rarely fitted. |
| | D6-function | c.1440 | D3 | This band is rarely fitted. Termed differently by Romero-Sarmiento et al. (2014). |

1099

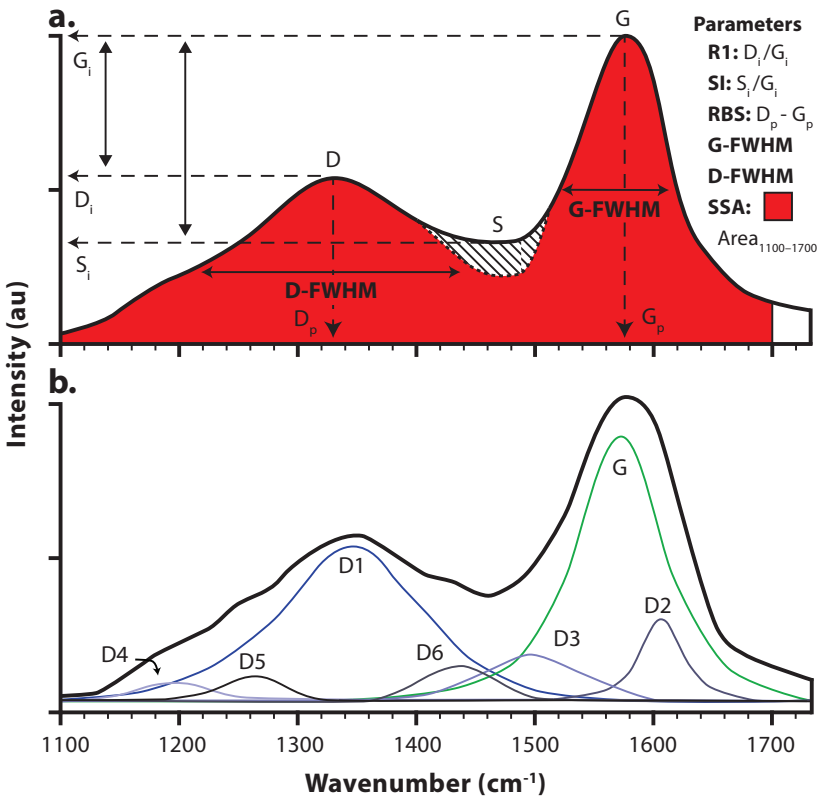


**Figure 3.2.** First-order Raman bands of OM. **(a)** Non-deconvolved spectrum, along with the Raman parameters that can be calculated. Note that the suffix is 'band' (Table 1). **(b)** 6-band deconvoluted spectrum with the proposed nomenclature of the bands when performing deconvolution. The suffix 'function' is employed to differentiate deconvoluted bands (Table 1). The number of bands fitted to the spectrum is subject to the operator's discretion; however, it is proposed that the band nomenclature presented here should be followed to avoid confusion. SI – saddle index; RBS – Raman band separation; G-FWHM – G-band/function full-width at half-maximum; D-FWHM – D-band/function full-width at half-maximum; SSA – scaled spectrum area.

For the second-order region, we propose the adoption of the nomenclature summarised in Fig. 3.3 and Table 3.2, which follows that used by Spötl et al. (1998), Jehlička and Beny (1999) and Zeng and Wu (2007). For immature samples there is a single broad band, and only with increasing maturity do the S2 (c. 2700 $cm^{-1}$), S3 (c. 2950 $cm^{-1}$) and S4 (c. 3200 $cm^{-1}$) bands become identifiable (Fig. 3.3; Zeng and Wu, 2007; Pan et al., 2019). Once the OM becomes anthracite and the graphitization process begins, the S2- and S3-bands become more discernible and separate into two clear bands (Fig. 3.3). Another small peak, termed the S1-band, also becomes visible at c. 2450 $cm^{-1}$ (Buseck and Beyssac, 2014; Pawlyta et al., 2015; Rantitsch et al., 2016). As the graphitization process continues with increasing thermal alteration, the S2-

band becomes stronger and the S1, S3 and S4 bands become weaker. In highly-ordered graphite, the S2-band splits into two separate peaks (Fig. 3.3), called the $G'_1$ (c. 2690 $cm^{-1}$) and $G'_2$ (2735 $cm^{-1}$) doublets (Lespade et al., 1982; Wopenka and Pasteris, 1993; Jehlička and Beny, 1999; Beyssac et al., 2002; Rantitsch et al., 2016), which indicate that the OM is changing to a tri-periodic structural organization (Lespade et al., 1982; Cuesta et al., 1994).

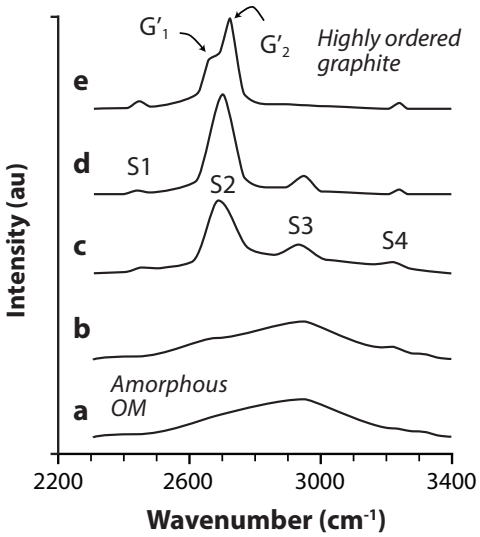


**Figure 3.3.** Illustration showing how the second-order region Raman bands of OM change with increasing maturity (ordering). **(a–b)** amorphous OM. **(c–e)** ordered graphite.

**Table 3-2.** Proposed nomenclature for the second-order region of the Raman spectrum.

| Proposed nomenclature | Position ($cm^{-1}$) | Alternative nomenclatures [a] | Notes |
|---|---|---|---|
| S1 | c.2450 | S5, D+D", D*, 2D4, 2450 $cm^{-1}$ | This band is often not named and is ignored as data are commonly not collected at <2600 $cm^{-1}$. |
| S2 | c.2700 | S1, S, 2D, 2'D1, 2D1 | The S1 band splits into two individual bands for highly ordered graphite. 2D = overtone of D-band (2 x 1350 = 2700 $cm^{-1}$). |
| $G'_1$ | c.2685 | NA | This band arises when the S2 band splits into two bands for highly ordered graphite. |
| $G'_2$ | c.2735 | NA | This band arises when the S1 band splits into two bands for highly ordered graphite. |

| | | | |
|---|---|---|---|
| S3 | c.2900 | S2, D1+G, D+G | Combination of the D1 and G bands (1580 + 1340 ≈ 2920 $cm^{-1}$) |
| S4 | c.3180 | S3, D+D'. 2D', 2'D2, G", 2D2 | This band is often ignored as data are not collected at >3000 $cm^{-1}$. |

[a] see Spötl et al. (1998); Jehlička and Beny (1999); Beyssac et al. (2002); Jehlička et al. (2003); Nestler et al. (2003); Rantitsch et al. (2004); Zeng and Wu (2007); Liu et al. (2013); Nakamura et al. (2015); Pawlyta et al. (2015); Hu et al. (2015); Childress and Jacobs (2017); Yuman et al. (2018). NA = not applicable.

## 3.5 Raman parameters for different applications

Here, different parameters will be summarised and their suitability for the three main Raman applications: (1) hydrocarbon exploration; (2) metamorphic studies; (3) estimating maximum heating along fault planes, will be assessed. Table 3.3 lists commonly recommended parameters along with their source references. The parameter values will not be discussed per se in this section, as the values are strongly dependent on the different methodologies applied (Lünsdorf et al., 2014; Henry et al., 2018); we will focus on each parameter's trend and its suitability for each application.

There is considerable confusion concerning parameter abbreviations. For example, Lahfid et al.'s (2010) RA1 and RA2 area ratio parameters were first used to represent the following equations, respectively: (D1+D4)/(D1+D2+D3+D4+G) and (D1+D4)/(D2+D3+G). Chen et al. (2017) then used the same abbreviations, RA1 and RA2, to indicate the area ratios of D/G and D2/G respectively. The same abbreviations were used again for different parameters by Schito et al. (2017): RA1=(S+Dl+D)/(S+Dl+D+Dr+Gl+G) and RA2=(S+Dl+D)/(Dr+Gl+G; see Schito et al. (2017) for definitions of their band nomenclature). The RA1 and RA2 Raman parameters sensu Lahfid et al. (2010) are most commonly used in metamorphic studies (Hara et al., 2013; Kouketsu et al., 2014; Lünsdorf et al., 2014; Delchini et al., 2016; Schito et al., 2017); therefore, we propose that these equations and abbreviations should be followed. There are also discrepancies in the definition of the R2 and R3 Raman parameters (Table 3.3) between Beyssac et al. (2002) and Hu et al. (2015). For these two parameters, we propose following Beyssac et al. (2002), as they

1158 are the most widely used (Beyssac et al., 2002; Rantitsch et al., 2004; Mathew et al.,
1159 2013; Childress and Jacobsen, 2017).

1160 The R1 and G-FWHM Raman parameters have also been defined in different ways.
1161 Depending on how the G-band region is fitted, whether it is a combination of the G-
1162 and D2-functions or fitted separately, different names have been used. When the R1
1163 ratio is calculated using the merged G- and D2-functions some have termed it simply
1164 the $I_D/I_G$ (Quirico et al., 2005; Nakamura et al., 2019; Schito et al. 2019), whereas
1165 others have continued to call it R1 (Eichmann et al., 2018; Henry et al., 2018, 2019).
1166 On the other hand, when the G-FWHM is calculated using a combination of the G+D2-
1167 functions it has been called the G+$D_2$ width (Eichmann et al., 2018), as well as the G-
1168 FWHM (Henry et al., 2018, 2019). We suggest that the R1 and G-FWHM names should
1169 continue to be used whether or not the G-band region is separated into the G- and
1170 D2-functions; however, operators should be aware that calculating these Raman
1171 parameters via the two methods may lead to significant differences in the values
1172 obtained.

1173

1174 **Table 3-3.** Raman parameters that have been recommended for maturity estimation, along with
1175 exemplar studies that have used these parameters.

| Method | Parameters | Abbreviations and notes | References |
|---|---|---|---|
| Full width at half maximum (FWHM) | G | G-FWHM | Roberts et al. (1995); Jehlička and Beny (1999); Guedes et al. (2005); Quirico et al. (2005); Yoshida et al. (2006); Guedes et al. (2010); Romero-Sarmiento et al. (2014); Zhou et al. (2014); Nakamura et al. (2015, 2018); Bonoldi et al. (2016); Rantitsch et al. (2016); Henry et al. (2019). |
| | D1 | D1-FWHM | Zhou et al. (2014); Chen et al. (2017). |
| | D1/G | $D1_{FWHM}/G_{FHWM}$ | Spötl et al. (1998); Zhou et al. (2014); Hu et al. (2015); Lupoi et al. (2017); Nakamura et al. (2018); Schito and Corrado (2018); Kaneki and Hirono (2019). |
| Raman band positions | G – D or G – D1 | Raman Band Separation (RBS) | Liu et al. (2013); Zhou et al. (2014); Bonoldi et al. (2016); Schmidt et al. (2017); Jubb et al. (2018); Schito and Corrado (2018); Henry et al. (2019). |

| | | | |
|---|---|---|---|
| Ratio of Raman band height | D/G or D1/G | R1 | Roberts et al. (1995); Rantitsch et al. (2004); Jurdik et al. (2008); Liu et al. (2013); Zhou et al. (2014); Nakamura et al. (2015); Lupoi et al. (2017); Sauerer et al. (2017); Childress and Jacobsen (2017); Kaneki and Hirono (2018); Schito and Corrado (2018); Kouketsu et al. (2019b). |
| | S/G | Saddle Index (SI) | Wilkins et al. (2014); Henry et al. (2018). |
| Ratio of band areas | D1/G | $A_D/A_G$ | Kribek et al. 1994; Guedes et al. (2005); Zhou et al. (2014); Nakamura et al. (2015); Chen et al. (2017); Schmidt et al. (2017); Schito and Corrado (2018); Mukoyoshi et al. (2018). |
| | D1/(G+D1+D2) | R2 | Beyssac et al. (2002); Rantitsch et al. (2004); Court et al. (2007); Aoya et al. (2010); Huang et al. (2010); Scharf et al. (2013); Delchini et al. (2016); Nakamura et al. (2015); Rantitsch et al. (2016); Chen et al. (2017); Childress and Jacobsen (2017); Kirilova et al. (2018); Beyssac et al. (2019); Kouketsu et al. (2019b). |
| | (D1+D4)/(D1+D2+D3+D4+G) | RA1 | Lahfid et al. (2010). |
| | (D1+D4)/(D2+D3+G) | RA2 | Lahfid et al. (2010). |
| Total Area | $\sum_{Area}$ 1100 – 1700 $cm^{-1}$ | Scaled Spectrum Area (SSA) – Scale G-Band to 2000 au. | Henry et al. (2019). |
| | $\sum_{Area}$ 1000 – 1800 $cm^{-1}$ | (1) Scaled total area (STA)<br>(2) Scaled Total Area (D_STA) – normalize to maximum D1 value.<br>(3) Scaled Total Area (G_STA) – normalize to maximum G value. | Lünsdorf (2016); Hackley and Lünsdorf (2018); Rantitsch et al. (2019). |
| | $\sum_{Area}$ (1575–1595 $cm^{-1}$) / $\sum_{Area}$ (1610–1630 $cm^{-1}$) | G_shape_factor | Lünsdorf et al. (2017) |
| Multi-linear regression | Uses a multi-linear regression, which include several Raman parameters to construct an empirical relationship with VR. See | RaMM (1) | Wilkins et al. (2014, 2015, 2018) |

| | | |
|---|---|---|
| | Wilkins et al. (2014, 2015) for further detail. | |
| | RaMM (2) | Wilkins et al. (2015, 2018) |

FWHM – Full–Width at Half–Maximum. au – arbitrary units.

### 3.5.1 *Diagenesis, catagenesis and metagenesis*

During normal burial conditions, OM remains disordered during diagenesis, catagenesis and metagenesis, as it has not been subject to high enough temperatures to transform into graphite (Fig. 3.4). During catagenesis and metagenesis, important thermal decomposition reactions occur in OM that lead to the generation of oil and gas. It is therefore of no surprise that there has been a tremendous amount of work trying to track the thermal evolution of OM during these stages, particularly to determine the onset of oil, wet gas and dry gas generation (Hartkopf-Fröder et al., 2015). The most common techniques used are vitrinite reflectance ($VR_o$) and Rock-Eval™ pyrolysis.

$VR_o$ is widely used to calibrate basin models that help petroleum exploration geologists delineate areas of interest by creating maturity maps used in common risk segment mapping. It is therefore of value to generate equivalent vitrinite reflectance ($\%_{eq}VR_o$) values when VR cannot be performed, such as in pre-Devonian and deep marine rocks where vitrinite particles are absent/rare, and when VR is subject to suppression and/or retardation, caused by macerals with high hydrogen concentration (e.g. liptinites, amorphous organic matter and hydrogen-rich vitrinites), different lithologies, and in overpressured basins (Carr, 2000; Hackley and Cardott, 2016). Reflectance data from graptolites, bitumen, chitinozoans and conodonts; thermal alteration indices (TAI) such as the spore colouration index (SCI); and geochemical techniques such as Rock-Eval™ pyrolysis and biomarkers have all been employed to estimate $\%_{eq}VR_o$ (Jarvie et al., 2001; Hartkopf-Fröder et al., 2015 and references therein).

Raman spectroscopy has been used recently to determine the $\%_{eq}VR_o$ of OM in the oil and gas windows (0.6–3.0 $\%VR_o$; Baludikay et al., 2018; Schito and Corrado, 2018; Henry et al., 2019) from a variety of different organic matter components including

vitrinite, graptolites and bitumen. The type of organic matter is not taken into account in Sections 3.5.1 –3.5.3, below, however it will be discussed in Section 3.6.2. A summary of how the Raman spectrum and Raman parameters evolve with increasing maturity is provided in Fig. 3.4. Visually, the main changes in the OM Raman spectrum with increasing maturity (increasing $VR_o$), are that the G-FWHM decreases and the distance between the D or D1-band and G-band increases.

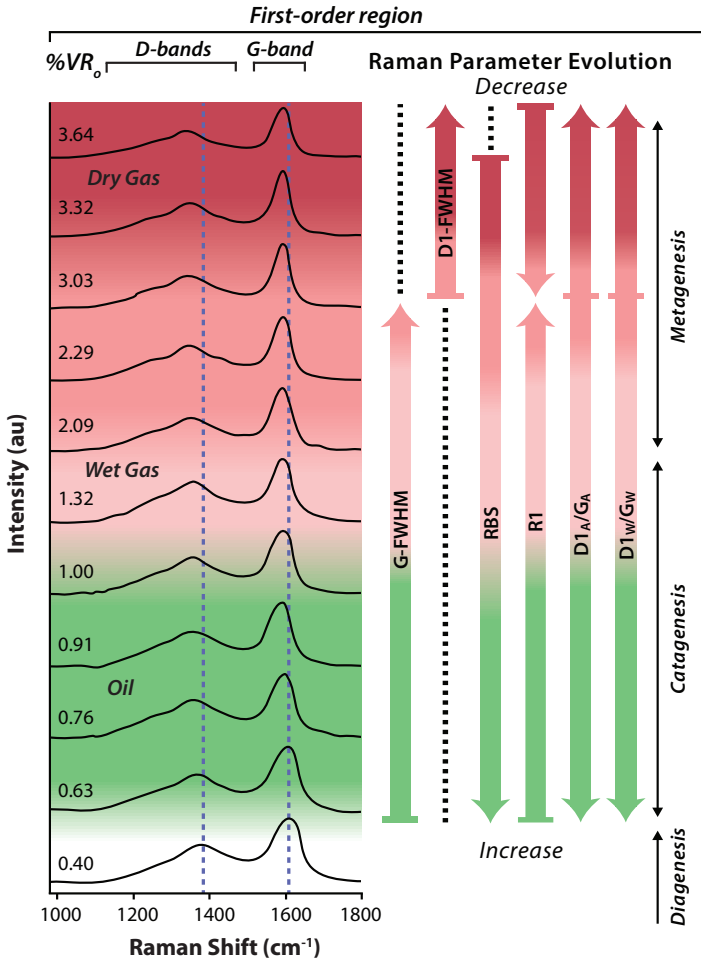


**Figure 3.4.** Summary of how the Raman spectrum of OM and parameters change with increasing $VR_o$. Dashed blue lines indicate the low maturity D-band and G-band peak positions. The dashed black lines for the Raman parameter evolution indicate invariable change in the parameter values.

The two most successful Raman parameters used to estimate VR in the range of 0.5–3.0 $\%VR_o$, are G-FWHM (Wopenka and Pasteris, 1993; Spötl et al., 1998; Kelemen and

Fang, 2001; Guedes et al., 2010; Hinrichs et al., 2014; Romero-Sarmiento et al., 2014; Eichmann et al., 2018; Schito and Corrado, 2018; Henry et al., 2019) and RBS (Kelemen and Fang, 2001; Zhou et al., 2014; Inan et al., 2016; Mumm and Inan, 2016; Sauerer et al., 2017; Khatibi et al., 2018a,b,c; Schito and Corrado, 2018) (Fig. 3.5). It is impossible to compare the absolute values between studies, as the deconvolution methods and Raman set-ups are highly variable. However, Fig. 3.5 shows that the parameters have a general trend. The G-FWHM parameter (Fig. 3.5a) has a non-linear relationship with $VR_o$: it sharply decreases from 0.5–2.0 $\%VR_o$, the gradient reduces to 3.0 $\%VR_o$, and then flattens out at >c. 3.0 $\%VR_o$ (Fig. 3.5). The RBS parameter behaves similarly, rising sharply to c. 2.0–4.0 $\%VR_o$ and then begins to flatten out (Fig. 3.5b). This shows that the G-FWHM and RBS are strong parameters to estimate the maturity of source rocks in the oil, wet gas, and dry gas generation stages. However, they cannot confidently be used to estimate the maturity of over-mature petroleum source rocks.

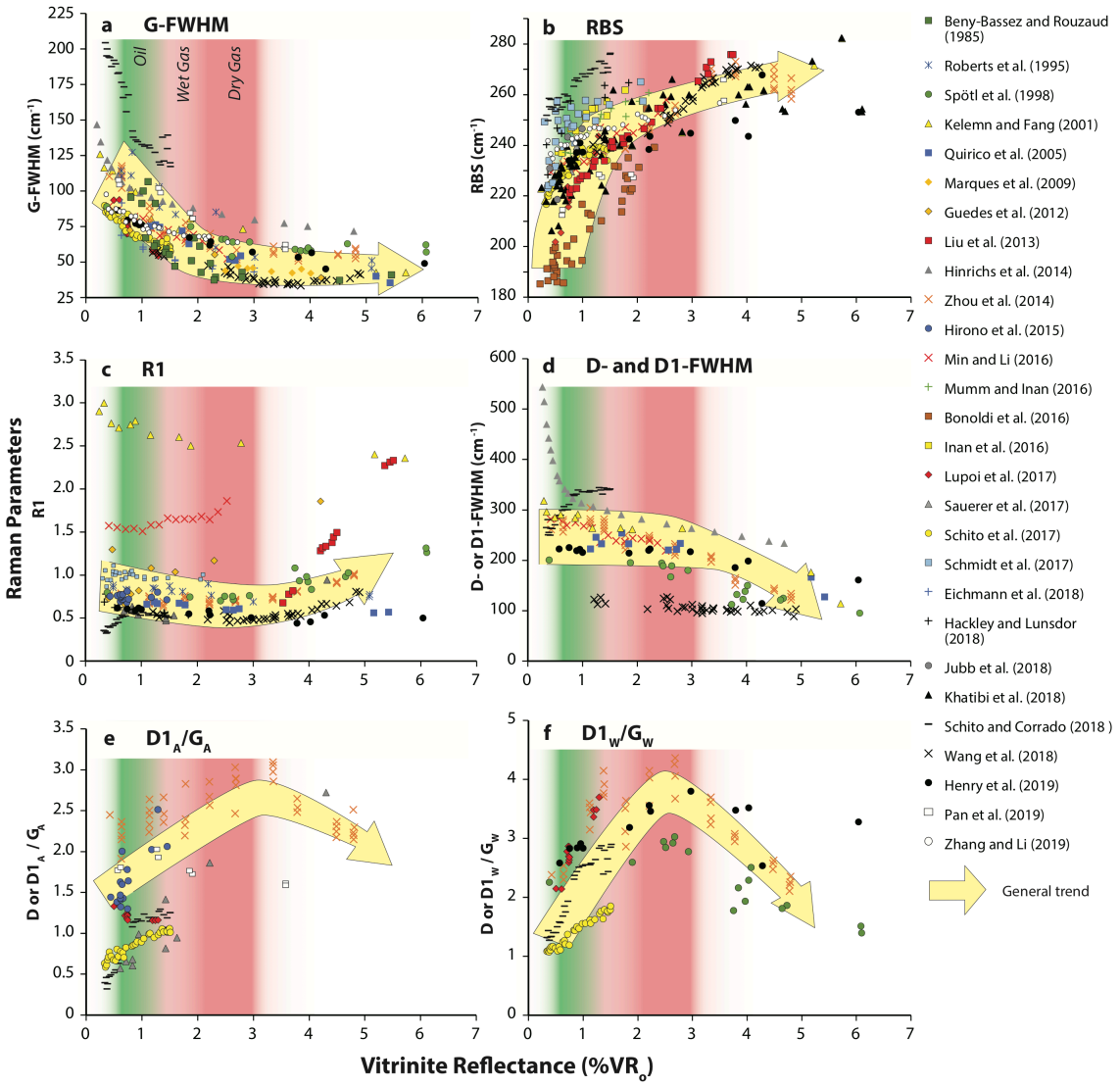


**Figure 3.5.** Raman parameters vs. vitrinite reflectance ($VR_o$) correlations derived from multiple studies, illustrating the general trend of parameter evolution with increasing $VR_o$. **(a)** G-FWHM. **(b)** RBS. **(c)** R1. **(d)** D- or D1-FWHM. **(e)** $D_A$ or $D1_A/G_A$. **(f)** $D_w$ or $D1_W/G_W$. Data sources listed in key.

The R1 parameter is commonly used in maturity studies (Table 3.1), however it is generally considered to be a poor parameter to estimate $\%_{eq}VR_o$ values in the oil and gas maturity range (Beny-Bassez and Rouzaud, 1985; Lünsdorf et al., 2017; Henry et al., 2019). The R1 value has a three-stage evolution, it: (1) decreases slightly up to c. 2.5 $\%VR_o$; (2) then increases up to low-grade metamorphism; and (3) sharply decreases for medium- to high-grade metamorphism, until the OM becomes a perfectly-ordered graphite and the disordered band region disappears (Beyssac et al.,

2002; Rahl et al., 2005; Lünsdorf et al., 2017) (Figs. 3.5–3.7). This trend for the R1 ratio makes assessing the maturity for oil and gas exploration ambiguous, as one R1 value offers three different possible $VR_o$ values; visual inspection of the spectrum is essential. The R1 parameter is also not as sensitive as G-FWHM and RBS, as small variations of R1 can give substantially different $\%_{eq}VR_o$ values, and the error associated with the R1 parameter is greater than the subtle decrease of the R1 for the oil and gas generation stages (Fig. 5c). However, these general observations are contrary to the results of Guedes et al. (2010) and Liu et al. (2013), who determined R1 parameter values that increased with increasing maturity up to c. 5.0 $\%VR_o$ with a steep linear calibration curve, albeit with significantly different values, attributable to the contrasting spectral processing methods used. On the other hand, the R1 results of Muirhead et al. (2017b) demonstrated opposite trends for samples in different localities that have been affected by igneous intrusions, which they proposed to be a result of the different heating rates experienced. This suggests that the R1 ratio may not be suited to determine the maximum temperature, but rather may be used as a means to compare different heating rates.

Studies of the D1-FWHM parameter show conflicting results (Fig. 3.5d). Some authors have shown that D1-FWHM has little to no use to estimate the maturity of OM for hydrocarbon exploration, as the band-width remains unchanged up to c. 3–4 $\%VR_o$ (Wopenka and Pasteris, 1993; Spötl et al., 1998), similar results derived from the D-FWHM were obtained by Henry et al. (2019). Other studies have concluded that the D1-FWHM is well suited to estimate maturities that are relevant for hydrocarbon studies, as the D1-FWHM decreases with increasing maturity (Fig. 3.5d; Cuesta et al., 1994; Hinrichs et al., 2014; Schito and Corrado, 2018). Some workers have used the ratio of the D- or D1-FWHM and G-FWHM, which also has a two-step evolution. It firstly increases rapidly as the G-FWHM decreases in width, and when the G-FWHM becomes invariable (at >3 %VR), the D1-FWHM starts to decrease in width, leading to a sharp decrease in the ratio value (Spötl et al. 1998; Zhou et al., 2014; Henry et al., 2019). The area ratio of the D1-band and G-band ($D1_A/G_A$) is a commonly used Raman parameter and has been shown to increase with increasing maturity up to c. 3.0 $\%VR_o$

(Fig. 3.5e; Zhou et al., 2014; Sauerer et al., 2017). It then decreases above c. 3.0 $\%VR_o$ (Zhou et al., 2014).

Other parameters that have been proposed include Wilkins et al.'s (2014, 2015) Raman Maturity Method (RaMM) that utilises two multi-linear regression equations to predict equivalent VR values between 0.4–1.2 $\%VR_o$ (RaMM 1) and 1.0–2.5 $\%VR_o$ (RaMM 2) using several Raman parameters. Wilkins et al. (2014) demonstrated that the operator does not need to discriminate vitrinite and inertinites, as both yield similar equivalent VR values. They also proposed that this method corrects for the suppression of VR values. Several integrated area Raman parameters that are calculated between wavenumber regions have also proved to be successful and include the SSA (scaled spectrum area) (Henry et al., 2018) and the STA (scaled total area), D_STA (D1-band STA), G_STA (G-band STA) and G_shape_factor (Lünsdorf and Lünsdorf, 2016; Lünsdorf et al., 2017) (Table 3).

SSA is the total area of the Raman spectrum between 1100–1700 $cm^{-1}$ after background subtraction and normalisation using a maximum G-band height value of 2000, and has a linear correlation with vitrinite reflectance up to c.6.0 $\%VR_o$ (Henry et al. 2019). Lünsdorf and Lünsdorf's (2016) Raman parameters are derived by using an automated iterative random-based curve-fitting approach to determine the optimum baseline characteristics, which is then used to calculate the: STA, which is the scaled total area between the region 1000–1800 $cm^{-1}$; D_STA, which is the scaled total area when the spectrum is normalized using the maximum D1-band height between 1000–1800 $cm^{-1}$; G_STA, which is the scaled total area when the spectrum is normalized using the maximum G-band height between 1000–1800 $cm^{-1}$. These parameters have a linear relationship with VR up to c. 6.0 $\%VR_o$, similar to Henry et al.'s (2019) SSA parameter. Lünsdorf et al. (2017) further developed this approach to include the G-shape-factor ratio, which is the area from 1575–1595 $cm^{-1}$ divided by the area from 1610–1630 $cm^{-1}$, which helps to combine both the D_STA and G_STA parameters to better determine the temperature of OM across a wider temperature range.

Several authors have proposed that different parameters are more sensitive to different maturity ranges (Liu et al., 2013; Du et al., 2014; Wilkins et al., 2014, 2015;

Zhou et al., 2014; Zhang and Li, 2019). Liu et al. (2013) and Zhou et al. (2014) recommended to use both the RBS and R1 Raman parameters: (1) RBS, for low maturity (0.6–3.5 %$VR_o$ and 1.5–3.5 %$VR_o$, respectively); and (2) R1 for high maturity OM (3.5–5.5 %$VR_o$ and 3.0–5.0 %$VR_o$, respectively). Wilkins et al. (2014, 2015) also developed two separate calibration curves using the RaMM mentioned above, RaMM 1 and RaMM 2. Employing two calibration curves solves the limited range of using one parameter and recognises that different parameters behave differently depending on the maturity. However, the results obtained will be subject to the deconvolution method that is applied.

Understanding the maturity of OM is important for shale gas exploration. Yuman et al. (2018) noted the necessity to recognise over-maturity (> 3.5 %$VR_o$; anthracite) for OM in shale gas reservoirs. The initiation of over-maturity at c. 3.5 %VR is a "turning point" for the Raman spectrum and represents a major chemical and structural change for the OM (Hou et al. 2019). This is also broadly demonstrated in Figure 5 for all the Raman parameters at c. 3.0 %VR. In such cases the reservoir quality is severely damaged, as the organic pores and intercrystalline pores of clay minerals are significantly reduced, and source rock quality is poor because the capability to generate hydrocarbons has been exhausted. This is a limiting factor for the two most widely used Raman parameters, G-FWHM and RBS, as they both have non-linear calibration curves that flatten out at c.3.0 %$VR_o$. To address this, Yuman et al. (2018) visually determined the onset of shale gas reservoir deterioration by assessing the appearance of the S2-band in the second-order region. Previously, Liu et al. (2013) had shown that the S2-band starts to appear at c. 3.0 %$VR_o$.

In addition to estimating the maturity of OM, several authors have used Raman spectroscopy to determine other properties in the diagenesis to metagenesis burial range. For example, Khatibi et al. (2018a) determined the Young's modulus of OM, using the RBS Raman parameter, which is important to understand the initiation and propagation of fractures during hydraulic fracturing for shale gas production. Romero-Sarmiento et al. (2014) proposed that Raman spectroscopy may have potential to estimate hydrocarbon retention within source rocks, which is a major factor in determining the total resources, by observing what we term the D6-band (c. 1480 $cm^{-}$

[1]) (Fig. 3.2c). However, no empirical relationship between hydrocarbon retention and D6-band parameters has been established.

Pan et al. (2019) applied Raman spectroscopy for coalbed methane studies, by determining the deformation of graphite in OM related to the adsorption and desorption of gas in coalbeds, which is important for predicting potential gas outbursts after $CO_2$ injection (Chen et al., 2009). Pan et al. (2019) demonstrated that after high-pressure gas adsorption and desorption experiments, the OM underwent deformation, which was evident in the Raman spectrum, as the G-band red-shifted, the D1-band blue-shifted and both the FWHM and the $D1_A/G_A$ ratio increased; this suggests that high-pressure gas adsorption and desorption induced defects in the OM lattice.

Wilkins et al. (2018) showed that a RaMM 1 vs. RaMM 2 plot can be used to differentiate bitumen from *Tasmanites*-related alginate. Similarly, Schito et al. (2019) demonstrated that Raman can be used to identify types of OM particle, using a multivariate Principal Component Analysis (PCA) and Partial Least Square - Discriminant Analysis (PLS-DA) method. They showed that using this approach, sporomorphs and phytoclasts can be differentiated. This application has potential to be taken further and might be used to determine other OM components, which will allow operators to perform high-resolution mapping of OM particles in a sedimentary rock.

To conclude, RBS and G-FWHM remain the most popular Raman parameters employed to determine OM maturity during diagenesis to metagenesis, however they have a limited range of application, up to c. 3.0 $\%VR_o$ equivalent. Methods that integrate areas of specific Raman regions such as the SSA, G_STA, D_STA parameters correlate well with higher VR values (up to c. 6.0 $\%VR_o$) and may extend the limited range of RBS- and G-FWHM-based maturity determinations. However, G-FWHM has by far the tightest correlation with $VR_o$ compared to other Raman parameters (Fig. 3.5; Henry et al., 2019), and should be the method of choice when assessing low-maturity rocks. Nonetheless, we propose that other parameters (RBS, R1, $D1_A/G_A$,

integrated area regions) should be calculated to cross-check and extend the G-FWHM results.

### *3.5.2 Metamorphism*

A substantial number of studies have used Raman spectroscopy as a tool to determine the maximum temperature reached during regional metamorphism (Rantitsch et al., 2004; Endo et al., 2012; Mathew et al., 2013; Scharf et al., 2013; Buseck and Beyssac, 2014; Muirhead et al., 2016; Hara and Hara, 2018) or to assess the extent of contact metamorphism due to igneous intrusions (Aoya et al., 2010; Chen et al., 2017; Mori et al., 2017; Henry et al., 2019). Being able to determine the distribution and values of maximum temperatures is extremely important, as it provides insights into the physical and chemical evolution that takes place deep in the Earth, as well as delineating the location of metamorphic facies and minerals that can have substantial economic value. Raman parameters have typically been calibrated against temperature for metamorphic studies, in order to quantify the maximum temperature reached by OM in metamorphic rocks (Figs. 3.6, 3.7).

The most widely used calibration curves are presented in Table 3.4, and a general summary of how the Raman spectrum of OM and Raman parameters change with increasing metamorphism is illustrated in Fig. 3.6. Examples of Raman parameter vs. temperature calibration curves are shown in Fig. 3.7. The G-FWHM parameter continues the decreasing trend from diagenesis–metagenesis up to c. 360 ºC (Fig. 3.7a) and then the D2-band begins to separate from the G-band (Fig. 3.6; Wopenka and Pasteris, 1993; Buseck and Beyssac, 2014). The D2-band separation transition from the G-band is a possible reason why the G-FWHM has a non-linear calibration curve with $VR_o$ and temperature (°C) values (Kouketsu et al., 2014; Henry et al., 2019), as the G-band FWHM initially begins to widen as the D2-band starts to detached and once it is fully detached, the G-FWHM then decreases again (Fig. 3.5a).

During catagenesis–metagenesis the RBS parameter increases with increasing temperature and then flattens at > 3 $\%VR_o$ (c. 250 ºC; Fig. 3.5b); a reversal occurs during metamorphism and the RBS begins to decrease as the G-band position moves

to lower wavenumbers (Figs. 3.6, 3.7b), which explains the separation of the D2-band from the G-band. The R1 parameter decreases slightly up to metagenesis, and then R1 begins to sharply increase as the D1/D-band height increases with respect to the G-band height up to c. 350 ºC (Fig. 3.7c); these observations contradict the view of some authors who have stated that the larger the ratio, the less ordered the OM structure (Huan et al., 2019). At c. 350 ºC, the R1 ratio displays another reversal (Figs. 3.6, 3.7c), and decreases until the D-band region eventually disappears, as the OM evolves to a perfectly ordered graphite.

A number of authors have constructed tailored calibration curves to be used for metamorphic studies, including: Beyssac et al. (2002); Rantitsch et al. (2004); Rahl et al. (2005); Aoya et al. (2010); Lahfid et al. (2010); and Kouketsu et al. (2014) (Table 3.4). Beyssac et al. (2002) developed the first Raman empirical equation to determine temperatures between 330–640 °C, using the R2 parameter (Fig. 3.7f). The R2 parameter empirical equation was subsequently modified by Rantitsch et al. (2004) who worked on isolated OM and Aoya et al. (2010) who worked on contact metamorphic rocks (Table 3.4). Endo et al. (2012) and Kouketsu et al. (2014) both tested the Beyssac et al. (2002) and Aoya et al. (2010) R2 calibration equations and demonstrated that the calibration curves showed no significant difference to their results (Fig. 3.7f). This would imply that the same calibration curve can be used for both regional and contact metamorphism. However, it should be noted that Endo et al. (2010) did not follow the exact method used by Beyssac et al. (2002) or Aoya et al. (2010), as they did not include the D3-band when performing deconvolution. Rahl et al. (2005) tested the R2 parameter for low-grade metamorphic temperatures and showed that R2 remains constant at <300 °C, and is therefore a poor parameter to quantify low-temperature metamorphism (Fig. 3.7f). Beyssac et al. (2002) explained that the R2 parameter remains constant below c.300–330 °C because the coherent domains composed by the aromatic rings in the organic matter structure are too small.

Rahl et al. (2005) created a new method combining both the R1 and R2 parameters, to cater for metamorphic rocks that have been exposed to lower temperatures (Table 3.4, Fig. 3.8; 100–700 °C ± 50 °C). They successfully tested the calibration equation on

low-grade metamorphic rocks in New Zealand and high-pressure metamorphic rocks in Crete (Greece). Rahl et al.'s (2005) wide temperature range offers better practicality, as no prior knowledge of the thermal maturity and geological context is needed. Scharf et al. (2013) tested Rahl et al.'s (2005) equation against those of Beyssac et al. (2002) and Aoya et al. (2010), and showed good consistency for all three methods. However, the Beyssac et al. (2002) and Aoya et al. (2010) calibration curves are in closer agreement with the petrology, especially for higher temperatures (> 500 °C). On the other hand, Mathew et al. (2013) demonstrated that Rahl et al.'s (2005) method better estimates temperatures of <340 °C and >600 °C than the approach of Beyssac et al. (2002). Chim et al. (2018) also successfully used Rahl et al.'s (2005) method to determine the metamorphic grade of detritus, to track the uplift and exhumation of an orogenic belt in Eastern Taiwan.

The RA1 and RA2 Raman parameters of Lahfid et al. (2010) also cater for low-temperature metamorphic rocks (Table 3.4; Figs. 3.6, 3.7g, h). Both parameters increase with increasing temperature. Hara et al. (2013) showed that the parameters can reliably estimate low-grade metamorphism (<300 °C), although Kouketsu et al. (2014) indicated that RA1 and RA2 overestimate the temperature of metamorphic rocks for temperatures <200 °C and of >300 °C by >+50 °C. By contrast, Schito et al.'s (2017) version of the RA1 and RA2 parameters, discussed in Section 3.5, were successfully applied to low-maturity rocks (0.5–1.5 %$VR_o$).

The D1-FWHM parameter of Kouketsu et al. (2014) has been calibrated for the temperature range 150–400 °C (Figs. 3.6, 3.7d). The D1-FWHM parameter remains invariable for temperatures >400 °C. Several authors have applied Kouketsu et al.'s (2014) D1-FWHM Raman method (Baludikay et al., 2018; Hara and Hara, 2018; Mészáros et al., 2019; Ye et al., 2019; Yu et al., 2019). For example, Hara and Hara (2018) used it to determine the temperatures reached in an accretionary complex, and Ye et al. (2019) used it to assess the temperature characteristics of detrital graphite particles and employed these as tracers in sediment provenance analysis. Kouketsu et al. (2014) also constructed an empirical relationship with the D2-FWHM parameter and temperature; however, this parameter may prove to be problematic

as it is difficult to differentiate between the D2- and G-functions for low-temperature metamorphic rocks (Fig. 3.6). Nevertheless, Mészáros et al. (2019) utilised the D2-FWHM parameter and got similar results to those obtained using Beyssac et al.'s (2002) and Rahl et al.'s (2005) R2 parameter and Kouketsu et al.'s (2014) D1 parameter.

Lünsdorf et al.'s (2017) G_STA, D_STA and G_shape_factor have been applied in diagenesis to metagenesis applications (Section 4.1), however, the temperature range of these parameters extend from 160 to 600 °C and they can therefore be used to determine metamorphic temperatures. The SSA parameter by Henry et al. (2018) also extends from 0.5 to 6 $\%VR_o$, which covers the metamorphic range. Both of these authors' methods derive parameters calculated by integrating area regions (Table 3.3), and do not use areas of individual bands as is commonly the case for parameters utilised in metamorphic studies (e.g. R2, RA1, RA2).

The second-order region of the Raman spectrum is also helpful for the analysis of metamorphic rocks (Fig. 3.6; Wopenka and Pasteris, 1993; Buseck and Beyssac et al., 2014). It is clear from Fig. 3.6 and from Beyssac et al. (2002) that the height or area ratio of the S2 and S3 peaks can be a powerful parameter, as the S2 height increases with respect to the S3 height with increasing temperature. The splitting of the S2 band into the $G'_1$ and $G'_2$ bands is also a sign that the metamorphic environment has reached extremely high temperatures and pressures (eclogite facies; Beyssac et al., 2002; Buseck and Beyssac, 2014; Rantitsch et al., 2016).

Similar to diagenesis–metagenesis, some authors have tried to use two calibration curves to analyse samples displaying a wide maturity range. Mori et al. (2017) successfully used a combination of Aoya et al.'s (2010) modified R2 equation and Kouketsu et al.'s (2014) D1-FWHM parameter to estimate the maximum temperature reached during contact metamorphism. Their criterion in determining which method to use was whether the D4-band was visibly present or not. If the D4-band was present then the D1-FWHM was used, if not, then the modified R2 parameter was employed. Mori et al. (2017) only used Aoya et al.'s (2010) method close to the intrusion, where the temperatures were high enough for the disappearance of the D4-band.

To summarise, the Raman community studying metamorphism has adopted a more consistent approach than those working on lower maturity rocks (diagenesis to metagenesis), as authors frequently apply and compare calibration curves that have been published in the literature. R2 is the most commonly used Raman parameter albeit calculated following several minor modifications; it appears to offer reliable temperature estimates, with only a small deviation in results obtained by different laboratories. However, the R2 parameter has a limited temperature range and it cannot be employed for low-temperature metamorphic studies (<300 °C), which is where Rahl et al.'s (2005) and Lahfid et al.'s (2010) Raman parameters can be used. Additionally, Lünsdorf et al. (2017) and Henry et al. (2018) have demonstrated that the integrated areas of specific regions on a smoothed, background-corrected spectrum (rather than individual bands areas), have good linear relationships with temperature and $VR_o$, and the parameters derived from these also have potential application in studies of low- to high-temperature metamorphism. There is therefore scope to unify several methods in order to determine metamorphic temperatures for a wide temperature range.

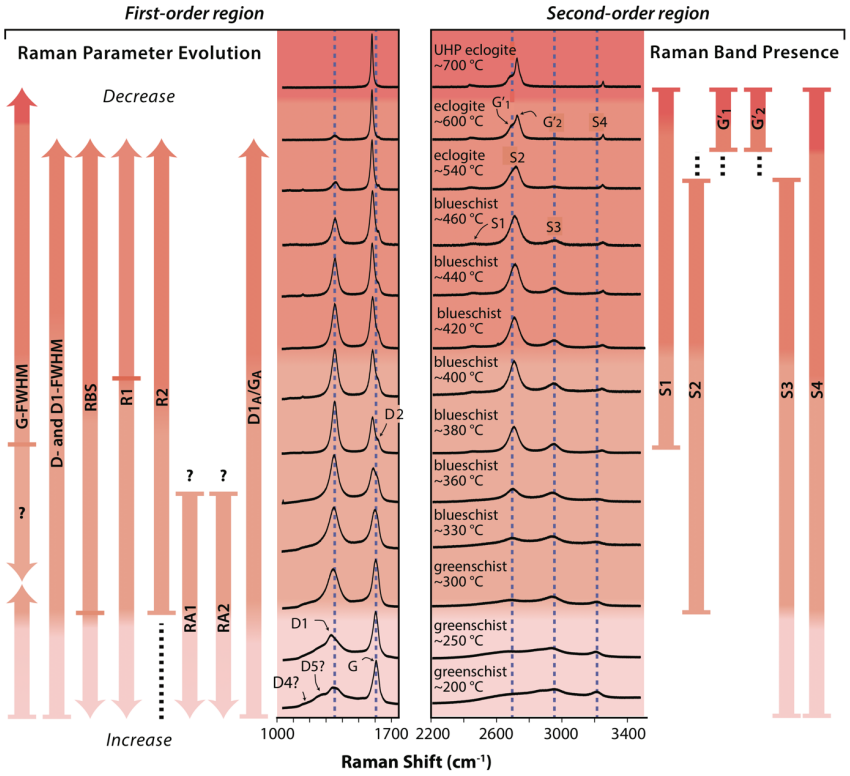


**Figure 3.6.** General evolution of the Raman spectrum of OM for the first-order and second-order regions and changes in Raman parameters with increasing metamorphism. Adapted from Buseck and Beyssac (2014).

**Table 3-4.** Calibration curves constructed in the literature that have been used for metamorphic rocks.

| Deconvolution (number of bands) | Laser wavelength (nm) | Raman parameters | Calibration equation T(°C) = | Temperature range (°C) [error] | Reference |
|---|---|---|---|---|---|
| G, D1, D2, D3 (4) | 514.5 | R2 | -445 * R2 + 641 | 330 – 640 | Beyssac et al. (2002) |
| G, D1, D2, D3 (4) | 532.2 Nd-YAG | R1 and R2 | 737.3 + 320.9 * R1 -1067 * R2 - 80.638 * $R1^2$ | 100 – 700 [± 50] | Rahl et al. (2005) |
| G, D1, D2, D3 (4) | 532.2 Nd-YAG | R2 | -(457±53) * R2 + (648±25) | 350 – 550 | Rantitsch et al. (2004) |
| G, D1, D2, D3 (4) | 514.5 | R2 | 221 * $R2^2$ - 637.1 * R2 + 672.3 | 340 – 655 [± 30] | Aoya et al. (2010) |
| G, D1, D2, D3 (4) | 532 | R2 | 91.4 * $R2^2$ - 556.3 * R2 + 676.3 | 340 – 655 [± 30] | Aoya et al. (2010) |

| | | | | | |
|---|---|---|---|---|---|
| G, D1, D2, D3, D4 (5) | 514 argon | RA1 | NA | 200 – 320 | Lahfid et al. (2010) |
| G, D1, D2, D3, D4 (5) | 514 argon | RA2 | NA | 200 – 320 | Lahfid et al. (2010) |
| Multiple fitting methods. See Kouketsu et al. (2014) | 532 Nd-YAG | D1-FHWM | -2.15 * (D1-FWHM) + 478 | 150 – 400 [± 30] | Kouketsu et al. (2014) |
| Multiple fitting methods. See Kouketsu et al. (2014) | 532 Nd-YAG | D2-FWHM | -6.78 * (D2-FHWM) + 535 | 150 – 400 [± 50] | Kouketsu et al. (2014) |

Na – no available information given in the paper.

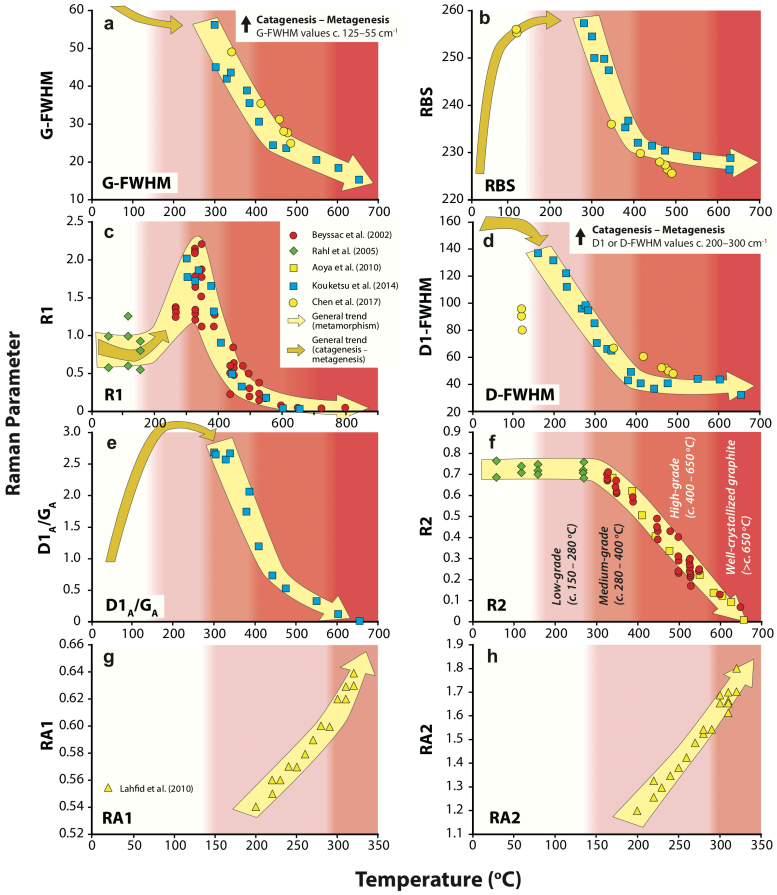


**Figure 3.7.** Raman parameter vs. temperature calibration curves constructed for metamorphic studies. The general trends for metamorphism and catagenesis–metagenesis are shown. The OM crystallinity grade is derived from Kouketsu et al. (2014). (a) G-FWHM. (b) RBS. (c) R1. (d) D1-FWHM. (e) $D1_A/G_A$. (f) R2. (g) RA1. (h) RA2. Data sources listed in key.

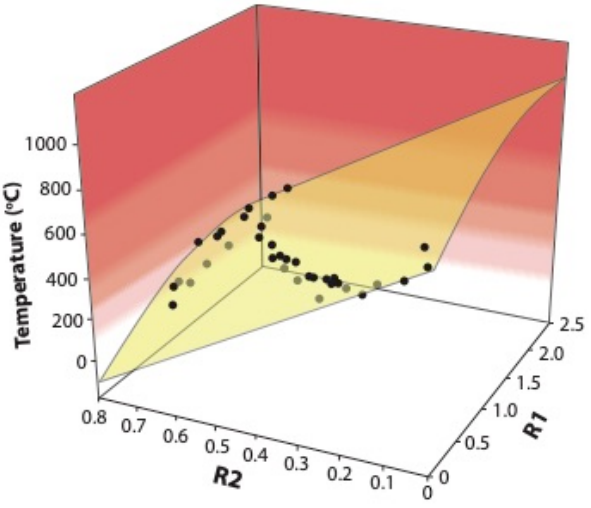


**Figure 3.8.** Calibration data and best fit-surface to determine metamorphic temperature from the R1 and R2 Raman parameters of OM. Adapted from Rahl et al. (2005).

### *3.5.3 Frictional heating along fault zones*

Determining the maximum temperature reached during frictional heating along fault planes can provide important information on the amount of total seismic energy released, shear stress, slip distance and the mechanochemistry (Kitamura et al., 2012; Kaneki et al. 2016; Kaneki and Hirono, 2018, 2019). Understanding the maximum temperature along a fault plane can also help predict potential future risks, as the formation of graphite will lead to the lubrication of faults, similar to clays, and magnify the movement along the fault (Oohashi et al., 2011; Kaneki and Hirono, 2018; Kuo et al., 2018).

Measuring the maximum temperature reached on fault planes has typically been performed using vitrinite reflectance (Furuichi et al., 2015; Kaneki et al., 2018). However, Kitamura et al. (2012) argued that VR cannot accurately estimate maximum temperature in a fault zone, as the mechanochemical effects that are associated with faulting lead to the overestimation of $\%VR_o$ maturity. By contrast, Nakamura et al. (2015) proposed that shearing during faulting leads to interlayer delamination and pulverization of OM, increasing edge plane defects and therefore lowering the crystallinity of OM, leading to an underestimation of maturity. On the other hand, it

has been suggested that Raman spectroscopy may provide information on both the maximum temperature reached and the deformation processes, unlike vitrinite reflectance (Nakamura et al., 2015; Kaneki et al., 2016; Kaneki and Hirono, 2018; Kuo et al., 2018).

Raman spectroscopy has been used in multiple studies in order to measure the maturity of OM in fault zones and there is clear evidence that the Raman spectra in pseudotachylytes, cataclasites and host rocks are different (Furuichi et al., 2015; Nakamura et al., 2015; Kaneki et al., 2016; Liu et al., 2016; Ito et al., 2017; Kouketsu et al., 2017; Kuo et al., 2017, 2018; Kaneki and Hirono, 2018; Mukoyoshi et al., 2018). The calibration curves constructed to estimate the thermal maturity of burial and contact metamorphism cannot be applied here, as there are other important factors that must be taken into consideration, such as: heating rates; duration of heating; slip rate; shearing; repeated heating episodes; and hydrothermal fluids. Different laboratory experiments have been performed in order to understand some of these effects, however it is very hard to replicate natural conditions in the laboratory and create reliable calibration curves (Hirono et al., 2015; Kaneki et al., 2016; Kaneki and Hirono, 2018; Mukoyoshi et al., 2018; Nakamura et al., 2019).

The $D1_A/G_A$ and R1 parameters are most commonly used to estimate frictional heating in fault zones. Figure 3.9 shows how the $D1_A/G_A$ and R1 parameters evolve with increasing frictional heating. $D1_A/G_A$ values remain relatively constant at <300 ºC although some authors have shown that they decrease slightly (Kaneki et al., 2016; Mukoyoshi et al., 2018), then begin to increase up to 1000 ºC (Fig. 3.9a). Beyond 1000 ºC, $D1_A/G_A$ values begin to decrease. This is a similar trend to that observed during diagenesis–metagenesis and metamorphism (Fig. 3.7e), albeit at substantially different temperatures. The R1 ratio remains constant at <c. 700 ºC and then begins to increase (Fig. 3.9b). However, unlike diagenesis–metagenesis and metamorphism, the ratio continues to increase to 1300 ºC. It could be that the R1 ratio will decrease at higher temperatures.

Hirono et al. (2015) demonstrated that shearing at <250 ºC does not influence the R1 ratio. Kaneki et al. (2018) confirmed that shearing does not impact the R1 parameter

at lower temperatures (<700 ºC), but they showed that at elevated temperatures >700 ºC, increased shearing pressures progressively increases the R1 ratio, as the increasing temperature allowed the formation of graphite that encourages even more shearing. This suggests two things: (1) Hirono et al.'s (2015) shearing experiment did not reach high enough temperatures to promote graphitization and encourage slippage; and (2) the formation of graphite promotes shearing that leads to increased interlayer delamination and pulverization, that has a direct impact on the R1 ratio. Therefore, the R1 parameter may potential be used to determine deformation processes, such as shearing pressures. Results from Kuo et al. (2018) demonstrated that for natural samples, the R1 ratio decreases in the gouge zones, in comparison with the less deformed brecciated zones, which is in disagreement with the experimental results of Kaneki et al. (2018). They also showed that the G-band position red-shifts with increasing strain during faulting. Kuo et al. (2018) also determined the ratio of the D1- and G-FWHM, and demonstrated that the D1-FWHM decreases with respect to the G-FWHM, with increasing frictional heating.

Hirono et al.'s (2015) heating experiments showed that the environmental conditions may potential lead to different types of reactions affecting the Raman parameters, as the $D1_A/G_A$ and R1 values for samples heated in air vs. argon were slightly different (Fig. 3.9). Kaneki and Hirono (2018) demonstrated that faster heating rates in the laboratory delayed the thermal alteration reactions of OM (Fig. 3.9) and proposed that such delays may also be present in fault rocks.

The laboratory experiments performed by Kaneki and Hirono (2019), demonstrated that with increasing maturity the carbonaceous matter weakens and has lower peak friction coefficients, hence promoting slippage. Interestingly, they observed that shearing increases the maturity for low to intermediate maturity carbonaceous matter, whereas shearing decreases the maturity of high-maturity carbonaceous matter. This further highlights the complexity of using Raman as maturity tool in fault zones.

Overall, the study of OM in fault zones using Raman spectroscopy is still in its infancy, and only the $D1_A/G_A$ and R1 parameters have been widely used in the literature. It is recommended that Raman parameters that are not derived from complex deconvolution methods should be tested, in order to minimise bias, similar to the approaches adopted by Lünsdorf and Lünsdorf (2016), Henry et al. (2018, 2019) and Schito and Corrado (2018). Studying graphite in fault zones has an inherent risk, as the carbon needed for graphite formation can originate directly from sedimentary organic matter or from non-organic carbon precipitated from carbon-rich fluids ($CO_2$ and $CH_4$; Cao and Neubauer, 2019 and references therein), hence why it is often referred to as 'carbonaceous materials' (CM) in fault zone studies. Unlike vitrinite reflectance, Raman spectroscopy may be able to differentiate between the different origins by using methods that have been previously applied by Wilkins et al. (2015) and Schito et al. (2019) to determine different types of OM. Another limitation in determining the frictional heating of OM in fault zones is that structural ordering may also be induced by the increased pressures and shearing during the physical movement of faults, which has been shown to alter the Raman spectrum (Huang et al., 2010; Kaneki et al., 2018; Kouketsu et al., 2019b).

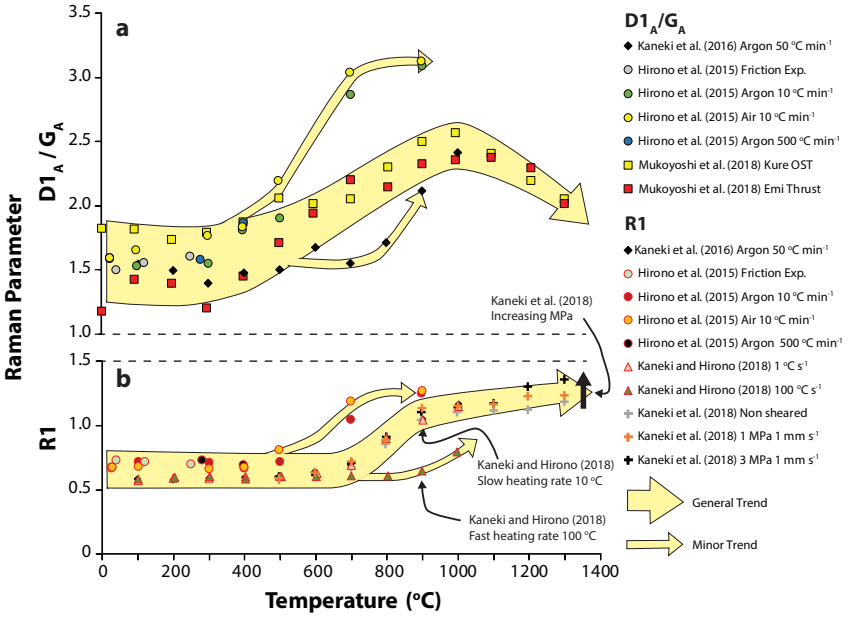


**Figure 3.9.** Trends of Raman parameters with increasing temperature due to frictional heating of OM along fault planes. **(a)** $D1_A/G_A$. **(b)** R1. Data sources in the key.

## 3.6 Developing a standardised approach

### *3.6.1 Deconvolution*

Deconvolution allows the operator to fit multiple functions to the Raman spectrum that represent different modes of vibration and to assess a suite of derived parameters (Beyssac et al., 2002; Wilkins et al., 2014; Sauerer et al., 2017; Schito and Corrado, 2018). Deconvolution is typically performed in the first-order region; however, several studies have also performed it in the second-order region (Beyssac et al., 2002; Rantitsch et al., 2004; Zeng and Wu, 2007; Childress and Jacobsen, 2017). The number of functions fitted when performing deconvolution in the first-order region is extremely variable, ranging from 2–10 functions (Table 3.5). This lack of consistency between authors makes it near impossible to compare results and biases.

We recommend that simplicity and consistency is key for the wider utilization of Raman spectroscopy as a geothermometer. However, performing a simple 2-band deconvolution of only the D1- and G-band (Kaneki et al., 2016; Liu et al., 2016;

Mukoyoshi et al., 2018; Pan et al., 2019**)** generates a poor fit with the raw spectra, especially for amorphous OM. Performing complex deconvolution methods with several fitted bands can also be highly subjective and create considerable bias, especially for low-maturity OM (Hinrichs et al., 2014; Lünsdorf et al., 2014; Lupoi et al., 2017; Henry et al., 2018). Some authors have performed several different types of deconvolution depending on how mature the OM is (Kouketsu et al., 2014; Ulyanova et al., 2014; Delchini et al., 2016; Schito et al., 2017); this requires visual identification of the spectra or prior knowledge regarding the burial of the samples. Nevertheless, the use of multiple deconvolution methods for different maturities is essential because with progressive maturation, individual disordered bands will begin to disappear and must be excluded from the deconvolution (Kouketsu et al., 2014; Delchini et al., 2016; Lünsdorf et al., 2017; Schito et al., 2017).

A major talking point is whether to fit the D2-band or not, in the G-band region. Kouketsu et al. (2014) claimed that the G-band is absent for low crystallinity OM (<165 ±35 °C), and that the region at c.1600 $cm^{-1}$ is composed solely of the D2-band. Only for higher crystallinity samples did they begin to fit the G-band. Several authors have highlighted the difficulty in fitting the D2-band for low maturity/poorly ordered OM (Beyssac et al., 2002; Brolly et al., 2016; Henry et al., 2018). Henry et al. (2018) avoided fitting the D2-band as there is no logical way in determining how the D2 or G-functions should fit. We continue with this school of thought and recommend that if deconvolution is performed, the D2-band should not be fitted, unless it is visible.

Several authors have set constraints when performing deconvolution (Kouketsu et al., 2014; Lünsdorf and Lünsdorf, 2016; Ito et al., 2017). Assigning constraints to peak widths, positions and heights is not advisable, as it forces the deconvolution outcome to work around the conditions that have been set, which may not be representative of the true nature of the Raman spectrum. On the other hand, it is understood that assigning constraints limits the number of potential deconvolution outcomes for a spectrum. Schopf et al. (2005) considered the best deconvolution outcome to have the best statistical fit with the original spectrum. Although statistical fit is important, operators should not fall into the trap that “if I have a good statistical fit, I have a

realistically fitted spectrum", as Henry et al. (2018) demonstrated that functions fitted with unrealistic positions, widths and heights can nonetheless yield good statistical fits. It is therefore recommended that if deconvolution is performed, visual analysis of the spectrum should also be performed in order to quality check the position, widths and heights of the fitted functions.

When performing deconvolution, Lünsdorf et al. (2017) determined three sources of bias: (1) operator bias; (2) sample heterogeneity bias; (3) different analytical conditions. They proposed that performing an automated method will rule out the operator bias. Several authors have developed an automated deconvolution method in order to determine maturity parameters from individual Raman bands (Lünsdorf and Lünsdorf, 2016; Bonoldi et al., 2016; Schito and Corrado, 2018). Lünsdorf et al. (2017) developed a robust open source software (http://www.sediment.uni-goettingen.de/download/) that automatically performs random curve fitting in an iterative approach in order to determine the optimum baseline correction, which avoids operator bias. Although deconvolution is performed during the iterative curve fitting steps, the individual bands are not used; it is only used to determine the optimum smoothed, baseline corrected spectrum, where the D_STA and G_STA parameters are calculated. This method has proved to be very successful and the parameters have a good relationship with VR. Lünsdorf et al.'s (2017) method tackles a very important issue, as the baseline correction can introduce substantial bias, the method also avoids using individual bands and uses the area ratios of the whole smooth, baseline corrected spectrum.

Henry et al. (2018) also used a smooth baseline corrected spectrum, however here the baseline is calculated using predefined control points and the accuracy of the baseline correction is determined by performing a visual inspection. This can create unnecessary bias in spectra with a non-linear fluorescence background. In order to avoid bias, Henry et al. (2018) rejected all spectra with substantial fluorescence. Schito and Corrado (2018) also developed a novel approach, where a linear baseline subtraction occurs at the shoulder points of the D1- and G-bands, and then after the baseline correction is performed, each band is fitted with a Gaussian fit separately.

1688 This method again tries to minimise the bias associated with the baseline correction,
1689 similar to Lünsdorf et al. (2017), but takes a different approach.

1690 A major barrier for the wider utilisation of Raman spectroscopy as a geothermometer,
1691 is to decide whether to perform deconvolution or not, as there are many different
1692 approaches and it is confusing for a new operator to determine which method to use.
1693 In order to encourage the wider use of the technique, Raman spectroscopy needs to
1694 be standardized. This review acknowledges that deconvolution has been extremely
1695 popular, but it is not an exact science for poorly ordered amorphous OM. Recent
1696 papers (Lünsdorf et al., 2017; Henry et al. 2018, 2019; Schito and Corrado, 2018; Mi
1697 et al., 2019) have now demonstrated that complex, ambiguous deconvolution
1698 methods of several bands are not needed, and that reliable results can be achieved
1699 otherwise. Lünsdorf et al. (2017) and Schito and Corrado (2018) have also developed
1700 novel approaches to reduce the operator bias in baseline subtraction. We believe that
1701 there is no need to perform deconvolution if several Raman parameters (e.g. RBS, G-
1702 FWHM, SI, R1, SSA) can be derived from an un-deconvolved spectrum that can track
1703 the thermal evolution of OM. This will allow for a more practical and faster analysis
1704 with less bias.

1705

1706 **Table 3-5.** Variety of deconvolution methods for the first order region in the literature.

| Bands (total bands) | References | Notes |
|---|---|---|
| No deconvolution | Spötl et al (1998); Jehlička and Beny (1999); Inan et al. (2016); Henry et al. (2018); Kaneki and Hirono (2019). | |
| G, D1 (2) | Bény-Bassez and Rouzaud (1985); Kelemen and Fang (2001); Quirico et al. (2005); Bonal et al. (2007); Zeng and Wu (2007); Liu et al. (2013); Hinrichs et al. (2014); Wilkins et al. (2014); Kaneki et al. (2016); Liu et al. (2016); Schmidt et al. (2017); Kaneki and Hirono (2018); Mukoyoshi et al. (2018) | |
| G, D1, D2 (3) | Court et al. (2007); Endo et al. (2012); Delchini et al. (2016); Kouketsu et al. (2019). | |
| G, D1, D3, D4 (4) | Allwood et al. (2006); Eichmann et al. (2018); Nakamura et al. (2019). | |

| | | |
|---|---|---|
| G, D1, D2, D3 (4) | Beyssac et al. (2002, 2003, 2019); Rantitsch et al. (2004); Marques et al. (2009); Aoya et al. (2010); Huang et al. (2010); Schiffbauer et al. (2012); Zhou et al. (2014); Nakamura et al. (2015); Chim et al. (2018) | |
| G, D1, D2, D4 (4) | Jubb et al. (2018) | |
| D1, D2, D3, D4 (4) | Ito et al. (2017); Kouketsu et al. (2017) | |
| G, D1, D2, D3, D4 (5) | Lahfid et al. (2010); Kouketsu et al. (2014); Bernard et al. (2015); Delarue et al. (2016); Delchini et al. (2016); Chen et al. (2017); Chesire et al. (2017); Childress and Jacobsen (2017); Kouketsu et al. (2017); Nakamura et al. (2017); Sauerer et al. (2017); Baludikay et al. (2018); Golubev et al. (2019); Song et al. (2019) | |
| G, D1, D2, D3, D4, D5 (6) | Romero-Sarmiento et al. (2014) | |
| G+D2, D3 (x2), D4, D5 | Ferralis et al. (2016) | Ferralis et al. (2016) interpreted two separate D3 bands (c. 1400 $cm^{-1}$ and c. 1500 $cm^{-1}$) when performing deconvolution. |
| G, D, + 4 bands (6) | Guedes et al. (2010) | |
| G, GI, Dr, D, DI, S | Schito et al. (2017) | |
| 8 band | Schopf et al. (2005) | |
| $G_L$, G, $G_R$, $V_L$, $V_R$, D, $S_L$, S, $S_R$, R (10) | Li et al. (2006); Li (2007); Guedes et al. (2012); Zhang and Li (2019) | Descriptions of what each band signifies is given in Li (2006) |
| G, D2, D3, D, SI, S (6) | Bonoldi et al. (2016) | |

FWHM – Full Width at Half Maximum. au – arbitrary units

### *3.6.2 Sample type*

Several different sample types have been tested using Raman spectroscopy to analyse OM: polished rock cut-surfaces and thin-sections (Beyssac et al., 2003; Rahl et al., 2005; Allwood et al., 2006; Quirico et al., 2011; Mathew et al., 2013; Hinrichs et al., 2014; Wilkins et al., 2014; Henry et al., 2018), strew slides (Schmidt et al., 2017;

Baludikay et al., 2018; Henry et al., 2018; Khatibi et al., 2018a) and rock chips (Muirhead et al., 2016; Sauerer et al., 2017; Henry et al., 2019).

It is widely acknowledged that polishing OM can alter the Raman spectrum (Beyssac et al., 2003; Ammar and Rouzaud, 2012; Lünsdorf, 2016; Henry et al., 2018). Results from Ammar and Rouzaud (2012), Lünsdorf (2016) and Henry et al. (2018) showed that polishing increases the relative height and blue-shifted the D1/D-band region. This has been attributed to the interlayer delamination of the carbon structures leading to the buckling of graphene layers (Ammar and Rouzaud, 2012; Lünsdorf, 2016), similar to that observed during frictional heating, as described by Nakamura et al. (2015).

Ammar and Rouzaud (2012) and Henry et al. (2018) demonstrated that after polishing OM with a 1 µm diamond and 0.04 µm colloidal silica slurry respectively, the D1-band region increases in height (increasing the R1 ratio), but the G-FWHM is invariable, suggesting that the G-FWHM parameter has the potential to be used on polished sections. This is valuable information, as polishing a sample may be the only way to locate rare dispersed OM in a rock, and knowing which Raman parameters may or may not be impacted by polishing is essential. Henry et al. (2018) further demonstrated that the change in the D1-band height is not systematic, so it cannot be assumed that polishing impacts all the OM components in a sample to the same degree. This challenges the assumption by Jubb et al. (2018) that polishing impacts all the OM structure by the same amount in a single sample. Lünsdorf et al. (2016) showed that polishing using a slurry with a grain size of P2500 to 1 µm does not alter the STA, R1 and position of the G-band; however, using a finer grain slurry of 0.05 µm does alters these parameters. Their results indicated that the D1-band decreases in height with polishing, which is the opposite of the results obtained by Ammar and Rouzaud (2012) and Henry et al. (2018) which showed increased values. Lünsdorf (2016) also demonstrated that after polishing the G-band position tends to red-shift for lower maturity samples (c. < 3.0 $\%VR_o$) and blue-shift for high maturity samples (> 4.0 $\%VR_o$). The red-shift of the G-band after polishing for low-maturity samples was not observed by Henry et al. (2018). Ammar and Rouzaud (2012), Lünsdorf (2016) and Henry et al. (2018) targeted polished OM; however, authors who have studied

polished thin sections have avoided analysing polished OM, by targeting OM that lies beneath the surface of transparent minerals (Pasteris, 1989; Beyssac et al., 2002; Aoya et al., 2010; Ammar and Rouzaud, 2012; Mathew et al., 2013; Kouketsu et al., 2014; Barzoi, 2015; Mészáros et al., 2019).

Analysis of OM in strew slides has been performed by Schmidt et al. (2017) and Henry et al. (2018) by isolating the OM from the rock using hydrofluoric (HF) and hydrochloric (HCl) acids. Both groups recognised the potential of performing palynofacies and multiple thermal alteration studies (e.g. thermal alteration indices, spore colouration index) contemporaneously, along with the Raman analysis. Performing Raman analysis on strew slides is also extremely useful if a rock is lean in OM and locating OM particles via polished sections or in rock-chips proves to be challenging. Schmidt et al. (2017) compared the results derived from translucent, degraded, opaque and bitumen particles, and showed translucent phytoclasts to be the most reliable. Henry et al. (2018) confirmed that opaque phytoclasts should be avoided, but that the Raman parameter results were similar for amorphous organic matter (AOM) and translucent phytoclasts; however, it should be noted that their study was performed on samples with similar low maturity. Lünsdorf et al. (2014) demonstrated another advantage of using strew strides, as treating samples with hydrofluoric (HF) acid lowered the standard deviation for both the RA1 and RA2 parameters; the reason for this was believed to be that the HF removed functional groups or clays, which led to a reduction in the background fluorescence.

It is important to prepare strew slides in a consistent manner and to then store them in a desiccator; however, for long term storage it may be best practice to store them in an inert atmosphere to avoid hydration and oxidation reactions. Schopf et al. (2005) showed that when the same isolated OM particle was dehydrated and hydrated, the G-FWHM values varied by 18 $cm^{-1}$, which would give significantly different and potentially misleading maturity results. Quirico et al. (2005) highlighted that moisture in the OM can lead to photo-oxidation of the OM which increases the fluorescence. To avoid the fluorescence caused by moisture, Lupoi et al. (2018) dehydrated their samples at 110 $^{\circ}C$ overnight in an oven prior to Raman analysis. This is inadvisable, as heating a sample at >60 $^{\circ}C$ can artificially thermally alter the OM. When preparing

strew slides for Raman analysis, we propose that the strew slides should be left to either air dry or oven dry at temperatures <60 °C for up to 24 hours, in order to remove the moisture, and then kept in a desiccator or, if stored for a longer period of time, sealed in an inert atmosphere. Sealing the samples without firstly drying them can lead to continuing oxidation, as the moisture will not have been removed and will persist in the OM (Quirico et al., 2005).

Sauerer et al. (2017), Henry et al. (2019) and Goryl et al. (2019) demonstrated that the Raman analysis of OM in unprepared rock-chips can be rapid, cheap and reliable; however, it may be difficult to locate OM particles under the microscope, especially for rocks lean in OM. The operator also needs to be careful that adjacent minerals do not produce significant fluorescence, which can obscure the OM Raman bands. Nevertheless, using rock-chips allows Raman spectroscopy to be used on-site, as no sample preparation is needed. However, this approach will work best on coal samples, rather than rocks with dispersed OM.

Brolly et al. (2016) showed that oxidation of rocks can dramatically impact the spectrum of OM, as haematite has a strong Raman band at c. 1300 $cm^{-1}$, which merges with the D-band region for OM. The presence of haematite will impact the D-band region by shifting the band to lower wavenumbers, reducing the width and increasing the height with respect to the G-band. The G-band is affected, as haematite increases the G-FWHM and blue-shifts the position. Haematite also drastically increases the noise of a Raman spectrum of OM. However, Brolly et al. (2016) showed that treating oxidised samples with HF will remove the interfering haematite signal, as well as removing fluorescence caused by clay minerals (Villanueva et al., 2008; Lünsdorf et al., 2014).

Wopenka and Pasteris (1993) expressed caution regarding the effects of the orientation of OM with respect to the incident laser, as it might potential lead to bias in the results. This is a common phenomenon when performing vitrinite reflectance and is known as bi-reflectance (Hartkopf-Fröder et al., 2015). Aoya et al. (2010) tested this by analysing thin sections that were cut perpendicular and parallel to bedding and demonstrated that the orientation of the elongated OM grains has an insignificant

effect when using the R2 Raman parameter for metamorphic rocks in the temperature range 300–650 °C. However, Lünsdorf et al. (2014) revealed that for highly crystalline samples, the structural orientation of the OM with respect to the laser can impact the R1 and R2 ratio. Kouketsu et al. (2014) also noted that the orientation of high crystallinity samples could potentially have a dramatic effect on the Raman spectrum; however, they demonstrated that this effect is negligible for low-temperature/low-crystallinity samples. Tunistra and Koenig (1970) expressed concern about intra-grain heterogeneity, and showed that the Raman spectra close to grain boundaries were different when compared to the spectra acquired from the internal body of the OM. Aoya et al. (2010) therefore proposed that at least 50 measurements should be performed in order to capture this heterogeneity and get reliable average results; this was further highlighted by Lünsdorf et al. (2014).

Kelemen and Fang (2001), Bonoldi et al. (2016) and Schito et al. (2018) showed that the thermal evolution of different kerogen types (I, II and III) follow similar trends. Raman spectroscopy has also been performed successfully on different OM components, including bitumen (Liu et al., 2013; Hackley and Lünsdorf, 2018), graptolites (Inan et al., 2016; Mumm and Inan, 2016), chitinozoans (Roberts et al., 1995) and agglutinated foraminifera (McNeil et al., 2016). Mori et al. (2017) demonstrated that Raman parameters derived from OM in limestones, sandstones and mudstones are similar, indicating that lithology does not affect the Raman spectrum. This suggests that Raman measurements may not be impacted by suppression, unlike vitrinite reflectance.

### *3.6.3 Laser Raman setup*

It is accepted that different laser wavelengths impact the Raman D-band region of OM (Vidano et al., 1981; Ferrari and Robertson, 2001; Starkey et al., 2013; Sauerer et al., 2017; Henry et al., 2018; Jubb et al., 2018). There is a progressive red-shift of the position of the D-band region with increasing excitation wavelength and vice-versa, whereas the position of the G-band remains unaffected (Vidano et al., 1981; Kouketsu et al., 2014; Jubb et al., 2018). Aoya et al. (2010) compared the R2 parameter values from a 514.5 nm and a 532 nm laser and demonstrated that the 532 nm laser had

systematically slightly larger R2 values. Starkey et al. (2013) demonstrated that increasing the laser wavelength from 473 nm to 632 nm, increases the D1-FWHM, whereas the G-FWHM have very similar values using a 473 and 514 nm system and only increases greatly when using a laser wavelength >632 nm. They also showed that the D1-band position blue-shifts and that the G-band position unpredictably changes with increasing laser wavelength. Visual inspection of the spectra in Starkey et al. (2013), suggests that the G-band height decreases with respect to the D1-band height with increasing wavelength, which has also been demonstrated by Lünsdorf and Lünsdorf (2016). D1-FWHM and G-FWHM results obtained by Kouketsu et al. (2014) showed little difference between the 514.5 nm and 633 nm lasers, whereas the D1-band position and R1 ratio were affected; however, they did not show any data that describes how these parameters are affected. Lünsdorf et al. (2017) demonstrated that the D_STA and G_STA parameters follow the same path with increasing maturity when using either a 488 nm or a 532 nm laser.

Current evidence suggests that the G-FWHM parameter may have good comparability between laboratories using different laser wavelengths and any differences will be related mostly to operator bias. By contrast, D1-FWHM, RBS and R1 values will be impacted by both the choice of laser wavelength and operator bias. Increasing the laser wavelength will also increase fluorescence and drastically reduce the quality of the Raman spectrum (Quirico et al., 2005; Lünsdorf and Lünsdorf, 2016; Henry et al., 2018; Goryl et al., 2019). It is therefore recommended to use a laser wavelength <532 nm, especially for low-maturity samples.

An interlaboratory experiment consisting of three laboratories was performed by Lünsdorf et al. (2014), who showed that the R1 and R2 results can be significantly different, even if the same laser wavelength is used. The disparity in the results may be attributed to other factors such as different gratings and CCD cameras, intra-sample heterogeneity and most importantly, operator bias. Further comparisons between different Raman spectroscopy setups will be essential to see whether laboratories can use the same calibration curves or not, and to determine which setups inherently generate the least bias.

Henry et al. (2018) demonstrated that in-situ burning of OM occurs when using a laser power >1 mW and this causes increased fluorescence in the Raman spectrum, as well as blue-shifting the G-band position and increasing the G-FWHM. Whereas the D-band region, other than being affected by fluorescence, remains invariable. This has subsequently also been shown by Nakamura et al. (2019). It is therefore advised that low laser powers are used (c. 0.02 mW) and inspection before and after the analysis should be performed to determine whether any damage has occurred (Henry et al., 2018).

### 3.6.4 Calibration

Raman studies on OM to date have been performed in a large number of laboratories world-wide by teams of researchers using different instrumentation and working on a variety of sample materials. The analytical precision of the data obtained may be readily determined by a laboratory, but the accuracy and transferability of results remain largely untested. There is a need for a suite of reference samples of known maturity, so that laboratories can perform in-house calibrations with a sub-sample set and then test the accuracy and precision of the calibration curve on another sub-sample set (Lünsdorf et al., 2017). This will make the comparison of vitrinite reflectance and temperature values more reliable between laboratories and allow to better assess and quantify the bias associated with different experimental set-ups, sample preparation and operator bias. Lünsdorf et al. (2017) have pioneered this work and compiled a set of 25 reference samples from the central and western Alps that covers the temperature range of c.160–600 °C, which are available upon request from the first author.

Vitrinite reflectance calibration is performed by analysing the reflectance of standards composed of crystalline material such as spinel (0.4 %) and yttrium-aluminium-garnet (YAG, 0.9 %). However, it is still unclear what the best sample type might be for the calibration of Raman spectrometry; whether it should be OM that has been naturally heated, or OM that has been artificially heated in the laboratory. The latter may exhibit similar Raman parameters to samples that have been matured naturally (Kelemen and Fang, 2001; Zhou et al., 2014; Bonoldi et al., 2016). However, Hackley

and Lünsdorf (2018) and Khatibi et al. (2019) demonstrated that Raman parameters derived from artificially heated OM do not follow the same trend as naturally matured samples. Hackley and Lünsdorf (2018) showed that the G_STA and RBS Raman parameters have higher values and the D/G values are lower for artificially heated samples, demonstrating that the artificial samples do not follow the same maturation pathway as natural samples.

In laboratory experiments by Huang et al. (2010), it was shown that under extremely high pressure (1000–6500 MPa), the D1-band red-shifts more than the G-band, decreasing the RBS, and the G-FWHM visually decreases with increasing pressures, suggesting that pressure is retarding the maturity values derived from these Raman parameters. However, it must be noted that the pressures used in this study far exceed pressures for sedimentary rocks and are only applicable to ultra-high-pressure metamorphism. Du et al. (2014) also showed that different pyrolysis set-ups impact the Raman parameters, suggesting that different environmental conditions can yield variable Raman results.

These results demonstrate that: (1) calibration curves constructed using artificially heated samples should be used with caution; (2) different pressures, heating rates and heating length impact the Raman spectrum of OM. It is therefore encouraged that further work on artificially heated samples with varying deformation styles, pressures and heating rates should be performed, and the results compared to samples that have been matured naturally. It must also be acknowledged that calibration curves constructed using naturally matured samples may only be relevant to that geological area.

## 3.7 Future

To progress Raman spectroscopy as a geothermometer we need to develop and follow a standardized method and undertake interlaboratory comparison tests, like those performed previously for VR (Hackley et al., 2015). It is recommended that a diverse set of natural reference samples should be assembled and tested. We advise that artificially heated samples should not be used to create calibration curves for

diagenesis to metamorphism studies. However, we would encourage experiments to test the effects of different heating rates, pressures and deformation styles, to get a better appreciation of how different environments may impact the Raman spectrum. This will be of particular value for the application of Raman analysis of OM to the interpretation of processes occurring in fault zones.

Suitable reference samples should be: homogenous, with large quantities of material available in order to create sub-sets for several laboratories; fully characterised using a range of maturity proxies, including VR and Rock-Eval™ pyrolysis for diagenesis to metagenesis, and include mineral assemblage and mineral chemistry data for metamorphic studies. An interlaboratory test can then be devised. We recommended that a workflow similar to that illustrated in Fig. 3.10 should be followed, in order to compare and quantify the bias associated with different instrumental set-ups, sample preparation and operators.

Selected laboratories should receive two suites of reference samples. One sample set will be used for Raman calibration and the other to perform a blind test to assess the accuracy of the calibration curves. Each calibration and blind test sample will be split into three sub-samples that will undergo different sample preparations (polished sections, strew slides and rock chips). Calibration curves will be constructed for each sample type and a blind test performed on each of these. The blind test Raman equivalent VR and temperature values will be compared with the prior measured VR and temperatures values. The results will then be reviewed, and data obtained by different laboratories, sample preparations, Raman instrumentation, and operators will be analysed statistically to identify the elements most subject to bias, and to determine the precision and accuracy of the results obtained using different methodologies.

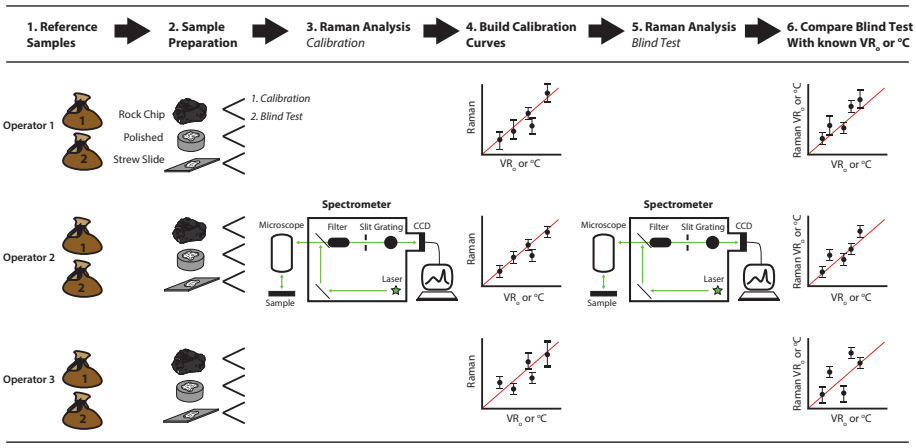


**Figure 3.10.** Example of a future inter-laboratory exercise to determine the bias associated with different methods and different Raman set-ups.

The deployment of portable Raman instrumentation is also of future interest, as it has the potential to allow operators to perform near real-time maturity analysis on a drilling rig or out in the field when performing metamorphic and structural geology studies. However, this approach has yet to be assessed and the technical feasibility operating in an environment with constant vibration, such as a drilling rig, is debatable. For field analysis, it will be necessary to attach a microscope with either a live streaming camera or eyepiece, so that the operator can target OM particles. Future studies will also need to assess the portable Raman suitability for the analysis of coal and rocks that contain dispersed OM. For dispersed OM, it will be necessary to design a portable Raman instrument with a small laser spot size, similar to the bench-top Raman (c. 2 µm). Having a means to target the OM and have a small laser spot size will help the operator avoid analysing adjacent non-organic grains that can cause fluorescence and obscure the OM Raman bands.

## 3.8 Conclusion

Raman spectroscopy offers a cheap, rapid, non-destructive and high-resolution alternative maturity tool than can be used independently or in combination with more conventional methods in order to: (1) reduce the risk in determining the maturity of

source rocks during hydrocarbon exploration; (2) determine temperatures associated with contact and / or regional metamorphism; (3) quantify the amount of frictional heating and deformation that has occurred along fault zones.

The G-FWHM and RBS parameters are the most reliable Raman variables that can be used to estimate the maturity of OM during diagenesis–metagenesis, whereas multiple parameters, including the R1, R2, RA1, RA2 and D1-FWHM, have proved to be robust for quantifying the temperatures reached by organic matter in metamorphic rocks. Using integrated areas from the whole spectrum to derive Raman parameter like SSA, D_STA and G_STA is also promising and as these have a wide temperatures range. Raman studies of organic matter in fault zones are still in their infancy, but they have great potential to determine not only maximum temperatures attained during frictional heating, but also to shed light on deformation processes.

To promote the wider application of Raman spectroscopy, the terminology for the Raman bands, and the definition and derivation of Raman parameters must be standardized. A unified terminology is proposed here and this should be universally adopted in the future. Raman reference materials are needed, so that inter-laboratory tests can be performed to better determine which methodology, Raman parameters and Raman instrumental set-ups introduce the least bias and generate the most precise and accurate maturity data.

# *Chapter 4* Assessing low-maturity organic matter in shales using Raman spectroscopy: Effects of sample preparation and operating procedure

This chapter is from: Henry, D.G., Jarvis, I., Gillmore, G., Stephenson, M., Emmings, J.F., 2018. *Assessing low-maturity organic matter in shales using Raman spectroscopy: Effects of sample preparation and operating procedure. International Journal of Coal Geology, 191, 135 – 151.*

## 4.1 Abstract

Laser Raman spectroscopy is used to assess the thermal maturity of organic matter in sedimentary rocks, particularly organic-rich mudstones. However, discrepancies exist between quantified Raman spectral parameters and maturity values obtained by vitrinite reflectance. This has prevented the adoption of a standard protocol for the determination of thermal maturity of organic matter (OM) by Raman spectroscopy. We have examined the factors influencing the Raman spectra obtained from low-maturity OM in potential shale gas reservoir rocks. The inconsistencies in Raman results obtained are due to three main factors that are critically evaluated: (1) different operational procedures, including experiment setup and spectral processing methods; (2) different methods of sample preparation; (3) the analysis of diverse types of OM. These factors are scrutinized to determine the sources of inconsistency and potential bias in Raman results, and guidance is offered on the development of robust and reproducible analytical protocols. We present two new Raman parameters for un-deconvolved spectra named the DA1/GA ratio (area ratio of 1100-1400 $cm^{-1}$/1550-1650 $cm^{-1}$) and SSA (scaled spectrum area: sum of total area between 1100-1700$cm^{-1}$) that offer potential maturity proxies. An automated spreadsheet procedure

is presented that processes raw Raman spectra and calculates several of the most commonly used Raman parameters, including the two new variables.

## 4.2 Introduction

Laser Raman spectroscopy is being increasingly used to assess the thermal maturity of organic matter (OM) in sedimentary rocks (Pasteris and Wopenka, 1991; Spötl et al., 1998; Kelemen and Fang, 2001; Beyssac et al., 2002; Jehlička et al., 2003; Marshall et al., 2005; Quirico et al., 2005; Rahl et al., 2005; Schopf et al., 2005; Zeng and Wu, 2007; Guedes et al., 2010; Liu et al., 2012; Muirhead et al., 2012, 2016; Aoya et al., 2014; Kouketsu et al., 2014; McNeil et al., 2015; Bonoldi et al., 2016; Deldicque et al., 2016; Ferralis et al., 2016; Lünsdorf, 2016; Lünsdorf et al., 2017; Lupoi et al., 2017; Sauerer et al., 2017; Schito et al., 2017). The novelty of Raman spectroscopy is that it is a non-destructive method that allows for rapid data acquisition with fast and easy interpretation, combining both optical microscopy and vibrational spectroscopy. Laser Raman has the ability to be used alongside other petrological parameters in order to reduce risk, as well as being applied where other maturity indicators such as vitrinite reflectance (VR), spore colouration index (SCI), fluorescence spectroscopy and Rock-Eval pyrolysis ($T_{max}$) fail to provide reliable results. It can also be used as a cheap and rapid means to screen samples before conducting more expensive and time-consuming destructive analyses.

The Raman spectrum of OM consists of two broad bands; the G band (~1600 $cm^{-1}$), known as the graphite band, and the D band (~1350 $cm^{-1}$), known as the disordered band (Fig. 4.1a). Deconvolution can further divide the spectrum into several disordered bands (Fig. 4.1b; e.g. D1, D2, D3, D4, D5). However, the number of disordered bands that are separated using deconvolution is controversial, and authors have used a combination of different bands to define laser Raman parameters that can be applied in maturity studies (Spötl et al., 1998; Beyssac et al., 2002; Schopf et al., 2005; Li et al., 2006; Guedes et al., 2010; Lahfid et al., 2010; Liu et al., 2012; Hinrichs et al., 2014; Wilkins et al., 2014; Lünsdorf et al. 2017).

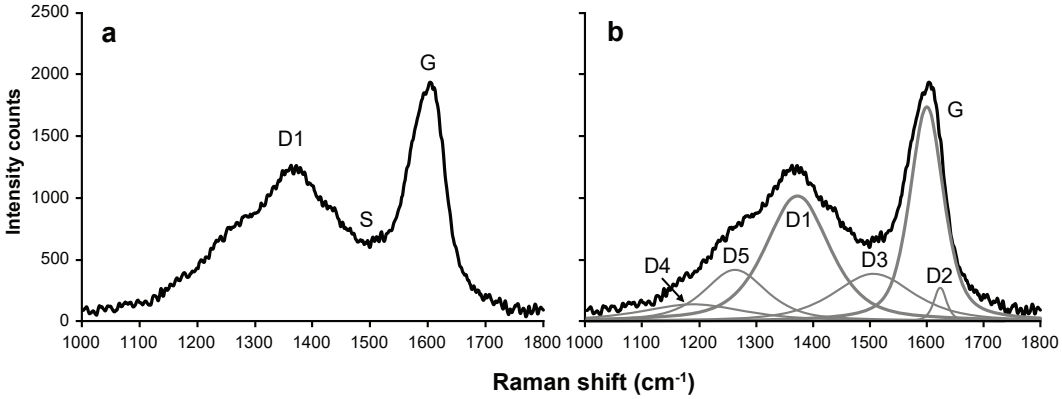


**Figure 4.1.** Raman spectral characteristics. **(a)** Un-deconvolved organic matter spectrum **(b)** Common six band deconvolution outcome for an organic matter spectrum. D = disordered bands (1, 2, 3, 4, 5); G = graphitic band; S = saddle.

The G band corresponds to an ideal graphitic structure, whereas the D bands are associated with chemical and structural defects in the crystal lattice. As temperature increases, the chemical defects are expelled from the crystal lattice and the remaining carbon undergoes reorganization into a more ordered carbon structure, until it reaches the metamorphism stage where the carbon residue transforms into perfectly ordered graphite (Buseck and Beyssac, 2014). Laser Raman analyses the chemical structure of OM, and in theory, should be able to track the thermal evolution of OM. The current study aims to assess the application of laser Raman to characterise OM maturity in the lower temperature oil- and gas-generation stages of catagenesis (50°–150°C). An improved analytical method has great potential to be used in the evaluation of shale gas plays, as well as being applied to the wider analysis of petroleum basins.

Some of the most commonly used parameters to track thermal maturity are summarized in Table 4.1, which include the heights, widths, areas and positions of the disordered and graphitic (ordered) bands. It should be noted that there is some ambiguity with the terms RA1 and RA2: Chen et al. (2017) used different

equations to calculate these parameters compared to variables of the same name reported previously by Lahfid et al. (2010).

Inconsistent quantified Raman parameter values and maturity values obtained by VR are apparent in the literature (Kelemen and Fang, 2001; Quirico et al., 2005; Guedes et al., 2010; Lahfid et al., 2010; Liu et al., 2013; Wilkins et al., 2014). In this study three factors are examined as likely sources for this inconsistency: (1) different operational procedures employed, including experiment setup and spectral processing methods; (2) different methods of sample preparation; (3) analysis of diverse types of OM and intra-particle variability. These three factors have also been discussed by Lünsdorf et al. (2014).

(1) Operational procedures may be divided into two categories: (a) experimental setup; (b) spectral processing methods.

(a) The laser wavelength, laser power, accumulation time and number of accumulations employed by different authors are highly variable (Appendix A). Here, we will assess the optimum experimental setup that considers the speed of analysis, damage to the sample, and the signal to noise ratio.

(b) Typically, processing the Raman spectra include smoothing, a linear or non-linear baseline correction, followed by deconvolution of two (Hinrichs et al., 2014; Wilkins et al., 2014; Schimdt et al., 2017), three (Court et al., 2007), four (Beyssac et al., 2002; Aoya et al., 2005; Rahl et al., 2005), five (Lahfid et al., 2010; Chen et al., 2017; Sauerer et al., 2017) or six or more bands (Schopf et al., 2005; Li et al., 2006; Guedes et al., 2010; Bonoldi et al., 2016; Ferralis et al., 2016; Schito et al., 2017) (Appendix A). Deconvolution enables the operator to assess a suite of Raman parameters (Table 4.1) for individual bands. Several common deconvolution methods will be tested against the automated method developed in this study, which does not perform

deconvolution, in order to acquire Raman parameters. The method and Raman parameters will be compared.

(2) A comparison of different sample types from several rock samples will be assessed to determine if there is a difference in Raman spectral parameters. Previous studies have analysed polished blocks of isolated OM (Pasteris and Wopenka, 1991; Beyssac et al., 2003; Nestler et al., 2003; Rahl et al., 2005; Allwood et al., 2006; Marques et al., 2009; Quirico et al., 2009; Guedes et al., 2010; Kwiecinska et al., 2010; Matthew et al. 2013; Hinrichs et al., 2014; Kouketsu et al., 2014; Wilkins et al., 2014; Mumm and Inan, 2016), as well as strew-mounted slides (Roberts et al., 1995; Spötl et al., 1998; Rantitsch et al., 2004; Lünsdorf et al., 2014), and rock chips (Muirhead et al., 2016; Sauerer et al., 2017). Some authors demonstrated that polishing OM impacts the Raman spectrum (Beyssac et al., 2003; Ammar and Rouzaud, 2012; Lünsdorf, 2016). This is examined further here.

(3) Different maceral types may behave differently under different thermal conditions as demonstrated by the Van Krevelen diagram (Tissot et al., 1974), so ensuring that the same maceral type is analysed throughout a geological section is generally essential. The effect of maceral type on Raman parameters is assessed here, together with an examination of intra-particle variability.

**Table 4-1.** Raman parameters used to determine the maturity of organic material, along with the abbreviations used in previous studies.

| Method | Parameters | Abbreviations | References |
|---|---|---|---|
| Full width at half maximum of a band (FWHM) | G | G-FWHM | Hinrichs et al. (2014); Zhou et al. (2014); Schimdt et al. (2017); This study. |
| | D1 | D-FWHM | Quirico et al. (2005); Bonoldi et al. (2016); Schito et al. (2017); This study. |
| | D1/G | | Spötl et al. (1998); Jehlicka et al. (2003). |

| | | | |
|---|---|---|---|
| Ratio of Raman band height intensity | D1/G | R1 | Rahl et al. (2005); Schimdt et al. (2017); Sauerer et al. (2017); Roberts et al. (1995); Spötl et al. (1998); Kelemen and Fang (2001); This study. |
| | G/S | Saddle Index | Wilkins et al. (2014); This study. |
| Ratio of band areas | D/G | RA1** | Chen et al. (2017). |
| | D1/(G+D1+D2) | R2 | Rahl et al. (2005); Chen et al. (2017). |
| | S2/(S1+S2) | R3 | Beyssac et al. (2002). |
| | (D1+D4)/(D1+D2+D3+D4+G) | RA1** | Lahfid et al. (2010). |
| | (D1+D4)/(D2+D3+G) | RA2** | Lahfid et al. (2010). |
| | D2/G | RA2** | Chen et al. (2017). |
| | D3/G | RA3 | Chen et al. (2017). |
| | D4/G | RA4 | Chen et al. (2017). |
| | G/(D1+D2+D3+D4+G) | RA5 | Chen et al. (2017). |
| Area of Raman spectra regions | $Area_{(1100–1400)}/Area_{(1550–1650)}$ | DA1/GA | This study. |
| | $Area_{(1100–1300)}/Area_{(1300–1370)}$ | RIP (Raman Index of Preservation) | Schopf et al. (2005); Du et al. (2014); This study. |
| Raman band position | G–D1 | RBS (Raman Band Separation) | Mumm and Inan (2016); Sauerer et al. (2017); Schimdt et al. (2017); Schito et al. (2017); This study. |
| | G | - | Spötl et al. (1998); Du et al. (2014); Inan et al. (2016). |
| | D1 | - | Spötl et al. (1998); Chen et al. (2007). |
| Scaled Spectrum Area | $Area_{(1100–1700)}$ | SSA | This study. |
| Scaled Total Area | Sum of scaled individual bands after deconvolution | STA | Lünsdorf (2016); Lünsdorf et al. (2017) |

* Refer to Figure 1 for G, D, S and D1–D4 band positions.

** It should be noted that there is some ambiguity with the terms RA1 and RA2: Chen et al. (2017) used different equations to calculate these parameters compared to variables of the same name reported previously by Lahfid et al. (2010).

## 4.3 Materials and methods

### *4.3.1 Materials*

The Late Mississippian (Namurian) Bowland Shale is the main target for shale gas exploration in the UK, with an estimated 1329 trillion cubic feet of hydrocarbons in-place (Andrews, 2013; Stephenson, 2014; Delebarre et al. 2017). The shales were

deposited in NE-SW epicontinental seaways between Gondwana and Laurussia. A phase of back-arc extension north of the Variscan orogenic front formed a series of interconnected graben and half-graben structures (Fig. 4.2; Waters et al., 2009). These basins accumulated Carboniferous organic-rich mudstones, which have been identified as a proven source rocks for many of the conventional oil and gas fields in the UK Midlands (DECC, 2010).

Four Mississippian (Arnsbergian; early Serpukhovian) Morridge Formation (equivalent to the Bowland Shale; Waters et al., 2009) core samples from the Carsington Dam Reconstruction C4 borehole (53.04898°N 1.63790°W, Derbyshire, England) in the Widmerpool Gulf were analysed (Fig. 4.2). Raman analyses were performed on polished blocks of isolated OM and strew slides. These samples are in the early oil window (Könitzer et al., 2014, 2016; Hennissen et al., 2017) and came with comprehensive palynofacies and geochemical data (Table 4.2). $T_{max}$ values range between 424–440°C (Könitzer et al., 2016), and the calculated $\%_{eq}VR_o$ using $T_{max}$ values (cf. Jarvie et al., 2001; Equation 3.1) range from 0.5–0.8 $\%_{eq}VR_o$, indicating immature to early maturity.

$$\text{Calculated } \%_{eq}VR_o = (0.0180 \times T_{max}) - 7.16 \qquad \textbf{Equation 4.1}$$

This agrees with the vitrinite reflectance values of <0.6 $\%VR_o$ obtained by Smith et al. (2010) from the area. Production Index (PI) values determined from Rock-Eval data by Könitzer et al. (2016) range from 0.06 to 0.09, straddling between immature and the oil generation window.

Two outcrop samples of the Upper Bowland Shale (Pendleian; early Serpukhovian) from a stream section in the Craven Basin (53.97373°N 2.54397°W), Lancashire (Fig. 4.2; Emmings et al., 2017), were also analysed and compared with the equivalent core material from the Carsington Dam Reconstruction C4 borehole (Table 2). $T_{max}$ values range between 431–442 °C, similar to the samples studied by Könitzer et al. (2016), and the calculated VR values using $T_{max}$ range from 0.6–0.8 $\%_{eq}VR_o$. However, the PI values range from 0.13–0.26, suggesting that these rocks had reached the oil generation window.

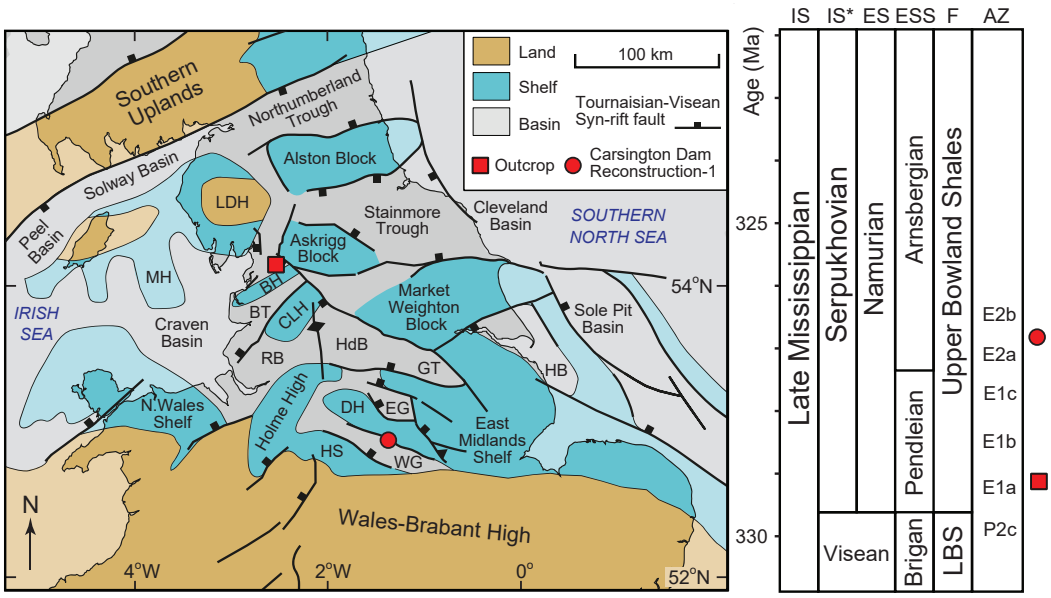


**Figure 4.2.** Tectonic framework of the Mississippian for northern England and Wales showing the location and stratigraphic ages of the samples used in this study. IS – International series; IS* – international stage; ES – European stage; ESS – European substage; F – Formation; AZ – ammonoid zones; Brigan – Brigantian; LBS – Lower Bowland Shales. Tectonic units: BH – Bowland High; BT– Bowland Trough; CLH– Central Lancashire High; DH – Derbyshire High; EG – Edale Gulf; GT – Gainsborough Trough; Hdb – Huddersfield Basin; HB – Humber Basin; HS – Hathern Shelf; LDH – Lake District High; MH – Manx High; RB – Rossendale Basin; WG– Widmerpool Gulf. Base map from Waters et al. (2009). Reproduced with the permission of the British Geological Survey ©NERC. All rights reserved.

**Table 4-2.** Samples studied from the Carsington Dam Reconstruction C4 borehole (CD) and outcrop section.

| Type | Sample name | Lithology | Summary of palynology | Rock-Eval parameters * | | | | | |
|---|---|---|---|---|---|---|---|---|---|
| | | | | TOC (%) | $T_{max}$ (°C) | HI | OI | PI | $\%_{eq}VR_o$ |
| CD | SSK 4522 | Calcareous mudstone | 90 % AOM; 10 % terrestrial | 1.8 | 425 | 330 | 17 | 0.06 | 0.49 |
| | SSK 4471 | Siltstone | 20 % AOM; 80 % terrestrial | nd | nd | nd | nd | nd | nd |
| | MPA 61616 | Silt-bearing mudstone | 30 % AOM; 70 % terrestrial | 1.1 | 440 | 96 | 29 | 0.09 | 0.76 |
| | MPA 61619 | Calcareous mudstone | 90 % AOM; 10 % terrestrial | nd | nd | nd | nd | nd | nd |

| | | | | | | | | | |
|---|---|---|---|---|---|---|---|---|---|
| Outcrop | HC01-04 | Mudstone | 90 % AOM; 10 % terrestrial | 3.87 | 432 | 141 | 0 | 0.18 | 0.62 |
| | HC02-73 | Mudstone | 80 % AOM; 20 % terrestrial | 2.19 | 431 | 163 | 1 | 0.26 | 0.60 |

* TOC = total organic carbon, HI = hydrogen index, OI = oxygen index, PI = production index. $\%_{eq}VR_o$ calculated using Jarvie et al. (2001) equation (Equation 1). AOM = amorphous organic matter, nd = not determined. CD data from Könitzer et al. (2016), outcrop data from Emmings et al. (2017).

## 4.3.2 Methods

### 4.3.2.1 Laser Raman

Analyses employed a Renishaw inVia™ laser Raman instrument connected to a Leica DMLM microscope. The Rayleigh scattering was removed using an edge filter and the Raman scattering was dispersed by an 18,000 lines/mm holographic grating and detected by a charged couple device (CCD). A standard silicon wafer sample was used to calibrate the instrument by matching the 520.5 $cm^{-1}$ band position, followed by manually aligning the laser beam with the crosshairs on the microscope. A 514.5 nm argon-ion green laser and a 633 nm HeNe red laser were used. The lasers deliver ~20 mW at 100% power.

The laser was focused through a x50 objective, with a laser spot size of c. 2 μm. The scan range was limited to 900–2000 $cm^{-1}$, in order to assess the first-order region. WiRE 3.3 software was used to acquire spectra and perform deconvolution using a pseudo-Voigt function to acquire the band heights, band areas, band positions and full width at half maximum (FWHM) for individual bands (Fig. 4.1b, cf. Table 4.1). A Microsoft Excel® spreadsheet was used to process un-deconvolved spectra (Fig. 4.1a) by performing smoothing operations, baseline corrections and normalization; to acquire the height and position of the saddle height, D1 and G band, G-FWHM, D-FWHM and areas of specific regions using the trapezoid area rule (cf. Table 4.1; Appendix B1; *since publishing this manuscript an updated version and a MATLAB code has been developed, see Appendix B2 and B3 respectively* ).

#### *4.3.2.2 Sample preparation*

Two different types of sample preparation were performed, both of which used isolated kerogen: (a) polished blocks and (b) strew slides. The kerogen for samples SSK 4522, SSK 4471, HC01–04 and HC02–73 were separated at Kingston University using HCl and HF acid at room temperature to remove the inorganic mineral fraction. Samples were first washed with tap water, air-dried and crushed to millimetre-sized fragments. The crushed material was treated with 100 mL of 12 M HCl for 24h, followed by 100 mL of 23 M HF for several days at room temperature, in order to digest carbonates and silicates, respectively. After each acid treatment, the concentrated solution was diluted with 900 mL of deionized water and then sieved through a 15-µm polyester mesh. Deionized water was used to rinse the sample through the sieve until pH neutral. Following the final rinse, samples were stored in 50 mL glass vials with deionized water. Samples MPA 61616 and MPA 61619 were prepared at the British Geological Survey using a similar technique and a 10-µm sieve (Könitzer et al., 2016).

The strew slides were prepared by spreading c. 0.5 mL of fluid mixture (composed of OM and deionized water) onto a glass slide using a pipette, which was then left to air dry. Polished blocks were constructed by embedding isolated kerogen with epoxy resin in 2.5 cm diameter moulds, followed by grinding using P400, P600, P800, P1200, P2500 silicon carbide paper using water as a lubricant. The samples were then polished using a diamond liquid suspension of 9 µm, 6 µm, 3 µm, 1 µm and were finished off with a 0.04 µm colloidal silica suspension. This grinding and polishing procedure follows the BS ISO 7404-2:2009 standard.

#### *4.3.2.3 Organic matter classification*

Strew slides were used to investigate whether different types of OM influence the Raman parameters. The OM categories identified in transmitted white light (Appendix C), following Tyson (1995) were:

(1) **Translucent phytoclast** (Appendix C1): Translucent particles under transmitted light with colours ranging from light brown to dark brown, typically equant or

lath-shaped with angular margins. The phytoclasts can be striate, striped, banded or pitted. Particles that appear opaque but have brown rims or brown patches are also included in this group.

(2) **Opaque phytoclast** (Appendix C2): The particles appear fully opaque under transmitted light. The shape of the particles varies from equant, lath or rounded, and the margins can be angular or corroded. They often have no internal structure, however, lath-shaped particles may be pitted. These particles are equivalent to inertinite when examining polished blocks under reflected light; they are the product of either intense oxidation or forest fires (Tyson 1995).

(3) **Pseudo-amorphous phytoclast** (Appendix C3): These amorphous particles exhibit a patchy, spotted appearance and are light brown to dark brown/black. Most of the biostructure has been lost and the edges are typically diffuse. However, some particle edges are sharp and straight, suggesting a remnant border of a degraded phytoclast.

(4) **AOM** (Appendix C4): The amorphous OM (AOM) is a structureless heterogeneous to homogenous particle with irregular diffuse margins under transmitted light. Colour typically ranges from pale yellow-brown to greyish. AOM may represent bacterial and/or reworked/degraded algal OM (Tyson 1995). Pyrite is often present as inclusions. Fluorescence microscopy was not used in this study, so further subdivision of the AOM group was not possible. Consequently, all AOM particles were grouped together.

#### *4.3.2.4 Experimental methodology*

i. **Testing different operational procedures**: Different operational procedures were tested on strew slides. First, the experimental setup was tested by comparing results from a 514.5 nm argon-ion green laser and a 633 nm HeNe red laser, followed by an analysis of how different accumulation times, number of accumulations, and laser powers affect the spectra. Spectral processing was assessed by comparing smoothing vs. non-smoothing, linear vs. 3$^{rd}$-order polynomial baseline corrections, and deconvolution vs. the automated non-

deconvolution method developed in this study to determine Raman parameters.

ii. **Testing different samples types**: the Raman characteristics of polished blocks and strew slides were tested using the optimum operational settings and procedures developed above: 514.5 nm argon-ion green laser wavelength, 10 s accumulation time, 2 accumulations and a 0.2 mW laser power, this was kept constant throughout. Following acquisition, a Microsoft Excel® worksheet (Appendix B1) processes and determines the Raman parameters by performing a Savitzky-Golay smoothing filter using a 21-point quadratic polynomial algorithm, a linear or a 3$^{rd}$-order polynomial baseline correction, followed by normalization at the same maximum G height intensity of 2000 counts, as well as automatically calculating the R1, RBS, G-FWHM, D-FWHM, RIP, DA1/GA and STA Raman parameters. Deconvolution was not performed. Comparisons between the different sample types were made by: (1) visual comparison of the spectra; and (2) comparing the Raman parameters.

iii. **Testing different organic matter types**: Different types of OM were assessed using strew slides in transmitted light. This experiment was performed under the optimum instrument conditions. Spectra processing and calculation of the Raman parameters were performed using the Microsoft Excel® automated worksheet (Appendix B1). Deconvolution was not performed.

## 4.4 Results

### *4.4.1 Experimental setup*

Figure 4.3 shows a comparison of the spectra obtained from a phytoclast in a strew slide using laser wavelengths of 514.5 (argon ion) and 633 nm (HeNe). The 514 nm laser wavelength produces a significantly better-quality spectrum that has a smoother more linear baseline, and better peak-to-background ratios, as observed previously by Quirico et al. (2005).

When using a laser power of 1 mW or greater, the laser damages the surface of the OM (Fig. 4.4). Evidence of in-situ burning caused by the laser was observed

as a small black spot (Fig. 4.4c, d). In-situ burning also influences the Raman spectrum (Fig. 4.4f). The position of the G band blue-shifts, as described by Allwood et al. (2006), and the saddle height and the D band also increases in height with respect to the G band. Consequently, laser powers greater than 0.2 mW are not advised as they alter the Raman spectrum.

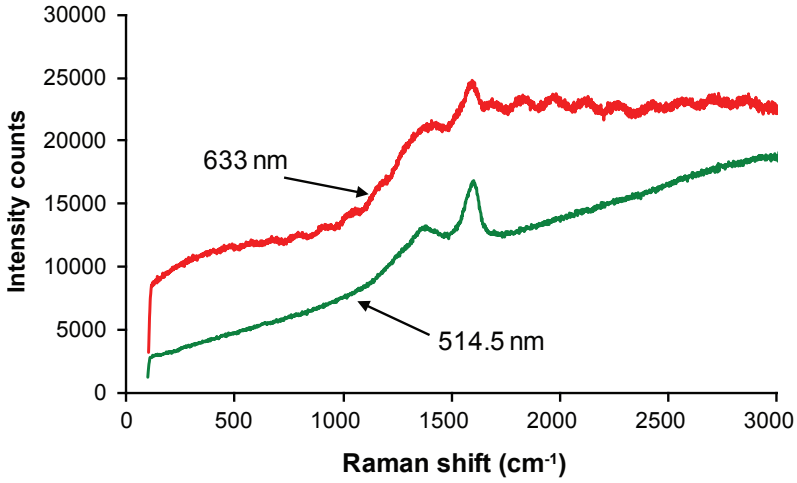


**Figure 4.3.** Comparison of the Raman spectra acquired for a translucent phytoclast in a strew slide from sample SSK 4471 using a 633 nm (red) and 514.5 nm (green) laser. The 633nm laser produces more fluorescence than the 514.5 nm wavelength.

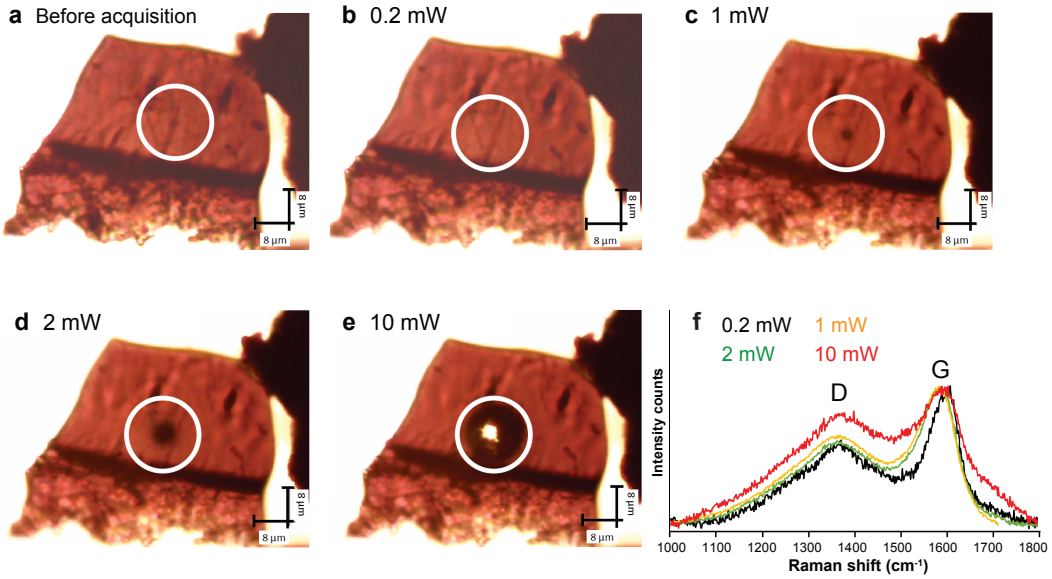


**Figure 4.4.** Images before and after spectra acquisition of a phytoclast from a strew slide (SSK 4471) using a laser wavelength 514 nm, with associated Raman spectra. The white circles highlight the area where the measurements were taken. Scale bar is 8 µm. **(a)** before spectra acquisition. Image after spectra acquisition using: **(b)** 0.2 mW; **(c)** 1 mW; **(d)** 2 mW; **(e)** 10 mW laser power. **(f)** associated spectra using the different laser powers.

Spectra acquired using a 0.02 mW and 0.2 mW laser power are consistent; therefore, the 0.2 mW laser power does not damage or alter the OM. Figure 4.5 demonstrates that using a 0.2 mW laser power improves the signal to noise ratio compared to using a 0.02 mW laser power. Increasing the accumulation time and number of accumulations also slightly increases the signal to noise ratio, particularly when using a lower laser power of 0.02 mW (compare Fig. 4.5a and b- d).

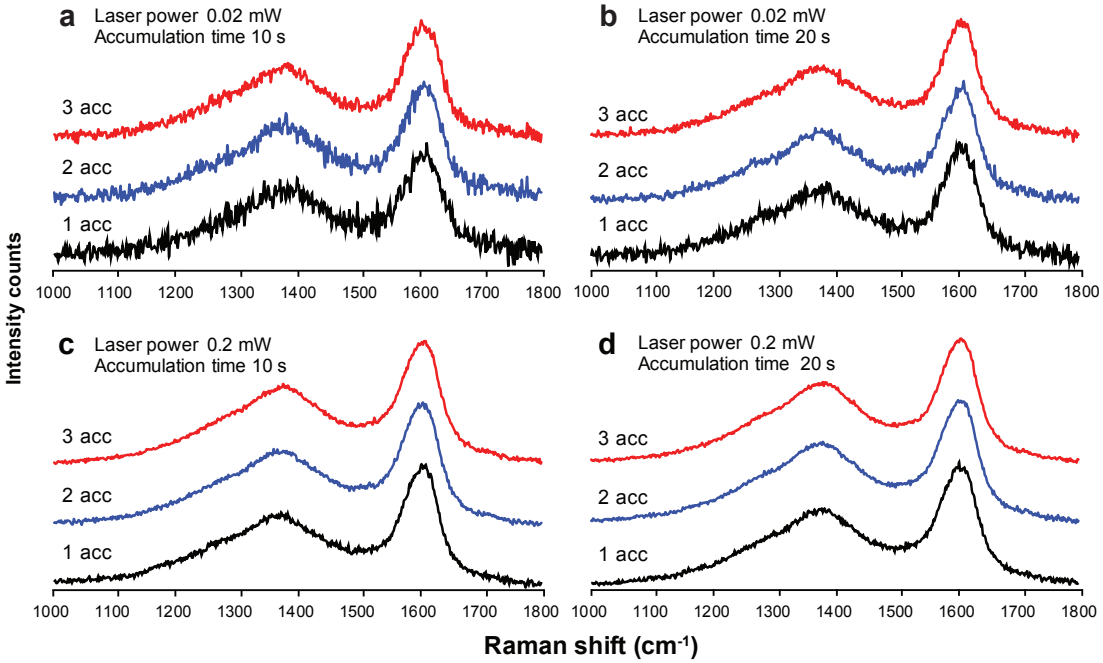


**Figure 4.5.** Comparison of the spectra acquired from the same spot using variable laser power, accumulation time and number of accumulations. **(a)** 0.02 mW laser power with a 10 s accumulation time, with 1 – 3 accumulations. **(b)** 0.02 mW laser power with a 20 s accumulation time. **(c)** 0.2 mW laser power with a 10 s accumulation time. **(d)** 0.2 mW laser power with a 20 s accumulation time. Note that the 0.2 mW laser produces a significantly better signal to noise ratio than using the 0.02 mW laser power, and shows no significant improvement for a signal accumulation time >10 s.

## *4.4.2 Processing the spectra*

### *4.4.2.1 Smoothing*

Performing a smoothing procedure removes noise from the spectrum, allowing the operator to pick band heights and positions with less ambiguity. Smoothing the spectrum also reduces uncertainty during baseline correction, as the noise in the spectrum can greatly influence the heights of individual control points, leading to anomalous baseline corrections (Fig. 4.6). This can be a major problem especially if control points are fixed when performing an automated procedure. After smoothing, noise is drastically reduced and the control points are less prone to sharp random increases in height, which makes the baseline corrections more reproducible (Fig. 4.6).

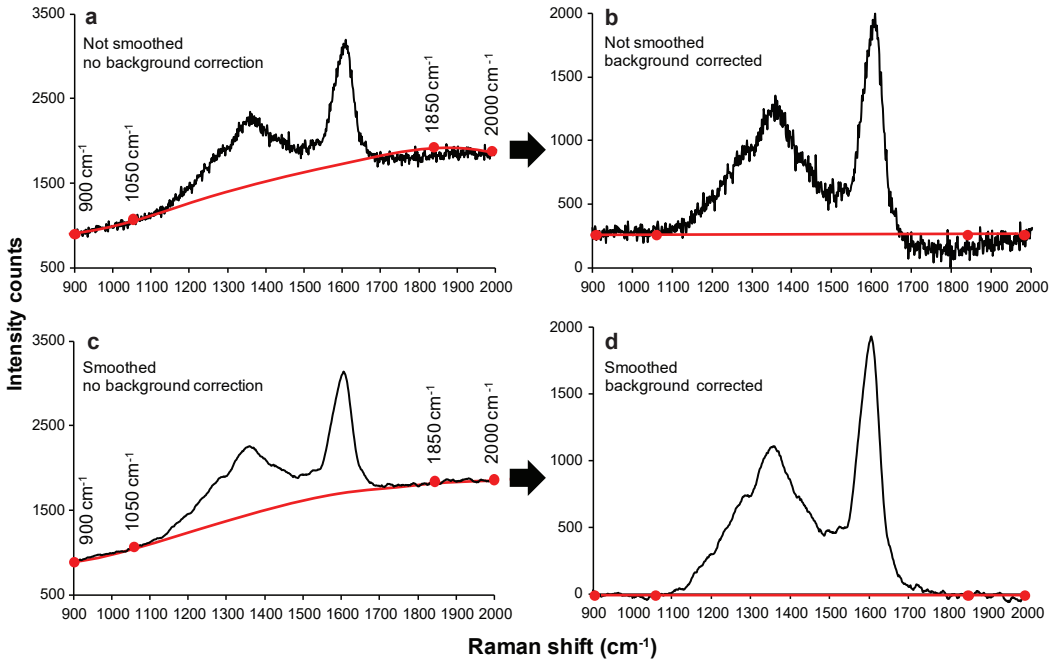


**Figure 4.6.** An example of how noise can affect an automated background correction; a–d are all the same original spectra from a translucent phytoclast (sample SSK 4471). **(a)** An unsmoothed spectrum with the predicted background shape. **(b)** Outcome of the background correction from spectra **(a)**. **(c)** A smoothed spectrum with the predicted background shape. (d) Outcome of the background correction **(c)**. Note the sharp peaks created by the noise in **(a)** affects the control point at 1850 $cm^{-1}$; here the control point lies above the trend of the background and the resulting spectrum **(b)** is unsuitable. For a smoothed spectrum the sharp peaks associated with noise are absent and therefore the control points are less affected by noise and produce a better background corrected spectrum.

Deconvolution also becomes more reproducible after smoothing, as noise can impact the fitted bands. Figure 4.7 shows that when smoothing is performed, the fitted spectrum has a better fit with the original spectrum. The height and widths for the D3, D4 and D5 fitted bands for an un-smoothed and smoothed spectrum are significantly different, even though the starting spectrum is the same. Raman parameters may also differ substantially (Fig. 4.8)**.**

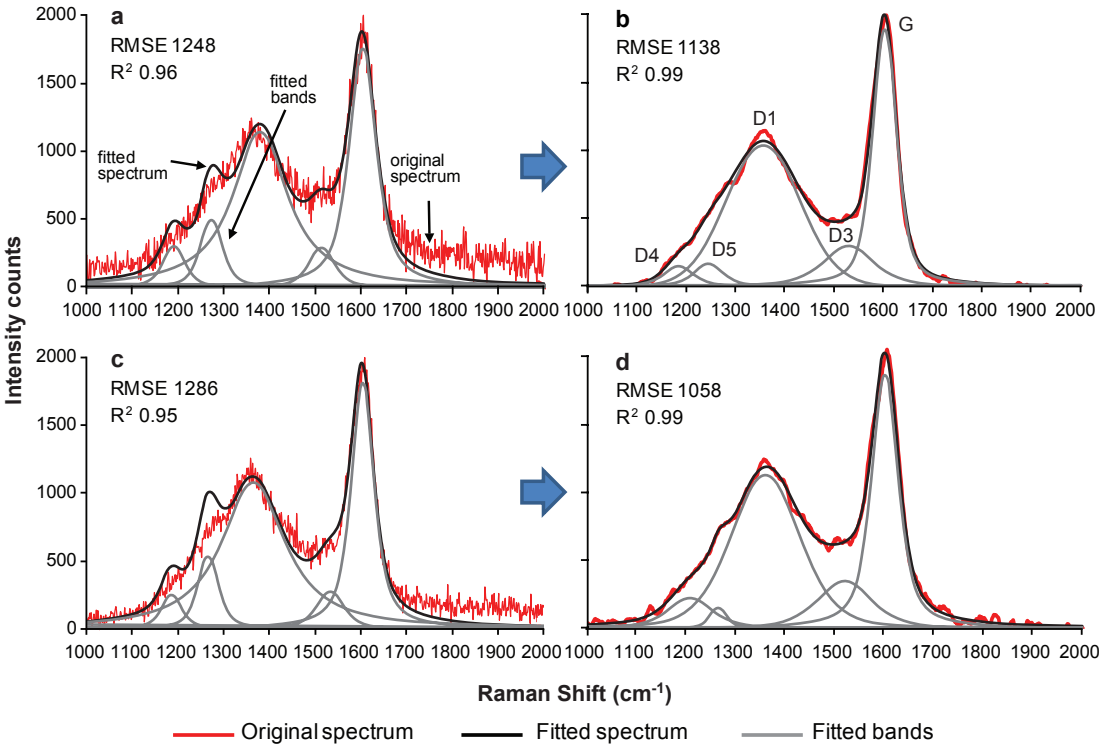


**Figure 4.7.** Different five band deconvolution outcomes when performed on an un-smoothed and smoothed spectrum using the same fitting constraints, from sample SSK 5422. **(a)** Phytoclast 1 un-smoothed spectra and deconvolution outcome. **(b)** Phytoclast 1 smoothed spectra and deconvolution outcome. **(c)** Phytoclast 2 un-smoothed spectra and deconvolution outcome. **(d)** Phytoclast 2 smoothed spectra and deconvolution outcome. Note that the fitted spectrum for a smoothed spectrum has a better fit with the original spectrum statistically and visually; and that the shape and position of the individual bands are different.

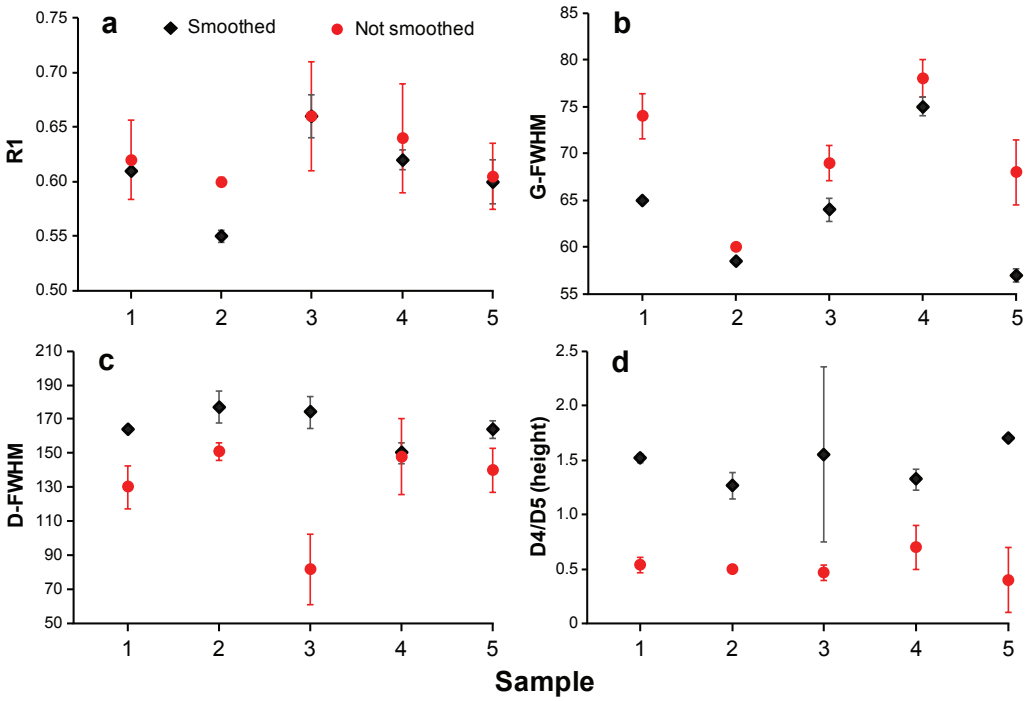


**Figure 4.8.** Raman parameters (Table 1) derived from un-smoothed and smoothed spectra after deconvolution from five translucent phytoclasts in sample HC01-04. **(a)** R1 ratio. **(b)** G-FWHM. **(c)** D-FWHM. **(d)** D4/D5 band height ratio.

#### *4.4.2.2 Baseline correction*

Fluorescence is a common problem in low-maturity OM that can alter the Raman spectra and parameters. Therefore, an unbiased baseline correction method needs to be adopted. Here, two of the most commonly used baseline corrections were tested: (1) linear; and (2) 3$^{rd}$-order polynomial. Each acquired spectrum has a wavenumber range from 900 to 2000 cm$^{-1}$ to better estimate the shape of the background fluorescence, and a smoothing procedure was performed before the baseline was corrected. The control points for the linear function were fixed at 1000 cm$^{-1}$ and 1800 cm$^{-1}$, and for the 3$^{rd}$-order polynomial function the control points are 2000 cm$^{-1}$, c.1850 cm$^{-1}$, c.1050 cm$^{-1}$ and 900 cm$^{-1}$. The positions of the control points were chosen, on the basis that they lie outside the spectral range influenced by OM. The position of the control points at c.1850 cm$^{-1}$ and c.1050 cm$^{-1}$ for the 3$^{rd}$-order

polynomial correction may be shifted ±20 $cm^{-1}$, if the baseline correction does not fit the background shape. An automated worksheet in Microsoft Excel® was developed to perform these tasks (Appendix B1).

When fluorescence is present, which is often the case for low-maturity OM, a 3rd-order polynomial baseline correction works best (Fig. 4.9). A linear baseline correction performed on samples that experience non-linear fluorescence will result in the D band and saddle height to increase in height in relation to the G band, which will lead to an increase in the R1 ratio, RIP, and SSA Raman parameters, and a decrease in the saddle index (Fig. 4.9). Figure 4.10 shows 20 overlain spectra that have had a linear and a 3rd-order polynomial baseline correction acquired from the same strew slide. Notice the larger scatter for the linear baseline correction, compared to the 3rd-order polynomial baseline correction.

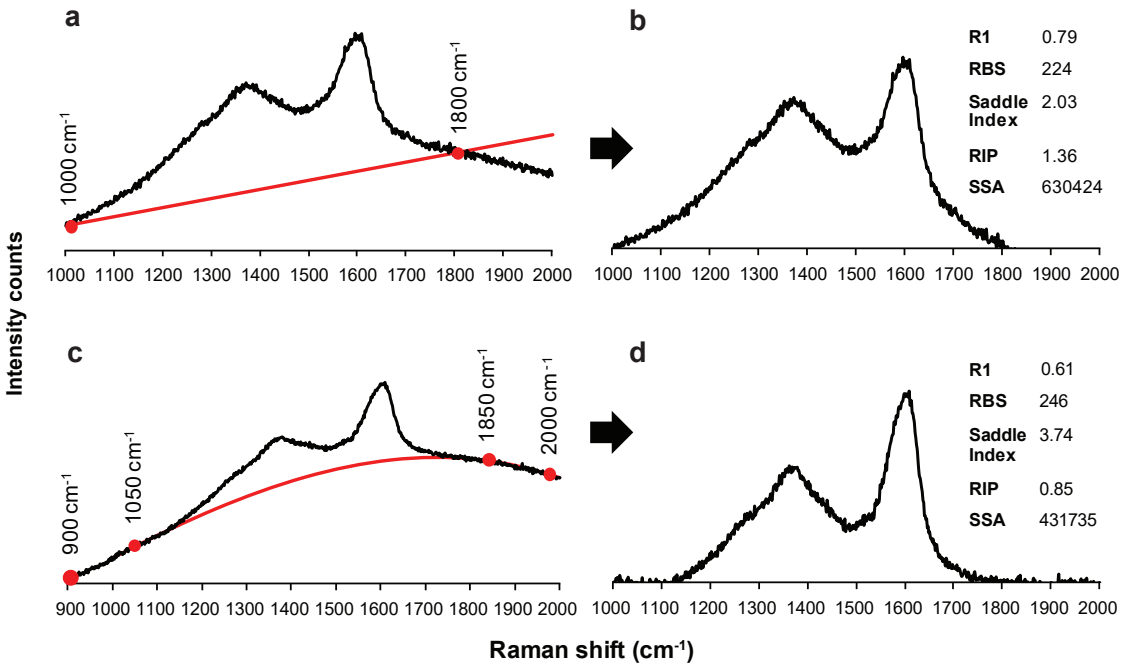


**Figure 4.9.** Comparison of different background corrections on a phytoclast spectrum from sample SSK 4471. **(a)** Linear baseline correction with the location of the control points. **(b)** Result of background deconvolution from spectrum (a). **(c)** 3rd-order polynomial baseline correction with the location of the

control points. **(d)** Result of background correction from spectrum (c). Note the difference in the shape of the spectra and the different Raman parameter values.

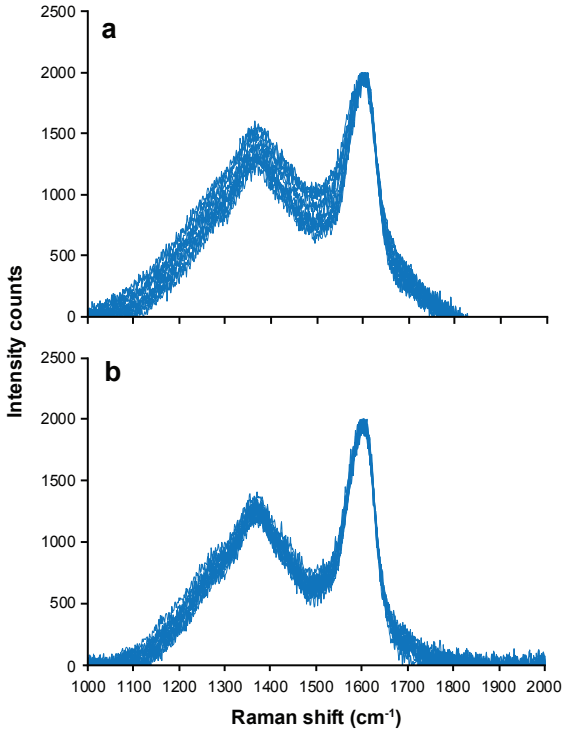


**Figure 4.10.** Twenty AOM spectra from sample HC02-73 overlain after performing **(a)** linear and **(b)** 3rd-order polynomial baseline correction. The same original spectra have been used for both methods.

### *4.4.2.3 Calculating Raman parameters*

Five methods to derive Raman parameters were assessed (Table 4.3). Deconvolution was not performed for the M-1 and M-2 methods, but is employed in the M-3, M-4 and M-5 methods (Fig. 4.11). Deconvolution was performed using Renishaw's WiRE 3.3™ software on a smoothed, 3rd-order polynomial baseline corrected, normalized spectra with a tolerance of 0.01 and a maximum of 15 iterations. The descriptions in Table 3 should be followed precisely, as the initial attributes (height, width, position) of the curves before fitting can significantly alter the parameters. The closeness of fit of the fitted spectrum to the original spectrum after deconvolution may be assessed by: (1) visually comparing the original and fitted spectrum; (2) root-mean-square error

(RMSE); and (3) the coefficient of determination ($R^2$). The D2 band was not included in any of the deconvolution methods, as it cannot be identified in low-maturity samples, as observed also by Beyssac et al. (2012) and Brolly et al. (2016).

**Table 4-3.** Methods used to process the spectra and calculate Raman parameters.

| Method | Deconvolution | Description | | | | |
|---|---|---|---|---|---|---|
| **M-1** | None | (1) Smooth spectra; (2) 3rd-order polynomial baseline correction. The position and heights of the G, D, saddle are recorded to calculate the R1, RBS, saddle index and G-FWHM. | | | | |
| **M-2** | None | (1) Smooth spectra; (2) 3rd-order polynomial baseline correction; (3) Normalize the spectra to have a G band intensity of 2000. Use trapezoid area rule to calculate the total area under the curve between 1100-1700 $cm^{-1}$ (SSA); 1100-1400 $cm^{-1}$ (DA1); 1550-1650 $cm^{-1}$ (GA). The RIP may also be calculated. | | | | |
| | | **Starting Conditions** | | | | |
| **M-3** | G, D1 | **Band** | **$cm^{-1}$*** | **Height** | **Width** | (1) Smooth spectra; (2) 3rd-order polynomial baseline correction; (3) Normalize the spectra to have a G band intensity of 2000; (4) Perform deconvolution using pseudo-Voigt function. Tolerance of 0.01 and maximum of 15 iterations. |
| | | D1 | 1360 | 1000 | 40 | |
| | | G | 1605 | 2000 | 40 | |
| **M-4** | G, D1, D3, D4 | D1 | 1360 | 1000 | 40 | (1) Smooth spectra; (2) 3rd-order polynomial baseline correction; (3) Normalize the spectra to have a G band intensity of 2000; (4) Perform deconvolution using pseudo-Voigt function. Tolerance of 0.01 and maximum of 15 iterations. |
| | | G | 1605 | 2000 | 40 | |
| | | D3 | 1500 | 500 | 40 | |
| | | D4+D5 | 1240 | 500 | 40 | |
| **M-5** | G, D1, D3, D4, D5 | D1 | 1360 | 1000 | 40 | (1) Smooth spectra; (2) 3rd-order polynomial baseline correction; (3) Normalize the spectra to have a G band intensity of 2000; (4) Perform deconvolution using pseudo-Voigt function. Tolerance of 0.01 and maximum of 15 iterations. |
| | | G | 1605 | 2000 | 40 | |
| | | D3 | 1500 | 500 | 40 | |
| | | D4 | 1160 | 250 | 40 | |
| | | D5 | 1260 | 500 | 40 | |

*$cm^{-1}$: centre position of the Raman band.

For the M-1 and M-2 methods, the spectra were copied into the automated Microsoft Excel® worksheet, which performs a Savitzky-Golay smoothing filter using a 21-point quadratic polynomial algorithm (Savitzky and Golay, 1964), a 3rd-order polynomial baseline correction, and normalizes the spectra to the same G band height at 2000 counts, followed by calculating the R1, RBS, saddle index, G-FWHM and D-FWHM Raman parameters (See Table 4.1 and Fig. 4.11a for how to calculate these

parameters). The M-2 method follows the same processing procedures as for M-1, however it also integrates the areas of specific regions using the trapezoid area rule to calculate the RIP (Schopf et al., 2005), DA1/GA and SSA (Tables 4.1, 4.3).

For the M-3 method, a two-band deconvolution method was applied for the D1 and G band using a pseudo-Voigt function (Fig. 4.11), similar to Hinrichs et al. (2014) and Wilkins et al. (2014, 2015). The calculated Raman parameters are R1, RA1, D-FWHM, G-FWHM and RBS (See Table 4.1 and Fig. 4.11 for how to calculate these parameters). Visually and statistically the fitted spectrum is a good fit with the original spectrum, however, some bumps on the D1 band limb at ~1250 $cm^{-1}$ are lost. The M-4 method fits four bands, G, D1, D3 and D4, using a pseudo-Voigt function, similar to Kouketsu et al. (2014) "fitting G" method. The M-5 method fits the G, D1, D3, D4 and D5 bands using a pseudo-Voigt function. Both methods have a good fit with the original spectrum and are statistically better than the M-3 method (Fig. 4.11).

For the M-5 method, the D3, D4 and D5 bands are highly unstable, and may have unrealistic positions, heights and widths after deconvolution, as illustrated in Figure 4.12. The closeness of fit of the fitted spectrum and the original spectrum may be very high for an unsuitable fit where the D3 and D5 bands go rogue. This is also the case for the M-4 method.

The Raman parameters that are compared using the M-1, M-3, M-4 and M-5 methods are the R1 ratio, RBS, G-FWHM and D-FWHM. The R1 and RBS parameter results differ slightly for the different methods (Table 4.4); the G-FWHM values are lower after performing deconvolution and the D-FWHM values are significantly lower after performing deconvolution. The M-1 method has a lower relative standard deviation (RSD) than the M-3, M-4 and M-5 methods, with some exceptions.

The outcrop samples (HC01-04 and HC02-73) have higher RBS and lower G-FWHM values for all the methods, suggesting that they are slightly more mature (Guedes et al., 2010; Liu et al., 2013). This is consistent with the PI (production index) data (Emmings et al., 2017), which also implies increased maturity compared to the Carsington Dam Reconstruction C4 borehole samples.

Overall, performing deconvolution slows down Raman spectra analysis and the Raman bands seldom behave themselves, making visual checks essential. This is not the case when performing the M-1 or M-2 methods, which do not involve deconvolution. Therefore, the M-1 and M-2 methods will be utilized in the subsequent sections.

**Table 4-4.** Comparison of the results for four Raman parameters derived from methods M-1, M-3, M-4 and M-5 for six samples.

| Method | Sample | Parameter | | | | | | | |
|---|---|---|---|---|---|---|---|---|---|
| | | R1 | RSD (%) | RBS | RSD (%) | G-FWHM | RSD (%) | D-FWHM | RSD (%) |
| M-1 | SSK 4522 | 0.64 | 10 | 240 | 4 | 77 | 8 | 204 | 18 |
| M-3 | | 0.65 | 14 | 241 | 2 | 77 | 9 | 235 | 6 |
| M-4 | | 0.61 | 16 | 236 | 4 | 65 | 19 | 128 | 22 |
| M-5 | | 0.64 | 14 | 236 | 3 | 67 | 16 | 130 | 9 |
| M-1 | SSK 4471 | 0.64 | 5 | 234 | 3 | 83 | 6 | 228 | 9 |
| M-3 | | 0.63 | 4 | 231 | 2 | 77 | 4 | 241 | 6 |
| M-4 | | 0.62 | 5 | 229 | 1 | 70 | 5 | 149 | 15 |
| M-5 | | 0.6 | 7 | 227 | 2 | 70 | 5 | 148 | 20 |
| M-1 | MPA 61616 | 0.61 | 7 | 242 | 4 | 71 | 4 | 215 | 8 |
| M-3 | | 0.56 | 10 | 243 | 1 | 69 | 7 | 236 | 4 |
| M-4 | | 0.58 | 10 | 236 | 4 | 62 | 5 | 157 | 9 |
| M-5 | | 0.55 | 8 | 233 | 2 | 62 | 5 | 138 | 7 |
| M-1 | MPA 61619 | 0.61 | 7 | 246 | 5 | 72 | 7 | 210 | 15 |
| M-3 | | 0.65 | 19 | 244 | 2 | 68 | 11 | 242 | 14 |
| M-4 | | 0.57 | 16 | 243 | 4 | 61 | 11 | 137 | 26 |
| M-5 | | 0.56 | 13 | 244 | 5 | 62 | 10 | 129 | 27 |
| M-1 | HC01-04 | 0.61 | 1 | 255 | 4 | 67 | 3 | 209 | 17 |
| M-3 | | 0.61 | 8 | 249 | 2 | 66 | 8 | 230 | 7 |
| M-4 | | 0.61 | 14 | 246 | 2 | 56 | 7 | 137 | 12 |
| M-5 | | 0.61 | 8 | 245 | 2 | 57 | 7 | 128 | 10 |
| M-1 | HC02-73 | 0.63 | 9 | 247 | 5 | 67 | 3 | 212 | 13 |
| M-3 | | 0.63 | 17 | 247 | 2 | 65 | 8 | 206 | 14 |
| M-4 | | 0.62 | 18 | 242 | 4 | 62 | 10 | 142 | 24 |
| M-5 | | 0.6 | 18 | 237 | 5 | 61 | 9 | 150 | 27 |

Mean calculated using a minimum of seven translucent phytoclasts per sample on a strew slide. RSD = relative standard deviation.

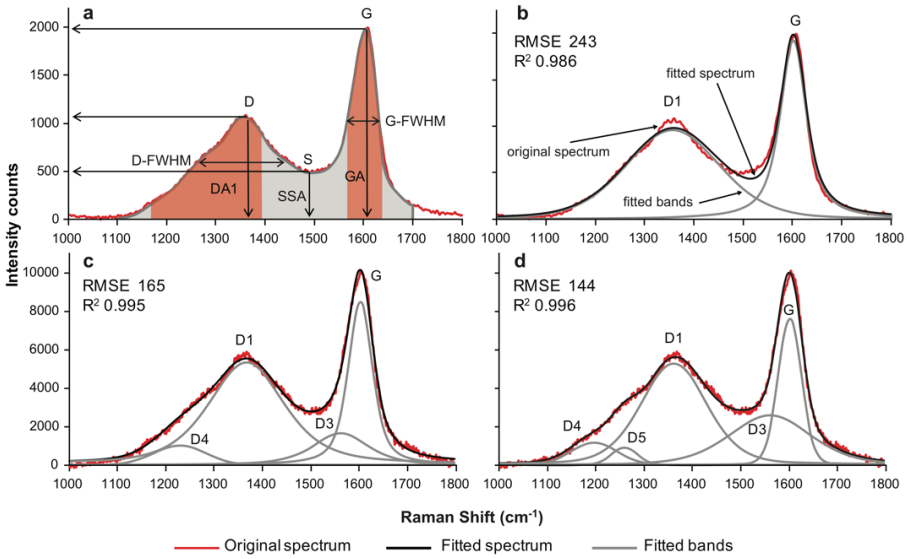


2461

2462 **Figure 4.11.** Comparison of the methods used in this study to determine the Raman features and bands
2463 to derive the Raman parameters (Table 1). **(a)** M-1 and M-2 methods. Deconvolution is not performed.
2464 **(b)** M-3 method. Deconvolution of the G and D1 bands are performed. **(c)** M-4 method. Deconvolution
2465 of the G, D1, D3 and D4 bands are performed. **(d)** M-5 method. Deconvolution of the G, D1, D3, D4 and
2466 D5 bands are performed. Note the RMSE and $R^2$ values, which statistically show how well the fitted
2467 spectrum correlates with the original spectrum, indicate a slightly better fit using method M-5.

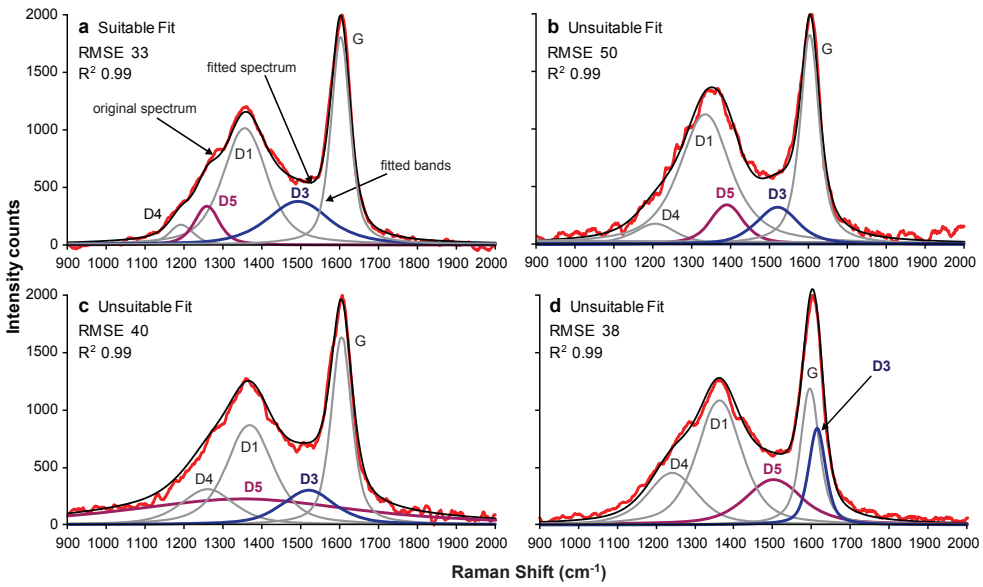


2468

2469 **Figure 4.12.** Common errors associated with deconvolution. Original spectrum is from a phytoclast in
2470 sample HC01-04. **(a)** The curve fitting results are suitable, and the bands have reasonable positions,
2471 heights and widths. **(b)** The D5 band has shifted to an unsuitable higher position. **(c)** The D5 band has
2472 moved to an unsuitable position as well as having an unrealistic bandwidth. **(d)** The D5 and D3 bands
2473 have moved to unrealistic positions and the D3 band has an unrealistic height.

#### *4.4.2.4 Sample types*

Raman spectra acquired from a polished block and a strew slide from the same sample (Fig. 4.13), indicates that polishing increases the relative intensity of the D band, the D band position blue-shifts by ~20 $cm^{-1}$, and the saddle height increases. The G band position remains relatively unaffected by the polishing procedure, however the G-FWHM is affected but not systematically (Fig. 4.13, Table 4.5). Table 4.5 shows that the polishing procedure increases the R1 ratio, in agreement with the results of Ammar and Rouzaud (2012) and Lünsdorf (2016). The R1 ratios from polished blocks also exhibit more scatter and have a random distribution compared to the R1 ratio calculated from strew slides (Fig. 4.14).

2485 **Table 4-5.** Mean values and percent relative standard deviation (%RSD) of Raman parameters obtained from strew slides and polished blocks of selected samples.

| Sample | Sample Type | Statistics | Raman Parameter Results | | | | | | | | | | | | | | | |
|---|---|---|---|---|---|---|---|---|---|---|---|---|---|---|---|---|---|---|
| | | | R1 | | RBS | | RIP | | Saddle Index | | G-FWHM | | D-FWHM | | DA1/GA | | SSA (x10$^3$) | |
| | | | Linear | 3rd-OP | Linear | 3rd-OP | Linear | 3rd-OP | Linear | 3rd-OP | Linear | 3rd-OP | Linear | 3rd-OP | Linear | 3rd-OP | Linear | 3rd-OP |
| SSK 4522 | Strew slide | x̄ | 0.64 | 0.64 | 240 | 240 | 0.81 | 0.96 | 4.13 | 3.45 | 79 | 77 | 168 | 204 | 1.22 | 1.34 | 434 | 457 |
| | | %RSD | 12 | 10 | 4.5 | 3.8 | 15 | 7.3 | 30 | 10 | 9.9 | 7.8 | 28 | 19 | 28 | 10 | 14 | 6.5 |
| | Polished Block | x̄ | 0.77 | 0.69 | 243 | 245 | 1.3 | 0.91 | 4.21 | 4.32 | 81 | 79 | 201 | 196 | 1.77 | 1.55 | 543 | 493 |
| | | %RSD | 20 | 12 | 5.5 | 5.1 | 20 | 18 | 28 | 21 | 9.3 | 8.2 | 28 | 22 | 25 | 15 | 23 | 8.3 |
| SSK 4471 | Strew slide | x̄ | 0.64 | 0.64 | 235 | 234 | 0.94 | 1.01 | 3.45 | 2.46 | 94 | 83 | 222 | 228 | 1.25 | 1.28 | 398 | 471 |
| | | %RSD | 7.5 | 4.5 | 3.2 | 2.9 | 12 | 9.8 | 36 | 27 | 10 | 6 | 16 | 9.4 | 12 | 8.9 | 13 | 8 |
| | Polished Block | x̄ | 0.71 | 0.65 | 233 | 234 | 1.17 | 1.03 | 2.8 | 3.7 | 84 | 78 | 214 | 216 | 1.47 | 1.32 | 534 | 463 |
| | | %RSD | 12 | 7.3 | 4.6 | 3.9 | 28 | 15 | 37 | 38 | 9.8 | 7.5 | 17 | 13 | 22 | 10 | 42 | 13 |
| MPA 61616 | Strew slide | x̄ | 0.61 | 0.61 | 262 | 242 | 1.06 | 1.02 | 3.85 | 4.21 | 74 | 71 | 218 | 215 | 1.39 | 1.35 | 447 | 424 |
| | | %RSD | 14 | 7.1 | 36 | 3.9 | 6.2 | 4.3 | 26 | 7.5 | 6.5 | 4.4 | 12 | 7.8 | 11 | 8.7 | 5.7 | 4.6 |
| | Polished Block | x̄ | 0.79 | 0.75 | 249 | 251 | 1.6 | 1 | 3.22 | 5.2 | 71 | 65 | 210 | 189 | 2.01 | 1.71 | 598 | 454 |
| | | %RSD | 13 | 15 | 3.8 | 3.7 | 37 | 17 | 27 | 39 | 12 | 5.3 | 22 | 26 | 25 | 51 | 29 | 11 |
| MPA 61619 | Strew slide | x̄ | 0.62 | 0.61 | 244 | 246 | 0.85 | 0.93 | 4.2 | 4.45 | 75 | 72 | 197 | 210 | 1.28 | 1.33 | 425 | 411 |
| | | %RSD | 8.9 | 6.9 | 5 | 5.2 | 36 | 14 | 40 | 14 | 6.8 | 6.7 | 34 | 15 | 23 | 11 | 14 | 10 |
| | Polished Block | x̄ | 0.78 | 0.75 | 255 | 254 | 1.03 | 0.9 | 2.75 | 3.1 | 87 | 81 | 211 | 194 | 1.68 | 1.53 | 532 | 492 |
| | | %RSD | 12 | 13 | 3.4 | 3.4 | 6.6 | 13 | 9.9 | 13 | 8.5 | 9.1 | 22 | 24 | 11 | 12 | 7.2 | 9 |
| HC01-04 | Strew slide | x̄ | 0.66 | 0.61 | 251 | 255 | 1.09 | 1.01 | 4.25 | 3.78 | 69 | 67 | 199 | 209 | 1.55 | 1.43 | 452 | 428 |
| | | %RSD | 5.8 | 1.3 | 4.8 | 3.5 | 16 | 4.1 | 26 | 2.5 | 11 | 3.2 | 15 | 17 | 11 | 1.4 | 13 | 1.9 |

| | | | | | | | | | | | | | | | | | |
|---|---|---|---|---|---|---|---|---|---|---|---|---|---|---|---|---|---|
| | Polished Block | x̄ | 0.91 | 0.94 | 262 | 258 | 1.68 | 0.84 | 4.67 | 4.05 | 64 | 60 | 180 | 196 | 1.53 | 1.82 | 437 | 469 |
| | | %RSD | 24 | 16 | 4.9 | 6.3 | 23 | 23 | 28 | 9.5 | 21 | 9.5 | 26 | 21 | 19 | 15 | 18 | 13 |
| HC02-73 | Strew slide | x̄ | 0.63 | 0.63 | 257 | 247 | 0.97 | 0.99 | 4.33 | 4.9 | 66 | 67 | 196 | 212 | 1.39 | 1.42 | 417 | 407 |
| | | %RSD | 11 | 8.9 | 3.9 | 5.2 | 11 | 9.3 | 17 | 8.9 | 3.3 | 3.3 | 17 | 13 | 14 | 9.5 | 6.1 | 6.1 |
| | Polished Block | x̄ | 0.77 | 0.76 | 248 | 253 | 1.45 | 0.92 | 2.74 | 3.16 | 84 | 78 | 204 | 195 | 1.8 | 1.56 | 604 | 491 |
| | | %RSD | 12 | 9 | 5 | 6 | 52 | 18 | 24 | 12 | 14 | 8 | 10 | 13 | 22 | 12 | 32 | 7 |

Note that linear baseline subtraction results in higher RSDs than 3$^{rd}$-order polynomial baseline subtraction (3$^{rd}$-OP) and the mean values also differ.

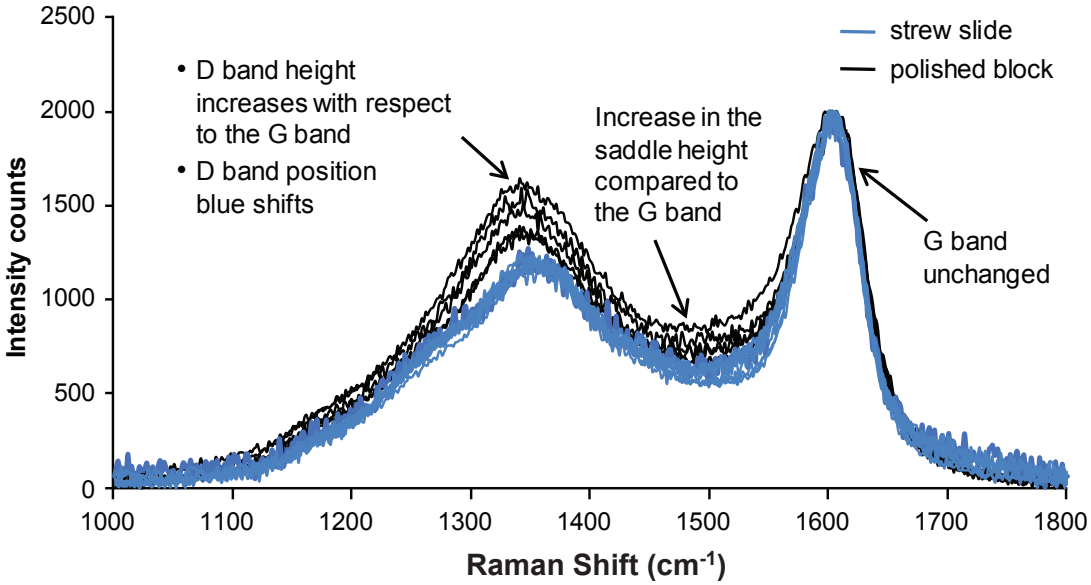


**Figure 4.13.** Comparison of Raman spectra from sample HC01-04 derived from a strew slide and polished block. Only phytoclasts were analysed.

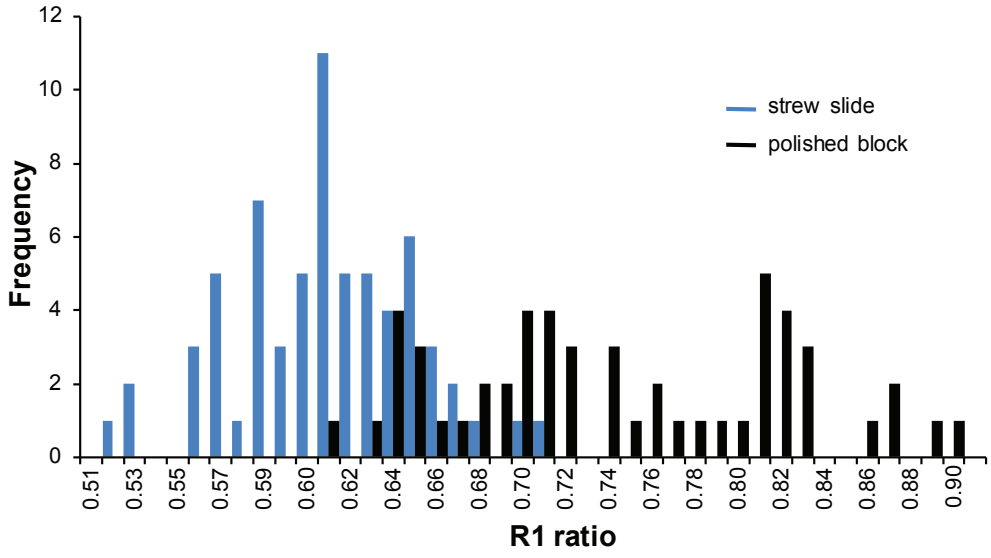


**Figure 4.14.** Comparison of the R1 ratio from sample HC01-04 for a strew slide and a polished block. Note that the polished block produces a greater range and more scattered distribution, whereas the strew samples produces a more normally distributed histogram with less scatter and a smaller range.

A linear baseline correction performed on polished blocks creates more scatter than 3rd-order polynomial baseline corrections (Table 4.5). The Raman parameters derived using the latter, lie closer to the strew slide results than for the linear-corrected data. It is clear that the R1 ratio, saddle index, D-FWHM, DA1/GA and SSA are affected by polishing; however, there is no clear evidence that polishing alters the RBS, G-FWHM and RIP values (Table 4.5). Sample SSK 4471 is an exception, since all the Raman parameters following a 3rd-order polynomial baseline correction become remarkably similar to the strew slide results (Table 4.5). This will be considered further in the discussion below.

Beyssac et al. (2003) and Kouketsu et al. (2014) reported that polishing effects might be avoided by analyzing immediately below the surface of a particle. Our results do not support this conclusion. Figure 4.15 shows the R1 ratio results of a depth profile from an exemplar sample (HC01-04). The mean value derived from a strew slide for the R1 parameter for this sample is 0.61 (horizontal red line in Fig. 4.15). The R1 values in the depth profiles are substantially greater than the mean value from the strew slide, and despite some scatter, the R1 value does not change systematically with depth.

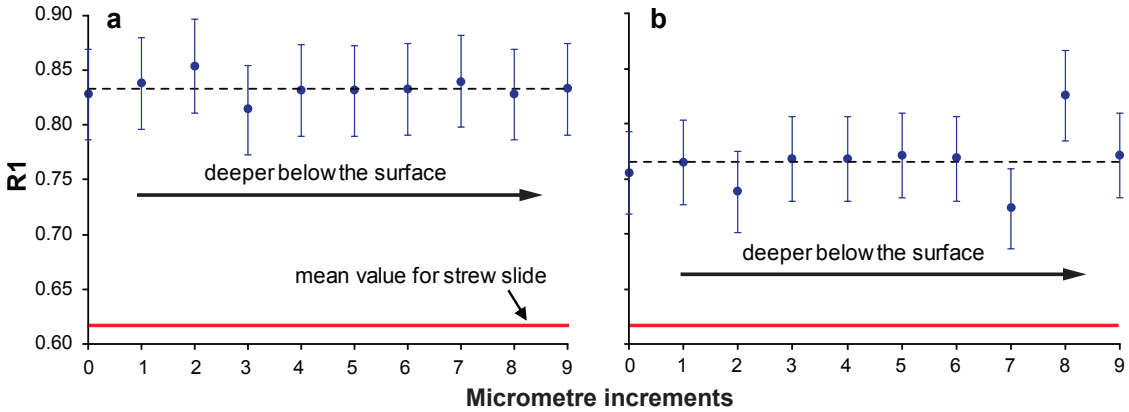


**Figure 4.15.** Depth profile of the R1 ratio derived from two phytoclasts **(a)** and **(b)** in a polished block (sample HC01-04), where 0 µm is the surface of the particle.

#### *4.4.2.5 Organic matter type and intra-particle variation*

The translucent phytoclast group (Appendix C1) has similar R1, RIP, D-FWHM, DA1/GA and SSA Raman parameters across the five samples tested (Type 4 in Fig. 4.16), which is in accordance that all these samples have similar maturities. The G-FWHM, RBS and the saddle index results are more varied across the sample set. The pseudo-amorphous phytoclast (Appendix C3) group behaves similarly to the translucent phytoclast group and the Raman parameters are similar (compare Types 3 and 4, Fig. 4.16). The AOM group (Type 1, Fig. 4.16; Appendix C4) is also similar, with the exception of the R1 and D-FWHM parameters, as the R1 tends to be greater than for other OM types and the D-FWHM is significantly more variable. The opaque phytoclast group (Type 2, Fig. 16; C2) displays the largest variation between OM types, as the parameter values commonly differ substantially from those obtained for coexisting translucent phytoclasts, pseudo-amorphous phytoclasts and AOM.

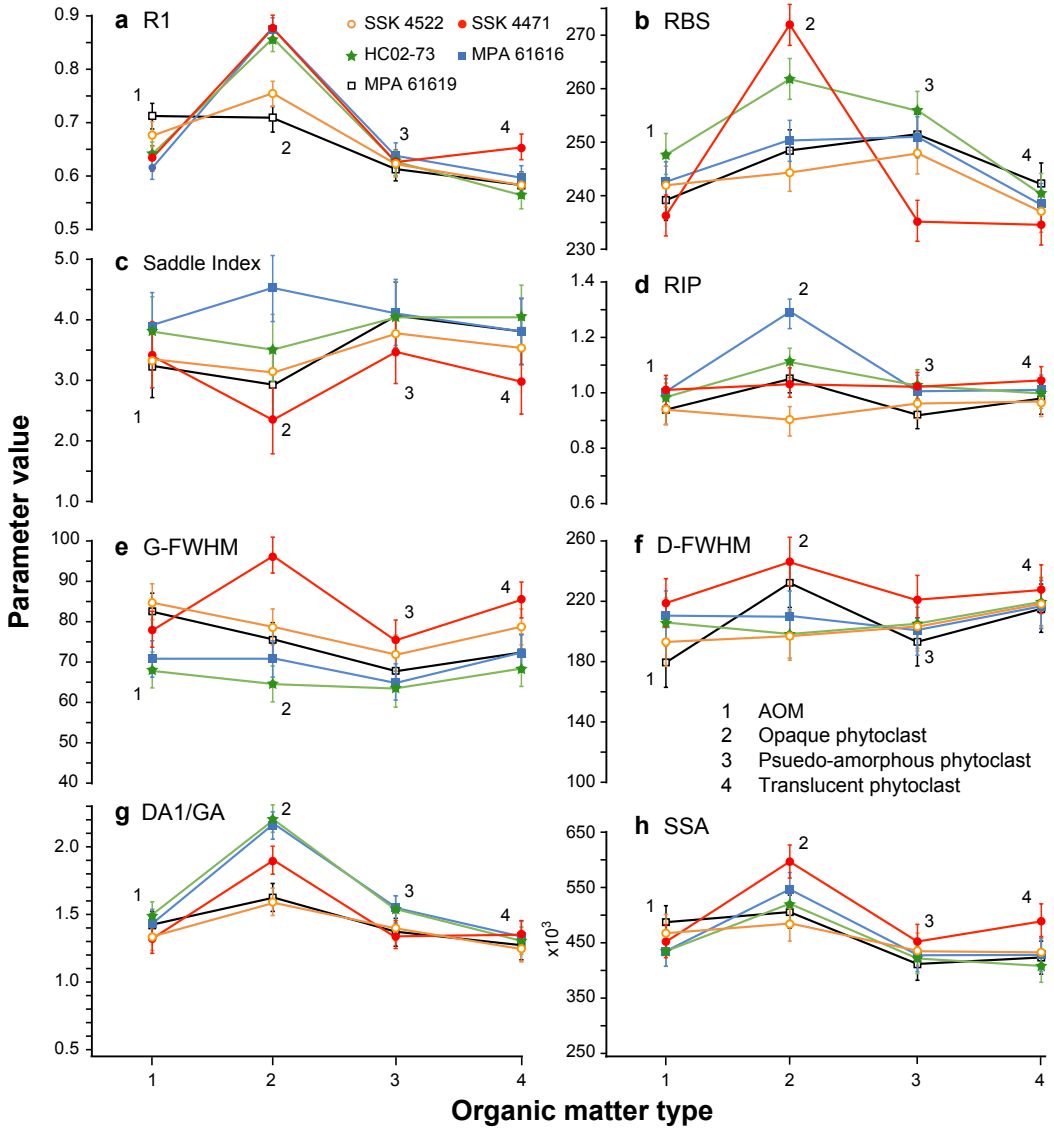


**Figure 4.16.** Raman parameter results of each organic matter type: 1 – AOM; 2 – opaque phytoclast; 3 – pseudo-amorphous phytoclast; 4 – translucent phytoclast (Appendix C). Data points for each sample are the mean of 7 to 15 measurements and the error bars are 1 sigma standard deviations. **(a)** R1, **(b)** RBS, **(c)** Saddle Index, **(d)** RIP, **(e)** G-FWHM, **(f)** D-FWHM, **(g)** DA1/DA, (h) SSA.

Intra-particle OM variation of the Raman parameters vary up to 2-9 %RSD. This creates large scatter in the Raman parameter values obtained if only one measurement is taken from an individual particle (Fig. 4.17). The scatter is reduced to 1-3 %RSD, if the average of three measurements from an individual particle is used (Fig. 4.17). The scatter does not significantly reduce further when performing >3 measurements.

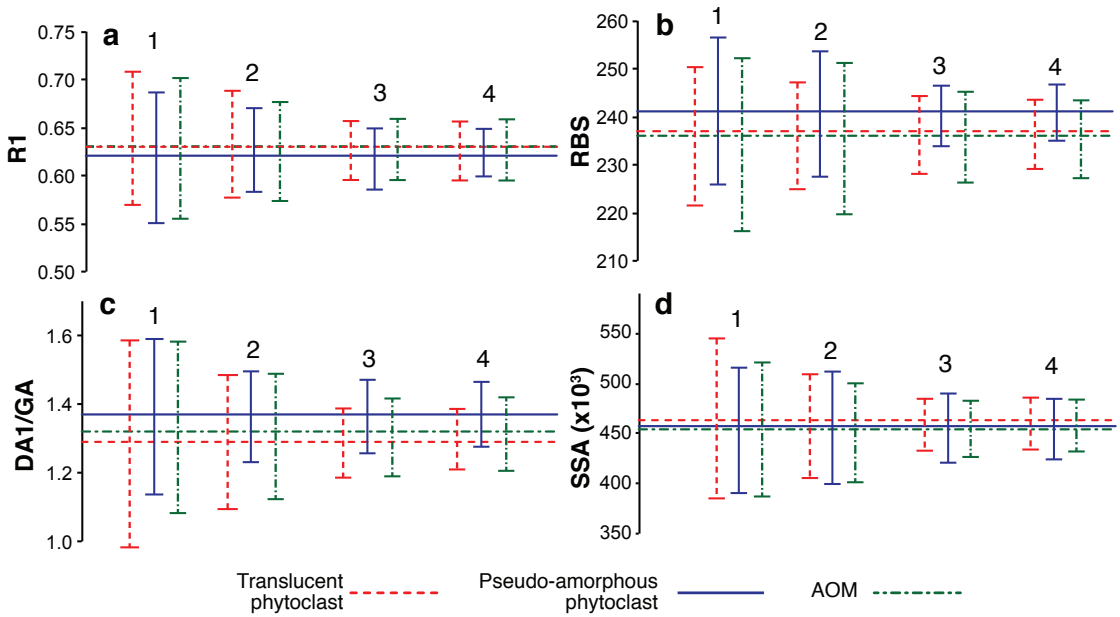


**Figure 4.17.** Intra-sample variation for a translucent phytoclast, pseudo-amorphous phytoclast and AOM in sample SSK 4471. 1: one measurement; 2: average of two measurements; 3: average of three measurements; 4: average of four measurements. The horizontal lines are the average results of 10 single measurements for each particle type. The scatter around the average reduces considerably if an average of ≥3 different measurements across a particle is calculated. **(a)** R1, **(b)** RBS, **(c)** DA1/GA, **(d)** SSA.

## 4.5 Discussion

This study demonstrates that polished blocks made from isolated OM and strew slides have differing Raman spectra and parameters. Previous authors have noted that polishing OM alters the D band height by inducing disorder in the crystal lattice as the parallel graphene layers "crumple up" (Ammar and Rouzaud, 2012; Lünsdorf, 2016). Our study confirms that R1 Raman parameter values increase after polishing. The R1 ratio from the strew slides have a normal distribution and low range, whereas the R1 ratio derived from polished blocks has a random distribution with a much larger range. This suggests that during polishing, different particles are affected unequally, as proposed by Ammar and Rouzaud (2012). This crumbling effect during polishing

affects the R1 ratio, the saddle index, D-FWHM, DA1/GA and the SSA parameters in a systematic manner. G-FWHM is also affected by polishing but in this case the changes in values are not systematic. The RBS parameter remains largely unaffected.

Sample SSK 4471 is an exception to the general trends, as the results derived from the polished block and strew slide are very similar after performing a 3$^{rd}$-order polynomial baseline correction. The reason for this exception is uncertain, but the isolated OM from this sample is composed almost entirely of phytoclasts, whereas the other samples consists predominantly of AOM and some pyrite. One hypothesis is that the varying hardness of the different types of OM and pyrite particles may lead to unequal degrees of polishing and potential heating of individual particles, which may impact the Raman parameters.

Beyssac et al. (2003) and Kouketsu et al. (2014) avoided analysing the damaged surface of the OM in polished blocks by focusing the laser beam a few micrometres below the surface. This was tested in this study; however, the R1 ratio for several polished blocks did not decrease with depth towards the strew slide sample mean, which suggests that polishing not only impacts the surface, but may also extend below the surface of individual OM particles.

Strew slides exhibit the least amount of bias, as sample preparation does not alter the Raman spectra. In addition, OM types can be easily identified, as well as having the ability to perform conventional standard palynological analysis, spore colouration index (SCI), and other thermal alteration indices (TAI) contemporaneously (cf. Hartkopf-Fröder et al., 2015).

Raman parameters from the opaque phytoclast group are substantially different compared to the other OM groups. Translucent phytoclast, pseudo-amorphous phytoclast and AOM groups have similar Raman parameter values. This is important, as it may be unnecessary to differentiate between these OM types for a rapid assessment of thermal maturity.

Intra-particle variation is apparent in the samples and the results range from 2–9 %RSD when performing only one measurement on a particle. However, this variation

2596 can be reduced to 1–3 %RSD, if the average value of 3 measurements is taken from a
2597 sample. The intra-particle variation can be attributed to the biogenic heterogeneity.
2598 Different thicknesses of the particle may also impact the results, as thinner particles
2599 allow the laser to interact with the glass slide, producing greater fluorescence. This
2600 could lead to bias in the Raman results if a linear or unsuitable non-linear background
2601 correction is performed. Greater fluorescence is also observed close to the edges of
2602 the particles and particles with a diameter of <3 µm. It is therefore recommended that
2603 thin parts of a particle, as judged by the degree of translucency, small particles of <3
2604 µm, and the edges of particles should be avoided.

2605 The experimental setup affects the OM Raman spectra and parameters. The 514.5 nm
2606 Ar-ion laser produces significantly less fluorescence than the 633 nm HeNe laser. Using
2607 high laser powers of ≥1 mW damages the surface of the OM, which leads to a blue-
2608 shift in the G band, the G-FWHM and SSA increases and the D band and saddle heights
2609 increase relative to the G band. We recommended a laser power of ~0.2 mW to
2610 analyse kerogens, as it does not damage the surface of OM or alter the Raman spectra.

2611 Some previous authors have also used laser powers of <1 mW (Quirico et al., 2005;
2612 Hinrichs et al., 2014; Lünsdorf et al., 2014; Mumm and Inan, 2016; Muirhead et al.,
2613 2016; Schito et al., 2017; Schimdt et al., 2017), but the majority of previous studies
2614 have employed laser powers >1 mW (Pasteris and Wopenka, 1991; Spötl et al., 1998;
2615 Beyssac et al., 2003; Nestler et al., 2003; Rahl et al., 2005; Schopf et al., 2005; Allwood
2616 et al., 2006; Marques et al., 2009; Guedes et al., 2010; Kwiecinska et al., 2010; Lahfid
2617 et al., 2010; Liu et al., 2013; Matthew et al., 2013; Kouketsu et al., 2014; Bonoldi et al.,
2618 2016; Delarue et al., 2016; Ferralis et al., 2016; Sauerer et al., 2017), which may have
2619 induced in-situ thermal damage. Jehlička et al. (2003) and Court et al. (2007) both used
2620 laser powers >1 mW but stated no induced damaged was observed. The reason for
2621 this, as mentioned by Court et al. (2007), could be due to the strong noise in the
2622 spectra making it difficult to interpret the blue-shift of the G band position. It is also
2623 difficult to see the damage if the particle is dark brown/black when analyzing a strew
2624 slide.

The Raman instrument set up used in this study showed than an accumulation time of >10 s does not significantly improve the signal to noise ratio, whereas the number of accumulations, does improve the signal to noise ratio. It is essential that optimum instrumental conditions are developed before conducting Raman analysis. Better quality spectra reduce the bias in picking peak heights and positions when using the M-1 method, and improve reproducibility when performing deconvolution. Some individual OM components generated very noisy spectra and increasing the accumulation time and number of accumulations did very little to improve the signal. These particles were identified as being strongly oxidized (cf. Brolly et al., 2016) and data from these particles are rejected.

Non-linear baseline correction is necessary to analyse low maturity samples, as fluorescence is often present. Linear baseline correction overestimates the R1 parameter, the G-FWHM, the Raman spectra area, and the saddle height, as the linear correction does not take into consideration the curved nature of the background created by the fluorescence. To predict the shape of the background fluorescence, a spectra range of 900–2000 $cm^{-1}$ is proposed in this study.

Five methods were tested in order to calculate Raman parameters, these included: two non-deconvolution methods, the M-1 and M-2 methods; and three deconvolution methods, the M-3, M-4 and M-5 methods. The deconvolution M-3 method has a poorer visual fit with the original spectrum and does not account for the finer detail of the disordered bands between 1200–1300 $cm^{-1}$. The fitted spectra for the M-4 and M-5 methods have a closer fit visually and statistically with the original spectrum. However, this can be misleading, as unrealistic band positions, heights and widths, which are a common problem for the M-4 and M-5 methods, can produce equally good visual and statistical fits.

Kouketsu et al. (2004) avoided the problem of unrealistic band positions in low maturity OM by fixing the position of the D4 band; this method could also be replicated for other bands. This is a more sensible approach than assigning threshold limits, as the experiment is kept consistent. However, this method was not chosen in the present study as the width and heights of the bands are unstable, which results in

discrepancies in the other bands. This is a major problem, as a fixed universal deconvolution method applied to low-maturity OM may produce considerable bias.

The M-3 method is simplistic, it ignores the finer detail, and the fitted spectra have a poor resemblance to the original spectrum. On the other hand, the extra bands for the M-4 and M-5 methods have too much freedom of movement, which produces unrealistic band positions, heights and widths. Visual inspection after deconvolution to assess the legitimacy of each band is necessary. A degree of manual tuning is essential. This poses an interesting challenge if an automated deconvolution method is to be developed (Lünsdorf and Lünsdorf, 2016; Lünsdorf et al. 2017).

Nevertheless, deconvolution is heavily used in the literature (Appendix A), although Kouketsu et al. (2014) and Lünsdorf et al. (2014) acknowledged that there is no agreement on the best way to perform deconvolution for low-maturity OM. Lupoi et al. (2017) also stated that deconvolution is too labour extensive and has inherent bias, which restricts the method as a widespread thermal maturity tool. This study is in agreement with Kouketsu et al. (2014) and Lupoi et al. (2017). We therefore propose that the M-1 and M-2 methods that do not perform deconvolution should be used for low-maturity OM. Both of these methods introduce minimal bias, as well as offering faster data acquisition.

## 4.6 Conclusions

(1) It is recommended that strew slides should be preferred over polished blocks for Raman analysis, which also allow the operator to perform palynofacies analysis and other types of thermal alteration studies (e.g. SCI, TAI) contemporaneously.

(2) The Raman parameters for our low-maturity sample set (0.5–0.8 $\%_{eq}VR_o$) show that there is little difference between the translucent phytoclast, pseudo-amorphous phytoclast and amorphous organic matter groups. However, opaque phytoclasts need to be differentiated. Taking the average value of three measurements across a single particle, as well as avoiding the edges of

particles, thin particles and particles with a diameter of <3 μm, reduce inter-particle variability.

(3) Minimising the noise in the spectra is achieved by using the highest laser power that does not induce damage to the sample. In this study a 514.5 nm laser power of 0.2 mW was used. A better-quality spectrum reduces the error associated with selecting the band heights, positions and widths, and makes the baseline correction and deconvolution more reproducible when using an automated method.

(4) A 3$^{rd}$-order polynomial baseline correction is advised for low-maturity OM. The spectrum needs to be acquired between 900–2000 cm$^{-1}$ to predict the non-linearity of the fluorescence.

(5) The reproducibility of using the same deconvolution method across a sample set can be poor and leads to errors. We recommend that deconvolution should not be performed for low-maturity samples. Raman parameters should be acquired using the M-1 and M-2 methods described in this study, which are rapid, robust and require minimal operator manipulation.

# *Chapter 5* A rapid method for determining organic matter maturity using Raman spectroscopy: Application to Carboniferous organic-rich mudstones and coals

This chapter is from: Henry, D.G., Jarvis, I., Gillmore, G., Stephenson, M., 2019. *A rapid method for determining organic maturity using Raman spectroscopy: Application to Carboniferous organic-rich mudstone and coals. International Journal of Coal Geology, 203, 87 – 98.*

## 5.1 Abstract

A simple and rapid automated Raman maturity method is calibrated using a suite of Carboniferous organic-rich mudstones and coals from the Inch of Ferryton-1 borehole in the Midland Valley of Scotland. Sediments in the borehole have been thermally matured by intrusion of a quartz dolerite sill, generating vitrinite reflectance (VR) values ranging from 0.5 to 6.0%VRo. Calibration curves are tested on eight other UK wells penetrating Carboniferous shales and coals in the Midland Valley and southern Pennine Basin. The G-band full-width at half-maximum (G-FWHM) is the best Raman parameter to estimate the thermal maturity of organic matter (OM) in the oil and gas window (0.5 to 3%$VR_o$) and has a very strong correlation with $VR_o$.

## 5.2 Introduction

Raman spectroscopy has been used to track the thermal maturity of organic matter (OM) in sedimentary and metamorphic rocks (Pasteris and Wopenka, 1991; Spötl et al., 1998; Kelemen and Fang, 2001; Beyssac et al., 2002; Jehlička et al., 2003; Marshall et al., 2005; Quirico et al., 2005; Rahl et al., 2005; Schöpf et al., 2005; Guedes et al., 2010; Liu et al., 2013; Muirhead et al., 2012, 2016; Aoya et al., 2010; Kouketsu et al., 2014; Zhou et al., 2014; McNeil et al., 2015; Bonoldi et al., 2016; Ferralis et al., 2016;

Lünsdorf, 2016; Sauerer et al., 2017; Schito et al., 2017; Schmidt et al., 2017; Baludikay et al., 2018; Khatibi et al., 2018). Studies have had various degrees of success and results show significant inconsistencies between Raman thermal maturity parameters and vitrinite reflectance (e.g. Quirico et al., 2005; Bonoldi et al., 2016; Sauerer et al., 2017; Schmidt et al., 2017; Schito et al., 2017; Khatibi et al., 2018). This is attributed to measuring different sample types and performing different methods of spectra acquisition and processing, which can significantly impact the Raman parameters (Lünsdorf et al., 2014; Henry et al., 2018). This paper applies the method of Henry et al. (2018) that does not perform spectral deconvolution and therefore avoids processing bias and longer processing time when deriving Raman parameters. The downside of not performing deconvolution is that the parameters cannot be assigned to specific modes of vibrations, as they are a result of several different modes interacting with each other (Beyssac et al., 2002; Ferralis et al., 2016).

The aim of this study is to: (1) apply the methodology developed by Henry et al. (2018) to construct Raman vs. vitrinite reflectance calibration curves using several Raman parameters; (2) test the calibration curves on several wells that intersect Carboniferous coals and shales and; (3) determine which is the best Raman parameter to provide equivalent VR values that are similar to measured VR values for samples in the oil and gas maturity ranges (0.6–3%$VR_o$). We confirm Raman spectroscopy as being a powerful new tool for the rapid quantification of organic matter maturity in petroleum basins, with particular application to shale gas exploration.

## 5.3 Material and methods

### *5.3.1 Material*

Washed and registered cuttings collected from the British Geological Survey (BGS) core store at Keyworth were used (Table 1, Fig. 1a). The cuttings were first analysed using laser Raman, and selected samples were subsequently prepared for vitrinite reflectance (VR) analysis; samples were selected to cross-check previously reported VR values (Raymond, 1991; Green et al., 2001; Smith et al., 2011; Andrews et al., 2013) and to obtain data for sample intervals where VR values were unavailable.

Samples from the Inch of Ferryton-1 borehole (Table 1), located in the Midland Valley of Scotland (Fig. 1), were used to correlate Raman parameters with $VR_o$ data. The well penetrates Carboniferous rocks that are similar in age to the Bowland Shale of central England, which is the main target for shale gas exploration in the UK (Andrews, 2013). The Inch of Ferryton-1 borehole has an unusually wide maturity range of 0.5 to 6.0 $\%VR_o$ (Table 1; Raymond, 1991), as the organic matter has been thermally matured by a c.150 m thick quartz dolerite sill of Stephanian (late Pennsylvanian) age that was intruded into the Pendleian (late Mississippian) Limestone Coal Group (Fig. 1b). There is significant literature discussing how igneous intrusions impact sediment host rocks (Dow, 1977; Raymond and Murchison, 1988; Raymond, 1991).

In summary, thermal alteration zones (aureoles) develop around the igneous intrusion; the extent of thermal aureoles is dependent on the thickness of the intrusion, the nature of the igneous rock, hydrothermal fluids and host rocks, and the degree of post-intrusion compaction, and it is typically delineated by performing vitrinite reflectance (VR) (Dow, 1977; Raymond and Murchison, 1988). VR values increase exponentially as the intrusion is approached and VR values tend to be higher above the intrusion due to the preferential upwards flow of hydrothermal fluids (Raymond and Murchison, 1988). The extent of thermal aureoles typically varies between 30 and 200% of the intrusion thickness (Dow, 1977; Aarnes et al., 2010). Therefore, by measuring VR at a distance>200% the thickness of the intrusion, the regional background burial VR values can be estimated.

The calibration curves derived from the Inch of Ferryton-1 analyses, were applied to samples from eight additional wells (Fig. 5.1; Table 5.1): two from the Midland Valley: Milton of Balgonie-1; Calais-3; and six from the Pennine Basin of central England: Kirk Smeaton-1; Gun Hill-1; Gainsborough-2; Duffield-1; Rufford-1; Carsington Dam Reconstruction-1. The aim was to test whether laser Raman can be used as a rapid means to reliably estimate the thermal maturity of Carboniferous rocks in the UK, with particular focus on the maturity range relevant to shale gas exploration (0.6–3 $\%VR_o$). All the wells intersect Carboniferous organic-rich mudstones and coals.

The Midland Valley of Scotland and Pennine Basin in central England were both formed in response to Late Devonian and Early Mississippian back-arc extension north of the Variscan orogenic front, forming a series of interconnected NE–SW graben and half-graben structures (Fig. 2; Waters et al., 2009). These basins accumulated Carboniferous organic-rich mudstones and coals, which have been identified as proven source rocks for many of the conventional oil and gas fields in central England (Andrews, 2013) and, historically, were an important source of oil shale in the Midland Valley of Scotland (Monaghan, 2014). Both the Midland Valley and Pennine Basin suffered from extensive tholeiitic magmatism during the Late Carboniferous, which led to the intrusion of sills and dykes into Lower Carboniferous strata. These intrusions led to local thermal alteration of the surrounding strata pushing the maturity of shales and coals into and above the oil and gas windows (Raymond, 1991; Monaghan, 2014).

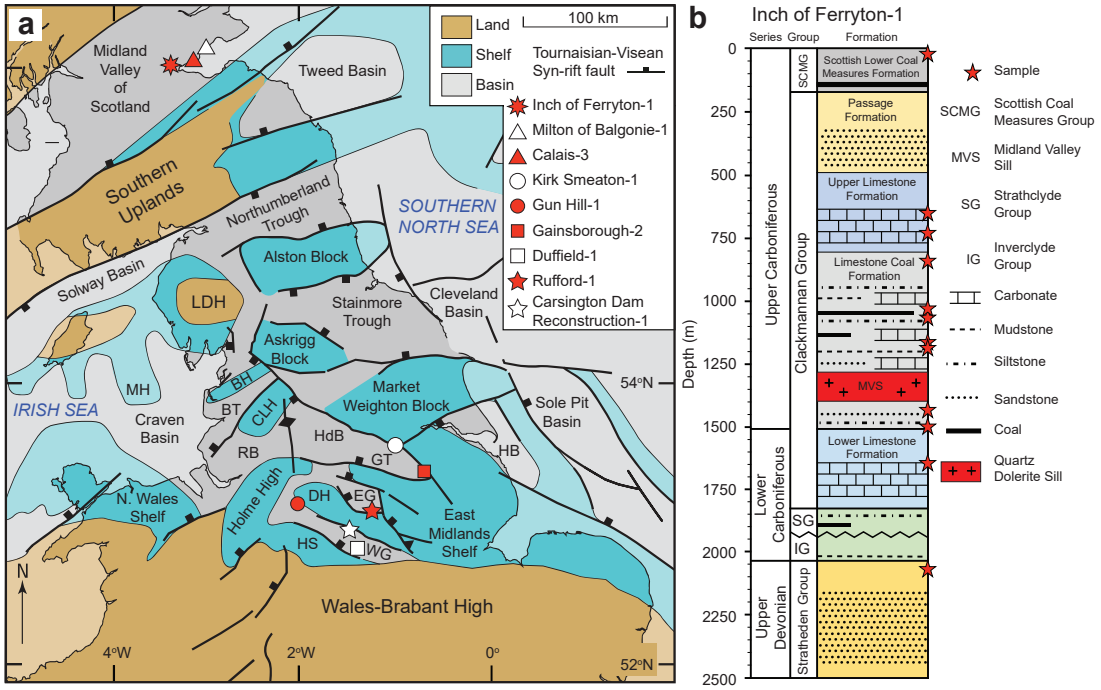


**Figure 5.1. (a)** Geological framework of the Carboniferous and the location of the wells used in this study. Base map from Waters et al. (2009). The Pennine Basin, a complex fault-controlled mosaic of shelves and sub-basins, extends between the Southern Uplands and the Wales-Brabant High. BH–Bowland High; BT–Bowland Trough; CLH–Central Lancashire High; DH–Derbyshire High; EG–Edale Gulf; GT–Gainsborough Trough; HB–Humber Basin; HdB–Huddersfield Basin; HS–Hathern Shelf; LDH–Lake District High; MH–Manx High; WG–Widmerpool Gulf. Reproduced with the permission of the British Geological Survey ©NERC. All rights reserved. **(b)** Core description of the Inch of Ferryton-1 borehole

2802 and the depths of samples used to calibrate the Raman with vitrinite reflectance. IG–Inverclyde Group;
2803 SG–Strathclyde Group. Adapted from Raymond (1991) and Monaghan (2014).

2804

2805 **Table 5-1.** Borehole samples used in this study along with depth, series /stage, rock unit and measured
2806 vitrinite reflectance (%$VR_o$).

| Well (British National Grid: E, N) (Lat, Long) | Sample No. (SSK) | Depth (m) | Series / Stage | Rock Unit | %$VR_o$ | Rock type analysed |
|---|---|---|---|---|---|---|
| **Inch of Ferryton-1** | 75826 | 24 | U. Carboniferous[a] | Scottish Lower Coal Measures Fm. | 0.57[a] | Coal |
| (NS 290777, 690150) | 75827 | 588 | U. Carboniferous[a] | Upper Limestone Fm. | 0.95[b] | Shale |
| (56.091618 N, 3.757062 W) | 75828 | 640 | U. Carboniferous[a] | Upper Limestone Fm. | 0.75[b] | Coal |
| | 75846 | 735 | U. Carboniferous[a] | Limestone Coal Fm. | 0.89[b] | Coal |
| | 75829 | 838 | U. Carboniferous[a] | Limestone Coal Fm. | 1.00[b] | Coal |
| | 75830 | 1021 | U. Carboniferous[a] | Limestone Coal Fm. | 1.85[b] | Coal |
| | 75831 | 1064 | U. Carboniferous[a] | Limestone Coal Fm. | 2.23[b] | Coal |
| | 75840 | 1155 | U. Carboniferous[a] | Limestone Coal Fm. | 3.79[a] | Coal |
| | 75841 | 1170 | U. Carboniferous[a] | Limestone Coal Fm. | 4.03[b] | Coal |
| | 75842 | 1423 | U. Carboniferous[a] | Limestone Coal Fm. | 6.04[b] | Coal |
| | 75843 | 1487 | U. Carboniferous[a] | Limestone Coal Fm. | 4.28[b] | Shale |
| | 75844 | 1637 | L. Carboniferous[a] | Lower Limestone Fm. | 2.97[b] | Coal |
| | 75845 | 2057 | Devonian[a] | Stratheden Group | 2.21[b] | Shale |
| **Milton of Balgonie-1** | 80037 | 305 | U. Carboniferous[a] | Upper Limestone Fm. | 0.48[a] | Shale |
| (NT 33173, 99335) | 80249 | 408 | U. Carboniferous[a] | Upper Limestone Fm. | 0.47[b] | Coal |
| (56.181942 N, 3.078141 W) | 80250 | 489 | U. Carboniferous[a] | Upper Limestone Fm. | 0.65[b] | Coal |
| | 80251 | 582 | U. Carboniferous[a] | Limestone Coal Fm. | 0.67[a] | Coal |
| | 80272 | 625 | U. Carboniferous[a] | Limestone Coal Fm. | nd | Coal |
| | 80252 | 649 | U. Carboniferous[a] | Limestone Coal Fm. | 0.83[b] | Coal |
| | 80253 | 704 | U. Carboniferous[a] | Limestone Coal Fm. | 1.95[b] | Shale |
| | 80254 | 762 | U. Carboniferous[a] | Limestone Coal Fm. | 2.18[a] | Coal |
| | 80255 | 777 | U. Carboniferous[a] | Limestone Coal Fm. | 3.02[b] | Coal |
| | 80256 | 799 | U. Carboniferous[a] | Limestone Coal Fm. | 3.32[b] | Coal |
| | 80273 | 805 | U. Carboniferous[a] | Limestone Coal Fm. | nd | Coal |
| | 80257 | 817 | L. Carboniferous[a] | Lower Limestone Fm. | 4.00[b] | Coal |
| | 80258 | 847 | L. Carboniferous[a] | Lower Limestone Fm. | 2.21[a] | Shale |
| | 80259 | 1030 | L. Carboniferous[a] | Lower Limestone Fm. | 3.74[b] | Coal |
| | 80260 | 1036 | L. Carboniferous[a] | Lower Limestone Fm. | 3.54[b] | Coal |
| | 80261 | 1082 | L. Carboniferous[a] | Lower Limestone Fm. | 2.11[b] | Shale |
| | 80262 | 1097 | L. Carboniferous[a] | Lower Limestone Fm. | 2.38[b] | Shale |
| | 80263 | 1125 | L. Carboniferous[a] | Lower Limestone Fm. | 1.44[b] | Coal |
| | 80264 | 1137 | L. Carboniferous[a] | Lower Limestone Fm. | 1.26[a] | Coal |
| | 80265 | 1195 | L. Carboniferous[a] | Lower Limestone Fm. | 1.56[a] | Coal |
| | 80266 | 1210 | L. Carboniferous[a] | Lower Limestone Fm. | 1.35[b] | Coal |
| | 80267 | 1222 | L. Carboniferous[a] | Lower Limestone Fm. | 0.75[b] | Coal |
| | 80268 | 1280 | L. Carboniferous[a] | Strathclyde Group | 0.84[b] | Shale |
| | 80277 | 1445 | L. Carboniferous[a] | Strathclyde Group | 0.87[b] | Shale |
| | 80269 | 1484 | L. Carboniferous[a] | Strathclyde Group | 0.90[a] | Coal |
| | 80278 | 1600 | L. Carboniferous[a] | Strathclyde Group | 0.90[b] | Shale |
| | 80279 | 1783 | L. Carboniferous[a] | Strathclyde Group | nd | Shale |
| | 80270 | 1911 | L. Carboniferous[a] | Strathclyde Group | 1.13[b] | Shale |
| | 80035 | 1966 | L. Carboniferous[a] | Strathclyde Group | 1.20[b] | Coal |
| | 80271 | 1975 | L. Carboniferous[a] | Strathclyde Group | 1.26[b] | Shale |
| | 80036 | 1981 | L. Carboniferous[a] | Strathclyde Group | 4.54[b] | Shale |
| **Calais-3** | 80232 | 24 | L. Carboniferous[a] | Lower Limestone Fm. | 1.71[b] | Coal |
| (NT 12764, 86386) | 80233 | 30 | L. Carboniferous[a] | Lower Limestone Fm. | 1.62[b] | Coal |
| (56.062333 N, 3.402583 W) | 80234 | 49 | L. Carboniferous[a] | Lower Limestone Fm. | 1.51[b] | Coal |
| | 80235 | 52 | L. Carboniferous[a] | Lower Limestone Fm. | 1.51[b] | Coal |
| | 80236 | 64 | L. Carboniferous[a] | Lower Limestone Fm. | 1.39[b] | Shale |
| | 80237 | 66 | L. Carboniferous[a] | Lower Limestone Fm. | nd | Coal |

| | | | | | | | |
|---|---|---|---|---|---|---|---|
| | 80238 | 88 | L. Carboniferous[a] | Strathclyde Group | | 1.32[b] | Shale |
| | 80239 | 98 | L. Carboniferous[a] | Strathclyde Group | | 2.03[b] | Shale |
| | 80040 | 111 | L. Carboniferous[a] | Strathclyde Group | | nd | Coal |
| | 80042 | 137 | L. Carboniferous[a] | Strathclyde Group | | 1.44[b] | Coal |
| | 80043 | 146 | L. Carboniferous[a] | Strathclyde Group | | 1.51[b] | Shale |
| | 80044 | 152 | L. Carboniferous[a] | Strathclyde Group | | 1.68[b] | Coal |
| | 80045 | 168 | L. Carboniferous[a] | Strathclyde Group | | 2.07[b] | Shale |
| | 80046 | 174 | L. Carboniferous[a] | Strathclyde Group | | 3.80[b] | Coal |
| **Kirk Smeaton-1** | 75847 | 250 | Westphalian C[c] | Pennine Upper Measures Fm. | Coal | 0.55[c] | Coal |
| (SE 51142, 16097) | 75848 | 512 | Westphalian B[c] | Pennine Middle Measures Fm. | Coal | 0.70[c] | Coal |
| (53.638899 N, 1.227966 W) | 75849 | 758 | Westphalian A[c] | Pennine Lower Measures Fm. | Coal | 0.80[c] | Coal |
| | 75850 | 1002 | Namurian[c] | Millstone Grit Group | | 0.90[c] | Shale |
| | 75851 | 1252 | Namurian[c] | Millstone Grit Group | | 1.20[c] | Shale |
| | 75852 | 1590 | Namurian[c] | Bowland Shale Fm. | | 1.40[c] | Shale |
| **Gun Hill-1** | 75853 | 250 | Namurian[c] | Millstone Grit Group | | 0.65[c] | Shale |
| (SJ 97230, 61820) | 75854 | 481 | Namurian[c] | Bowland Shale Fm. | | 0.70[c] | Shale |
| (53.153506 N, 2.042876 W) | 75855 | 503 | Namurian[c] | Bowland Shale Fm. | | 1.50[c] | Shale |
| | 75856 | 622 | Namurian[c] | Bowland Shale Fm. | | 1.40[c] | Shale |
| | 75857 | 839 | Namurian[c] | Bowland Shale Fm. | | 1.10[c] | Shale |
| | 75858 | 956 | Namurian[c] | Bowland Shale Fm. | | 1.20[c] | Shale |
| | 75859 | 1401 | Namurian[c] | Bowland Shale Fm. | | 1.60[c] | Shale |
| **Gainsborough-2** | 75860 | 764 | Westphalian B[c] | Pennine Middle Measures Fm. | Coal | 0.45[c] | Coal |
| (SK 81774, 90785) | 75861 | 897 | Westphalian B[c] | Pennine Middle Measures Fm. | Coal | 0.65[c] | Shale |
| (53.407555 N, 0.771360 W) | 75862 | 1089 | Westphalian B[c] | Pennine Middle Measures Fm. | Coal | 0.60[c] | Coal |
| | 75863 | 1302 | Westphalian A[c] | Pennine Lower Measures Fm. | Coal | 0.71[c] | Shale |
| | 75864 | 1797 | Namurian[c] | Millstone Grit Group | | 0.75[c] | Shale |
| | 75865 | 1844 | Namurian[c] | Bowland Shale Fm. | | 0.80[c] | Shale |
| | 75866 | 1900 | Namurian[c] | Bowland Shale Fm. | | 0.75[c] | Shale |
| **Duffield-1** (SK 34280, 42170) (52.975790 N, 1.490946 W) | 75869 | 1046 | Visean[d] | Bowland Shale Fm. | | 1.25[d] | Shale |
| **Rufford-1** | 80051 | 451 | Westphalian[e] | nd | | 0.59[e] | Coal |
| (SK 64718, 62200) | 80052 | 499 | Westphalian[e] | nd | | 0.59[e] | Coal |
| (53.153012 N, 1.033694 W) | 80053 | 748 | Westphalian[e] | nd | | 0.71[e] | Coal |
| | 80056 | 1126 | Namurian[e] | nd | | 0.82[e] | Coal |
| | 80055 | 1174 | Tournaisian-Visean[e] | nd | | 0.85[e] | Shale |
| | 80054 | 1201 | Tournaisian-Visean | nd | | 0.76[e] | Shale |
| **Carsington Dam Reconstruction-1** (SK 24285, 50473) (53.050970 N, 1.639168 W) | 4471 | 39 | Namurian | Bowland Shale Fm. | | 0.62[a] | Shale |

[a] VR values determined in this study; additional VR data and ages from: [b] Raymond (1991); [c] Andrews et al. (2013); [d] Smith et al. (2011); [e] Green et al. (2001). Fm. = Formation. nd = not determined.

The Midland Valley of Scotland boreholes: Inch of Ferryton-1; Milton of Balgonie-1; and Calais-3, penetrate thick Carboniferous strata with interbedded coals, siltstones,

sandstones, mudstones and carbonates with igneous intrusions. Inch of Ferryton-1 was drilled by Tricentrol in 1986 to test the conventional hydrocarbon potential of the Namurian and Dinantian sandstones (Monaghan, 2014). The well includes the Carboniferous Scottish Lower Coal Measures Formation, Clackmannan Group (Passage Formation, Upper Limestone Formation, Limestone Coal Formation, Lower Limestone Formation), Strathclyde Group and Inverclyde Group, followed by the Devonian Stratheden Group at the base (Fig. 5.1). The quartz-dolerite Midland Valley Sill is intruded into the Limestone Coal Group Formation (Namurian). Thin tuff intervals are also present below the sill. Milton of Balgonie-1 was drilled by Burmah Oil Exploration in 1984 to test the conventional hydrocarbon potential of the Earl's Sear Anticline targeting the Lower Carboniferous sandstones (Monaghan, 2014). Similar to the Inch of Ferryton-1, the Midland Valley Sill intruded in the Clackmannan Group (Namurian) with several minor tuff, lava and quartz-dolerite sills deeper in the Strathclyde Group (Visean), below. Calais-3 was an appraisal well drilled by Berkeley Resources Limited in 1986 (Monaghan, 2014). The well intersected the Lower Limestone Formation and the Strathclyde Group. An igneous sill was encountered at the base of the well at c. 185 m depth, in the Strathclyde Group.

The remaining six wells are located in the Carboniferous Pennine Basin, an interconnected mosaic of rift basins and shelves in central England (Fig. 5.1). The wells are associated with interbedded coals, siltstones, sandstones, mudstones and carbonates, with some minor igneous intrusions and lavas. Kirk Smeaton-1 was a wildcat well drilled in the Gainsborough Trough by RTZ Oil and Gas Limited in 1985 (Andrews, 2013). The well encountered the Triassic-Permian Sherwood Sandstone Group (SSG), followed by the Carboniferous Pennine Coal Measures Group (Westphalian A–C), Millstone Grit Group and the Bowland Shale Formation. There is no evidence of igneous intrusions. Gun Hill-1 was drilled by D'Arcy Exploration in 1938 and is on the western flank of the Derbyshire High in the Widmerpool Gulf (Andrews, 2013). The well intersects a thick Carboniferous sequence including the Millstone Grit Group and the Bowland Shale Formation. There are also several intervals of lava flows known as the Gun Hill lava between 400–900 m in Visean aged strata. Gainsborough-2 was drilled by British Petroleum in 1959 in the Gainsborough Trough (Andrews,

2013). The well intersects the Triassic–Permian Sherwood Sandstone Group, before it encounters a thick sequence of Carboniferous Pennine Coal Measures Group (Westphalian A and B), and Bowland Shale Formation. The well terminated in the Upper Bowland Shales just below a thin dolerite sill at c.1900 m. Duffield-1 was drilled by the BGS in 1966 and intersects a thick sequence of Bowland Shales (Aitkenhead, 1977; Andrews, 2013). A quartz-dolerite sill intruded at the base of the well at c. 1000 m in the Lower Bowland Shales. Rufford-1 was drilled by British Petroleum in 1986 to test the hydrocarbon potential of the Westphalian and Namurian sandstones and the Dinantian limestones (Hodge, 1986). Similar to Gainsborough-2 and Kirk Smeaton-1, the well intersects Triassic and Permian strata, followed by a thick sequence of Carboniferous Pennine Coal Measures Group (Westphalian A and B), Millstone Grit Group and the Carboniferous Limestone Supergroup. Carsington Dam Reconstruction-1 was drilled in the 1990 to assess the hydrological conditions and pressures of the reconstructed Carsington Dam following its failure in 1984 (Banyard et al., 1992; Skempton and Vaughan, 1993) and intersects Namurian Bowland Shale.

### *5.3.2 Methods*

#### *5.3.2.1 Laser Raman spectroscopy*

Coal particles were hand-picked from the bulk samples, however, when coal particles were not present, black shale particles were selected (Table 5.1). Each particle was stored in a plastic bag and labelled. The particles were analysed by a Renishaw inVia™ laser Raman instrument connected to a Leica DMLM microscope. The Rayleigh scattering was removed using an edge filter and the Raman scattering was dispersed by an 18,000 lines/mm holographic grating and detected by a charged couple device (CCD). A standard silicon wafer sample was used to calibrate the instrument by matching the 520.5cm$^{-1}$ band position, followed by manually aligning the laser beam with the crosshairs on the microscope. A 514.5 nm argon-ion green laser delivering c. 2 mW was used. The laser was focused through a x50 objective, with a laser spot size of c. 2 μm. The scan range was limited to 900–2000 cm$^{-1}$, in order to assess the first-order region.

Where possible, up to 30 measurements from different cuttings (pieces of coal/shale) where analysed per sample depth. The data are generally normally distributed. However, as the samples are cuttings, cavings and recycled vitrinite may be present. These were identified, and the corresponding data removed before parameterising the population to represent the true maturity. Two types of data manipulation were performed: (1) isolated anomalous data points ('flyers') were excluded; and (2) populations of caved or reworked material were identified using histograms (where present), and the corresponding data excluded before calculating the mean Raman parameter values to represent the true maturity of the sample. The same approach is routinely applied in the petroleum industry for the determination of VR values from wells (Dow, 1977; wiki.aapg.org/vitrinite_reflectance).

Renishaw WiRE 3.3 software was used to acquire spectra, which were processed in the automated Microsoft Excel® spreadsheet of Henry et al. (2018) that performs a Savitzky-Golay smoothing filter using a 21-point quadratic polynomial algorithm, a 3$^{rd}$-order polynomial baseline correction, and normalizes the spectra to a common G-band height of 2000 au. The automated method is set to calculate the following Raman parameters (Fig. 5.2, Table 5.2): G-band full-width half-maximum (G-FWHM); D-band full-width half-maximum (D-FWHM); Raman band separation (RBS); R1 (D/G height ratio); saddle index (SI; G/S height ratio)**;** and scaled spectrum area (SSA; total area under a baseline corrected curve when the G band has been normalized to an intensity count of 2000 a.u. between 1100 – 1700 cm$^{-1}$). The D-FWHM cannot be calculated if the saddle height ("S", Fig. 5.2) is above the height of the half maximum height of the D band.

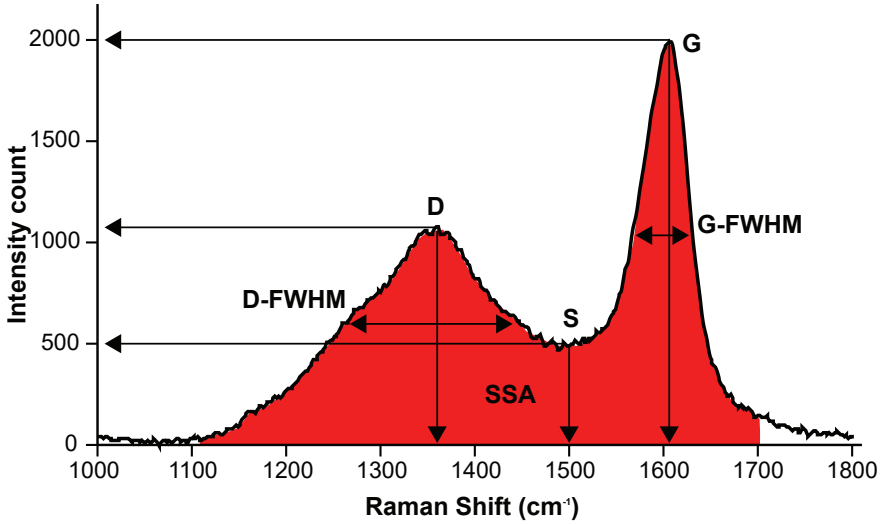


**Figure 5.2.** Illustration of the Raman parameters. The horizontal and vertical arrows for the D (disordered, D-band), G (graphite, G-band) and S (saddle) are used to measure the height intensity and position respectively, and the double-ended arrows are used to measure the full-width half-maximum (FWHM). The SSA (scaled spectrum area) is the total area under the curve between 1100–1700 $cm^{-1}$ (red shaded area).

**Table 5-2.** Raman parameters used to determine the maturity of organic matter examined in this study, along with the abbreviations and reference to previous studies.

| Method | Parameters | Abbreviations | References |
|---|---|---|---|
| Full-width at half-maximum (FWHM) | G | G-FWHM | e.g. Hinrichs et al. (2014); Zhou et al. (2014); Schmidt et al. (2017); Henry et al. (2018). |
| | D | D-FWHM | e.g. Quirico et al. (2005); Bonoldi et al. (2016); Schito et al. (2017); Henry et al. (2018). |
| Raman band position | G–D | RBS (Raman Band Separation) | e.g. Mumm and Inan (2016); Sauerer et al. (2017); Schmidt et al. (2017); Schito et al. (2017); Henry et al. (2018). |
| Ratio of Raman band height intensity | D/G | R1 | e.g. Rahl et al. (2005); Schmidt et al. (2017); Sauerer et al. (2017); Roberts et al. (1995); Spötl et al. (1998); Kelemen and Fang (2001); Henry et al. (2018). |

| | | | |
|---|---|---|---|
| | G/S | SI (Saddle Index) | Wilkins et al. (2014); Henry et al. (2018). |
| Scaled spectrum area | Area ($_{1100–1700}$) | SSA | Henry et al. (2018). |

### 5.3.2.2 *Vitrinite reflectance*

Polished blocks were prepared by embedding the same particles that were used for Raman analysis in an epoxy resin, followed by grinding and polishing according to the ISO 7404-2:2009 standard. Vitrinite reflectance (VR) was carried out using a Carl Zeiss Axio Imager.A2m microscope equipped with a halogen light source light at 546 nm and following the ISO 7404-5:2009 standard. Calibration was performed using spinel ($R_o$=0.420%) and gadolinium.gallium-garnet ($R_o$=1.722%) standards. We did not possess a standard with a higher reflectance value, therefore our own VR analyses were limited to $VR_o$ measurements of <1.5% (the oil window; Dow, 1977). Random reflectance measurements were taken in oil with a refractive index of 1.519. Samples selected for VR determinations were the same as those used for Raman analysis. Up to thirty measurements from the particles selected during the hand-picking were taken per sample, where possible. The mean vitrinite reflectance results were calculated after the removal of measurements that were judged to be form cavings and/or recycled vitrinite (cf. Dow, 1977).

## 5.4 Results and discussion

### *5.4.1 Calibration*

A core depth plot of the Raman parameters derived from coals and shales in this study, demonstrates that the laser Raman method differentiates the extent of the thermal aureole of the sill in the Inch of Ferryton-1 borehole just as effectively as measured vitrinite reflectance (%$VR_o$) (Fig. 5.3). The G-FWHM, SSA, R1 and D-FWHM values decrease with increasing maturity and the saddle index (SI) and Raman band separation (RBS) increase with increasing maturity (Fig. 5.4). The dashed lines in Figure 3 represent the general trend of the parameters with depth above and below the

thermal aureole. There is a pronounce change in the values for all the Raman parameters close to the top and base of the sill, however, the almost vertical general depth trend lines for the SI and D-FWHM parameters (Fig. 5.3d, g) suggest that these parameters lack the sensitivity necessary to quantify lower thermal maturities further away from the aureole. Note that vitrinite reflectance has a non-linear general depth trend, which is a common phenomenon when not plotted on a log scale (Dow, 1977). Whether the Raman parameters have a non-linear depth trend is uncertain, as samples deeper than c. 2050 m were not tested. The aureole symmetry (the red shaded region above and below the sill) in Figure 5.3 for VR and G-FWHM, SSA, SI and R1 is almost identical, as the increase in maturity starts at c. 700 m, however, due to the lack of samples in the lower section, the thickness of the aureole cannot be predicted with confidence using the Raman parameters. The RBS parameter (Fig. 5.3e) significantly overpredicts the aureole thickness above the sill and the D-FWHM (Fig. 5.3g) under-predicts the width of the aureole above and below the sill.

The Raman parameters that are most sensitive to smaller incremental maturity changes in the Inch of Ferryton-1 well between maturity values of 0.6 to 3 %$VR_o$, are the G-FWHM, SSA, SI, RBS and R1 parameters (Fig. 5.3b–f). Hence, these are considered to be the most reliable Raman parameters for estimating organic matter maturities in the oil and gas windows.

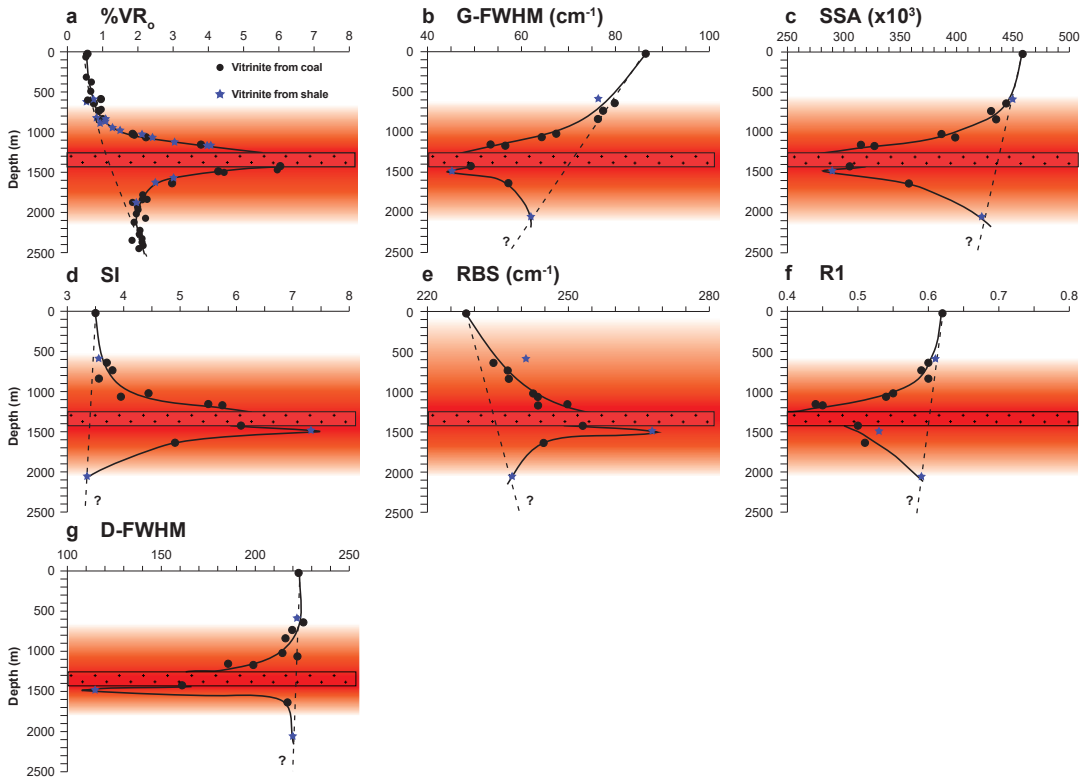


**Figure 5.3.** Vitrinite reflectance and Raman parameters depth plots, mapping out the thermal aureole around the quartz dolerite sill (Midland Valley Sill) in the Inch of Ferryton-1 borehole. $\%VR_o$ values from Raymond (1991). The stippled area represents the vertical extent of the sill. The red shading indicates the extent of the thermal aureole as determined from each analytical parameter. **(a)** Measured $\%VR_o$, **(b)** G-FWHM, **(c)** SSA, **(d)** RBS, **(e)** SI, **(f)** R1, **(g)** D-FWHM. Numerical data are presented in Appendix E

Raman parameters vs. vitrinite reflectance ($VR_o$) calibration curves (Fig. 5.4), indicated that the G-FWHM is the most promising parameter for maturity analysis with an $R^2$ of 0.96 (Fig. 5.4a). The G-FWHM calibration curve has a steeper curve and less scatter compared to the other parameters in the oil and gas windows (0.6–3 $\%VR_o$), making maturity analysis less ambiguous. Our data show similar trends to Spötl et al. (1998), Kelemen and Fang (2001), Quirico et al. (2005), Marques et al. (2009), Guedes et al. (2010), Zhou et al. (2014), Schito et al. (2017) and Schmidt et al. (2017) but differ significantly from Hinrichs et al. (2014), Bonoldi et al. (2016), and Lupoi et al. (2017) (Fig. 5.5a). These discrepancies are explained by differences in the processing methods, particularly performing variable deconvolution methods.

The SSA (scaled spectrum area) parameter was developed by Henry et al. (2018) and measures the total area under the curve from 1100-1700 $cm^{-1}$ using the trapezoid area rule after the curve has been normalized to the same G band height of 2000 au. The SSA parameter decreases with increasing maturity and is the second-best Raman parameter with an $R^2$ of 0.88 (Fig. 5.4b). The SSA parameter has good potential to estimate the maturity of organic matter (OM) in the oil and gas windows as it has a clear linear trend with a low standard deviation for VR values <3 $\%VR_o$, compared to VR values > 3 $\%VR_o$.

The R1 parameter determined by several authors shows a trend that initially decreases and then begins to increase (Fig. 5.5b). The point at which the R1 ratio trend reverses varies between different studies. Sauerer et al. (2017) demonstrated an increase starting at c. 1.5 $\%VR_o$, whereas other authors document that the increase starts between 2.0 to 5.5 $\%VR_o$ (e.g. Spötl et al., 1998; Quirico et al., 2005; Zhou et al., 2014). This large variation is again attributed to variable processing methods. In this study, R1 values do not show a clear reversal of trend, but there are signs that they may start to increase at c. 4.0 $\%VR_o$ (Fig. 5.4c). Guedes et al. (2010) and Liu et al. (2013) showed a strong linear increase with substantially greater R1 values compared to the other calibration curves (Fig. 5.5b). Liu et al. (2013) suggested the R1 ratio is suitable for measuring the maturity of over-mature OM with VR values > 3.5 %VR. Unlike the G-FWHM, Spötl et al.'s (1998) R1 calibration curve is not similar to this study's R1 calibration curve, as those authors' values begin to increase at c. 2.5 %VR (Fig. 5.5b).

The saddle index (SI) was first used by Wilkins et al. (2014) who integrated this parameter into a multi-linear regression equation known as the 'RaMM' technique. In this study, the SI increases with increasing maturity with an $R^2$ of 0.75 (Fig. 5.4d), in agreement with Wilkins et al. (2014).

The RBS increases linearly with increasing maturity (Figs. 5.4e and 5.5c), as the D band position shifts to lower wavenumbers ($cm^{-1}$) and the G band shifts to higher wavenumbers. However, the RBS values have a large standard deviation. This may lead to significant errors when using the RBS calibration curve and it should therefore not be used independently to estimate the maturity of OM. This contradicts the

conclusion of Liu et al. (2013) who proposed using the RBS parameter to estimate lower maturity OM (0.5 to 3.5 %VR). The large scatter for the RBS is similar to that reported by Kelemen and Fang (2001).

The D-FWHM parameter results follow a similar trend to calibration curves in the literature (Spötl et al., 1998; Kelemen and Fang, 2001; Quirico et al., 2005; Zhou et al., 2014; Figs. 5.4f and 5.5d). The values remain relatively consistent up to c. 3 %$VR_o$ and then begin to decrease. Hinrichs et al. (2014) calibration curve is significantly different compared to other published calibration curves, particularly at low VR values. This is attributed to the deconvolution method used. Negligible variation between maturity values of 0.5 to 3 %$VR_o$, makes the D-FWHM parameter unsuitable for determining the maturity of organic matter for the oil and gas industry.

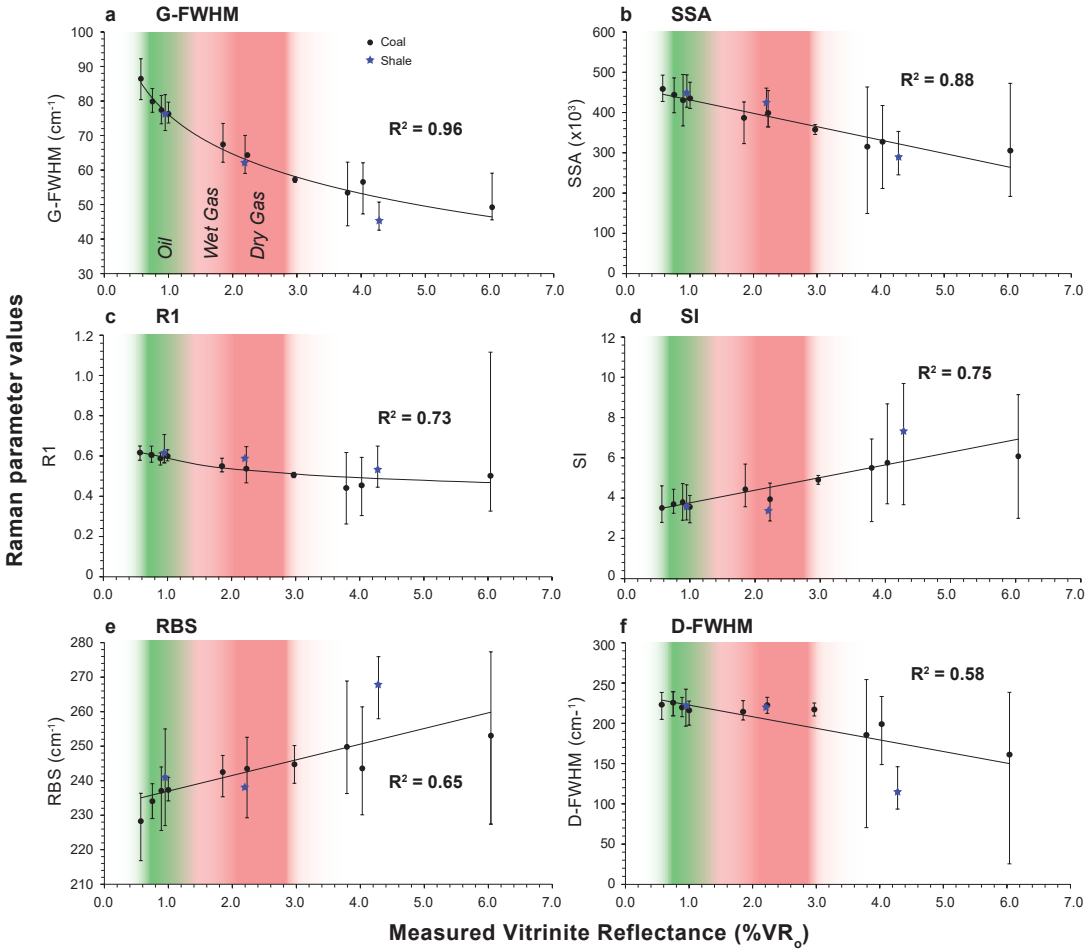


**Figure 5.4.** Vitrinite reflectance (VR) and Raman parameter calibration curves, constructed using the values acquired from the Inch of Ferryton-1 borehole, overlain by the oil, wet gas and dry gas zones

(after Dow, 1977) based on $VR_o$. The error bars are the calculated standard deviations for each sample. **(a)** G-FWHM, **(b)** SSA, **(c)** RBS, **(d)** SI, **(e)** R1, **(f)** D-FWHM. Numerical data are presented in Appendix E.

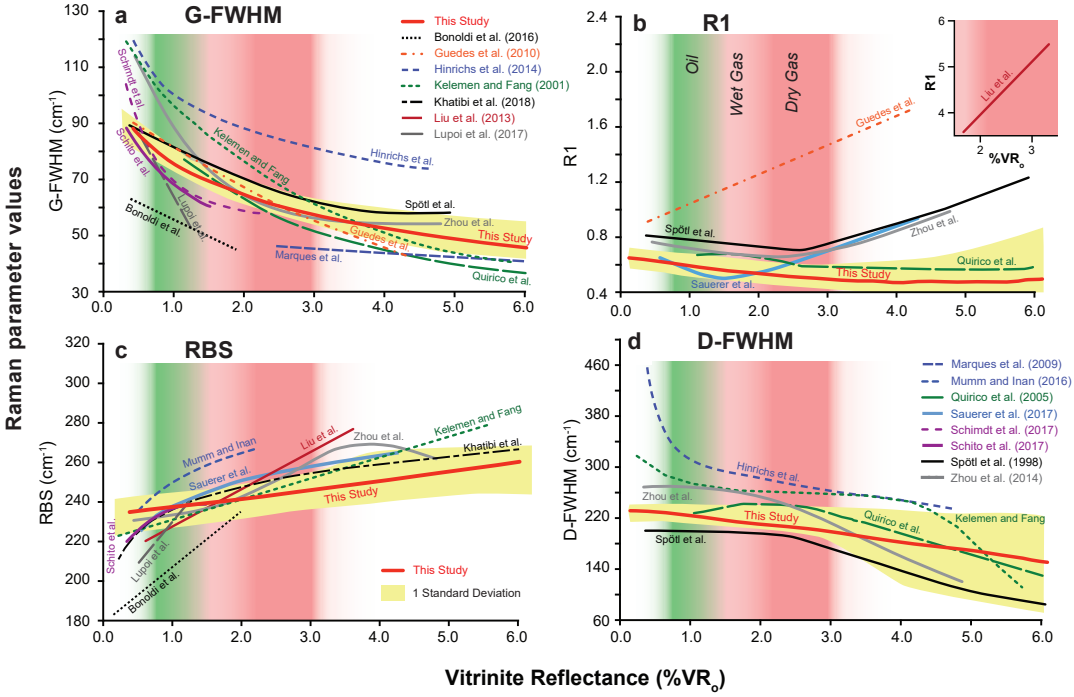


**Figure 5.5.** Superimposed key Raman parameter calibration curves from selected publications, compared to this study. **(a)** G-FWHM, **(b)** R1, **(c)** RBS, **(d)** D-FWHM.

### *5.4.2 Case study on Carboniferous samples in the UK*

A blind test was conducted to estimate the equivalent VR for 78 Carboniferous samples using the G-FWHM, SSA, SI, RBS and R1 calibration curve equations (Table 5.3) derived from the Inch of Ferryton-1 borehole study. The results are then compared to measured VR values.

**Table 5-3.** G-FWHM, SSA, RBS and SI vs. VR calibration curve equations for the maturity range 0.5 to 6 $\%VR_o$.

| Parameters | $R^2$ | Equation |
|---|---|---|

| | | |
|---|---|---|
| G-FWHM | 0.96 | $\%_{eq}VR = 85.7830385291 * EXP^{(-0.058254813 * G\text{-}FWHM)}$ |
| SSA | 0.88 | $\%_{eq}VR = -0.0000264097 * SSA + 12.6257416613$ |
| SI | 0.75 | $\%_{eq}VR = 1.1765899192 * SI - 2.9499539579$ |
| R1 | 0.73 | $\%_{eq}VR = 1945.4938205866 * EXP^{-11.6106553161 * R1)}$ |
| RBS | 0.62 | $\%_{eq}VR = 0.1359255714 * RBS - 30.6210791875$ |

#### *5.4.2.1 Midland Valley Sites*

The Milton of Balgonie-1 results shows a close correlation between $\%VR_o$ and $\%_{eq}VR$ for most Raman parameters (Fig. 5.6a). Notable, both $VR_o$ and Raman parameters have sharp decrease in the VR values in close proximity (above and below) to the quartz dolerite sill (Midland Valley Sill). This has been observed near the contact of igneous intrusions by several authors (Raymond and Murchison, 1988; Bishop and Abbott, 1995; Yao et al., 2011; Wang and Liu, 2015). Bishop and Abbott (1995) showed that the decrease starts at about 10% distance of the thickness of the dyke; in this study, the decrease in VR starts at about 10% above and 15% below the intrusion. This difference is due to more compaction above the sill, compared to below the sill. Khorasani et al. (1990) proposed two reasons for this sharp decrease in VR close to intrusions: (1) difficulty in polishing high maturity vitrinite particles; and (2) differences in molecular disordering that occurs at high heating rates near the sill. Our study suggests that polishing is not the reason for this phenomenon, as the laser Raman analysed unpolished rock chips. It is concluded that the apparent decrease in maturity near the intrusion is a result of natural thermochemical reactions that occur at a distance of <15% thickness of the intruded dolerite sill.

The Raman spectra of the samples taken close to the Midland Valley Sill in the Milton of Balgonie-1 well are significantly different from the Raman spectra at a greater distance from the sill (Fig. 5.6aiii). Similar spectra have been reported by Rantitsch et al. (2014) and Morga et al. (2015) from coke samples. with R1 ratios > 1.00. The coke spectra are similar to spectrum 3 in Figure 5.6aiii (sample SSK 80259), which is

substantially different compared to the R1 ratio measured in coals (<0.80). This is also observed in the inch of Ferryton-1 well and is accompanied by a sharp decrease in VR values in very close proximity of the sill.

The G-FWHM, SSA, SI and RBS $\%_{eq}$VR results have a strong correlation with VR data, whereas the R1 parameter has $\%_{eq}$VR that are shifted to higher values. However, anomalous Raman and VR results below the sill at depths >1200 m (circled in Figure 5.6a) are present and could be due to the complex stratigraphy that includes multiple extruded lava flows and thin quartz dolerite sills in the lower section (Raymond, 1991), although the possibility of unrecognised cavings cannot be excluded.

The $\%VR_o$ and $\%_{eq}$VR values follow a similar trend for the Calais-3 borehole (Fig. 5.6b). The G-FWHM, SSA, SI and RBS parameters yield $\%_{eq}$VR values that are closest to $VR_o$, whereas the R1$\%_{eq}$VR data are again shifted to higher values. The strange concave VR maturity trend for Calais-3 (Fig. 5.6b) is most likely the result of a previously overlying sill that has been eroded, combined with the basal dolerite sill below 190 m. The Raman parameters also show an increase in maturity values between 57 and 82 m, which suggests that there may be another igneous intrusion nearby (Fig. 5.6biii), that has not been picked out by the VR results. Although an igneous intrusion has not been identified previously at that level, the well report indicates evidence of baking at c.95m (Aitkenhead, 1977), implying that an igneous body may be present.

#### *5.4.2.2 Southern Pennine Basin sites*

One sample was analysed for the Duffield-1 well, from a depth of c.1100 m (Fig. 5.6c). The G-FWHM, SSA, RBS and SI1 $\%_{eq}$VR values are in good agreement with $\%VR_o$; R1 values are again too high. The sharp increase in $\%VR_o$ is attributed to a sill near the base of the well (Andrews, 2013).

The VR data for Gainsborough-2 fluctuates between 0.4 – 0.7 $\%VR_o$ down to 1800 m and then there is an increase to 1.1 $\%VR_o$ just below the sill at the base of the well (1900 m) (Andrews, 2013). An increase in the G-FWHM, SSA, RBS and SI1 $\%_{eq}$VR is also evident (Fig. 5.6d). The G-FWHM data have the best correlation with $\%VR_o$. The G-FWHM $\%_{eq}$VR and $\%VR_o$ results are very similar for the Rufford-1 well, whereas, the

SSA, RBS, SI and R1 $\%_{eq}$VR data show substantial more discrepancies (Fig. 5.6e). At 1300 m in Gainsborough-2 there is a negative value for the SI parameter, which occurs when the background fluorescence curvature is underestimated. This leads to a higher saddle height and a lower SI ratio number, which can result in a lower than expected maturity or a negative value. This issue could be addressed with further spectrum processing, but this negates the objective of having an automated approach. It is advised to reject these spurious data points, as is common practice when reviewing vitrinite reflectance and Rock-Eval pyrolysis data sets.

There is substantial scatter in $\%VR_o$ for the Gun Hill-1 well above 700 m depth, which is replicated by the G-FWHM, SSA, SI and RBS $\%_{eq}$VR profiles, (Fig. 5.6f). The RBS substantially overestimates the maturity of the samples but follows the same trend as the other parameters (Fig. 5.6f). The SSA fails to generate acceptable $\%_{eq}$VR values, as some of the results are negative. The reason for this is that the background correction has underestimated the curvature of the background fluorescence, and therefore increased the total area under the curve to the baseline, resulting in very low or negative maturity results. G-FWHM $\%_{eq}$VR has the best correlation with measured VR values. The results for the Kirk Smeaton-1 well show a smooth $\%VR_o$ profile that increases with depth (Fig. 5.6g). The G-FWHM, SSA, RBS and SI1 $\%_{eq}$VR profile follow the same trend but with higher VR values and greater variance. The G-FWHM $\%_{eq}$VR values are closest to the $\%VR_o$ data and the R1 and RBS parameters overestimate the VR values.

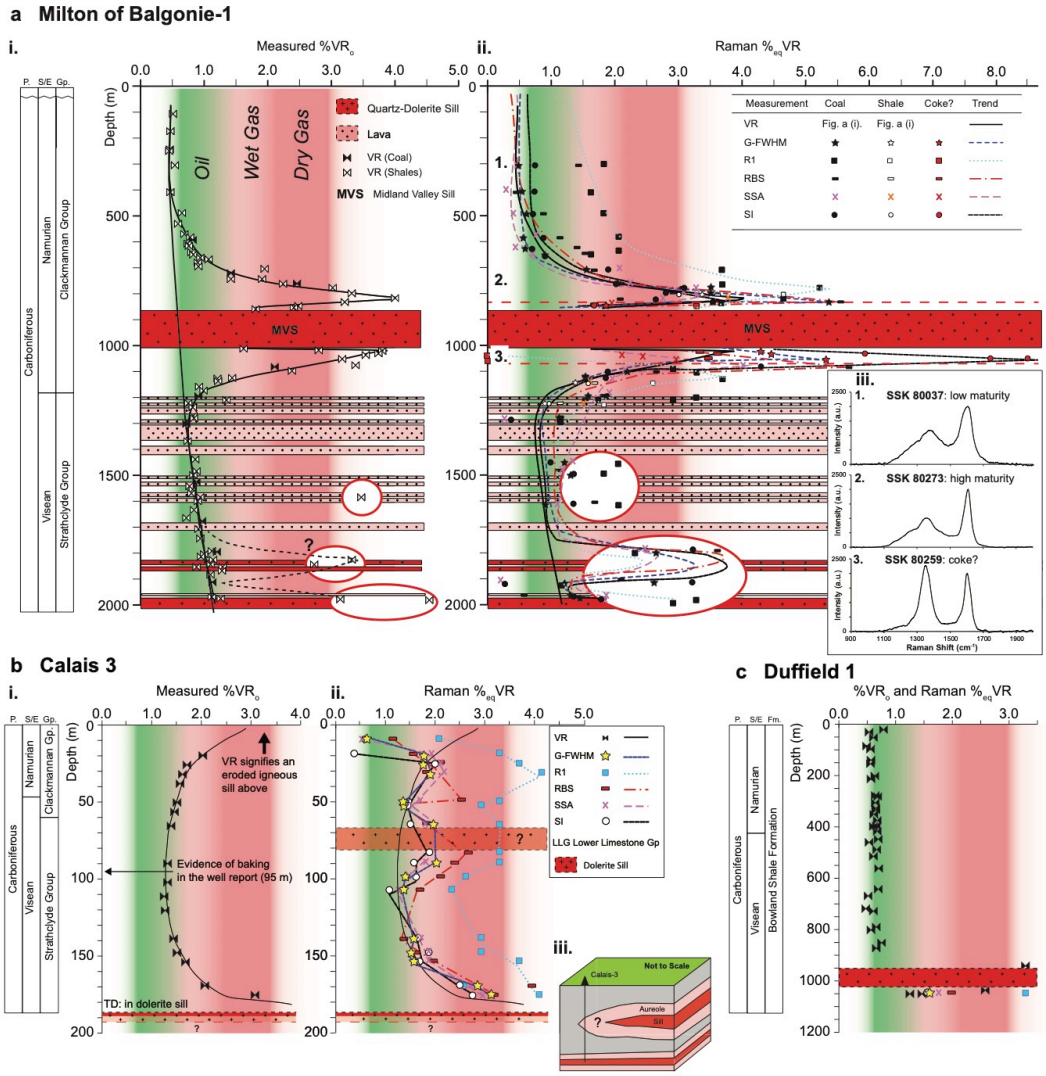


**Figure 5.6.** Core depth plots vs. maturity measurements for the several wells estimated using the G-FWHM, SSA and RBS calibration curve equations in Table 3. Midland Valley: **(a)** Milton of Balgonie-1. **(b)** Calais-3. Southern Pennine Basin: **(c)** Kirk Smeaton-1. **(d)** Gainsborough-2. **(e)** Gun Hill-1. **(f)** Rufford-1. **(g)** Duffield-1. Numerical data are presented in Appendix E. LLG: Lower Limestone Group. MG: Millstone Grit Group. MMG: Mercia Mudstone Group. SSG: Sherwood Sandstone Group. BS: Bowland Shale Formation. CL: Carboniferous Limestone. L1: Green Vesicular Lava. L2: Green tuffaceous pillow lava. L3: Green tuffacesous lava.

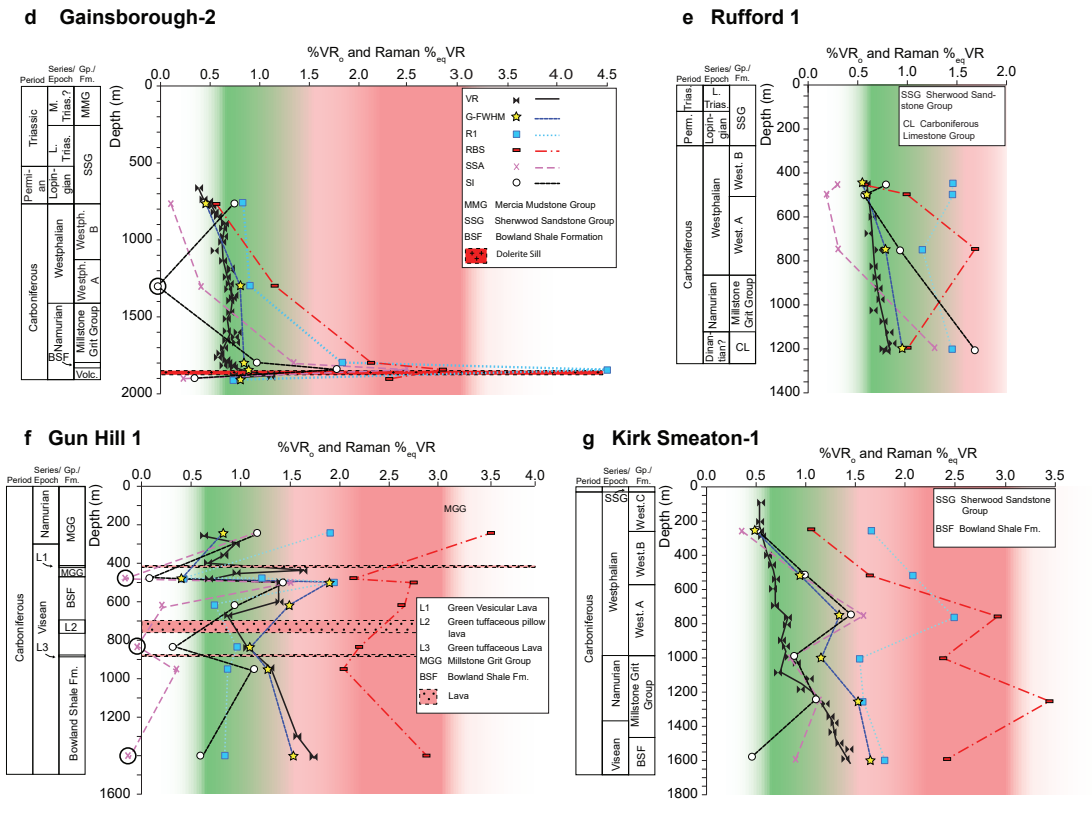


**Figure 5.6 continued…**

Figure 5.7 is a summary of %VR$_o$ vs. %$_{eq}$VR for the G-FWHM, SSA, SI, R1 and RBS parameters for all the samples analysed. Overall, G-FWHM has the tightest correlation with %VR$_o$ with an $R^2$ of 0.84 and can successfully generate %$_{eq}$VR values that are similar to measured %VR$_o$ values, as the trend line lies almost on top of the 1:1 line (Fig 5.7a). The SSA and SI %$_{eq}$VR parameters correlate well with %VR$_o$, yielding $R^2$ values of 0.75 and 0.71, respectively (Fig. 5.7b-c), but have greater scatter than the G-FWHM Raman parameter. The R1 and RBS calibration curves have the greatest scatter for maturities in the oil and gas maturity ranges (0.6–3.5 %VR) and they both overestimate %$_{eq}$VR for maturities < 3.0 %VR$_o$.

The G-FWHM parameter has the greatest potential to be used as a universal maturity proxy, however there is large scatter for higher maturities (Fig. 5.7a). This is because the calibration curve is non-linear and flattens out for higher maturities, therefore small changes in the G-FWHM for higher maturity samples give large differences in

$\%_{eq}VR$ (Fig. 5.4a). This is not the case for maturities <3.5%$VR_o$ as the calibration curve is steep and linear. The other calibration curves may be used to confirm the results, but they should not be used independently, as there is significant scatter. The Pennine Basin and Midland Valley of Scotland samples also follow a similar maturity path for the G-FWHM Raman parameter (Fig. 5.7a), however the Pennine Basin data have greater scatter than the Midland Valley of Scotland results for the rest of the Raman parameters (Fig. 5.7b-e). This is likely caused by more intense and variable background fluorescence in the Pennine Basin samples compared to those from the Midland Valley of Scotland, which tends to have a greater impact on the SSA, SI, R1 and RBS Raman parameters.

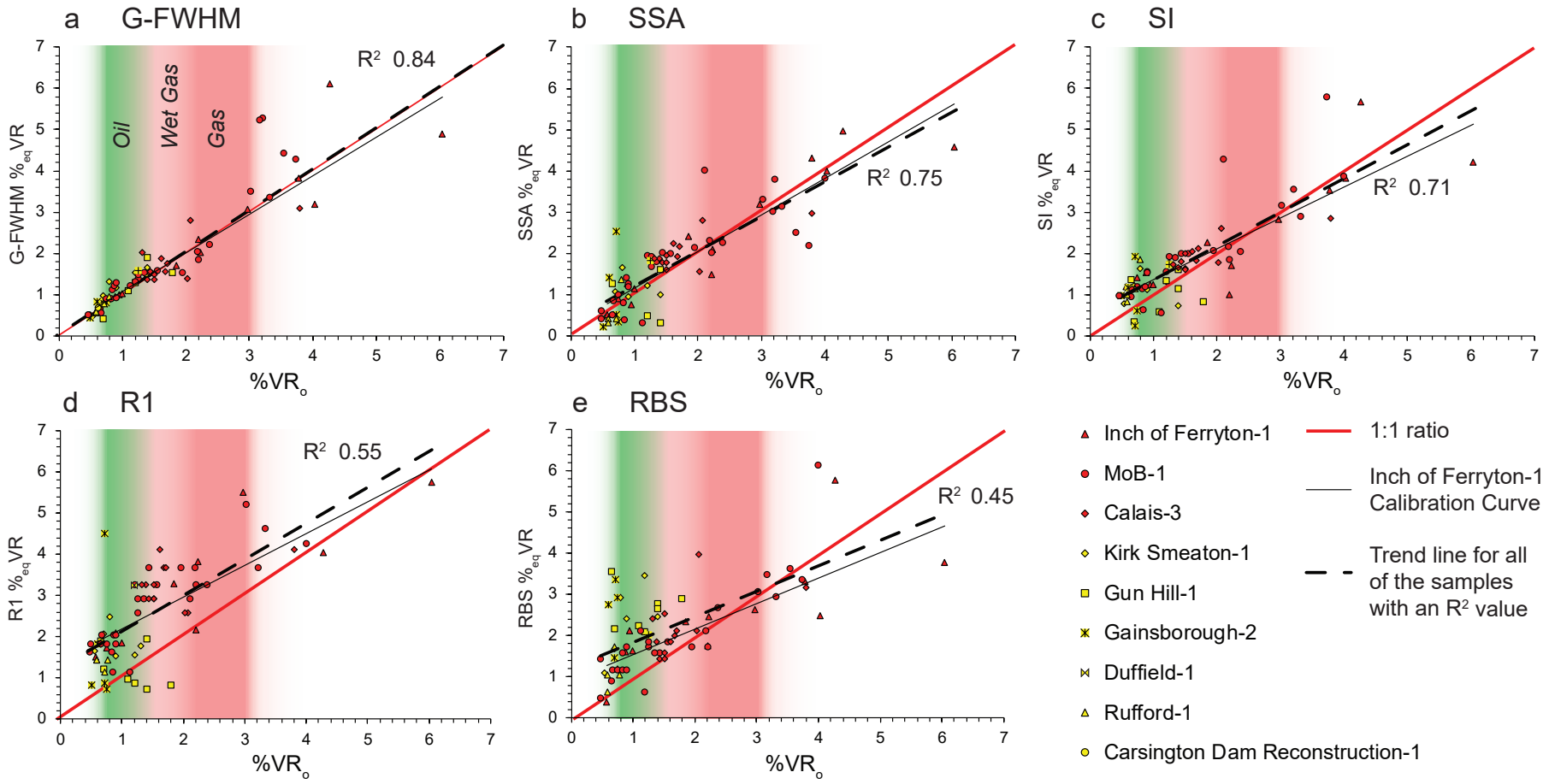


**Figure 5.7.** Comparison of the $\%_{eq}VR$ and $\%VR_o$ for 78 Carboniferous rock samples from the UK. **(a)** G-FHWM. **(b)** SSA. **(c)** SI. **(d)** R1. **(e)** RBS. Red data points: Midland Valley of Scotland. Yellow data points: Pennine Basin

## 5.5 Conclusion

Raman parameter calibration curves constructed using samples from the Inch of Ferryton-1 borehole have been successfully tested on Carboniferous organic-rich sediments from the Midland Valley of Scotland and the southern Pennine Basin, central England. The Raman parameter with the strongest correlation with measured vitrinite reflectance (%$VR_o$) is the G-FWHM, which can successfully generate similar VR equivalent values in the oil and gas windows (0–3.0%$VR_o$). Due to the non-linear nature of the G-FWHM calibration curve, unreliable results may be derived for samples that have a maturity >3.5% $VR_o$.

Maturity measurements can be acquired rapidly on well cuttings, with the potential to be performed on-site using a portable Raman instrument early in an oil and/or gas fields life cycle. The SSA, RBS, R1, D-FWHM and SI Raman parameters may be used alongside the G-FWHM parameter to better constrain the maturity of OM, but they should not be used independently due to large scatter in the results.

The G-FWHM calibration curve has the potential to be used universally, but further work must be performed to refine the calibration curve and test it in a wider range of sedimentary basins around the world. Testing the method in areas of known VR suppression and/or retardation caused by the presence of Type II hydrogen-rich macerals, lithological variation, and overpressurized basins would also be instructive; as well as testing laser Raman in scenarios where VR cannot be measured, such as pre-Devonian and deep marine shales where vitrinite particles are absent or rare.

# *Chapter 6* Raman spectroscopy, vitrinite reflectance, Rock-Eval pyrolysis and illite crystallinity maturity indices: a critical comparison for Carboniferous shale gas exploration in the UK

This Chapter is from: *Henry, D.G., Jarvis, I., Gillmore, G., Stephenson, M., Vane, C.H., Huggett, J., Wray, D., in revision. Raman spectroscopy, vitrinite reflectance, Rock-Eval pyrolysis and illite crystallinity maturity indices: a critical comparison for Carboniferous shale gas exploration. Submitted to J. Mar. Petrol. Geol. Short comm. Paper.*

So far, the results from Raman spectroscopy have been taken from a bench-top Raman spectrometer and compared with vitrinite reflectance (VR). Here, the bench-top Raman and VR results will be compared with Rock-Eval pyrolysis, illite crystallinity and a portable Raman instrument.

## 6.1 Abstract

Five thermal maturity methods are compared for a suite of Carboniferous shales and coals from formations in the UK that are prospective shale gas targets: Raman spectroscopy; vitrinite reflectance (VR); $T_{max}$ and production index (PI) from Rock-Eval pyrolysis; and illite crystallinity (IC). The comparison demonstrates that: (1) Raman spectroscopy is a powerful alternative method to estimate equivalent VR values from shales and coals. (2) A portable Raman instrument has the potential to be used on-site or in the field to determine the maturity of coals. (3) Comparing organic matter maturity proxies with IC can help to qualitatively determine changes in thermal gradients, as clay minerals take longer time to equilibrate to the surrounding temperatures than organic matter. (4) VR and $T_{max}$ values have a strong relationship, which may be used to estimate equivalent VR values and calibrate basin models; these have been used previously to estimate the volume of shale gas resources in the Pennine Basin of central England. Anomalously low $T_{max}$ values (<400 °C) for samples with maturity values >1.5 %VR, indicate that these had free heavy hydrocarbons present, which

had not been expelled prior to pyrolysis. This highlights the need to perform solvent extraction on high maturity samples in the Carboniferous successions of the UK. This is particularly important for shale gas exploration, as the sweet spots typically occur at maturity values >1.4 %VR.

## 6.2 Introduction

Thermal maturity measurements made on source rocks are essential to calibrate basin models that help reconstruct the thermal and subsidence history of a basin (Tissot et al., 1987). These models allow petroleum geologists to determine the timing, quantities, type and location of hydrocarbon generation and expulsion, as well as quantifying missing sedimentary stratigraphy, and constrain poroperm-critical diagenetic reactions such as quartz and carbonate cementation and illitization (Susanne et al., 2008; Allen and Allen, 2013; Andrews, 2013).

Using a combination of thermal maturity techniques is standard practice in oil and gas exploration, as it decreases risk by cross-checking results, as no single maturity method is universally reliable (Whelan and Thompson-Rizer, 1993; Wilkins, 1999). Having a selection of methods to determine the thermal maturity of rocks allows geoscientists to optimize their analysis based on the quantity, composition and age of the sample, maturity grade, operator expertise, equipment availability, and time and money constraints. There are often discrepancies in the thermal maturity results obtained when using several methods, which are due to technical, methodological and theoretical problems inherent for each technique (Espitalie et al., 1977; Merriman and Kemp, 1996; Wilkins, 1999; Hartkopf-Fröder et al., 2015). Such discrepancies may help to determine important changes in thermal regimes and organic matter (OM) composition. For instance, comparing illite crystallinity with maturities derived from OM can help to qualitatively predict changes in thermal gradient (Merriman and Kemp, 1996). The suppression and retardation phenomenon that impacts vitrinite reflectance (VR) (Carr, 2000) can be understood by comparing VR with the spore colouration index and/or the fluorescence alteration of multiple macerals (Wilkins, 1999), as well as Raman spectroscopy (Wilkins et al., 2015; Schito et al., 2019).

To our knowledge, no other study has directly compared different thermal maturity indicators for Carboniferous rocks in the UK; it is therefore not known whether discrepancies exist. Here, we compare VR with Rock-Eval pyrolysis and illite crystallinity maturity indices, as well as Raman spectroscopy (bench–top and portable instruments), which has been advocated as a new maturity assessment tool (e.g. Henry et al., 2018, 2019). We identify discrepancies that occur and build a calibrated maturity chart that can be used for thermal maturity studies of Carboniferous rocks in the UK.

## 6.3 Materials and methods

### *6.3.1 Materials and geological setting*

Washed and registered Carboniferous cuttings from seven wells were collected from the British Geological Survey (Fig. 6.1; Appendix E) that were divided into three sub-sets for: (1) VR and Raman analysis; (2) Rock-Eval pyrolysis; (3) illite crystallinity, where there was sufficient material available (Appendix E; Fig. 3.1). VR was performed on selected samples to cross-check the reported VR values of samples that have been used in this study (Appendix E; Raymond, 1991; Green et al., 2001; Smith et al., 2011; Andrews et al., 2013). A more detailed description of the wells has been provided by Henry et al. (2019).

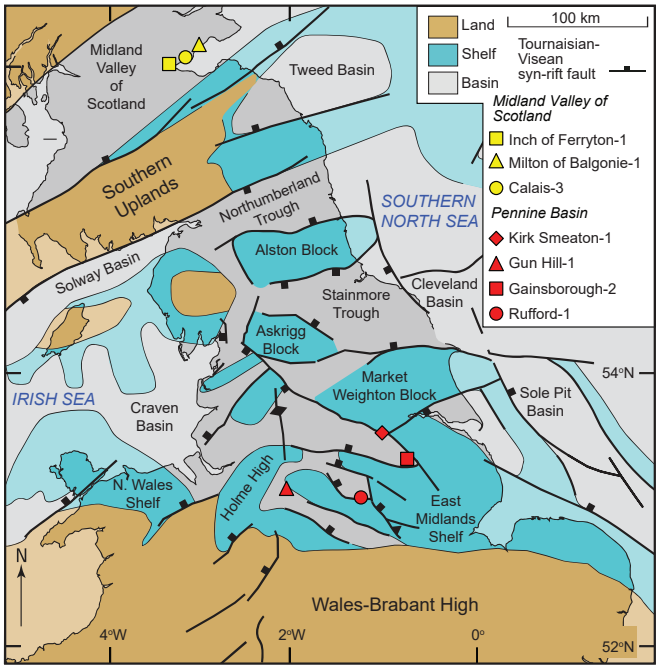

**Figure 6.1.** Geological framework of the Carboniferous and the location of the wells used in this study. Base map from Waters et al. (2009). The Pennine Basin, a complex fault-controlled mosaic of shelves and sub-basins, extends between the Southern Uplands and the Wales-Brabant High.

Back-arc extension north of the Variscan orogenic front during the Late Devonian and Early Mississippian led to the development of both the Midland Valley of Scotland and Pennine Basin (Fig. 3.1). This resulted in the formation of a complex mosaic of NE–SW graben and half-graben structures (Waters et al., 2009, 2019). Deposition of Carboniferous organic-rich mudstones and coals in these structures have had significant economic and social benefits, as they have provided much of the hydrocarbons for conventional oil and gas fields in central England (Andres, 2013), as well as historically providing oil shale in the Midland Valley of Scotland (Monaghan, 2014). Both the Midland Valley and Pennine Basin experienced magmatism during the Late Carboniferous, accompanied by igneous intrusions into Lower Carboniferous strata, which have locally elevated the thermal maturity of shales and coals (Raymond, 1991; Monaghan, 2014).

## *6.3.2 Methods*

### *6.3.2.1 Raman spectroscopy*

Bench-top Raman results (Appendix A; Henry et al., 2019) were obtained using a Renishaw inVia™ Raman instrument with a 514.5 nm laser and c. 2 µm spot diameter. A portable B&WTek i-Raman Plus instrument was tested on 14 selected samples (Appendix E) with a 532 nm laser with a spot diameter of c.100 µm; an attached video microscope projected a live video stream to a laptop computer. Raman spectra were processed following the methodology of Henry et al. (2018). Only the Raman parameter G-band full-width at half-maximum (G-FWHM) data are reported, as this is considered to be the most reliable for estimating equivalent VR values for oil and gas exploration (Henry et al., 2019). The different laser wavelengths used is not expected to alter the G-FWHM (Kouketsu et al., 2014).

### *6.3.2.2 Rock-Eval pyrolysis*

A Rock-Eval 6 instrument (Vinci Technologies) at the British Geological Survey was used for Rock-Eval pyrolysis of 83 samples (Appendix E). The samples were grounded and

homogenized using an agate pestle and mortar and no further processing was executed. The samples were heated in a nitrogen atmosphere between 300 – 650 °C at 25 °C/minute, followed by oxidising the residual carbon at 300 – 650 °C at 20 °C/minute. The hydrocarbons released during pyrolysis and oxidation were measured using a flame ionisation detector (FID) and the CO and $CO_2$ were measured using an infrared cell. The $T_{max}$ (temperature at which the maximum quantities of hydrocarbons were generated from kerogen) and the production index (PI = S1/[S1+S2]) maturity parameters are presented in this study (see Peters and Rodriguez (2017) for further explanation). Total organic carbon, hydrogen index and oxygen index values are reported in Appendix E.

#### *6.3.2.3 Illite crystallinity*

Illite crystallinity (IC) determinations were performed on 24 samples (Appendix E). Sample preparation was undertaken at Petroclays (Heathfield, UK) with x-ray diffraction (XRD) analysis at the University of Greenwich. Rock samples were gently crushed and mixed with distilled water, followed by an ultrasonic bath for 20 minutes to release the clays into suspension. The suspension is decanted and centrifuged at 1000 rpm for four minutes. The remaining suspension is again decanted and centrifuged at 4000 rpm for 20 minutes, depositing the < 2 µm clay fraction. The resulting slurry was spread over an unglazed ceramic tile and air dried, and analysed using a Bruker D8 Advance fitted with a LYNEYE detector and Ni-filtered CuK$\alpha$ radiation. Samples were scanned sequentially after air drying, after treating with glycol, after heating for four hours at 400 °C, and again after heating at 550°C for an additional four hours. The FWHM of the illite 10/Å peak was measured at each stage. The raw data were processed following the method developed by Warr and Rice (1994) to derive IC values.

## 6.4 Results and discussion

Raman spectroscopy can be used to track the thermal maturity of OM in sedimentary rocks. The G-FWHM has a strong relationship with $\%VR_o$, as demonstrated by Henry et al. (2019) who used a bench-top instrument to analyse a suite of Carboniferous rocks from the UK (calibration curve in Fig. 6.2). We show here, using a sample subset, that a portable Raman system can also track the thermal maturity of coals using the G-FWHM and has a good

relationship with VR (Fig. 6.2, Appendix E). However, the two shale samples that were tested have higher G-FWHM values than coals for the portable Raman instrument. This is due to an underestimation of the baseline subtraction, which has led to a lower placement of the FWHM for the G-band. The underestimation is a result of intense background fluorescence caused by the inclusion of both OM and the surrounding mineral matrix, a result of the c.100 µm laser spot size deployed in the instrument. This makes baseline subtraction extremely difficult and can create significant bias, and in some cases may completely obscure the Raman OM signal. The smaller spot size (c. 2 µm diameter) of the bench-top Raman enables the analysis of isolated OM grains, thereby minimising matrix effects. Nevertheless, both data sets follow a similar trend, albeit with different values, which demonstrates considerable potential for the use of a portable Raman in the field or on-site on a drilling rig (although the impact on the performance of the spectrometer of the vibrations experienced on a drilling rig has not been investigated).

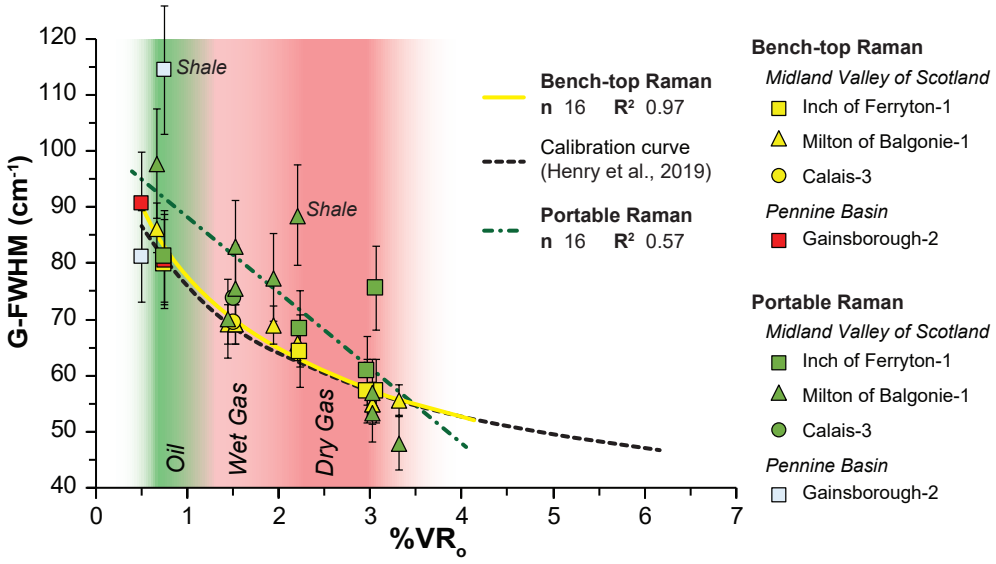


**Figure 6.2.** Bench-top Raman and portable Raman G-FWHM vs. $VR_o$ from selected UK Lower Carboniferous samples. The calibration curve of Henry et al. (2019) derived from a larger sample set using a bench-top instrument is shown for comparison.

Rock-Eval pyrolysis is an all-in-one method that can be used to quantify the quantity, quality and thermal maturity of sedimentary rocks. However, it is mostly used to screen large number of samples before more expensive and time-consuming analysis (Peters and Rodriguez, 2017).

Here, the $T_{max}$ and production index (PI) are used to assess thermal maturity. Jarvie et al. (2001) constructed a $T_{max}$ vs. $\%VR_o$ calibration curve for US Carboniferous Barnett Shale samples which was used by Andrews (2013) to calculate equivalent VR values in their UK Bowland shale gas study where measured VR data was missing. Results were used to estimate total in-place gas resources for the Bowland shales across northern England. Slowakiewicz et al. (2014) also used Jarvie et al.'s (2001) equation to estimate equivalent VR for Carboniferous rocks in the UK. Figure 6.3a shows that Jarvie et al.'s (2001) equation is within error of the $T_{max}$ vs. VR calibration curve obtained from low-maturity (<1.5 $\%VR_o$) samples in this study, confirming that the equivalent VR values calculated using $T_{max}$ by Andrews (2013) and Slowakiewicz et al. (2014) are reliable.

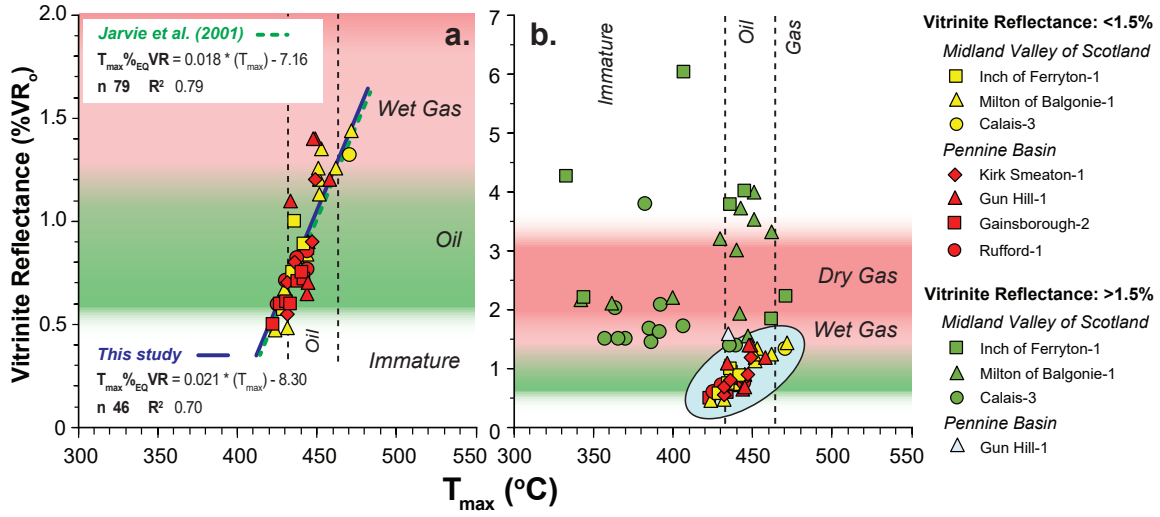


**Figure 6.3.** VR vs. $T_{max}$ values. **(a)** Calibration curve for low-maturity samples. **(b)** VR vs. Rock-Eval $T_{max}$ for all samples (lower-maturity subset circled). Note that samples with $VR_o$ values >1.5 %, have anomalously low $T_{max}$ values.

Samples with $VR_o$ values >c.1.5 % show considerable scatter and yield anomalously low $T_{max}$ values (between 350 – 450 °C) with respect to their VR values (Fig. 6.3b), attributable to the presence of free heavy hydrocarbons in the cuttings (cf. Clementz, 1979). In order to avoid this problem, washing samples with an organic solvent prior to pyrolysis is recommended, so that only hydrocarbons generated from the insoluble kerogen fraction are analysed (Clementz, 1979). This is particularly relevant to shale gas exploration, as shale gas sweet

3330 spots occur at VR values > 1.4% (Jarvie, 2012). The production index (PI) vs. $T_{max}$ plot confirms
3331 the presence of free heavy hydrocarbons (Fig. 6.4).

3332 The PI increases with increasing maturity and samples with $VR_o$ values >c.1.5 %, have
3333 anomalously low, high and scattered PI values, with respect to VR (Fig. 6.5c).

3334 The thermal evolution for the PI values with increasing VR and $T_{max}$ is different for the Midland
3335 Valley of Scotland and Pennine Basin (Figs. 6.4 and 6.5). There are also intra-basin differences
3336 for the Pennine Basin (Fig. 6.5b), as the PI values follow a similar trend with VR for Rufford-1
3337 and Gainsborough-2, whereas the Kirk Smeaton-1 and Gun Hill-1 wells have a steeper
3338 gradient (Fig. 6.4b). This is common when the depositional environments and kerogen types
3339 are significantly different (Peters and Cassa, 1994) and suggests that a separate VR and $T_{max}$
3340 vs. PI relationships must be established for individual wells.

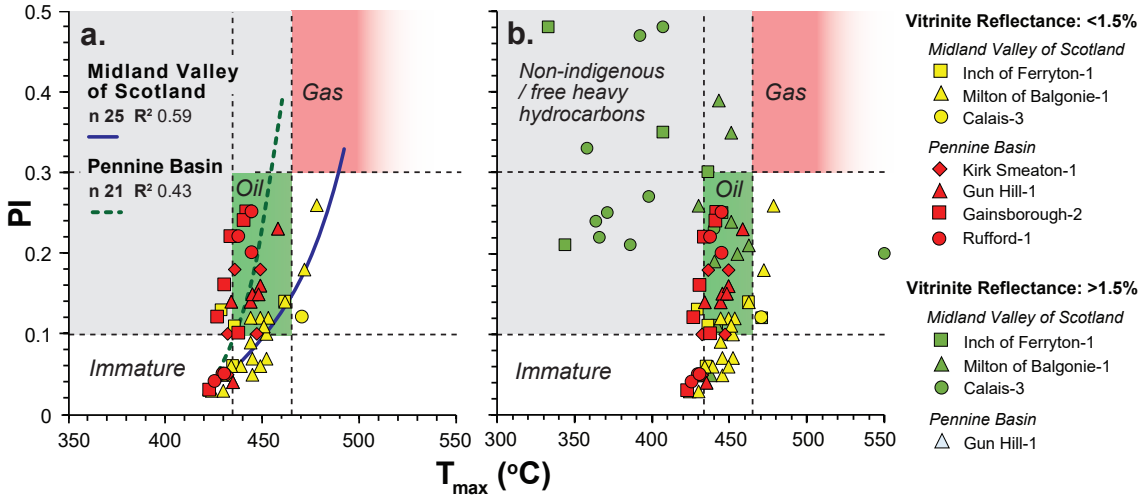


3341

3342 **Figure 6.4.** Production index (PI) vs. $T_{max}$. **(a)** Midland Valley of Scotland and Pennine Basin low-maturity samples
3343 show different tends. **(b)** PI vs $T_{max}$ for all the samples. Samples with $VR_o$ values > 1.5 % plot in the non-
3344 indigenous/free heavy hydrocarbon segment.

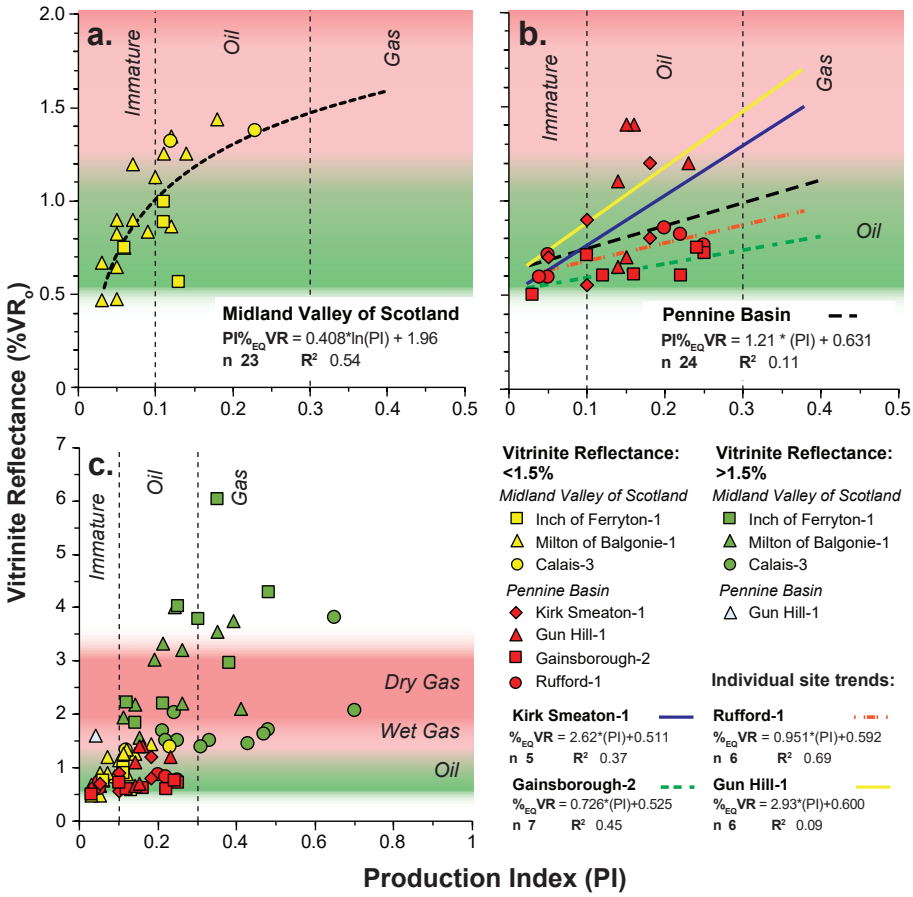


**Figure 6.5.** VR vs. production index (PI). **(a)** Low-maturity samples (<1.5 $\%VR_o$) from the Midland Valley. **(b)** Low-maturity samples for the Pennine Basin. Note that individual wells display different trends. **(c)** VR vs. PI for all samples; those with $VR_o$ >1.5 % have anomalous scattered PI values.

Illite crystallinity (IC) tracks the transformation of smectite to illite, as the interstitial $Na^+$ and $Ca^{2+}$ ions from smectite are replaced by $K^+$, and $Al^{3+}$ substitutes for $Si^{4+}$ which progressively converts the smectite to mixed layer/smectite to an authigenic illite (Ferreiro Mählmann et al., 2012). This transformation is mostly controlled by the maximum temperature. However, time, thermal gradient, the original clay-mineral assemblage, the chemical environment, fluids, pressure regime and deformation can all impact IC values (Ferreiro Mählmann et al., 2012 and references therein). IC is a valuable maturity method when OM is absent; however, it is also useful when compared to OM maturity, to qualitatively determining changes in thermal regimes (Merriman and Kemp, 1996). In addition to determining the hydrocarbon maturity and thermal gradients of a sedimentary basin, the degree of transformation of

smectite to illite, can be used to infer overpressure in shales caused by the release of water during the mineral transformation (Bruce, 1984).

Plotting IC vs. VR and G-FWHM can help to qualitatively compare changes in thermal gradients between different wells (Fig. 6.6). In the Pennine Basin, the IC values are relatively constant at 0.44 – 0.55 °Δ2θ, with a weak trend towards falling values (increasing crystallinity) with increasing VR and G-FWHM. For Milton of Balgonie-1 from the Midland Valley of Scotland, the IC vs. $VR_o$ and G-FWHM plots shift farther to the right with increasing VR, which is typical for short-lived increases in thermal gradients caused by contact metamorphism, as clays take a longer time to reach equilibrium with the surrounding temperature (Merriman and Kemp, 1996). The highest maturity samples (>3 $\%VR_o$), which originate from closest to the Midland Valley Sill, plot farthest to the right; with decreasing VR and increasing distance from the igneous intrusion, samples shift farther to the left. Samples farthest away from the intrusion with the lowest VR values (<1.2$\%VR_o$) plot along a similar trend to those from the Pennine Basin, suggesting that the OM in these samples was not impacted by the local increase in thermal gradient caused by the igneous intrusion (Fig. 6). It is unclear why there is substantial scatter in the IC results for Milton of Balgonie-1and why there is not a systematic shift in IC values, especially for the two high crystallinity values >0.7 °Δ2θ. However, the succession is very complex, with several smaller intrusive sills and extrusive lava horizons complicating the thermal regime and chemical environment (Henry et al 2019 fig. 6a). Other aspects that might relate to the poor IC correlation with VR and G-FWHM include changes in mineral assemblages associated with variable volcanic input, the availability of K, and fluid-rock interactions in the mixed sediment – lava sequence (Ferreiro Mählmann et al., 2012 and references therein).

Merriman and Kemp (1996) determined hydrocarbon generation zones based on IC values: oil window at c.1.0 °Δ2θ; wet gas at c.0.65 °Δ2θ; and dry gas at c.0.42 °Δ2θ (Fig. 6.6). If we only consider the samples that have not been affected by an igneous intrusion (Pennine basin and Milton of Balgonie-1 samples with VR <1.2 %), our study shows that in this case the hydrocarbon zones correspond to: oil window at c.0.6– 0.8 °Δ2θ; wet gas at c.0.35–0.45 °Δ2θ; and dry gas at c.0.15–0.25 °Δ2θ. If we include samples that have been affected by igneous intrusions, then we get significantly different results. This demonstrates that IC thresholds for

hydrocarbon generation zones cannot be universally applied and that IC must be calibrated with VR for individual wells.

Figure 6.7 shows a calibrated basin maturity chart for the Pennine Basin and the Midland Valley of Scotland the thermal maturity values derived from this study. Creating maturity charts for different basins is advised and can be used to compare and cross-check results derived from different maturity methods, as well as determining potential theoretical differences in the results that could be due to the nature of rock and the surrounding thermal environment, as well as technical and/or methodological differences.

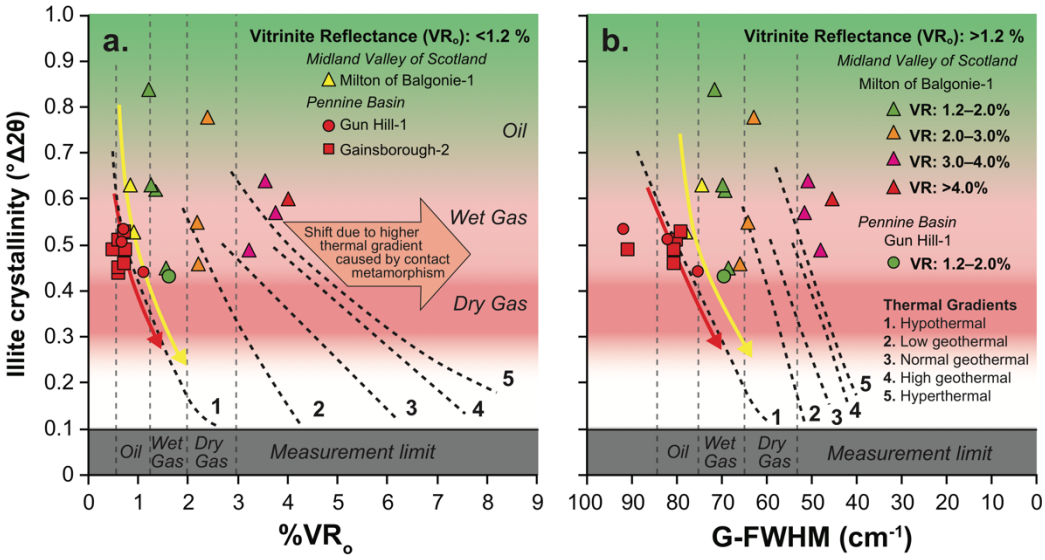


**Figure 6.6.** Illite crystallinity vs. **(a)** VR and **(b)** G-FWHM, superimposed on a thermal gradient plot modified from Ferreiro Mählmann et al. (2012). The illite crystallinity hydrocarbon zones are derived from Merriman and Kemp (1996). IC vs. VR and G-FWHM relationships are strongly dependent on local thermal gradients.

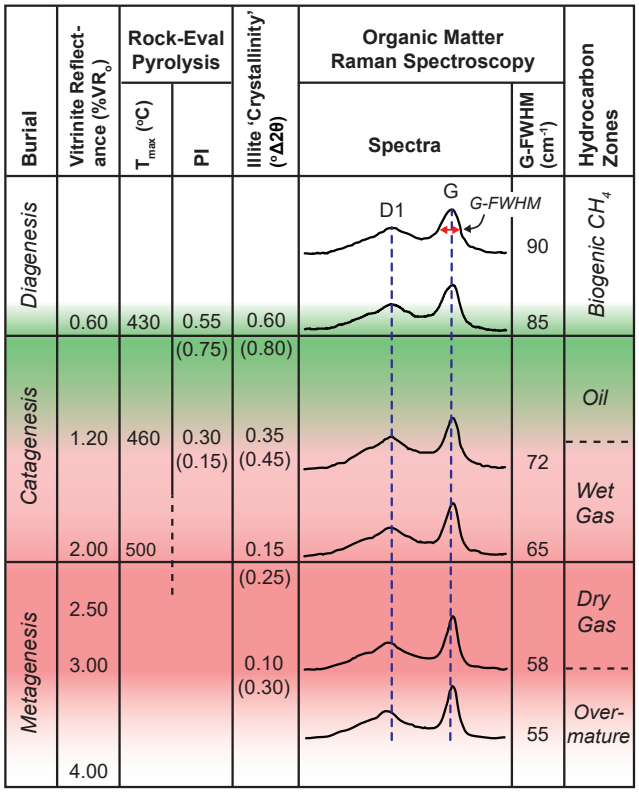


**Figure 6.7.** Thermal maturity chart for the Pennine Basin and Midland Valley of Scotland. Values in parentheses are for the Midland Valley where these differ from the Pennine Basin.

## 6.5 Conclusion

Standard thermal maturity relationships for different maturity techniques cannot always be applied universally, and if performed, should be interpreted with caution; an operator must understand how discrepancies in the results may occur. Nevertheless, we demonstrate that: (1) the Raman G-FWHM can be used as a maturity proxy in both the Pennine Basin and the Midland Valley of Scotland, using the same calibration curves. (2) a portable Raman can be used successfully on coals, but due to technical limitations (large laser spot width), shale samples should be avoided. (3) the $T_{max}$ vs. $VR_o$ calibration curve is within error of that presented by Jarvie et al. (2001), demonstrating an identical relationship in Carboniferous shales from the US and UK. (4) VR and PI plots show that different thermal maturity pathways exist in the Pennine Basin, which is also different to wells from the Midland Valley of Scotland.

(5) Illite crystallinity values should not be used to determine the onset of the oil and gas windows without first calibrating with VR or G-FWHM, as the relationships may be strongly affected by changes in the thermal gradient, which can give significantly different crystallinity values.

It is concluded that several thermal maturity techniques should be routinely employed to reduce risk when estimating the thermal maturity of OM in petroleum basins. Different methods should be cross-referenced to VR in order to create calibrated basin maturity charts for prospective basins. Not only will this reduce the risk by cross-checking the results, but discrepancies in the data can be used to gain a better understanding of the thermal regime, as well as identifying poor technical and/or methodological practices.

# *Chapter 7* Characterising candidate shale geological reference materials from the United States Geological Survey (USGS)

## 7.1 Abstract

Six candidate shale geological reference materials from the United States Geological Survey (USGS) have been characterised using Henry et al.'s (2018) Raman spectroscopy method. The calibration curves of Henry et al. (2019) have been applied successfully to rock-chip samples. Strew slides display different responses, as isolating the organic matter using HCl and HF alters the Raman spectrum, including values for the G-band full-width at half-maximum (G-FWHM), scaled spectrum area (SSA; area under the curve from 1100 – 1700 $cm^{-1}$), Raman band separation (RBS; G-band position minus the D-band position) and the R1 (height ratio of the D-band/G-band) parameters. These differences are attributed to the removal/reduction of non-organic components in the rock, which significantly reduces the background fluorescence. This reduction or removal of the fluorescence in the strew slides leads to less scatter in the G-FWHM, SSA, RBS and R1 results. The strew slide samples show a stronger correlation with measured vitrinite reflectance ($VR_o$) values compared to the equivalent rock-chip material. Our Raman results follow the same trends as those of Jubb et al. (2018) for these materials, albeit with significantly different values, attributable to the different sample preparation and data processing methods used.

## 7.2 Introduction

The United States Geological Survey (USGS) are developing geological reference samples relevant to source rocks for unconventional petroleum systems. A subset of six reference samples was acquired along with a complete geochemical data set, including major- and trace-element concentrations, mineralogy from X-ray diffraction (XRD), vitrinite reflectance (VR), Rock-Eval pyrolysis and Raman spectroscopy (Birdwell and Wilson, 2017; Jubb et al., 2018). The aim of the USGS reference material project is to allow petroleum geologists and

geochemists to use these samples for quality control and as assurance standards for mineralogical, organic and inorganic geochemical studies and thermal maturity analysis (Birdwell and Wilson, 2017; Jubb et al., 2018).

Raman analysis of four USGS shale reference materials (Table 7.1) has previously been conducted by Jubb et al. (2018); however, their methodological approach was different to that performed here. Jubb et al. (2018) analysed polished surfaces of resin-embedded rock chips and performed deconvolution of the Raman spectra with four Lorentzian bands (G, D1, D2, D4 functions). We have studied unprepared rock chips and strew slide preparations, with Raman analysis following the method of Henry et al. (2018), which does not involve deconvolution. Here, we compare the Raman results obtained using Henry et al.'s (2018) and Jubb et al.'s (2018) methods. The study offers an opportunity to test Henry et al.'s (2019) calibration curves, developed using a suite of Carboniferous organic-rich mudstone and coal rock chips from the UK, on samples of different ages and from different basins. We will also compare results from strew slides vs. rock-chip samples to see whether isolating the organic matter using HCl and HF impacts the Raman spectra and parameters.

## 7.3 Material and methods

### *7.3.1 Material*

Six shale rock reference materials from Devonian to Eocene age shale gas plays were collected at outcrop by the United States Geological Survey (USGS) (Fig. 7.1; Table 7.1). Sample data available include previously determined vitrinite reflectance (VR), Rock-Eval™ pyrolysis and/or Raman results (Jubb et al., 2018; Appendix E), which will be compared with the Raman results obtained here.

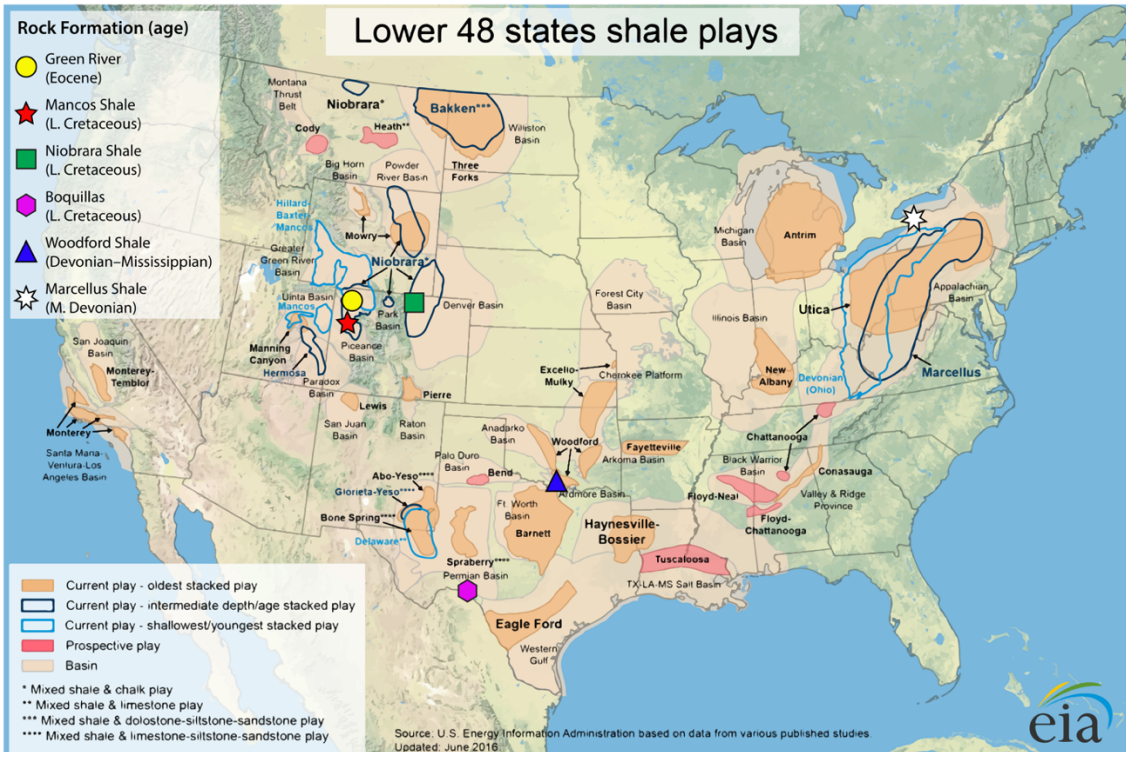


**Figure 7.1.** Location of the sampling areas superimposed on the main shale plays in the United States of America. From the Energy Information Administration (EIA): www.eia.gov/maps/images/shale_gas_lower48.pdf

Sample ShPYR-1 was collected at the Unocal Mine in Garfield County, Colorado and is representative of the Mahogany zone of the Eocene Green River Formation in the Piceance Basin (Fig. 7.1; Table 7.1 and 7.2). The ShMCO-1-1C was collected at US-50 in Delta County, Colorado and is representative of the Late Cretaceous Mancos Shale of the Piceance Basin. Sample ShNIO-ICP is representative of the Late Cretaceous Niobrara Shale in the Denver-Julesburg Basin and was sampled at the CEMEX quarry near Lyons in Boulder Country, Colorado. Sample ShBOQ-1C is representative of the Late Cretaceous (Cenomanian – Turonian) Boquillas Shale in the Gulf Coast Basin, stratigraphically equivalent to the Eagle Ford Shale of South Texas, and was collected from a road cut on US-90 west of Del Rio in Val Verde County, Texas. Sample ShWFD-1C is representative of the Devonian – Mississippian Woodford Shale in the Anadarko Basin and was collected at a road cut on I-35 near Ardmore and Springer in Carter County, Oklahoma. Finally, the ShMAR-1C samples is representative of the Devonian Marcellus Shale in the Appalachian Basin and was collected at the Oatka Creek outcrop in the village of Le Roy in Genesee County, New York.

It should be noted that vitrinite reflectance (VR) values for sample ShMCO-1-1C is absent and that Raman analysis was not performed on the strew slide sample for ShPYR-1.

**Table 7-1.** Outcrop samples from the USGS, along with their geological basins, age and rock units.

| Sample | Co-ordinates | Basin | Age | Rock Unit |
|---|---|---|---|---|
| ShPYR-1 | 39.657 N, 107.705 W | Piceance | Eocene | Green River |
| ShMCO-1-1C | 38.86 N, 107.86 W | Piceance | Late Cretaceous | Mancos |
| ShNIO-ICP [a] | 40.2230 N, 105.2315 W | Denver-Julesburg | Late Cretaceous | Niobrara |
| ShBOQ-1C [a] | 29.7028 N, 101.2111 W | Gulf Coast | Late Cretaceous | Boquillas |
| ShWFD-1C [a] | 34.3520 N, 97.1489 W | Anadarko | Devonian – Mississippian | Woodford |
| ShMAR-1C [a] | 42.9787 N, 77.9884 W | Appalachian | Middle Devonian | Marcellus |

[a] Raman analysis has been performed by Jubb et al. (2018). The accompanying data set for the samples is presented in Appendix E.

**Table 7-2.** Vitrinite reflectance, Raman and Rock-Eval $T_{max}$ (°C) results for the Geological reference samples from the USGS.

| Sample (SSK) | VR [a] (%$VR_o$) | Raman [b] G-FWHM | 1σ | SSA ($x10^3$) | 1σ ($x10^3$) | R1 | 1σ | RBS | 1σ | $T_{max}$ (°C) [a] |
|---|---|---|---|---|---|---|---|---|---|---|
| **Rock chips** [c] | | | | | | | | | | |
| ShBOQ-1C | 0.54 | 85.26 | 2.33 | 479 | 83 | 0.63 | 0.03 | 225 | 22 | 422 |
| ShWFD-1C | 0.4 | 101.2 | 7.45 | 508 | 51 | 0.72 | 0.07 | 201 | 6 | 427 |
| ShMAR-1C | 0.73 | 82.83 | 3.87 | 514 | 32 | 0.68 | 0.04 | 222 | 23 | 436 |
| ShNIO-ICP | 0.99 | 75.88 | 6.65 | 530 | 51 | 0.70 | 0.07 | 239 | 24 | 455 |
| ShPYR-1 | 0.83 | 89.62 | 11.51 | 504 | 73 | 0.65 | 0.07 | 256 | 22 | na |
| ShMCO-1-1C | na | 82.58 | 7.70 | 489 | 43 | 0.67 | 0.06 | 233 | 16 | na |

| | | | | | | | | | | |
|---|---|---|---|---|---|---|---|---|---|---|
| **Strew slides** [d] | | | | | | | | | | |
| ShBOQ-1C | 0.54 | 76.05 | 2.87 | 458 | 9 | 0.68 | 0.02 | 250 | 2 | 422 |
| ShWFD-1C | 0.4 | 94.69 | 14.55 | 473 | 24 | 0.66 | 0.03 | 232 | 17 | 427 |
| ShMAR-1C | 0.73 | 69.61 | 3.96 | 422 | 19 | 0.63 | 0.03 | 248 | 4 | 436 |
| ShNIO-ICP | 0.99 | 62.27 | 2.07 | 396 | 10 | 0.60 | 0.02 | 255 | 5 | 455 |
| ShPYR-1 | 0.83 | na | na | na | na | na | na | na | na | na |
| ShMCO-1-1C | na | 76.17 | 6.74 | 467 | 28 | 0.69 | 0.06 | 247 | 13 | na |

[a] VR and Rock-Eval are from the USGS: Birdwell and Wilson (2017) and Jubb et al. (2018). [b] Raman results from this study. [c] Raman instrument from National Physical Library. [d] Newly installed Raman instrument at Kingston University.

### *7.3.2 Methods*

Jubb et al. (2018) questioned the reliability of performing Raman analysis on samples with minimal sample preparation, and chose to study polished surfaces of rocks chips embedded in resin blocks. Henry et al. (2019) demonstrated the viability of analysing unprepared rock chip surfaces, so for this study we performed Raman analysis on both unprepared rock-chips and kerogen isolates on glass slides (strew slides). The organic matter isolation procedure of Henry et al. (2018) was followed for the latter.

Raman results (Table 7.2) acquired from rock-chips were obtained using a Renishaw inVia microscope with a 532 nm wavelength and a 2400 $mm^{-1}$ grating at the National Physical Library (NPL) in Teddington (UK); results for the kerogen isolates (strew slides) were acquired using a newly installed Renishaw inVia microscope with a 532 nm wavelength laser and a 1800 $mm^{-1}$ grating at Kingston University, as the Raman instrument used by Henry et al. (2018, 2019) had been destroyed by a flood in December 2018. It should be noted that the new Kingston Raman instrument is identical to that used previously at the University, apart from the laser wavelength, which was 514 nm in the old instrument. The 532 nm laser wavelength was chosen as it offers better stability, longer lifetime and generates less heat, therefore an air extraction hose is not required. In all cases a laser power of c. 0.2 mW was used to avoid

damage to the organic matter (cf. Henry et al., 2018), and the analysis was performed with a 50x objective.

The raw Raman data were processed using Henry et al.'s (2018) automated spreadsheet (Appendix B2) that calculates the G-FWHM, RBS, SSA and R1 Raman parameters. Both instruments were calibrated using rock-chips of UK Carboniferous shales and coals from the Milton of Balgonie-1 borehole (Henry et al., 2019; Appendix E – Table 1), to test the reproducibility of the data between instruments. The results show that the calibration curves follow similar trends and that the values are mostly within the error range for all parameters (Fig. 7.2). However, there is some deviation from Henry et al.'s (2019) calibration curves. These discrepancies in the calibration curves could yield notably different outcomes for hydrocarbon exploration. For example, when using Henry et al.'s (2019) calibration curve a G-FWHM value of 80 $cm^{-1}$ suggests that the rock has just entered the oil window, whereas for the NPL calibration curve the OM is entering the wet gas generation window; the same is true when considering an SSA value of 450 ($x10^3$) (Fig. 7.2). The RBS calibration curve constructed using the Kingston University 532 nm Raman instrument is also significantly different from the NPL 532 nm and the Kingston University 514 Raman instruments. The modified calibration curves equations for the different instruments and samples types are presented in Appendix E. The results demonstrate that calibration of individual instruments is essential to ensure optimum data quality when deriving $VR_{eq}$% values from Raman parameters.

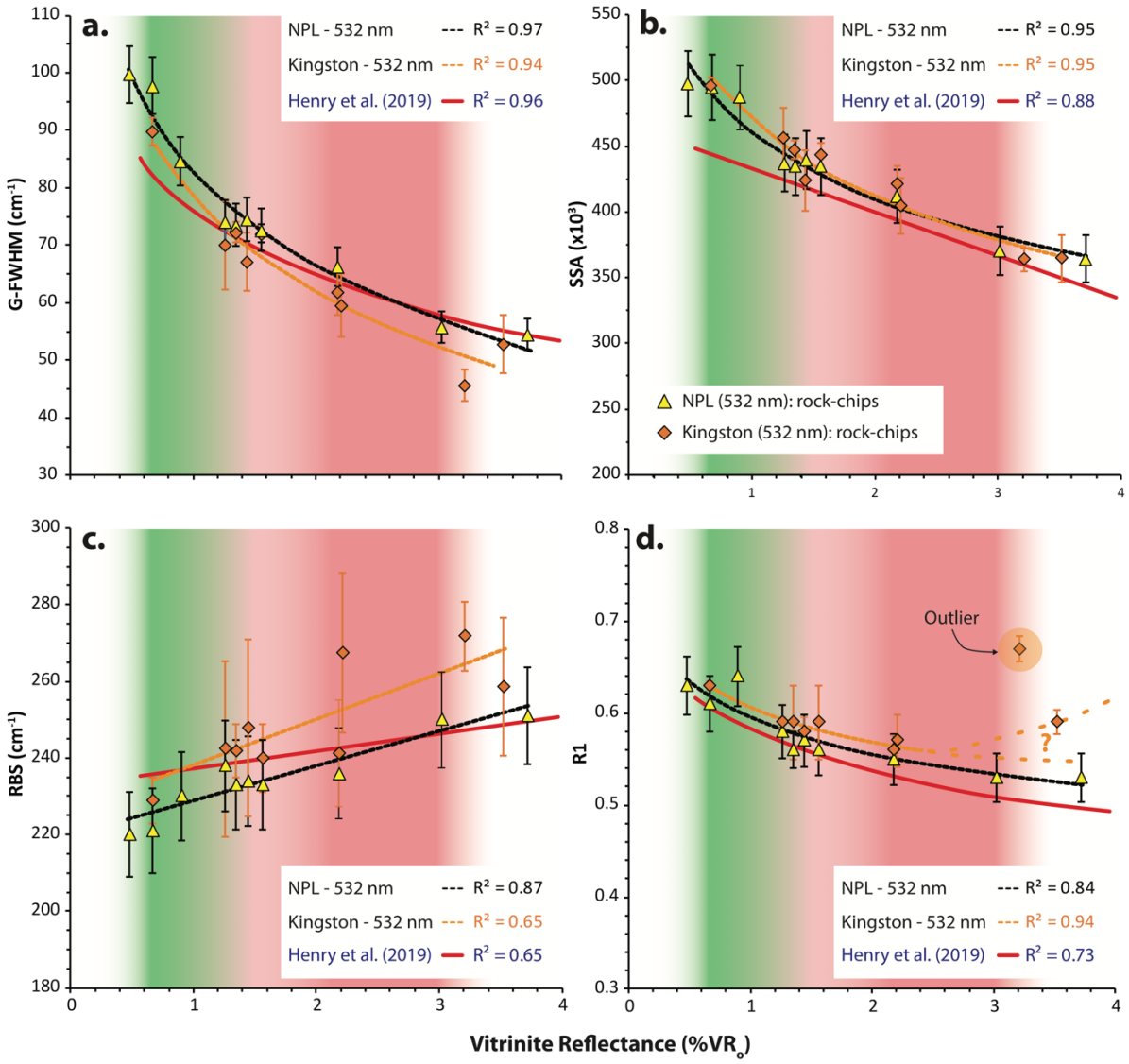


**Figure 7.2.** Calibration curves for several Raman parameters using different Renishaw Raman instruments from NPL (532 nm), Kingston University (532 nm) and the original Raman instrument used in this study (Henry et al., 2018, 2019) with a 514 nm laser wavelength. See Appendix F to see what samples were used to calibrate the NPL (532 nm) Kingston University (532 nm) Raman instruments. **(a)** G-FWHM vs. VR calibration curves. **(b)** SSA vs. VR calibration curves. **(c)** RBS vs. VR calibration curves. **(d)** R1 vs. VR calibration curves. The error bars are one standard deviation,

## 7.4 Results and discussion

Henry et al. (2018) recommended that strew slides should be used for Raman analysis but Henry et al. (2019) later demonstrated that where suitable lithologies are available, analysing unprepared rock-chips is a rapid alternative that can reliably predict equivalent vitrinite

reflectance (VR) values. However, there is no literature comparing maturity analysis for strew slides vs. rock-chips. We therefore do not know whether Henry et al.'s (2019) calibration curves based on rock chips can be applied on strew slides or not.

A comparison of the Raman results acquired from rock-chips, strew slides and Jubb et al.'s (2018) data is shown in Fig. 7.3. The data are superimposed on the calibration curves from Fig. 7.2 and their standard deviations. The rock-chip results demonstrate that the G-FWHM and RBS follow the same path as the calibration curves, whereas the SSA and R1 values have higher values and show no correlation with VR. The G-FWHM and RBS results for the strew slides samples display tightly defined trends but follow different paths compared to the calibration curves in Fig. 7.2. In contrast, the SSA and R1 are within one standard deviation of the calibration curves; however, their values are not identical. Therefore, using Henry et al.'s (2019) rock chip calibration curves for strew slide data will in many cases yield erroneous equivalent VR values.

The G-FWHM and SSA values for the strew slide samples have a stronger correlation and less scatter with VR than the rock-chip samples (strew slides, $R^2$ = 0.96 and 0.99; rock-chips:, $R^2$ = 0.67 and 0.37 for the two parameters, respectively). The G-FWHM values from Jubb et al. (2018) also follow a different path to our data set, as they define a steeper gradient with lower G-FWHM values; nevertheless, they also show a strong correlation with VR ($R^2$ = 0.80). The lower G-FWHM values for Jubb et al.'s (2018) results are to be expected, as deconvolution was performed. Their RBS values plot in a similar region to our data and are within the range of error for the calibration curves in Fig. 7.2; whereas, the R1 values they obtained are significantly lower with substantial scatter and large error bars, that show no correlation with VR ($R^2$ = 0.07) (Fig. 7.3). We would normally attribute this lack of correlation to the use of deconvolution, which has been shown to substantially impact the R1 ratio (Henry et al., 2018); however, the R1 ratios calculated here using our method that avoids deconvolution, also show no correlation with VR ($R^2$ of <0.01). However, the strew slide R1 results have a relatively strong correlation with an $R^2$ of 0.72.

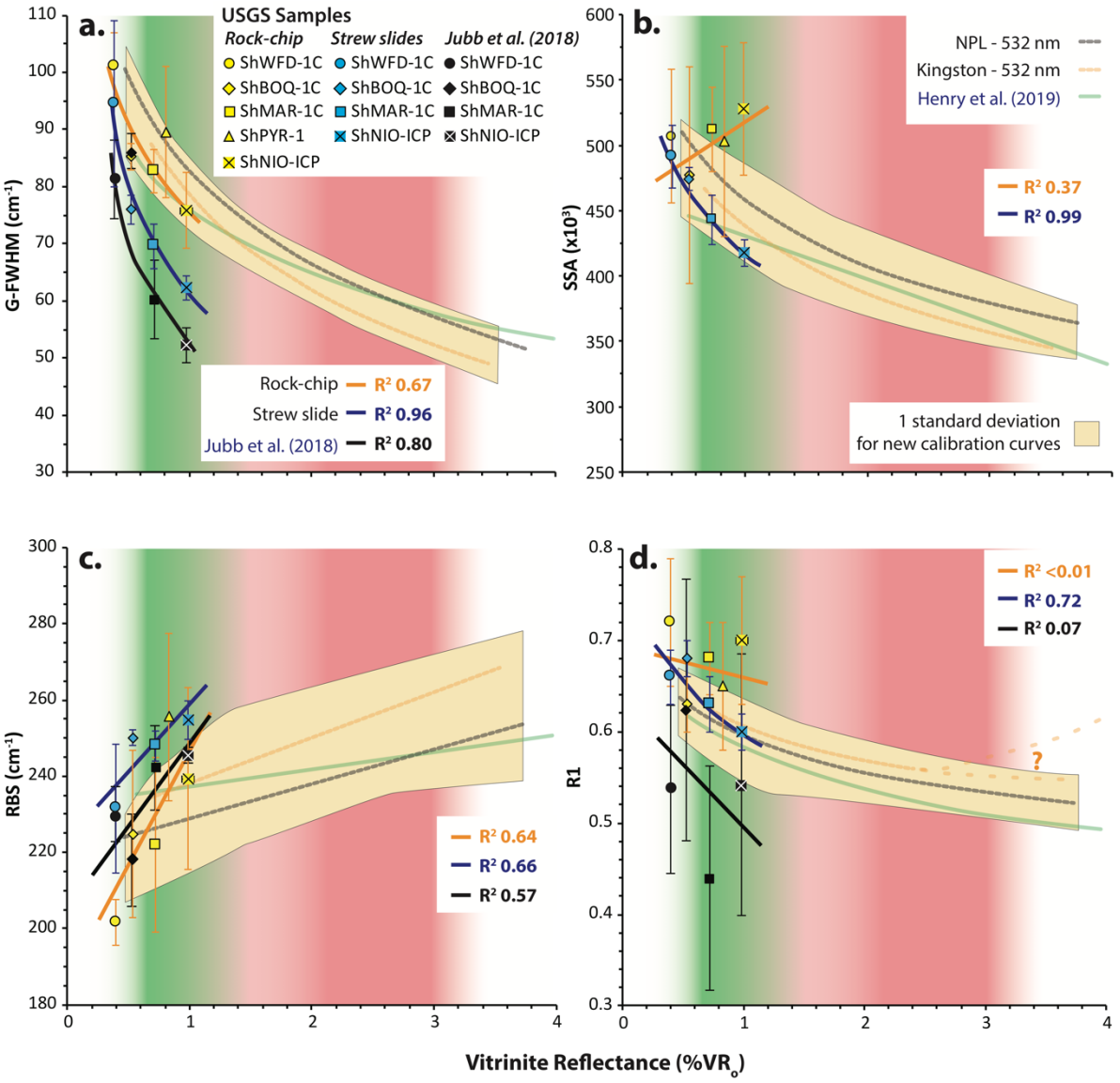


**Figure 7.3.** Comparison of the Raman parameters vs. VR for this study and Jubb et al.'s (2018) data, superimposed on the calibration curves in Fig. 7.2 and Henry et al.'s (2019) calibration curve. **(a)** G-FWHM vs. VR. **(b)** SSA vs. VR. **(c)** RBS vs. VR. **(d)** R1 vs. VR.

Figure 7.4 is a cross-plot of the Raman parameters for the USGS samples and the UK Carboniferous dataset. The G-FWHM vs. RBS cross-plot shows that the rock-chip and strew slide results plot on different paths, as the strew slide results have lower G-FWHM and higher RBS values. The USGS rock-chip data plot on a similar trend to the UK Carboniferous rock-chip dataset of Henry et al. (2019; see Chapter 5) and they also agree with the hydrocarbon generation zones, whereas the strew slide results substantially overestimate the maturity.

This confirms that the Henry et al. (2019) calibration curve based on rock chips cannot be used for the strew slides. However, Jubb et al.'s (2018) G-FWHM vs. RBS results plot along the same path as the UK Carboniferous samples. The G-FWHM vs. R1 cross-plot shows considerable scatter, although the values follow an overall trend that fits the general trend of the UK Carboniferous data set. Jubb et al.'s (2018) data also fits the general trend of our results, albeit with significant scatter.

The G-FWHM vs. SSA cross-plot demonstrates that the strew slides results follow a subtly different path to the UK Carboniferous rock-chip data set of Henry et al. (2019; see Chapter 5), as the G-FWHM values are slightly lower. Nevertheless, the results overall follow a similar trend. The same is true for the rock-chip samples, however, the SSA values of samples ShMAR-1C and ShNIO-ICP are offset to higher values. The most likely reason for this is that both these samples have high fluorescence, which may have led to an underestimation of background subtraction and increased SSA values. The R1 vs. SSA Raman parameters have a strong correlation and all the data sets follow the same trend with similar values. However, the strew slide results again overestimate the maturity of the samples with respect to the rock chip samples, when using the Raman hydrocarbon generation zones derived from Henry et al. (2019).

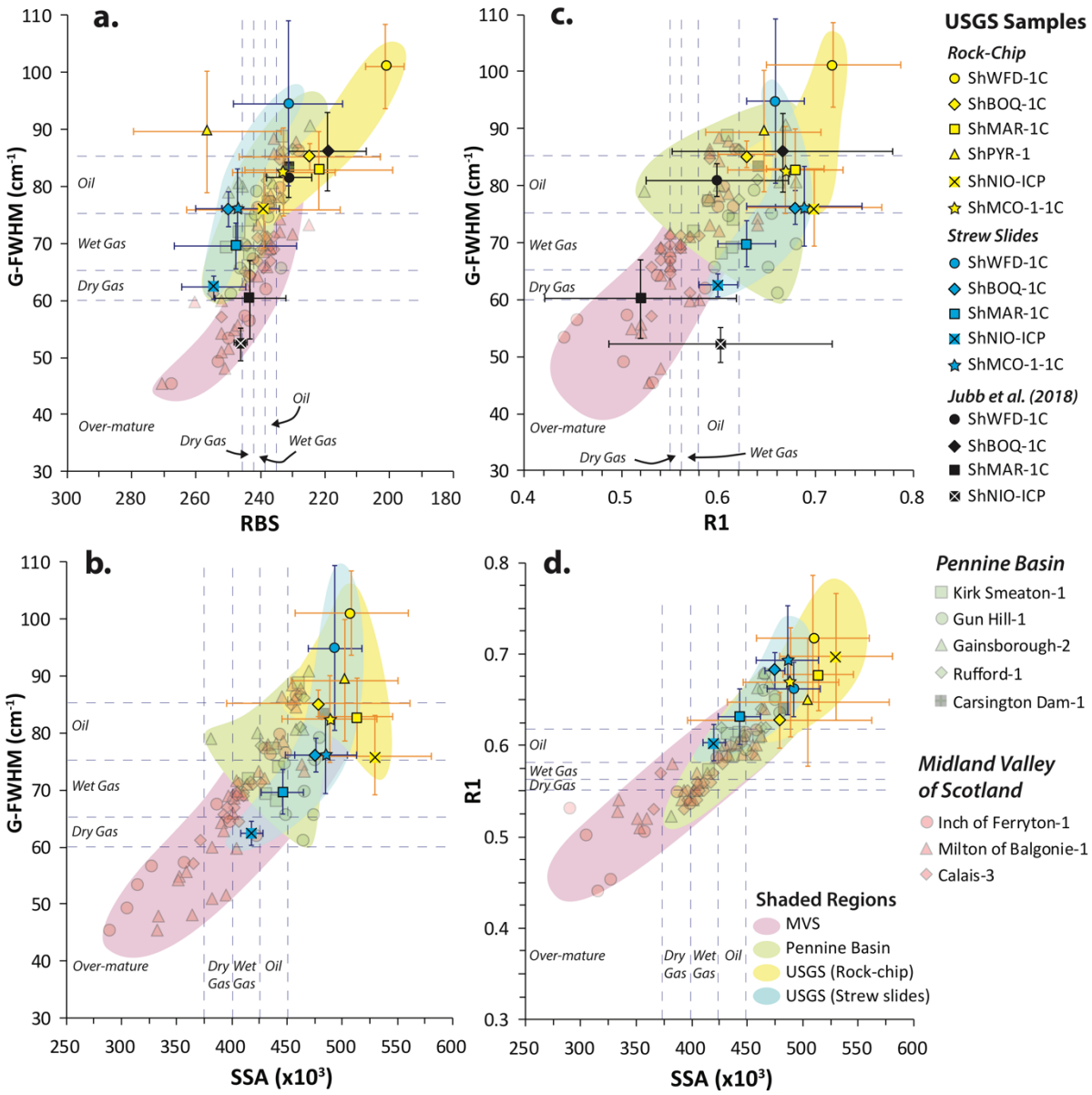


**Figure 7.4.** Cross-plots of the Raman parameters for the USGS samples and the UK Carboniferous dataset. **(a)** G-FWHM vs. RBS. **(b)** G-FWHM vs. SSA. **(c)** G-FWHM vs. R1. **(d)** R1 vs. SSA. MVS–Midland Valley of Scotland.

These results demonstrate that Raman parameters vary between rock-chip and strew slides, and that calibration curves constructed using rock-chip samples cannot be used for strew slides. This confirms that the organic matter isolation procedure using HCl and HF acids has altered the OM Raman spectrum. Several studies have shown that the removal of non-organic components using mineral acids can reduce the fluorescence in the organic matter Raman spectrum (Villanueva et al., 2008; Lünsdorf et al., 2014; Brolly et al., 2016). This will have a

significant impact when performing background subtraction. An underestimation of the background fluorescence would lead to higher G-FWHM and SSA values; whereas the reduction or removal of fluorescence (due to HCl and HF treatment) will lead to a less ambiguous background subtraction with less probability of underestimating the background fluorescence, thus producing more reliable R1 values with less scatter, as well as more reliable and lower G-FWHM and SSA values, which is confirmed in Figs 7.3–7.4. The removal of fluorescence would also lead to less bias during the background subtraction processing. This is evident, as the Raman parameters for the strew slides have less scatter compared to the rock-chip results (Fig. 7.3, Appendix E).

Raman parameters acquired from the strew slides have a stronger correlation with VR (Fig. 7.3) than those derived from rock chips. We therefore propose that strew slide calibration curves should be constructed independently from rock-chips. However, this does not reduce the importance of having calibration curves for rock-chip samples, as these can be used to screen samples early in a study lifecycle to rapidly determine which samples should be used for more expensive, longer and technical analysis.

## 7.5 Conclusion

The Raman G-FWHM calibration curve of Henry et al. (2019) can be used to obtain equivalent $\%VR_o$ maturity values from unprepared shale rock-chips of different ages and from different basins; however, rock-chip calibration curves cannot be applied to strew slide samples. Rock-chips also introduce greater bias due to enhanced background non-linear fluorescence when compared to strew slide samples, as isolating the kerogen using HCl and HF can reduce or removed the non-linear background. We recommend that calibration curves for strew slides should be constructed separately. G-FWHM is confirmed as the most reliable Raman parameter to provide an organic matter maturity proxy, as it has the best correlation with vitrinite reflectance values for both rock-chips and strew slides.

# *Chapter 8* Applying Raman spectroscopy to Late Jurassic and Late Cretaceous aged samples from the UK and Norwegian continental shelves

## 8.1 Abstract

The Raman maturity method developed by Henry et al. (2018) is extended to Jurassic and Cretaceous aged Type II kerogen samples from the Norwegian (rock-chip samples) and UK (strew slide samples) continental shelves. The results confirm that the G-band full-width at half-maximum (G-FWHM), scaled spectrum area (SSA; total area under the curve between 1100–1700 $cm^{-1}$) and Raman band separation (RBS; G-band position minus the D-band position) are the most reliable Raman parameters that can successfully estimate sensible hydrocarbon generation zones and have similar values to the measured vitrinite reflectance from the UK continental shelf samples. Whereas, the vitrinite reflectance values derived using Jarvie et al.'s (2001) Rock-Eval™ $T_{max}$ equation, for the Norwegian shelf samples have anomalously low maturity values and under-predict the maturity of the organic matter (OM) with respect to the Raman parameters. The source of the anomalously low $T_{max}$ values is uncertain, however it is most likely to be due to contamination of lignite material (which is present in the rock-chips) and/or the presence of free heavy hydrocarbons that were not expelled by means of solvent extraction or the initial heating phase prior to performing Rock-Eval pyrolysis.

The vitrinite reflectance (VR) hydrocarbon generation zones from the UK continental shelf samples from previously acquired VR results are very similar to the estimated Raman hydrocarbon generation zones based on the calibrations curves constructed using the USGS shale geological reference material strew slides in Chapter 7. However, samples from the high-pressure/high-temperature Shearwater gas field, which have previous been determined to have retarded VR values, underestimate the maturity of the OM with respect to the G-FWHM, SSA and RBS Raman parameters; again, based on the hydrocarbon generation zones estimated using the shale reference material calibration curves. The study highlights the

importance to perform several maturity methods, in order to decrease the risk in estimating the maturity of source rocks for hydrocarbon exploration, as contamination and theoretical issues such as retardation or suppression (which is not taken into consideration here) can lead to unreliable results.

## 8.2 Introduction

Henry et al.'s (2018) Raman method has mostly been performed on Type III and Type II/III organic matter in Carboniferous samples from onshore UK. Testing the method on samples with different kerogen types, different ages and from different basins is necessary to assess whether a universal calibration curve can be used to estimate equivalent vitrinite reflectance (VR) values, when the same technical and methodological approach is followed. If a universal calibration curve cannot be used, then we can assume that there are inherent theoretical problems that are creating discrepancies, which may be related to factors such as: the composition of the organic matter; different lithologies; and/or different thermal, pressure and geodynamic histories. No thermal maturity technique can be ubiquitously applied (Nuccio, 1991; Wilkins, 1999), therefore it is naive to assume that Raman can correct for all discrepancies. Here, we aim to gain some insight into the potential discrepancies that may occur when using Raman spectroscopy to assess the maturity of organic matter.

The objectives of this chapter are to: (1) test whether Henry et al.'s (2018, 2019) method and calibration curves are applicable on Type II kerogen, and rocks of different ages and from different geological basins and; (2) assess further if there are significant differences between Raman data derived from rock-chip and strew-slide samples (see Chapter 7); (3) investigate whether Raman spectroscopy is affected by retardation effects, which is a known phenomenon that occurs when performing vitrinite reflectance on samples that have experience substantial overpressure (Teichmüller, 1974; Carr, 2000). In order to test the above, Jurassic and Cretaceous offshore borehole samples with Type II kerogen from the UK and Norwegian continental shelves were obtained from 8 petroleum exploration wells with available Rock-Eval™ $T_{max}$ and/or vitrinite reflectance (VR) maturity data (Table 7.1). Samples from the high-pressure/high-temperature Shearwater gas field offer an opportunity to test whether vitrinite reflectance retardation, due to overpressure, can be corrected using Raman spectroscopy.

## 8.3 Geological settings of the materials studied

All the wells are located in the North Sea, apart from Skalle well 7120/2-3 S, which is located in the southwestern Barents Sea (Figs 8.1 and 8.2). Only a summary of the geological settings will be outlined here. For more detailed information see Evans et al. (2013) for the North Sea and Smelror et al. (2009) and www.npd.no for the southwestern Barents Sea.

### *8.3.1 North Sea*

The main structural units of the North Sea Basin formed as a result of the Middle Jurassic to Early Cretaceous rifting that led to the development of what is known as the North Sea 'triple-junction' (Central Graben, Moray Firth Basin and Viking Graben), which represents a failed rift system and was followed by thermal subsidence (Fig. 8.1; Ziegler, 1989; Underhill and Partington, 1993). The North Sea Basin stratigraphy from the Triassic to present can be subdivided into three main depositional phases: The pre-rift, syn-rift and post-rift.

The pre-rift Triassic sediments deposited the aeolian sediments of the Zechstein and Rotliegend groups (Ziegler, 1989). During the Early Jurassic there was a widespread marine transgression that led to the deposition of shallow marine shales, sandstone and siltstones. Thermal doming during the Middle Jurassic led to subaerial exposure and the formation of the mid-Cimmerian unconformity (Underhill and Partington, 1993). The uplift and erosion of the dome led to the deposition of paralic sediments, including the deposition of the Brent Group, which is composed of the most prolific reservoirs in the central North Sea (Richards, 1992).

Collapse of the thermal dome during the Late Jurassic (Middle Oxfordian) marked the onset of the syn-rift deposition (Underhill and Partington, 1993). This led to a marine transgression that inundated paralic depositional environments and led to the deposition of deeper marine deposits, such as the Kimmeridge Clay Formation (Fraser et al., 2003), which is the main source rock in the North Sea and a major focus of this study.

Rifting stopped during the Early Cretaceous and was followed by thermal subsidence and the formation of the regional Base Cretaceous Unconformity (Rawson and Riley, 1982; Coward et al., 2013). By Late Cretaceous the post-rift pelagic chalks blanketed the North Sea (Surlyk et

al., 2003), which act as important seals to hydrocarbon reservoirs, as well fracture reservoirs. Mantle underplating associated with the opening of the North Atlantic Ocean during the Paleocene, led to the uplift and erosion of NW Scotland and the deposition of Paleocene-Eocene clastic fan deposits (Reynolds, 1994).

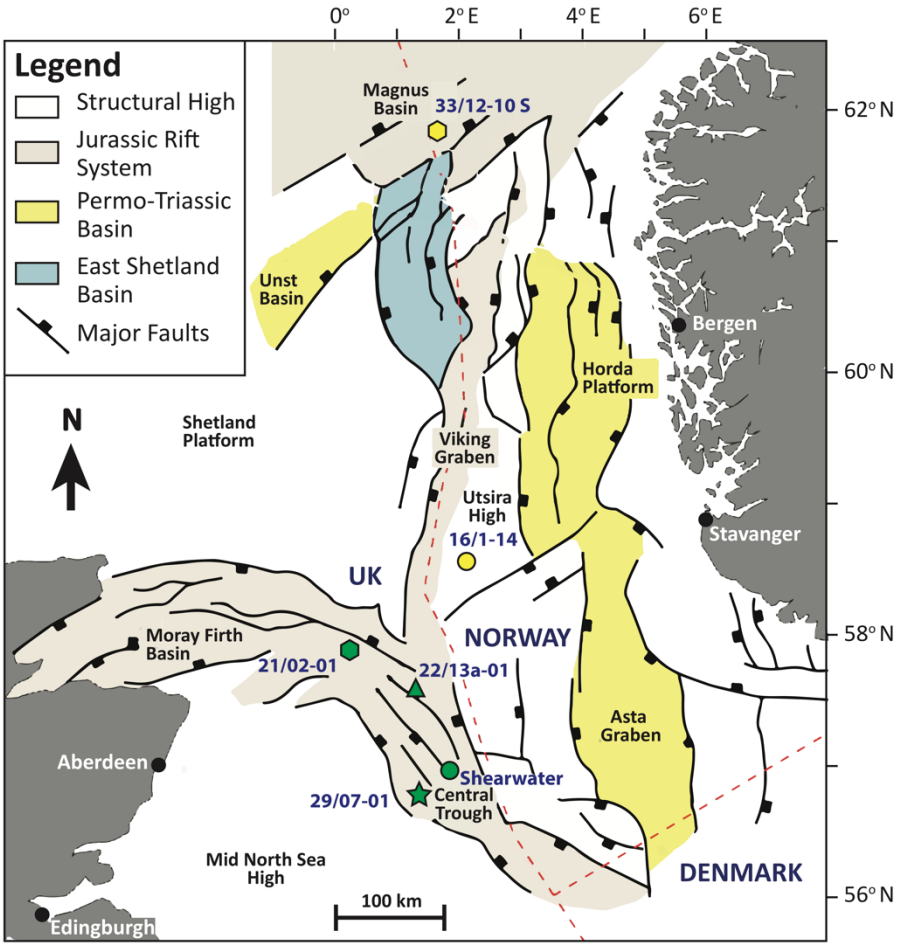


**Figure 8.1.** Structural setting of the northern North Sea and the location of the borehole samples used in this study. Adapted from Dominguez (2007), as modified from Faerseth (1996).

### *8.3.2 Southwestern Barents Sea*

The southwestern Barents Sea (SWB) continental margin extends c. 100 km NNW along the Norwegian continental shelf (Fig. 8.2). This area has undergone several complex tectonic phases during the Devonian to Middle Carboniferous; Middle Carboniferous to Permian, Triassic to Jurassic; Late Jurassic to Early Cretaceous; and Tertiary deformation, that led to the development of complex mosaic of basins and platforms (Faleide et al., 1993; Gernigon et al.,

2014). The main structural units in the SWB are the Hammerfest, Tromsø and Nordkapp basins, the Finnmark and Bjarmeland platforms and the Loppa High (Fig. 8.2).

The metamorphic remnants of Caledonian orogeny make up the basement rock of the Barents Sea basin (Dengo and Røssland, 1992; Gac, et al., 2018) which is overlain by thick continental clastic sediments, followed by shallow-water carbonates and sabkha evaporites that were deposited in grabens during the Late Devonian to Middle Carboniferous (Faleide et al., 1984; Worsley, 2006). A marine transgression during the Late Carboniferous led to the development of a widespread carbonate platform that covered the topography of the Carboniferous grabens (Wood et al., 1989). Rifting during the Late Permian then led to the deposition of large volumes of clastic sediments (Faleide et al., 2015; Gac et al., 2018).

The Triassic was a period of tectonic quiescence and was dominated by the deposition of thick deltaic transgressive-regressive cycles, that initiated halokinesis of the Carboniferous sabkha evaporites in the Nordkapp basin (Mørk et al., 1989; Gabrielsen et al., 1990). Clastic sedimentation continued throughout the Jurassic in the SWB (Gac et al., 2018). Major rifting during the Middle Jurassic to Early Cretaceous led to the development of narrow and deep basins, followed by passive subsidence during the Late Cretaceous. The passive subsidence was interrupted by the crustal break-up and sea floor spreading and opening of the North Atlantic Ocean during the Paleogene, which led to tectonism and uplift. Glaciation during the Late Pliocene and Pleistocene led to large scale erosion in the Barents Sea (Cavanagh et al., 2006). These phases of uplift and erosion caused the breaching of seals and reservoirs and re-migration of hydrocarbons, as well having important consequences for reservoir quality and source rock maturity (Henriksen et al., 2011).

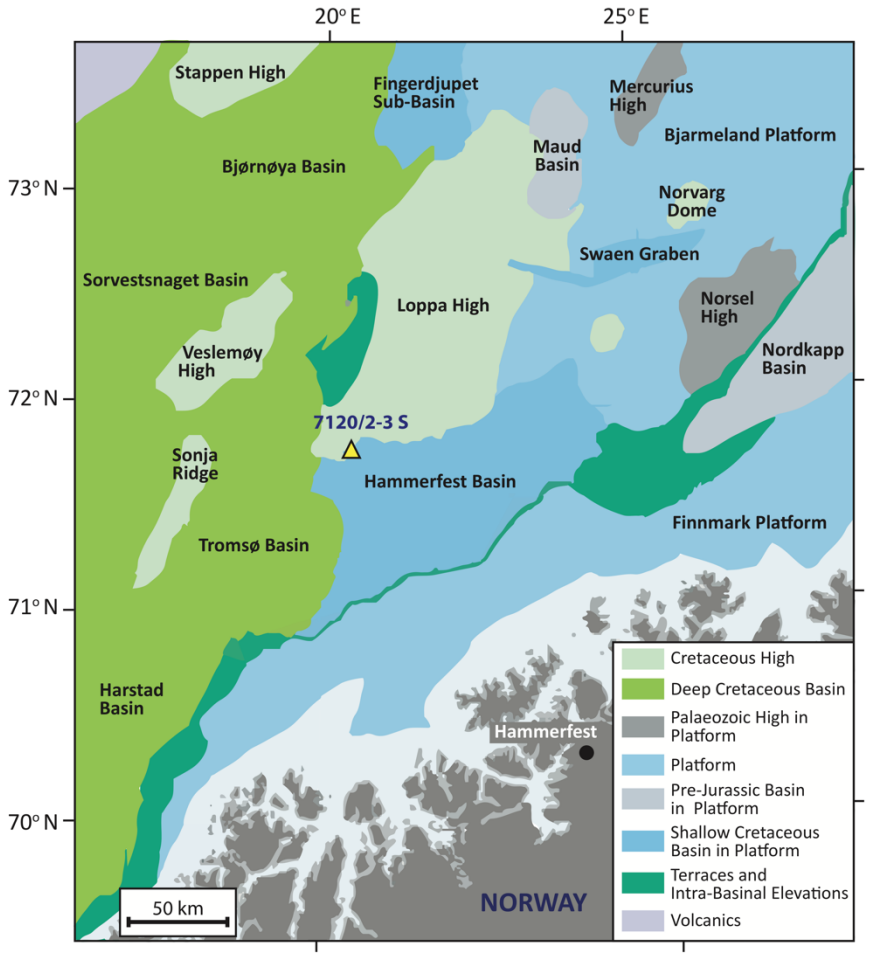


**Figure 8.2.** Main structural units in the southwestern Barents Sea and location of the borehole studied (yellow filled triangle). Modified from www.npd.no/.

## 8.4 Materials and methods

### *8.4.1 Materials*

Twenty-three cuttings and one core sample from eight wells were studied (Figs 8.1 and 8.2; Table 8.1 and Table 8.2). The Norwegian samples were provided by Dr Holly Turner courtesy of Mike Charnock and Lundin Norway AS (Turner et al., 2018) and the UK samples were provided by Dr Manuel Viera from Shell UK. VR data for the Norwegian shelf samples was estimated using Jarvie et al.'s (2001) $T_{max}$ equation ($VR = 0.018*T_{max} - 7.16$) using Tmax values from Turner (2018), whereas measured VR values were acquired from Shell UK for the UK continental shelf samples.

Well 7120/2-3 S is located on the ENE edge of Hammerfest Basin and is bordered to the north by the Loppa High in the southwestern Barents Sea. The well was drilled in 2011 as a wildcat well operated by Lundin Norway AS and was completed as a gas discovery, known as the Skalle field; however, it has now been plugged and abandoned. Well 33/12-10 S is in the Norwegian northern North Sea and was a drilled in 2014 as a wildcat well in the Tampen Spur north of the Viking Graben and was determined dry by Lundin Norway AS. The 16/01-14 well is located in the Southern Viking graben in the Gundrun Terrace, west of the Utsira High. The well was completed in 2010 and discovered oil by Lundin Norway AS, but was later plugged and abandoned.

Well 21/02-01 completed drilling in 1981 and was operated by Britannia Operator Ltd. It aided the discovery of the Ettrick oil field in the Outer Moray Firth. The well was later plugged and abandoned. Well 22/13a-1 was drilled in 1988 at the edge of the Bardolino oil field in the Witch Ground Graben, which was discovered by Shell in 1989. The well is now plugged and abandoned. Shell drilled well 29/7-1 and discovered the Curlew-A oil accumulation in 1979, which is composed of a series of terraces in the western Central Graben. The well is now plugged and abandoned. Shell completed well 30/19a-05S3 in 1974 and drilled into the Affleck field in the Central Graben area in the Central North Sea. The well is now plugged and abandoned.

Wells SW01 and SW04 were drilled in the high-pressure/high-temperature Shearwater field in the Central Graben area of the central North Sea. The Central Graben area of the Central North Sea is widely known to be highly overpressured (Gaarenstroom et al., 1993; Petersen et al., 2012) and samples from the area offer a good opportunity to assess potential suppression of Raman maturity values. Previously acquired VR data from Shell, demonstrate that the values have been suppressed (Appendix E). Ideally, a wide depth range would be studied, however only four samples were available. The complexity of the Shearwater samples is increased by the presence of lignite and oil-based mud contamination (OBM).

**Table 8-1.** Borehole samples studied from the UK and Norwegian continental shelves, along with depths, sample type, location, age and rock unit.

| Well (Lat, Long) (Sea) | Sample Depth (m) | Samples | Sample type analysed | Hydrocarbon Field | Series/Stage | Rock Unit |
|---|---|---|---|---|---|---|
| **Norwegian continental shelf** | | | | | | |
| **7120/2-3 S**[a] | 2003.6 | Cuttings | Rock-chip | Skalle Field | Late Jurassic | Hekkingen Fm. |
| (71.47 N, 20.22 E) | 2005.3 | Cuttings | Rock-chip | Skalle Field | Late Jurassic | Hekkingen Fm. |
| (SWB) | 2012.4 | Cuttings | Rock-chip | Skalle Field | Late Jurassic | Hekkingen Fm. |
| | 2019.95 | Cuttings | Rock-chip | Skalle Field | Late Jurassic | Hekkingen Fm. |
| **33/12-10 S**[a] | 2944.01 | Cuttings | Rock-chip | Volgrav Field | Late Jurassic | Draupne Fm. |
| (61.78 N, 1.56 E) | 2958.44 | Cuttings | Rock-chip | Volgrav Field | Late Jurassic | Draupne Fm. |
| (NNS) | 2970.24 | Cuttings | Rock-chip | Volgrav Field | Late Jurassic | Draupne Fm. |
| | | | Rock-chip | | | |
| **16/1-14**[a] | 2384.25 | Cuttings | Rock-chip | Apollo | Late Cretaceous | Kyrre Fm. |
| (58.54 N, 2.12 E) | 2388.8 | Cuttings | Rock-chip | Apollo | Late Cretaceous | Kyrre Fm. |
| (NNS) | 2405.05 | Cuttings | Rock-chip | Apollo | Late Cretaceous | Kyrre Fm. |
| | 2410.9 | Cuttings | Rock-chip | Apollo | Late Cretaceous | Kyrre Fm. |
| **UK continental shelf** | | | | | | |
| **21/02-01**[b] | 3758 | Cuttings | Strew slide | Glenn Field | Late Jurassic | KCF |
| 57.92 N, 0.26 E | 3961 | Cuttings | Strew slide | Glenn Field | Late Jurassic | KCF |
| (UKNS) | | | | | | |
| **22/13a-01**[b] | 3596 | Cuttings | Strew slide | Bardolino | Late Jurassic | KCF |
| (57.63 N, 1.42 E) | 3608 | Cuttings | Strew slide | Bardolino | Late Jurassic | KCF |
| (UKNS) | 3645 | Cuttings | Strew slide | Bardolino | Late Jurassic | KCF |
| | 3672 | Cuttings | Strew slide | Bardolino | Late Jurassic | KCF |
| **29/07-01**[b] | 3398 | Cuttings | Strew slide | Curlew A | Late Jurassic | KCF |
| (56.79 N, 1.27 E) | 3490 | Cuttings | Strew slide | Curlew A | Late Jurassic | KCF |
| (UKNS) | | | | | | |
| **SW01**[b] | 5209 | Cuttings | Strew slide | Shearwater | Late Jurassic | Heather Fm. |
| (57.01 N, 1.95 E) | 5218 | Cuttings | Strew slide | Shearwater | Late Jurassic | Heather Fm. |
| (UKNS) | 5230 | Cuttings | Strew slide | Shearwater | Late Jurassic | Heather Fm. |
| **SW04**[b] | 5211 | Core | Strew slide | Shearwater | Late Jurassic | Heather Fm. |
| (57.01 N, 1.95 E) | | | | | | |
| (UKNS) | | | | | | |

SWB = southwestern Barents Sea. NNS = Norwegian North Sea. UKNS = United Kingdom North Sea. KCF = Kimmeridge Clay Formation. [a] Samples analysed using the National Physical Laboratory (NPL) 532 nm Raman instrument. [b] Samples analysed using the Kingston University 532 nm Raman instrument.

**Table 8-2.** Corresponding measured VR and equivalent VR estimated using $T_{max}$ ($T_{max}$%$_{eq}$VR), Raman and Rock-Eval $T_{max}$ results for the samples in Table 8.1.

| Wells | Depth (m) | VR[a] %VR$_o$ | $T_{max}$[b] %$_{eq}$VR | Raman[d] G-FWHM | 1 σ | SSA (x10$^3$) | 1 σ (x10$^3$) | R1 | 1 σ | RBS | 1 σ | $T_{max}$ (°C) [c] |
|---|---|---|---|---|---|---|---|---|---|---|---|---|
| **Norwegian continental shelf[e]** | | | | | | | | | | | | |
| **7120/2-3 S** | 2003.6 | na | 0.63 | 88.56 | 14.24 | 447 | 37 | 0.56 | 0.05 | 220 | 12 | 433 |
| | 2005.3 | na | 0.53 | 89.55 | 4.03 | 486 | 10 | 0.60 | 0.02 | 234 | 9 | 427 |
| | 2012.4 | na | 0.62 | 90.05 | 7.96 | 493 | 19 | 0.63 | 0.03 | 228 | 1 | 432 |
| | 2020.0 | na | 0.65 | 94.15 | 3.09 | 524 | 3 | 0.67 | 0.01 | 221 | 15 | 434 |
| **33/12-10 S** | 2944.0 | na | 0.42 | 73.57 | 1.69 | 452 | 9 | 0.63 | 0.03 | 251 | 15 | 421 |
| | 2958.4 | na | 0.49 | 69.80 | 3.48 | 430 | 12 | 0.63 | 0.02 | 255 | 7 | 425 |
| | 2970.2 | na | 0.42 | 73.19 | 9.06 | 448 | 23 | 0.60 | 0.04 | 246 | 16 | 421 |
| **16/1-14** | 2384.3 | na | 0.29 | 75.79 | 5.64 | 453 | 33 | 0.60 | 0.06 | 242 | 9 | 414 |
| | 2388.8 | na | 0.47 | 78.96 | 8.66 | 456 | 23 | 0.60 | 0.04 | 240 | 9 | 424 |
| | 2405.1 | na | 0.11 | 78.62 | 12.84 | 458 | 42 | 0.61 | 0.05 | 241 | 17 | 404 |
| | 2410.9 | na | na | 79.96 | 6.73 | 452 | 15 | 0.58 | 0.04 | 235 | 11 | na |
| **UK continental shelf[f]** | | | | | | | | | | | | |
| **21/02-01** | 3758.2 | 0.67 | 0.58 | 75.61 | 1.94 | 373 | 16 | 0.66 | 0.02 | 254 | 4 | 430 |
| | 3861.8 | 1.05 | 0.40 | 74.65 | 4.60 | 361 | 15 | 0.62 | 0.03 | 250 | 6 | 420 |
| **22/13a-01** | 3596.6 | 0.57 | 0.76 | 82.90 | 8.90 | 351 | 31 | 0.65 | 0.02 | 241 | 10 | 440 |
| | 3608.8 | 0.36 | 0.76 | 82.82 | 10.87 | 351 | 36 | 0.66 | 0.04 | 240 | 14 | 440 |
| | 3645.4 | 0.54 | 0.74 | 79.75 | 11.47 | 343 | 29 | 0.63 | 0.04 | 243 | 15 | 439 |
| | 3672.8 | 0.64 | 0.78 | 81.84 | 15.57 | 389 | 48 | 0.67 | 0.05 | 247 | 8 | 441 |
| **29/07-01** | 3398.5 | 0.58 | 0.72 | 77.36 | 9.25 | 348 | 24 | 0.61 | 0.02 | 245 | 6 | 438 |
| | 3490.0 | 0.42 | na | 71.89 | 2.06 | 335 | 13 | 0.61 | 0.01 | 254 | 5 | na |
| **SW01** | 5209.0 | 0.75 | na | 69.28 | 4.62 | 325 | 52 | 0.65 | 0.08 | 253 | 8 | na |
| | 5218.2 | 0.75 | na | 64.29 | 4.18 | 319 | 30 | 0.63 | 0.05 | 258 | 3 | na |
| | 5230.4 | 0.74 | na | 64.26 | 9.38 | 310 | 17 | 0.6 | 0.03 | 256 | 7 | na |
| **SW04** | 5211.7 | 0.75 | na | 58.48 | 1.74 | 306 | 11 | 0.6 | 0.03 | 261 | 3 | na |

[a] measured VR values acquired from Shell UK. [b] VR values estimated using Jarvie et al.'s (2001) $T_{max}$ equation (VR=0.018*$T_{max}$ – 7.16). [c] $T_{max}$ results acquired from Turner (2018) (Norwegian continental shelf) and Dr. Manuel Viera (UK continental shelf). [d] Raman results acquired in this study. [e] Raman analysis performed on rock chip samples. [f] Raman analysis performed on strew slide samples.

### *8.4.2 Sample preparation*

Raman analysis was performed on rock-chips for the southwestern Barents Sea (well 7120/2-3 S) and Norwegian North Sea samples (wells 33/12-10 S, 16/1-14) as a sufficient number of phytoclasts could be identified using a microscope. The organic matter (OM) had to be isolated using HCl and HF for the UK North Sea samples (wells 21/02-01, 22/13a-01, 29/07-01, SW01, SW04), as phytoclasts could not be visually identified in the rock-chip/hand specimens (Table 8.2). The kerogen isolation procedure outlined in Chapter 4.3.2.2 (Henry et al., 2018) was followed. It has been shown in Chapter 7 that strew slide results differ from rock-chip samples and that Henry et al.'s (2019) calibration curves could not be used on strew slides. This will be further assessed here.

### *8.4.3 Instruments and data processing methods*

The rock-chip Raman results were acquired using a Renishaw inVia microscope with a 532 nm wavelength and a 2400 $mm^{-1}$ grating at the National Physical Library (NPL) in Teddington (UK). Results obtained from the kerogen isolates (strew slides) were acquired using a newly installed Renishaw inVia microscope with a 532 nm wavelength laser and a 1800 $mm^{-1}$ grating at Kingston University. The Kingston Raman system was a replacement like-for-like for the instrument used by Henry et al. (2018, 2019); however, a 532 nm solid state laser was installed instead of a 514 nm laser. On both occasions a laser power of 0.2 mW was used to avoid damage to the organic matter and the analysis was performed through a 50x objective. The raw data were processed using Henry et al.'s (2018) version 2 method (Appendix B2).

## 8.5 Results and discussion

A depth plot of the maturity indicators helps petroleum geologists determine at what depths hydrocarbon generation is expected in a specific region (Petersen et al., 2011). Figure 8.3 shows how $VR_o$, $T_{max}$ derived equivalent VR values ($T_{max}\%_{eq}VR$) and several Raman parameters evolve with increasing depth for the Norwegian and UK continental shelf samples.

For the Norwegian continental shelf samples, the $T_{max}\%_{eq}VR$ values for wells 16/1-14 and 33/12-10 S d are lower than expected due to the depth of the samples. This is in contrast to

the G-FWHM and SSA results, which show that the maturity of the samples increases with increasing depth for the different wells. The RBS also shows increasing values with depth but with substantially more scatter. The R1 values suggest that the maturity of the results decrease with increasing depth, however, there is considerably greater standard deviation for each sample that ranges across the whole hydrocarbon generation zones, which makes it an unreliable maturity proxy. There are discrepancies between the different maturity proxies. The $T_{max}$ values which were used to calculated equivalent VR values for the Norwegian continental shelf suggest that the 7120/2-3 S samples have just entered the oil window, whereas the deeper samples are immature (Fig. 8.3a). The anomalously low values and large scatter for the samples in well 16/1-14 suggest that the samples may have been contaminated or had free heavy hydrocarbons present in the rock prior to pyrolysis. Assuming an average geothermal gradient of c.30 $^{o}$C per/km for the Central Graben (Petersen et al., 2012), we can also assume that the samples from well 33/12-10 S should have entered the oil window.

Strew slides were analysed for the UK continental shelf samples and therefore the hydrocarbon generation zones were derived from the USGS strew slide calibration curve equations calculated in Chapter 7 and shown in Appendix F. The USGS samples had a limited maturity range of up to c.1 %$VR_o$, therefore the equations were extrapolated to estimate Raman values for higher VR values. Figure 8.3 also shows Henry et al.'s (2019) rock-chip Raman hydrocarbon generation zones superimposed for comparison (the stippled vertical lines in the bottom half of Figure 8.3). Overall, the vitrinite reflectance values increase with increasing depth, albeit with some scatter; however, the SW01 and SW04 samples from the high-pressure/high-temperature Shearwater gas field, have retarded VR values and do not fall on the general depth trend evolution for VR. The 3,861 m sample for Well 21/02-01 also shows a strong positive deviation in VR, compared to sample 3,758 m for the same well (Fig. 8.3), which could be a result of misinterpreting the primary vitrinite population for either the secondary and/or inertinite population.

G-FWHM values increase with increasing depth (Fig. 8.3b). The samples from SW01 and SW04, which have been interpreted as having retarded VR values, lie on the same general maturity trend as the other samples, in contrast to VR. The G-FWHM values suggests that the samples have entered the oil to wet gas generation zones, which conforms with the hydrocarbon production data for the Shearwater gas field area (Taylor et al., 2015). This

contradicts the VR values, which suggest that the samples have only entered the oil generation window with VR values of c.0.75 %$VR_o$. Using the same crude thought process as before, for well 33/12-10 S, and again assuming an average geothermal gradient of c.30 $^oC$ per/km for the Central Graben area (Petersen et al., 2012), we should expect the samples to have reached temperatures of c.150 $^oC$, which would be the equivalent of c.1 %VR (Barker and Goldstein, 1990; Burnham and Sweeney, 1989). However, the measured VR values are 0.75 %$VR_o$, whereas the equivalent G-FWHM VR values using the USGS strew slide calibration curve equation is c. 0.90 %$VR_o$.

The wide discrepancy in the $VR_o$ maturity values for the two samples from well 21/02-01 are not apparent in the G-FWHM depth plot, the values from which suggest that the samples have just entered the oil hydrocarbon generation zone. The G-FWHM and VR values for wells 22/13a-01 and 29/07-01 are very similar and both predict that the samples are bordering immature to early oil maturity. The SSA and RBS Raman parameters estimate similar maturity values to the G-FWHM Raman parameter for wells 22/13a-01, 21/02-01 and 29/07-01, and also predict that the SW01 and SW04 samples have entered well into the oil generation zone and border the wet gas zone. The R1 Raman parameter also estimates similar hydrocarbon generation zones for all the UK continental shelf samples, albeit, with substantially more scatter.

These results demonstrate that Raman spectroscopy can be applied to Type II organic matter in Jurassic and Cretaceous shales and can be used to estimate reasonable hydrocarbon generation zones similar to VR. These results also suggest that the Raman parameters may correct for the VR retardation effect, however this is not conclusive. Further tests on samples with known retarded values and laboratory tests are needed, in order to confirm whether or not Raman can correct VR retardation. We again demonstrate that Raman results from strew slide samples differ to rock-chip samples. Figures 8.4 and 8.5 show that the strew slide data from the UK continental shelf plot along a similar path as the USGS shale reference material strew slide results, suggesting that a universal strew slide calibration curve may be feasible.

The UK continental shelf samples contain substantial lignite contamination. This was not an issue for Raman spectroscopy, as the lignite grains can be easily avoided visually when using either rock-chips or strew slides. This is not the case when performing vitrinite reflectance, as

polishing the grains make the discrimination of lignite material much harder (Hackley and Cardott, 2016). Misinterpretation of lignite material would underestimate the VR values and Rock-Eval maturity estimations (Bostick and Apern, 1977; Nzoussi-Mbassani et al., 2005; Hackley and Cardott, 2016). Raman analysis is therefore an extremely useful tool for avoiding contamination that would otherwise be an issue for vitrinite reflectance and Rock-Eval pyrolysis, as noted recently by Goryl et al. (2019).

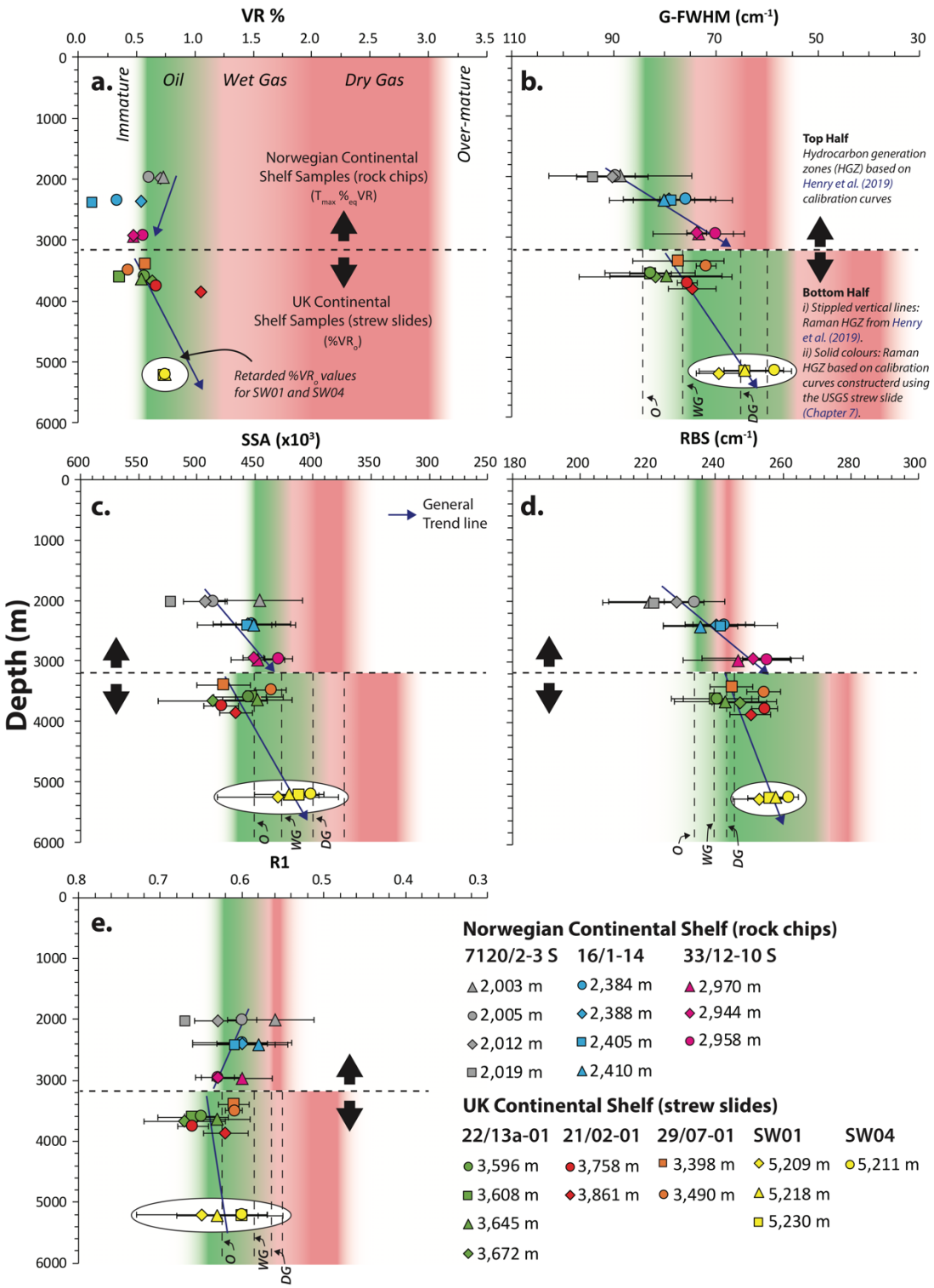


**Figure 8.3.** Depth plots for $\%VR_o$, $T_{max}\%_{eq}VR$ and Raman parameters for the Norwegian and UK continental shelf samples. **(a)** Depth vs. VR and $T_{max}\%_{eq}VR$. **(b)** Depth vs. G-FWHM. **(c)** Depth vs. SSA. **(d)** Depth vs. RBS. **(e)** Depth vs. R1. The oil and gas generation zones for the Raman parameters in the top panel are from Henry et al. (2019), whereas the bottom panel are from the USGS strew slide Raman calibration equation from Chapter 7 and Appendix F. Both the Raman hydrocarbon generation zones are based from the VR values from Dow (1977). O–Oil generation zone. WG–Wet Gas generation zone. DG–Dry Gas generation zone.

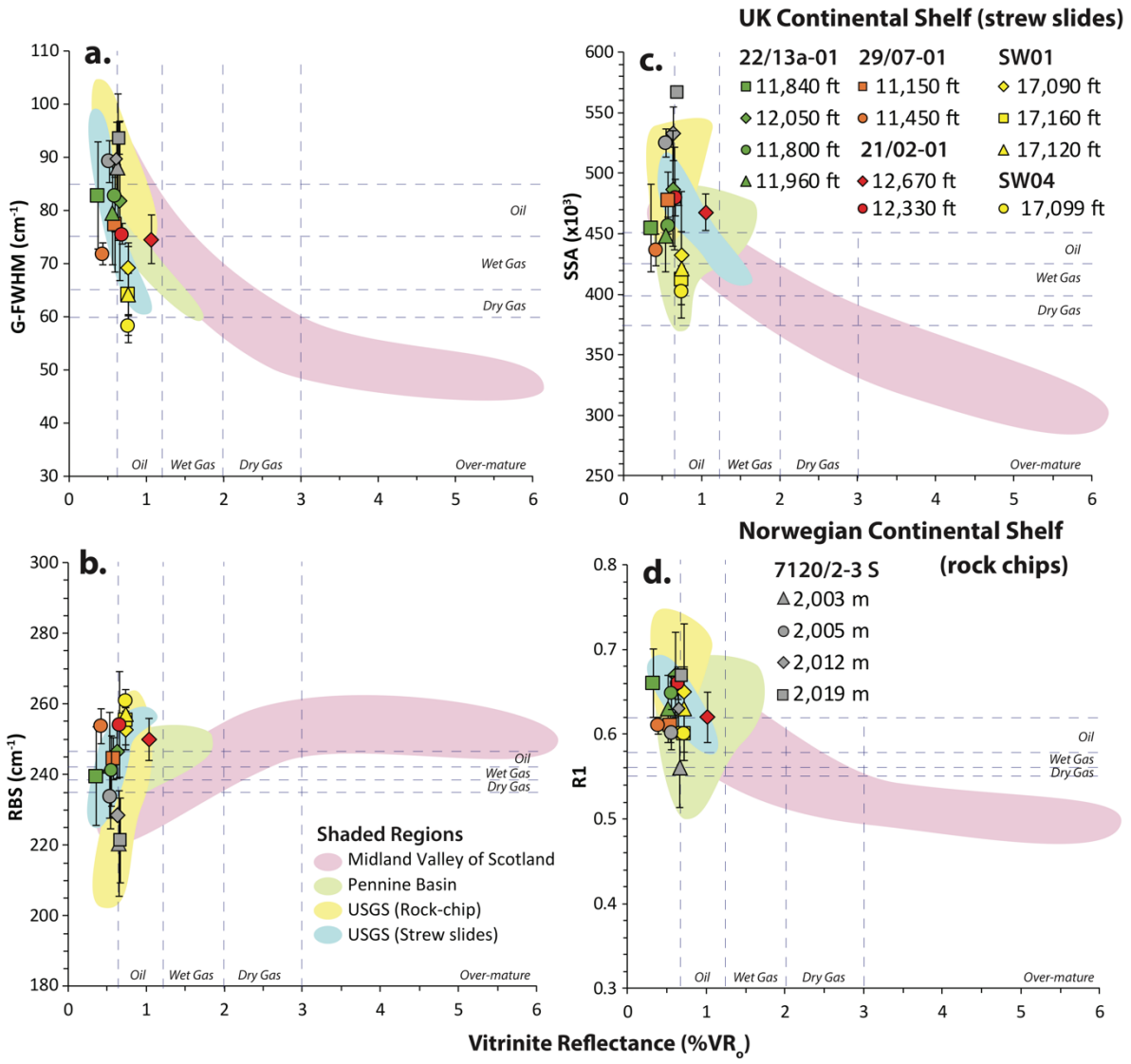


**Figure 8.4.** Comparison of the Raman results for the UK and Norwegian continental shelf samples with VR. The results are superimposed on the areal trends for the Carboniferous and USGS dataset. Note that for the Norwegian samples the VR was calculated from $T_{max}$ using Jarvie et al.'s (2001) equation. **(a)** G-FWHM vs. VR. **(b)** RBS vs. VR. **(c)** SSA vs. VR. **(d)** R1 vs. VR.

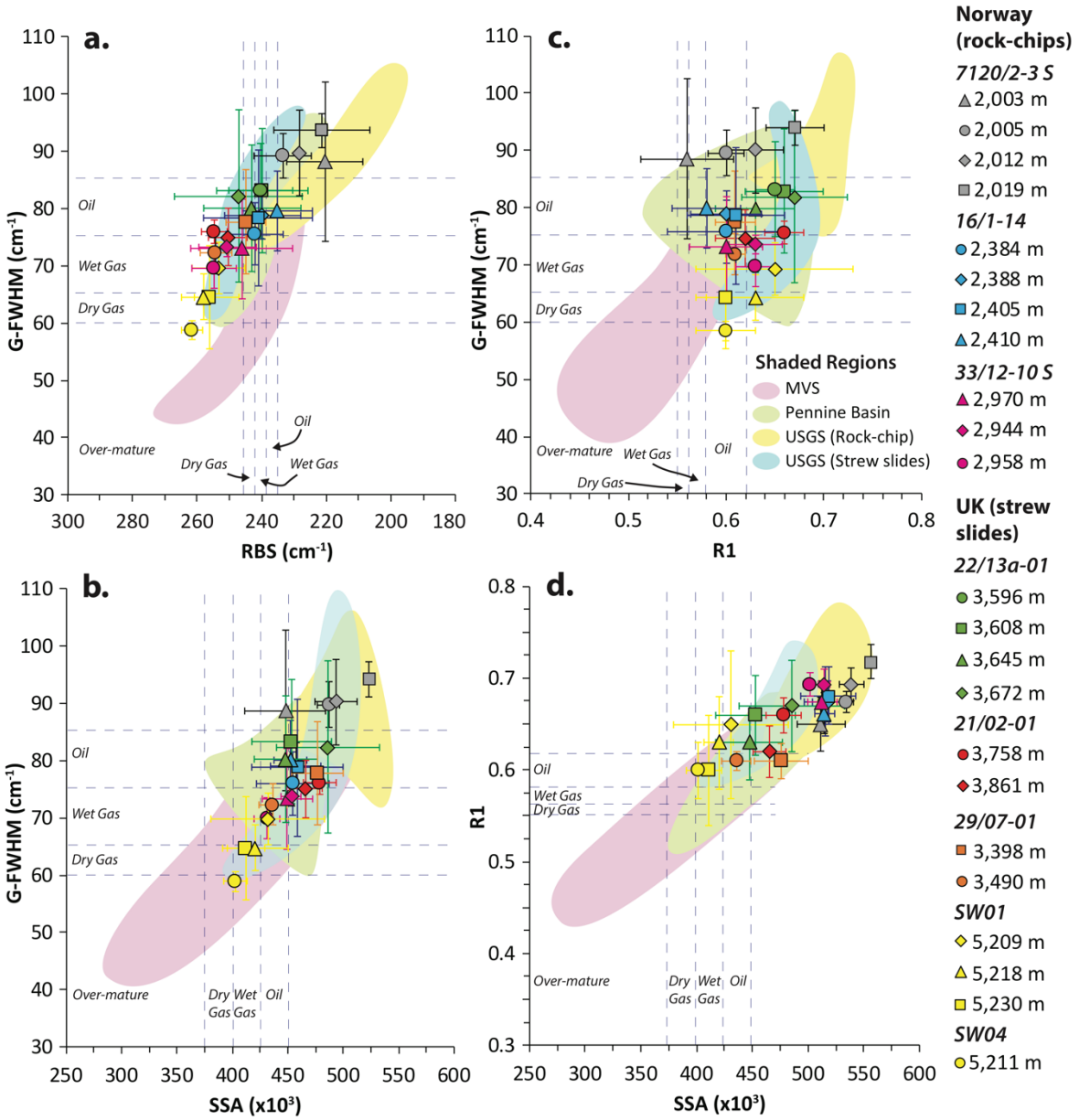


**Figure 8.5.** Cross-plot of the Raman parameter results for the UK and Norwegian continental shelf samples, superimposed on the areal trends for the Carboniferous and USGS dataset. **(a)** G-FWHM vs. RBS. **(b)** G-FWHM vs. SSA. **(c)** G-FWHM vs. R1. **(d)** R1 vs. SSA. MVS–Midland Valley of Scotland. Hydrocarbon zones from Henry et al. (2019).

## 8.6 Conclusion

The chapter demonstrates the need to perform more than one maturity method, as factors such as retardation and contamination may impact the maturity results. Here, we demonstrate that the G-FWHM, SSA and RBS are reliable Raman parameters to determine

the maturity of Type II Jurassic and Late Cretaceous shale samples from the UK and Norwegian continental shelf. Raman spectroscopy may also correct for VR retardation effect that is commonly seen in high pressure boreholes; however, the results from this study do not ascertain this. In order to confirm the validity of this, it is necessary to study a suite of samples with variable depths from a borehole with known retardation. As only four samples from the Shearwater samples are used in this study and they have a very narrow depth range. Raman is also highly advantageous when analysing samples that are contaminated with lignite, as these particles can be easily avoided when analysing either rock-chips or strew slides.

# *Chapter 9* Round-up and the future of Raman spectroscopy as a tool to determine the maturity of organic matter

## 9.1 Main outcomes

A novel, bespoke and rapid Raman automated method that does not perform spectral deconvolution has been developed (Henry et al., 2018; Chapter 4), which processes the raw analytical data and determines several Raman maturity parameters. The method has been calibrated with vitrinite reflectance using a suite of rock-chip samples with a wide maturity range (0.6–6.0 $\%VR_o$; Henry et al., 2019; Chapter 5).

Henry et al.'s (2018) method and calibration curves have been tested on 72 Carboniferous shales and coals from the UK (Henry et al., 2019; Chapter 5) and has successfully predicted equivalent vitrinite reflectance (VR) values that are comparable to measured VR values. The best Raman parameter to predict vitrinite reflectance is the G-band full-width at half-maximum (G-FWHM), which has a calibration curve with an $R^2$ of 0.96. The estimated VR values using the calibration curve, had a strong correlation with the measured VR values for the 72 samples, with an $R^2$ of 0.80. Other notable Raman parameters include the scaled spectrum area (SSA) ($R^2$ of 0.88), R1 ($R^2$ of 0.73) and Raman band separation (RBS) ($R^2$ of 0.65), which have an $R^2$ of 0.75, 0.55 and 0.45 respectively, when correlated with all 72 samples. It is recommended that the other Raman parameters should not be used independently, and rather act as a means to cross-check and corroborate the G-FWHM results.

The Raman method developed here and the G-FHWM, SSA and RBS calibration curves have been successfully extended to several other rock formations of different ages and from different basins:

- Jurassic Kimmeridge Clay and equivalent formations and Cretaceous mudstones from the UK and Norwegian continental shelves.

- Individual outcrop samples provided by the USGS from several USA shale gas plays including the: Marcellus Shale (Middle Devonian), Woodford Shale (Devonian–Mississippian), Boquillas Formation (Upper Cretaceous), Mancos Shale (Upper Cretaceous), Niobrara Formation (Upper Cretaceous) and Green River Shale (Eocene).

The main finding from analyzing the USGS samples is that Henry et al.'s (2019) calibration curve based on unprepared rock chips should not be used for strew slides, as the removal of non-organic components using HCl and HF leads to a reduction or removal of background fluorescence, which impacts the background subtraction processing step. However, removing the non-organic components increases analytical precision, and hence minimizes the bias associated with performing Raman spectroscopy.

The Raman results from the UK and Norwegian continental shelf demonstrate that the G-FWHM, SSA and RBS calibration curve can be applied to different aged rocks and rocks from different basins that have experienced different thermal–pressure histories. It also demonstrates that the G-FWHM, SSA and RBS Raman parameters can be applied on Type II kerogen-bearing sedimentary rocks. Raman results for samples from the high-pressure/high-temperature Shearwater gas field in the central North Sea, indicate that Raman spectroscopy may be used to overcome the issue of inaccurate maturity assessments due to VR retardation. However, due to the small sample size and narrow depth range, results are not conclusive and further work must be undertaken in order to confirm this.

It is strongly advised that multiple maturity methods are performed, as no maturity method is universally applicable to all rock types. Comparing thermal maturity results can help identify and overcome technical, methodological and theoretical discrepancies. For example.

- **Technical:** Different instrumental set-ups, contamination, and operator inexperience can lead to bias in the results.
- **Methodological:** Poor polishing of vitrinite particles can lead to suppressed VR values, while polishing vitrinite particles prior to Raman analysis generates greater analytical scatter, as well as reducing maturity values. Operator inexperience can also lead to misinterpretation of primary vitrinite particles and produce unreliable results.

Not performing solvent extraction of high-maturity rocks (>1.5 %$VR_o$) prior to Rock-Eval pyrolysis, can lead to suppressed $T_{max}$ values and an underestimation of OM maturity, whereas this is not a problem for Raman analysis.

- **Theoretical:** Not all maturity methods are affected by the same kinetic reactions. For example, comparing illite crystallinity with organic matter maturity methods (VR or Raman) can help to determine different thermal conditions. Methods are also age, rock-type, and maturity stage limited; and therefore, a wide selection of maturity tools needs to be at the operator's disposal. Vitrinite reflectance is affected by suppression and retardation and preliminary results in this study demonstrates that the G-FWHM and SSA may be able to correct this.

A portable Raman instrument has the potential to be used on-site for rapid determination of OM maturity, as the data obtained have a similar trend to a bench-top Raman instrument. However, preliminary results suggest that a portable Raman is more suited to coals and not dispersed OM in shales as the laser spot size is too large and there is no control on what is being analysed. This can lead to significant non-linear fluorescence due to incorporating emission from the surrounding non-OM matrix.

## 9.2 What next?

The future of Raman spectroscopy is promising, and it is increasingly being used to determine the thermal maturity of sedimentary and metamorphic rocks, and to study fault movements in structurally complex settings. Nevertheless, there remains several concerns that need to be addressed:

A simple, easy, fast analytical protocol needs to be adopted as an accredited test method to encourage the wider use of Raman spectroscopy. However, it may be the case that different methodologies may be needed and adopted for different applications (e.g. hydrocarbon exploration, metamorphic studies, determining frictional heating in fault rocks).

Excluding deconvolution, background subtraction is the most subjective processing step that is routinely applied to Raman spectra. An unbiased background subtraction method needs to be adopted. Further testing on the simple method developed in this study and by Schito and Corrado (2018), as well as the more complex Lünsdorf et al. (2017) method should be tried

and tested. The bias in background subtraction is mostly associated with the oil and gas exploration thermal maturity zones. In order to completely remove the bias, it may be necessary to isolate the organic matter in shales using mineral acids, as described in Chapters 7 and 8. Background subtraction is mostly linear and easy to perform for coals.

An interlaboratory test between different operators, with different instrumentation, that assesses the most commonly used methods is necessary in order to promote unanimous agreement on the best methodology to be adopted.

Additional reference samples need to be created and circulated, such as the USGS shale geological reference samples used in this thesis from Jubb et al. (2018), and those made available by Lünsdorf et al. (2017). These reference materials need to be characterized and have a suite of organic and inorganic geochemical data, and organic petrology and maturity data derived from multiple methods. A substantial quantity of homogenous material should be available so that samples can be circulated for round-robin exercises, as well as being used to calibrate Raman instruments.

The Raman analysis of samples with different properties, of different ages and from different basins needs to be continued to see whether re-calibration is required for different rocks. So far, this study has demonstrated that the G-FWHM, SSA and RBS calibrations can be used universally when analysing the same sample type (e.g. rock-chip vs. strew slide). Analyzing natural samples with known vitrinite reflectance suppression and retardation also needs to be further investigated.

Further work on the ability to determine different organic types using Raman is needed, which has the potential to allow the organic petrologist to automatically map different organic matter particles for a given area. Novel work has been performed by Schito et al. (2019) in this field, by using a multivariate Principal Component Analysis (PCA) and Partial Least Square - Discriminant Analysis (PLS-DA) method.

This is the first study that has tested the applicability of a portable Raman to determine the thermal maturity of organic matter, which could be applied on-site or in the field. The following questions have been raised regarding the portable Raman instrument capabilities:

- Is the portable Raman only applicable to coals?
- Can the laser spot size be reduced, to avoid the fluorescence caused by the matrix?
- Can a portable microscope be installed so that operators can confidently identify what is being analyzed?

# References

Allen, P.A., Allen, J.R., 2013. Basin Analysis: Principles and Application to Petroleum Play Assessment, Third Edn, Wiley-Blackwell, Oxford, 619pp.

Allwood, C.A., Walter, M.R., Marshall, C.P., 2006. Raman spectroscopy reveals thermal palaeoenvironments of c.3.5 billion-ear-old organic matter. Vibration Spectrosc. 41, 190–197.

Ammar, M.R., Rouzaud, J.N., 2012. How to obtain a reliable structural characterization of polished graphitized carbons by Raman microspectroscopy. J. Raman Spectrosc. 41, 207–211.

Andrews, I.J., 2013. The Carboniferous Bowland Shale gas study: geology and resource estimation. British Geological Survey for Department of Energy and Climate Change, London, UK. https://www.gov.uk/government/publications/bowland-shale-gas-study

Aoya, M., Kouketsu, Y., Endo, S., Shimizu, H., Mizukami, T., Nakamura, D., Wallis, S., 2010. Extending the applicability of the Raman carbonaceous material geothermometer using data from contact metamorphic rocks. J. Metamorph. Geol. 28, 895–914.

Arostegul, J., Arroyo, X., Nieto, F., Bauluz, B., 2019. Evolution of clays in Cretaceous marly series (Álava Block, Basque Cantabrian Basin, Spain): diagenesis and detrital input control. Minerals, 9, 40.

Arrhenius, S., 1889. On the reaction rate of the inversion of non-refined sugar upon souring. Z. Phys. Chem. 4, 226–248.

Baludikay, B., François, C., Sforna, M., Beghin, J., Cornet, Y., Storme, J., Fagel, N., Fontaine, F., Littke, R., Baudet, D., Delvaux, D., Javaux, E., 2018. Raman microspectroscopy, bitumen reflectance and illite crystallinity scale: comparison of different geothermometry methods on fossiliferous Proterozoic sedimentary basins (DR Congo, Mauritania and Australia). Int. J. Coal Geol. 191, 80–94.

Barker, C.E., 1979, Organic geochemistry in petroleum exploration. Am. Assoc. Pet. Geol., Contin, Educ. Course Note Ser. 10, 159.

Barker, C.E., Goldstein, R.H., 1990. Fluid-inclusion technique for determining maximum temperature in calcite and its comparison to the vitrinite reflectance geothermometer. Geology, 18, 1003–1006.

4096 Barnard, P.C., Cooper, B.S., 1981. Oils and source rocks of the North Sea area. In: Illing, L.V., Hobson,
4097 G.D. (Eds.), Petroleum Geology of the Continental Shelf of Northwest Europe. Heyden, London,
4098 Institute of Petroleum, 169–175.

4099 Barzoi, S.C., 2015. Shear stress in the graphitization of carbonaceous matter during the low-grade
4100 metamorphism from the northern Parang Mountains (South Carpathians) - Implications to
4101 graphite geothermometry. Int. J. Coal. Geol. 146, 179–187.

4102 Baskin, D.K., Peters, K.E., 1992. Early Generation Characteristics of a Sulfur-Rich Monterey Kerogen.
4103 Am. Assoc. Pet. Geol. Bull. 76, 1–13.

4104 Batten, D.J., 1996. Palynofacies and petroleum potential. In: Jansonius, J., McGregor, D.C. (Eds.),
4105 Palynology: Principles and Applications. Am. Assoc. Strat. Paly. Found., Dallas, 1065–1084.

4106 Behar, F., Vandenbrouke, M., 1987. Chemical Modelling of Kerogens. Org. Geochem. 11, 15–24.

4107 Beny-Bassez, C., Rouzaud, J.N., 1985. Characterization of carbonaceous materials by correlated
4108 electron and optical microscopy and Raman microspectroscopy. Scanning Electron Microsc. 1,
4109 119–132.

4110 Bernard, S., Benzerara, K., Beyssac, O., Balan, E., Brown, G.E., 2015. Evolution of the macromolecular
4111 structure of sporopollenin during thermal degradation. Heliyon 1, 1–28.

4112 Berner, R.A., Raiswell, R., 1983. Burial of organic carbon and pyrite sulfur in sediments over
4113 Phanerozoic time: a new theory. Geochim. Cosmochim. Acta. 47, 855–862.

4114 Bertrand, R., 1990. Correlations among the reflectances of vitrinite, chitinozoans, graptolites and
4115 scolecodonts. Org. Geochem. 15, 565–574.

4116 Bertrand, R., Malo, M., 2012. Dispersed organic matter reflectance and thermal maturation infour
4117 hydrocarbon exploration wells in the Hudson Bay Basin: regional implications. Geological Survey
4118 of Canada, Report 7066, 54.

4119 Beyssac, O., Goffé, B., Chopin, C., Rouzaud, J.N., 2002. Raman spectra of carbonaceous material in
4120 metasediments: a new geothermometer. J. Metamorph. Geol. 20, 859–871.

4121 Beyssac, O., Goffé, B., Petitet, J-P., Froigneux, E., Moreau, M., Rouzaud, J-N., 2003. On the
4122 characterization of disordered and heterogenous carbonaceous materials by Raman
4123 spectroscopy. Spectrochim, Acta. 59, 2267–2276.

Beyssac, O., Pattison, D.R.M., Bourdelle, F., 2019. Contrasting degrees of recrystallization of carbonaceous material in the Nelson aureole, British Columbia and Ballachulish aureole, Scotland, with implications for thermometry based on Raman spectroscopy of carbonaceous material. J. Metamorph. Geol. 37, 71–95.

Bohacs, K.M., Grawbowski, G.J., Carroll, A.R., Mankeiwitz, P.J., Miskell-Gerhardt, J.R., Schwalbach, J.R., Wegner, M.B., Simo, J.A., 2005. Production, destruction, and dilution – the many paths to source-rock development. In: Harris, N.B. (Eds.) The deposition of organic-carbon-rich sediments; models, mechanisms, and consequences: SEPM Special Publications, 82, 61–101.

Bonal, L., Bourot-Denise, M., Quirico, E., Montagnac, G., Lewin, E., 2007. Organic matter and metamorphic history of CO chondrites. Geochim. Cosmochim. Acta. 71, 1605–1623.

Bonoldi, L., Di Paolo, L., Flego, C., 2016. Vibrational spectroscopy assessment of kerogen maturity in organic-rich source rocks. Vibration. Spectrosc. 87, 14–19.

Bostick, N.H., Alpern, B., 1977. Principles of sampling, preparation and constituent selection for microphotometry in measurement of maturation of sedimentary organic matter. J. Microscopy. 109, 41–47.

Brolly, C., Parnell, J., Bowden, S., 2016. Raman spectroscopy: Caution when interpreting organic carbon from oxidising environments. Planet. Space Sci. 121, 53–59.

Bruce, C.H., 1984. Smectite dehydration - its relation to structural development and hydrocarbon accumulation in northern Gulf of Mexico Basin. AAPG Bull. 68, 673–683.

Burnham, A.K., Sweeney, J.J., 1989. A chemical kinetic model of vitrinite maturation and reflectance. Geochim. Cosmochim. Acta, 53, 2649–2657.

Buseck, P.R., Beyssac, O., 2014. From organic matter to graphite: Graphitization. Elements 10, 421–426.

Cao, S., Neubauer, F., 2019. Graphitic material in fault zones: Implications for fault strength and carbon cycle. Earth-Sci. Rev. 194, 109–124.

Carr, A.D., 2000. Suppression and retardation of vitrinite reflectance, part 1. Formation and significance for hydrocarbon generation. J. Petrol. Geol. 23, 313–343.

Castiglioni, C., Tommasini, M., Zerbi, G., 2004. Raman spectroscopy of polyconjugated molecules and materials: confinement effect in one and two dimensions. Philos. Trans. A. Math. Phys. Eng. Sci. 362, 2425–2459.

Cavanagh, A.J., Di Primio, R., Scheck-Wenderoth, M., Horsfield, B., 2006. Severity and timing of the Cenozoic exhumation in the southwestern Barents Sea. J. Geol. Soc. London. 163, 761–774.

Chen, Z., Liu, J., Elsworth, D., Connell, L., Pan, Z., 2009. Investigation of CO2 injection induced coal-gas interactions. 43rd U.S. Rock Mechanics Sympo. Asheville, NC.

Chen, S., Wu, D., Liu, G., Sun, R., 2017. Raman spectral characteristics of magmatic-contact metamorphic coals from Huainan Coalfield, China. Spectrochim. Acta A: Molec. Biomolec. Spectrosc. 171, 31–39.

Chesire, S., Craddock, P.R., Xu, G., Sauerer, B., Pomerantz, A.E., McCormick, D., Abdallah, W., 2017. Assessing thermal matuirity beyond the reaches of vitrinite reflectance and Rock-Eval pyrolysis: A case study from the Silurian Qusaiba formation. Int. J. Coal. Geol. 180, 29–45.

Childress, L.B., Jacobsen, S.D., 2017. High-pressure high-temperature Raman spectroscopy of kerogen: Relevance to subducted organic carbon. Am. Mineral. 102, 391–403.

Chim, L.K., Yen, J-Y., Huang, S-Y., Liou, Y-S., Tsai, L. L-Y., 2018. Using Raman spectroscopy of carbonaceous materials to track exhumation of an orogenic belt: An example from Eastern Taiwan. J. Asian Earth Sci. 164, 248–259.

Clementz, D.M., 1979. Effect of oil and bitumen saturation on source-rock pyrolysis. AAPG Bull. 63, 2227–2232.

Corrigan, J.D. 1993. Apatite fission-track analysis of Oligocene strata in South Texas, U.S.A.: testing annealing models. Chemical Geology, 104, 227-249.

Court, R.W., Sephton, M.A., Parnell, J., Gilmour, I., 2007. Raman spectroscopy of irradiated organic matter. Geochim. Cosmochim. Acta. 71, 2547–2568.

Coward, M.P., Dewey, J., Mange, M.A., Hempton, M. and Holroyd, J., 2003. Tectonic Evolution. In: Evans, D., Graham, C., Armour, A., Bathurst, P. (Eds.): The Millennium Atlas: Petroleum Geology of the Central and Northern North Sea. 17–33.

4178 Cuesta, A., Dhamelincourt, P., Laureyns, J., 1994. Raman microprobe studies on carbon materials.
4179 Carbon 32, 1523–1532.

4180 Dean, M.T., Turner, N., 1994. Conodont Colour Alteration Index (CAI) values for the Carboniferous of
4181 Scotland. Earth and Environmental Science Transactions of the Royal Sociey of Edinburgh, 85,
4182 211–220.

4183 Delarue, F., Rouzaud, J-N., Derenne, S., Bourbin, M., Westall, F., Kremer, B., Sugitani, K., Deldicque, D.,
4184 Robert, F., 2016. The Raman-derived carbonization continuum: A tool to select the best-preserved
4185 molecular structures in Archean kerogens. Astrobiology 16, 407–417.

4186 Delchini, S., Lahfid, A., Plunder, A., Michard, A., 2016. Applicability of the RSCM geothermometry
4187 approach in a complex tectono-metamorphic context: The Jebilet massif case study (Variscan
4188 Belt, Morocco). Lithos 256–257, 1–12.

4189 Dembicki, H., 2009. Three common source rock evaluation errors made by geologists during prospect
4190 or play appraisals, AAPG Bull. 93, 341–356.

4191 Deming, J.W., Baross, J.A., 1993. The early diagenesis of organic matter: bacterial activity. In: Engel,
4192 M.H., Macko, S.A. (eds). Organic Geochemistry, Principles and Applications. Topics in Geobiology,
4193 Springer, Boston. pp. 119–144.

4194 Dengo, C.A., Røssland, K.G., 1992. Extensional tectonic history of the western Barents Sea In: Larsen,
4195 R.M., Brekke, H., Larsen, B.T., Talleraas, E. (Eds.) Structural and Tectonic Modelling and its
4196 Application to Petroleum Geology edited. Elsevier, Amsterdam, pp. 91–107.

4197 DeVanney, K.F., Stanton, R.W., 1994. Chapter 2: Need for Standardization of Vitrinite Reflectance
4198 Measurements. Fuel and Energy Abstracts, 3, pp. 303.

4199 Domínguez, R., 2007. Structural evolution of the Penguins Cluster, UK northern North Sea. J. Geol. Soc.
4200 London. 292, 25–48.

4201 Dow, W.G., 1978. Petroleum source beds on continental slopes and rises. AAPG Bulletin 62, 9 1584–
4202 1606.

4203 Du, J., Geng, A., Liao, Z., Cheng, B., 2014. Potential Raman parameters to assess the thermal evolution
4204 of kerogens from different pyrolysis experiments. J. Anal. Appl. Pyrolysis 107, 242–249.

Duggan, C.M.B., Clayton, G., 2008. Colour change in the acritarch Veryhachium as an indicator for thermal maturity. GeoArabia. 13, 125–136.

Eichmann, S.L., Jacobi, D., Haque, M.H., Burnham, N.A., 2018. Non-destructive investigation of the thermal maturity and mechanical properties of source rocks. J. Petrol. Geol. 41, 421–446.

Endo, S., Wallis, R., Tsuboi, M., Torres de Leon, R., Solari, L.A., 2012. Metamorphic evolution of lawsonite eclogites from the southern Motagua fault zone, Guatemala: Insights from phase equilibria and Raman spectroscopy. J. Metamorph. Geol. 30, 143–164.

Engel, M.H., Macko, S.A., 1993. Organic Geochemistry: Principles and Applications. Springer.

Espitalie, J., Laporte, J.L., Madec, M., Marquis, F., Leplat, P., Paulet, J., Boutefeu, A., 1977. Méthode rapide de caractérisation des roches mères, de leur potential pétrolier et de leur degré d'évolution. Rev. Inst. Fr. Pétrol. 32, 23–42.

Evans, D., Graham, C. Armour, A., Bathurst, P. 2003. The millennium atlas: Petroleum geology of the central and northern North Sea: Geological Society, London.

Ewen, S., Dent, G., 2005. Modern Raman Spectroscopy – A Practical Approach. John Wiley & Sons, Ltd.

Færseth, R.B., 1996. Interaction of Permo–Triassic and Jurassic extensional fault–blocks during the development of the northern North Sea. J. Geol. Soc. 153. 931–944.

Faleide, J.I., Gudlaugsson, T., Jacquart, G., 1984. Evolution of the western Barents Sea. Mar. Petrol. Geol. 1, 129–136.

Faleide, J.I., Vågnes, E., Gudlaugsson, S.T., 1993. Late Mesozoic-Cenozoic evolution of the southwestern Barents Sea. Geol. Soc. London. Petrol. Geol. Conf. series. 4, 933–950.

Faleide, J.I., Bjørlykke, K., Gabrielsen, R.H., 2015. Geology of the Norwegian continental shelf. In: Bjørlykke, K. (Ed.), Petroleum Geoscience: from sedimentary environments to rock physics. Springer-Verlag, Berlin, 603-605.

Ferrari, A.C., Robertson, J., 2001. Resonant Raman spectroscopy of disordered, amorphous, and diamondlike carbon. Phys. Review B. 64, 075414.

Ferralis, N., Matys, E.D., Knoll, A.H., Hallmann, C., Summons, R. E., 2016. Rapid, direct and non-destructive assessment of fossil organic matter via micro-Raman spectroscopy. Carbon. 108, 440–449.

Ferraro, J.R., Nakamoto, K., Brown, C.W., 2003. Introductory Raman spectroscopy. Elsevier. pp 434.

Ferreiro Mählmann, R., Bozkaya, Ö., Potel, S., Le Bayon, R., Segvić, B., Nieto, F., 2012. The pioneer work of Bernard Kübler and Martin Frey in very low-grade metamorphic terranes: paleo-geothermal potential of variation in Kübler-Index/organic matter reflectance correlations. A review. Swiss J. Geosci. 105, 121–152.

Fomina, E., Kozlov, E., Lokhov, K., Lokhova, O., Bocharov, V., 2019. Carbon sources and the graphitization of carbonaceous matter in Precambrian rocks of the Keivy Terrane (Kola Peninsula, Russia). Minerals. 9, 94.

Fraser, S., Robinson, A., Johnson, H., Underhill, J., Kadolsky, D., Connell, R., Johannessen, P. and RAVNAS, R., 2003. Upper Jurassic. In: Evans, D., Graham, C., Armour, A., Bathurst, P. (Eds.). The Millennium Atlas: Petroleum Geology of the Central and Northern North Sea. 157–189.

Furuichi, H., Ujiie, K., Kouketsu, Y., Saito, T., Tsutsumi, A., Wallis, S., 2015. Vitrinite reflectance and Raman spectra of carbonaceous material as indicators of frictional heating on faults: Constraints from friction experiments. Earth Planet Sci. Lett. 424,191–200.

Gaarenstroom, L., Tromp, R.A.J., De Jong, M.C., Brandenburg, A.M., 1993. Overpressures in the Central North Sea: implications for trap integrity and drilling safety. In: Parker, J.R. (ed.) Petroleum Geology of North west Europe: Proceedings of the 4th Conference. Geol. Soc. London, 2, 1305–1313.

Gabrielsen, R.H., Færseth, R.B., Jensen, L.N., Kalheim, J.E., Riis, F., 1990. Structural elements of the Norwegian Continental Shelf. Part I: The Barents Sea Region. Norwegian Petroleum Directorate, Bull. 6, 5–7.

Gac, S., Hansford, P.A., Faleide, J.I., 2018. Basin modelling of the SW Barents Sea. Mar. Petrol. Geol. 95, 167–187.

Gautier, D.L., 2005, Kimmeridgian Shales Total Petroleum System of the North Sea Graben Province: U.S. Geological Survey Bulletin 2204-C, 24 p.

Gernigon, L., Brönner, M., Roberts, D., Olesen, O., Nasuti, A., Yamasaki, T., 2014. Crustal and basin evolution of the southwestern Barents Sea: from Caledonian orogeny to continental breakup. Tectonics, 33, 347–373.

Golubev, Y. A., Martirosyan, O.V., Kuzmin, D.V., Isaenko, S.I., Makeev, B.A., Antonets, I.V., Utkin, A.A. 2019. Transformations of natural bitumens of different degrees of metamorphism at a low vacuum heating in the temperature range of 400–1000 °C. J. Petrol. Sci. Eng. 173, 315–325.

Goryl, M., Banasik, K., Smolarek-Lach, J., Marynowski, L., 2019. Utility of Raman spectroscopy in estimates of the thermal maturity of Ediacaran organic matter: An example from the East European Craton. Geochemistry, in press doi.org/10.1016/j.chemer.2019.06.001.

Green P.F., Thomson, K., Hudson, J.D., 2001. Recognition of tectonic events in undeformed regions: contrasting results from the Midland Platform and East Midlands Shelf, Central England. J. Geol. Soc. 158, 59–73.

Guedes, A., Noronha, F., Prieto, A.C., 2005. Characterisation of dispersed organic matter from lower Palaeozoic metasedimentary rocks by organic petrography, X-ray diffraction and micro-Raman spectroscopy analyses. Int. J. Coal Geol. 62, 237–249.

Guedes, A., Valentim, B., Prieto, A.C., Rodrigues, S., Noronha, F., 2010. Micro-Raman spectroscopy of collotelinite, fusinite and macrinite. Int. J. Coal Geol. 83, 415–422.

Guedes, A., Valentim, B., Prieto, A.C., Noronha, F., 2012. Raman spectroscopy of coal macerals and fluidized bed char morphotypes. Fuel. 97, 443–449.

Hackley, P. C., Burruss, R. C., Boyd, J., 2013. Application of excitation-emission fluorescence microscopy to thermal maturity of geological samples. Geological Society of America Abstracts with Programs, 45, 650.

Hackley, P.C., Cardott, B.J., 2016. Application of organic petrography in North American shale petroleum systems: A review. Int. J. Coal Geol. 163, 8–51.

Hackley, P.C., Lewan, M., 2018. Understanding and distinguishing reflectance measurements of solid bitumen and vitrinite using hydrous pyrolysis: Implications to petroleum assessment. AAPG Bull. 102, 6, 1119–1140.

Hackley, P.C., Lünsdorf, N.K., 2018. Application of Raman spectroscopy as thermal maturity probe in shale petroleum systems: Insights from natural and artificial maturation series. Energy Fuel. 32, 11190–11202.

Hackley, P.C., Araujo, C.V., Borrego, A.G., Bouzinos, A., Cardott, B., Cook, A.C., Eble, C., Flores, D., Gentzis, T., Gonçalves, P.A., Mendonça-Filho, J.G., Hámor-Vidó, M., Jelonek, I., Kommeren, K., Knowles, W., Kus, J., Mastalerz, M., Menezes, T.R., Newman, J., Oikonomopoulos, I.K., Pawlewicz, M., Pickel, W., Potter, J., Ranasinghe, P., Read, H., Reyes, J., Rodriguez, G.D.L.R., Fernandes de Souza, I.V.A., Suarez-Ruiz, I., Sýkorová, I., Valentine, B.J., 2015. Standardization of reflectance measurements in dispersed organic matter: Results of an exercise to improve interlaboratory agreement. Mar. Petrol. Geol. 59, 22–34.

Hara, H., Hara, K., 2018. Radiolarian and U–Pb zircon dating of Late Cretaceous and Paleogene Shimanto accretionary complexes, southwest Japan: Temporal variations in provenance and offset across an out-of-sequence thrust. J. Asian Earth Sci. 170, 29–44.

Hara, H., Kurihara, T., Mori, H., 2013. Tectono-stratigraphy and low-grade metamorphism of Late Permian and Early Jurassic accretionary complexes within the Kurosegawa belt, southwest Japan: Implications for mechanisms of crustal displacement within active continental margin. Tectonophysics 592, 80–93.

Hartkopf-Fröder, C., Königshof, P., Littke, R., Schwarzbauer, J., 2015. Optical thermal maturity parameters and organic geochemical alteration at low grade diagenesis to anchimetamorphism: A review. Int. J. Coal Geol. 150–151, 74–119.

Henriksen, E., Bjørnseth, H.M., Hals, T.K., Heide, T., Kiryukhina, T., Kløvjan, O.S., Larssen, G.B., Ryseth, A.E., Rønning, K., Sollid, K., StoupakovaHenry, A., 2011. Chapter 17 Uplift and erosion of the greater Barents Sea: impact on prospectivity and petroleum systems. Geological Society, Lonon, Memoirs. 35, 271–281.

Henry, D.G., Jarvis, I., Gillmore, G., Stephenson, M., Emmings, J., 2018. Assessing low-maturity organic matter in shales using Raman spectroscopy: Effects of sample preparation and operating procedure. Int. J. Coal Geol. 191, 135–151.

Henry, D.G., Jarvis, I., Gillmore, G., Stephenson, M., 2019. A rapid method for determining organic matter maturity using Raman spectroscopy: Application to Carboniferous organic-rich mudstones and coals. Int. J. Coal Geol. 203, 87–98.

Hilchie L.J., Jamieson, R.A. 2014. Graphite thermometry in a low-pressure contact aureole, Halifax. Lithos. 208–209, 21–33.

Hinrichs, R., Brown, M.T., Vasconcellos, M.A.Z., Abrashev, M.V., Kalkreuth, W., 2014. Simple procedure for an estimation of the coal rank using micro-Raman spectroscopy. Int. J. Coal Geol. 136, 52–58.

Hirono, T., Maekawa, Y., Yabuta, H., 2015. Investigation of the records of earthquake slip in carbonaceous materials from the Taiwan Chelungpu fault by means of infrared and Raman spectroscopies. Geochem. Geophys. Geosyst. 16, 1233–1253.

Hoinkes, G., Hauzenberger, C.A., Schmid, R., 2005. Metamorphic rocks: classification, nomenclature, and formation. In: Encyclopedia of Geology, Selley R., Cocks, R., Plimer, I. 386–402.

Hou Y., Zhang, K., Wang, F., He, S., Dong, T., Wang, C., Qin, W., Xiao, Y., Tang, B., Yu, R., Du, X., 2019. Structural evolution of organic matter and implications for graphitization in overmature marine shales, south China. Marine Petrol. Geol. 109, 304–316.

Houseknecht, D.W., Weesner, C.M.B., 1997. Rotational reflectance of dispersed vitrinite from the Arkoma basin. Org. Geochem. 26, 191-206.

Hu, S., Evans, K., Craw, D., Rempel, K., Bourdet, J., Dick, J., Grice, K., 2015. Raman characterization of carbonaceous material in the Macraes orogenic gold deposit and metasedimentary host rocks, New Zealand. Ore Geol. Rev. 70, 80–95.

Huang, E.P., Huang, E., Yu, S-C., Chen, Y-H., Lee, J-S., Fang, J-N., 2010. In situ Raman spectroscopy on kerogen at high temperatures and high pressures. Phys. Chem. Mineral. 37, 593–600.

Huber B.T., Hodell D.A., Hamilton C.P., 1995. Middle-Late Cretaceous climate of the southern high latitudes: Stable isotopic evidence for minimal equator-to-pole thermal gradients. Geol. Soc. Am. Bull.107, 1164–1191.

Hurford. A.J., 1986. Cooling and uplift patterns in the Lepontine Alps. South Central Switzerland and an age of vertical movement on the Insubric fault line: Contributions to Mineralogy and Petrology. 92, 413–427.

Ibach, J., 1982. Relationship between sedimentation rate and total organic carbon in ancient marine sediments. AAPG Bulletin. 66, 170–188.

Inan, S., Goodarzi, F., Mumm, A.S., Arouri, K., Qathami, S., Ardakani, O.H., Inan, T., Tuwailib, A.A., 2016. The Silurian Qusaiba Hot Shales of Saudi Arabia: An integrated assessment of the thermal maturity. Int. J. Coal Geol. 159, 107–119.

ISO 7404-1., 2016. Methods for the petrographic analysis of coals – Part 1: Vocabulary. International Organization for Standardization, 3rd edition, Geneva, Switzerland, 12 pp.

ISO 7404-2., 2009. Methods for the petrographic analysis of coals – Part 2: Methods of preparing coal samples. International Organization for Standardization, 3rd edition, Geneva, Switzerland, 12 pp.

ISO 7404-3., 2009. Methods for the petrographic analysis of coals – Part 3: Method of determining maceral group composition International. Organization for Standardization, 3rd edition, Geneva, Switzerland, 7 pp.

ISO 7404-5., 2009. Methods for the petrographic analysis of coals – Part 5: Method of determining microscopically the reflectance of vitrinite. International Organization for Standardization, 3rd edition, Geneva, Switzerland, 14 pp.

Ito, K., Ujiie, K., Kagi, H., 2017. Detection of increased heating and estimation of coseismic shear stress from Raman spectra of carbonaceous material in pseudotachylytes. Geophys. Res. Lett. 44, 1749–1757.

Jarvie, D.M., 2012. Shale resource systems for oil and gas: Part 1 - Shale-gas resource systems, in J. A. Breyer (ed.). Shale reservoirs - Giant resources for the 21st century. AAPG Mem. 97, 69–87.

Jarvie, D.M., Claxton, B.L., Henk, F., Breyer, J.T., 2001. Oil and shale gas from the Barnett Shale, Fort Worth basin, Texas. AAPG Annu. Meet. Progr. 10, A100.

Jarvie, D.M., Lundell, L.L., 2001. Amount, type, and kinetics of thermal transformation of organic matter in the Miocene Monterey Formation, in: Isaacs, C.M., Rullkotter, J. eds., The Monterey Formation: From rocks to molecules: New York, Columbia University Press, Chapter 15. 268 – 295.

Jarvie, D.M., Morelos, A., Han, Z., 2001. Detection of pay zones and pay quality, Gulf of Mexico: Application of geochemical techniques. Gulf Coast Association of Geological Societies Transactions. 51, 151–160.

Jarvie, D.M, Hill, R.J., Pollastro, R M., 2005. Assessment of gas potential and yields from shales: the Barnet Shale model, in Cardott, B. J. (ed.), Unconventional energy resources in the southern Midcontinent, Oklahoma Geological Survey Circular. 110, 37-50.

4372 Jarvie, D.M., Hill, R.J., Ruble, T.E., Pollastro, R.M., 2007. Unconventional shale gas systems: The
4373 Mississippian Barnett Shale of north-central Texas as one model for thermogenic shale gas
4374 assessment, in: Hill, R.J., Jarvie, D.M., 2008. eds., AAPG Bulletin Special Issue: Barnett Shale. 90,
4375 475 –499.

4376 Jarvie, D. M., 2012. Shale resource systems for oil and gas: Part 1 - Shale-gas resource systems, in: J.
4377 A. Breyer, ed., Shale reservoirs - Giant resources for the 21st century: AAPG Memoir. 97, 69–87.

4378 Jehlička, J., Beny, C., 1999. First and second order Raman spectra of natural highly carbonified organic
4379 compounds from metamorphic rocks. J. Molec. Struct. 480–481, 541–545.

4380 Jehlička, J., Urban, O., Pokorný, J., 2003. Raman spectroscopy of carbon and solid bitumens in
4381 sedimentary and metamorphic rocks. Spectrochim. Acta A Mol. Biomolec. Spectrosc. 59, 2341–
4382 2352.

4383 Jubb, A.M., Botterell, P.J., Birdwell, J.E., Burruss, R.C., Hackley, P.C., Valentine, D.J., Hatcherian, J.J.,
4384 Wilson, S.A., 2018. High microscale variability in Raman thermal maturity estimates from shale
4385 organic matter. Int. J. Coal Geol. 199, 1–9.

4386 Jurdik, K., Rantitsch, G., Rainer, T.M., Árkai, P., Tomljenovic, B., 2008. Alpine metamorphism of organic
4387 matter in metasedimentary rocks from Mt. Medvednica (Croatia). Swiss J. Geosci. 101, 605–616.

4388 Kalkreutha, W., Sherwoodb, N., Cioccaria, G., Corrêa da Silvaa, Z., Silvaa, M., Zhongc, N., Zufad, L.,
4389 2003. The application of FAMM (Fluorescence Alteration of Multiple Macerals) analyses for
4390 evaluating rank of Paraná Basin coals, Brazil. Int. J. Coal Geol. 57, 167–185

4391 Kaneki, S., Hirono, T., 2018. Kinetic effect of heating rate on the thermal maturity of carbonaceous
4392 material as an indicator of frictional heat during earthquakes. Earth Planet. Space 70:92
4393 doi:10.1186/s40623-018-0868-7.

4394 Kaneki, S., Hirono, T., 2019. Diagenetic and shear-induced transitions of frictional strength of carbon-
4395 bearing faults and their implications for earthquake rupture dynamics in subduction zones. Sci.
4396 Rep. 9, 7884.

4397 Kaneki, S., Hirono, T., Mukoyoshi, H., Sampei, Y., Ikehara, M., 2016. Organochemical characteristics of
4398 carbonaceous materials as indicators of heat recorded on an ancient plate-subduction fault.
4399 Geochem. Geophys. Geosyst. 17, 2855–2868.

4400 Kaneki, S., Ichiba, T., Hirono, R., 2018. Mechanochemical effect on maturation of carbonaceous
4401 material: Implications for thermal maturity as a proxy for temperature in estimation of coseismic
4402 slip parameters. Geophys. Res. Lett. 45, 2248–2256.

4403 Katz, B.J., 1995. The Green River Shale: an Eocene carbonate lacustrine source rock. In Katz, B.J. ed.,
4404 Petroleum Source Rocks. Berlin, Springer-Verlag. 309–332.

4405 Kelemen, S.R., Fang, H.L., 2001. Maturity trends in Raman spectra from kerogen and coal. Energy Fuel
4406 15, 653–658.

4407 Kendall, G.St.C., Chiarenzelli, J. Hassa, H.S., 2009. World source rock potential through geological time:
4408 A function of basin restriction, nutrient level, sedimentation rate, and sea-level rise. Search and
4409 Discovery Article, 40472.

4410 Khatibi, S., Ostadhassan, M., Tuschel, D., Gentzis, T., Bubach, B., Carvajal-Ortiz, H., 2018a. Raman
4411 spectroscopy to study thermal maturity and elastic modulus of kerogen. Int. J. Coal. Geol. 185,
4412 103–118.

4413 Khatibi, S., Ostadhassan, M., Tuschel, D., Gentzis, T., Carvajal-Ortiz, H., 2018b. Evaluating molecular
4414 evolution of kerogen by Raman spectroscopy: Correlation with optical microscopy and Rock-Eval
4415 pyrolysis. Energies 11, 1406.

4416 Khatibi, S., Ostadhassan, M., Aghajanpour, A., 2018c. Raman spectroscopy: An analytical tool for
4417 evaluating organic matter. J. Oil Gas Petrochem. Sci. 1, 28–33.

4418 Khatibi, S., Ostadhassan, M., Hackley, P., Tuschel, D., Abarghani, A., Bubach, B., 2019. Understanding
4419 organic matter heterogeneity and maturation rate by Raman spectroscopy. Int. J. Coal Geol. 206,
4420 46–64.

4421 Kirilova, M., Toy, V., Rooney, J.S., Giorgetti, C., Gordon, K.C., Collettini, C., Takeshita, T., 2018.
4422 Structural disorder of graphite and implications for graphite thermometry. Solid Earth 9, 223–
4423 231.

4424 Kitamura, M., Mukoyoshi, H., Fulton, P.M., Hirose, T., 2012. Coal maturation by frictional heat during
4425 rapid fault slip. Geophys. Res. Lett. 39, 1–5.

4426 Kribek, B., Hrabal, J., Landais, P., Hladíkova, J., 1994. The association of poorly ordered graphite, coke
4427 and bitumnes in greenschist facies rocks of the Poniklá Group, Lugicum, Czech Republic: The

4428 results of graphitization of various types of carbonaceous matter. J. Metamorph. Geol. 12, 493–
4429 503.

4430 Kouketsu, Y., Mizukami, T., Mori, H., Endo, S., Aoya, M., Hara, H., Nakamura, D., Wallis, S., 2014. A
4431 new approach to develop the Raman carbonaceous material geothermometer for low grade
4432 metamorphism using peak width. Island Arc 23, 33–50.

4433 Kouketsu, Y., Shimizu, I., Wang, Y., Yao, L., Ma, S., Shimamoto, T., 2017. Raman spectra of
4434 carbonaceous materials in a fault zone in the Longmenshan thrust belt, China: Comparisons with
4435 those of sedimentary and metamorphic rocks. Tectonophysics 699, 129–145.

4436 Kouketsu, Y., Tsai, C.H., Enami, M., 2019a. Discovery of unusual metamorphic temperatures in the Yuli
4437 belt, eastern Taiwan: New interpretation of data by Raman carbonaceous material
4438 geothermometry. Geology. 47, 522–526.

4439 Kouketsu, Y., Miyake, A., Igami, Y., Taguchi, T., Kagi, H., Enami, M., 2019b. Drastic effect of shearing
4440 on graphite microtexture: attention and application to Earth science. Prog. Earth Planet. Sci. 6, 23
4441 doi.org/10.1186/s40645-019-0271-4.

4442 Kuo, L.W., Felice, F.D., Spagnuolo, E., Di Toro, G., Song, S.R., Aretusini, S., Li, H., Suppe, J., Si, J., Wen,
4443 C.Y., 2017. Fault gouge graphitization as evidence of past seismic slip. Geology 45, 979–982.

4444 Kuo, L.W., Huang, J.R., Fang, J.N., Si, J., Li, H., Song, S.R., 2018. Carbonaceous materials in the fault
4445 zone of the Longmenshan Falt Belt: 1. Signatures within the deep Wenchuan earthquake fault
4446 zone and their implications. Minerals. 8, 385.

4447 Lahfid, A., Beyssac, O., Deville, E., Negro, F., Chopin, C., Goffé, B., 2010. Evolution of the Raman
4448 spectrum of carbonaceous material in low-grade metasediments of the Glarus Alps (Switzerland).
4449 Terra Nova 22, 354-360.

4450 Landis, C.A. 1971. Graphitisation of dispersed carbonaceous material in metamorphic rocks. Contrib.
4451 Mineral. Petrol. 30, 34–45.

4452 Legall, F.D., Barnes, C.R., MacQueen, R., 1981. Thermal maturation, burial history and hotspot
4453 development, Paleozoic strata of Southern Ontario - Quebec, from conodont and acritarch colour
4454 alteration studies. Bull. Canadian Petrol. Geol. 29, 492–539.

4455 Lespade, P., Al-Jishi, R., Dresselhaus, M.S., 1982. Model for Raman scattering from incompletely
4456 graphitized carbons. Carbon 20, 427–431.

4457 Lewis, I.R., Edwards, H.G.M., 2001. Handbook of Raman spectroscopy: from the research laboratory
4458 to the process line. Marcel Dekker, Inc.

4459 Li, X., Hayashi, J-I., Li, C-Z., 2006. FT-Raman spectroscopic study of the evolution of char structure
4460 during the pyrolysis of a Victorian brown coal. Fuel 85, 1700–1707.

4461 Li, C.Z., 2007. Some recent advances in the understanding of the pyrolysis and gasification behaviour
4462 of Victorian brown coal. Fuel. 1664–1683.

4463 Liu, D., Xiao, X., Tian, H., Min, Y., Zhou, Q., Cheng, P., Shen, J., 2013. Sample maturation calculated
4464 using Raman spectroscopic parameters for solid organics: Methodology and geological
4465 applications. Chin. Sci. Bull. 58, 1285–1298.

4466 Liu, J., Li, H., Zhang, J., Zhang, B., 2016. Origin and formation of carbonaceous material veins in the
4467 2008 Wenchuan earthquake fault zone. Earth Planets and Space. 68:19.

4468 Lo, H.B., Wilkins, R.W.T., Ellacott, M., Buckingham C.P., 1997. Assessing the maturity coals and other
4469 rocks from North America using the fluorescence alteration of multiple macerals (FAMM)
4470 technique. Int. J. Coal Geol. 33, 67–71.

4471 Lünsdorf, N.K., 2016. Raman spectroscopy of dispersed vitrinite - Methodical aspects and correlation
4472 with reflectance. Int. J. Coal Geol. 153, 75–86.

4473 Lünsdorf, N.K., Lünsdorf, J.O., 2016. Evaluating Raman spectra of carbonaceous matter by automated,
4474 iterative curve-fitting. Int. J. Coal. Geol. 160–161, 51–62.

4475 Lünsdorf, N.K., Dunkl, I., Schmidt, B.C., Rantitsch, G., von Eynatten, H., 2014. Towards a higher
4476 comparability of geothermometric data obtained by Raman spectroscopy of carbonaceous
4477 material. Part I: Evaluation of biasing factors. Geostand. Geoanal. Res. 38, 73–94.

4478 Lünsdorf, N.K., Dunkl, I., Schmidt, B.C., Rantitsch, G., von Eynatten, H., 2017. Towards a higher
4479 comparability of geothermometric data obtained by Raman spectroscopy of carbonaceous
4480 material. Part 2: A revised geothermometer. Geostand. Geoanal. Res. 41, 593-612

4481 Lupoi, J.S., Fritz, L.P., Parris, T.M., Hackley, P.C., Solotky, L., Eble, C.F., Schlaegle, S., 2017. Assessment
4482 of thermal maturity trends in Devonian–Mississippian source rocks using Raman spectroscopy:
4483 Limitations of peak-fitting method. Front. Energy Res. 5, 24.

Lupoi, J.S., Fritz, L.P. Hackley, P.C., Solotky, L., Weislogel, A., Schlaegle, S., 2018. Quantitative evaluation of vitrinite reflectance and atomic O/C in coal using Raman spectroscopy and multivariate analysis. Fuel. 230, 1–8.

Lupoi, J.S., Hackley, P.C., Birsic, E., Fritz, L.P., Solotky, L., Weislogel, A., Schlaegle, S., 2019. Quantitative evaluation of vitrinite reflectance in shale using Raman spectroscopy and multivariate analysis. Fuel 254, 115573 doi.org/10.1016/j.fuel.2019.05.156.

Mählmann, R.F., Le Bayon, R., 2016. Vitrinite and vitrinite like solid bitumen reflectance in thermal maturity studies: Correlations from diagenesis to incipient metamorphism in different geodynamic settings. Int. J. Coal Geol. 157, 52–73.

Malusà, M.G., Fitzgerald, P.G., 2019. Fission-Track Thermochronology and its Application to Geology, Springer.

Marques, M., Suárez-Ruiz, I., Flores, D., Guede, A., Rodrigues, S., 2009. Correlation between optical, chemical and micro-structural parameters of high-rank coals and graphite. Int. J. Coal Geol. 77, 377–382.

Marshall, J.E.A., 1991. Quantitative spore colour. J. Geol. Soc. London. 148, 223–233.

Marshall, C., Javaux, E., Knoll, A., Walter, M., 2005. Combined micro-Fourier transform infrared (FTIR) spectroscopy and micro-Raman spectroscopy of Proterozoic acritarchs: A new approach to palaeobiology. Precamb. Res. 138, 208–224.

Mathew, G., De Sarker, S., Pande, K., Dutta, S., Ali, S., Rai, A., Netrawali, S., 2013. Thermal metamorphism of the Arunachal Himalaya, India: Raman thermometry and thermochronological constraints on the tectono-thermal evolution. Int. J. Earth Sci. 102, 1911–1936.

McNeil, D.H., Schulze, H.G., Matys, E., Bosak, T., 2016. Raman spectroscopic analysis of carbonaceous matter and silica in the test walls of recent and fossil agglutinated foraminifera. AAPG Bull. 99, 1081–1097.

Merriman, R.J., Kemp, S.J., 1996. Clay minerals and sedimentary basin maturity. Min. Soc. Bull. 111, 7–8.

Meyer, K.M., Ridgwell, A., Payne, J.L., 2016. The influence of the biological pump on ocean chemistry: implications for long-term trends in marine redox chemistry, the global carbon cycle, and marine animal ecosystems. Geobiology, 14, 207–219.

Mészáros, E., Varga, A., Raucsik, B., Benkó, Z., Heincz, A., Hauzenberger, C.A., 2019. Provenance and Variscan low-grade regional metamorphism recorded in slates from the basement of the (SW Hungary). Int. J. Earth Sci. 1–23.

Mi, J., He, K., Fan, J., Hu, G., Zhang, B., 2019. Thermal maturity determination for oil prone organic matter based on the Raman spectra of artificial matured samples. Vib. Spectrosc. 102940, in press doi.org/10.1016/j.vibspec.2019.102940.

Min, W., Zhongsheng, L., 2016. Thermal maturity evaluation of sedimentary organic matter using laser Raman spectroscopy. Acta Petrolei Sinica. 37, 1129–1136.

Mishra, V., Sharma, M., Chakravarty, S., Banerjee, A., 2016. Changes in organic structure and mineral phases transformation of coal during heat treatment on laboratory scale. Int. J Coal Sci. Tech. 3, 418–428.

Monaghan, A.A., 2014. The Carboniferous shales of the Midland Valley of Scotland: geology and resource estimation. British Geological Survey for Department of Energy and Climate Change, London, UK. http://nora.nerc.ac.uk/id/eprint/514893.

Mori, H., Mori, N., Wallis, S., Westaway, R., Annen, C., 2017. The importance of heating duration for Raman CM thermometry: Evidence from contact metamorphism around the Great Whin Sill intrusion, UK. J. Metamorph. Geol. 35, 165–180.

Mørk, A., Embry, A.F., Weitschat, W., 1989. Triassic transgressive-regressive cycles in the Barents Sea, Svlbard and Barents Shelf. In: COLLINSON, J.D., (ed.) Correlation in Hydrocarbon Exploration. Graham & Trotman, London, pp. 113-156.

Muirhead. D.K., Parnell, J., Taylor, C., Bowden, S.A., 2012. A kinetic model for the thermal evolution of sedimentary and meteoritic organic carbon using Raman spectroscopy. J. Anal. Appl. Pyrolysis. 96, 153–161.

Muirhead, D.K., Parnell, J., Spinks, S., Bowden, S.A., 2017a. Characterization of organic matter in the Torridonian using Raman spectroscopy. In: Brasier, A.T., Mcilroy, D., Mcloughlin, N. (Eds) Earth System Evolution and Early Life: A Celebration of the Work of Martin Brasier. Geol. Soc. London Spec. Publ. 448, 71–80.

Muirhead, D.K., Bowden, S.A., Parnell, J., Schofield, N. 2017b. Source rock maturation due to igneous intrusion in rifted margin petroleum systems. J. Geol. Soc. London 174, 979.

Mukhopadhyay, P.K., Dow, W.G., 1994. Vitrinite reflectance as maturity parameter – applications and limitations. ACS Symposium Series, 570.

Mukoyoshi, H., Kaneki, S., Hirono, T., 2018. Slip parameters on major thrusts at a convergent plate boundary: Regional heterogeneity of potential slip distance at the shallow portion of the subducting plate. Earth Planet. Space 70:36.

Müller, P.J., Suess, E., 1979. Productivity, sedimentation rate, and sedimentary organic matter in the oceans – I. Organic carbon preservation. Deep-Sea Res. 26, 1347–1362.

Mumm, A.S., Inan, S., 2016. Microscale organic maturity determination of graptolites using Raman spectroscopy. Int. J. Coal Geol. 162, 96–107.

Murray, J.W., Jannasch, H.W., Honjo, S., Anderson, R.F., Reeburgh, W.S., Top, Z., Friederich, G.E., Codispoti, L.A., Izdar, E., 1989. Unexpected changes in the oxic/anoxic interface in the Black Sea. Nature, 338, 411–413.

Nakamura, Y., Oohashi, K., Toyoshima, T., Satish-Kumar, M., Akai, J., 2015. Strain-induced amorphization of graphite in fault zones of the Hidaka metamorphic belt, Hokkaido, Japan. J. Struct. Geol. 72, 142–161.

Nakamura, Y., Yoshino, T., Satish-Kumar, M., 2017. An experimental kinetic study on the structural evolution of natural carbonaceous material to graphite. Am. Mineral. 102, 135–148.

Nakamura, Y., Hara, H., Kagi, H., 2019. Natural and experimental structural evolution of dispersed organic matter in mudstones: The Shimano accretionary complex, southwest Japan. Island Arc. E12318 doi.org/10.1111/iar.12318.

Nestler, K., Dietrich, D., Witke, K., Röβler, R., Marx, G. (2003) Thermogravimetric and Raman spectroscopic investigations on different coals in comparison to dispersed anthracite found in permineralized tree fern Psaronius sp. J. Molec. Struct. 661–662, 357–362.

Nuccio, V.F., 1991. Combining methods yields best source rock maturity. World Oil. 212, 63–72.

Nzoussi-Mbassani, P., Copard, Y., Disnar, J.-R., 2005. Vitrinite recycling: diagnostic criteria and reflectance changes during weathering and reburial. Int. J. Coal Geol. 61, 223–239.

Oohashi, K., Hirose, T., Shimamoto, T., 2011. Shear-induced graphitization of carbonaceous materials during seismic fault motion: Experiments and possible implications for fault mechanics. J. Struct. Geol. 33, 1122–1134.

Pacton, M., Gorin, G.E., Vasconcelos, C., 2011. Amorphous organic matter – Experimental data on formation and the role of microbes. Review of Palaeobotany and Palynology, 166, 253–267.

Pan, J., Lv, M., Hou, Q., Han, Y., Wang. K., 2019. Coal microcrystalline structural changes related to methane adsorption/desorption. Fuel 239, 13–23.

Pasteris, J.D., 1989. In situ analysis in geological thin-sections by laser Raman microprobe microscopy: A cautionary note. Applied Spectrosc. 43, 567–570.

Pasteris, J.D., Wopenka, B., 1991. Raman spectra of graphite as indicators of degree of metamorphism. Can. Mineral. 29, 1–9.

Passey, Q.R., Bohacs, K., Esch, W.L., Klimentidis, R., Sinha, S., 2010. From oil-prone source rock to gas-producing shale reservoir – geologic and petrophysical characterization of unconventional shale gas reservoirs. Soc. Petrol. Eng. Int. Oil Gas Conf. Exhib. Beijing, China. SPE-131350-MS.

Pawlyta, M., Rouzaud, J.N., Duber, S., 2015. Raman microspectroscopy characterization of carbon blacks: Spectral analysis and structural information. Carbon 84, 479–490.

Pearson, D.L., 1984. Pollen/spore color “standard”. Phillips Petroleum Company Geological Branch.

Pedersen T.F., Calvert S.E., 1990. Anoxia vs. productivity: what controls the formation of organic-carbon-rich sediments and sedimentary rocks? Am. Assoc. Pet. Geol. Bull. 74, 454–466.

Peters, K.E., Moldowan, J.M., 1993. The Biomarker Guide, Interpreting molecular fossils in petroleum and ancient sediments, Prentice Hall, 363 p.

Peters, K.E., Cassa, M.R., 1994. Applied source-rock geochemistry. Am. Assoc. Petrol. Geol. Mem. 60, 93–120.

Peters, K.E., Walters, C.C., Moldowan, J.M., 2005. The Biomarker Guide, Biomarkers and Isotopes in the Environment and Human History, 2nd Edition. Cambridge.

Peters, K.E., Rodriguez, L.B., 2017. Programmed Temperature Pyrolysis. In: White W. (eds) Encyclopaedia of Geochemistry. Encyclopaedia of Earth Science Series. Springer. Cham.

4595 Petersen, H.I., Nytoft, H.P., Vosgerau, H., Andersen, C., Bojesen-Koefoed, J.A., Mathiesen, A., 2011.
4596 Source rock quality and maturity and oil types in the NW Danish Central Graben: implications for
4597 petroleum prospectivity evaluation in an Upper Jurassic sandstone play area. Geol. Soc. London.
4598 Petrol. Geol. Conf. 7, 95–111.

4599 Petersen, H.I., Andersen C., Holme, A.C., Carr, A.D., Thomsen, E., 2012. Vitrinite reflectance gradients
4600 of deep wells with thick chalk sections and high pressure: Implications for source rock maturation,
4601 Danish–Norwegian Central Graben, North Sea. Int. J. Coal Geol. 100, 65–81.

4602 Petkovic, L.M., 2017. Shale oil. In: Ramirez-Corredores, M.M., 2017. The science and technology of
4603 unconventional oils. Elsevier. pp. 677–693.

4604 Pimenta, M.A., Dresselhaus, G., Dresselhaus, M.S., Cancado, L.G., Jorio, A., Saito, R., 2007. Studying
4605 disorder in graphite-based systems by Raman spectroscopy. Phys. Chem. Chem. Phys. 9, 1276–
4606 1291.

4607 Quirico, E., Rouzaud, J., Bonal, L., Montagnac, G., 2005. Maturation grade of coals as revealed by
4608 Raman spectroscopy: Progress and problems. Spectrochim. Acta A Mol. Biomol. Spectrosc. 61,
4609 2368–2377.

4610 Quirico, E., Montagnac, G., Rouzaud, J.-N., Bonal, L., Bourot-Denise, M., Duber, S., Reynard, B., 2009.
4611 Precursor and metamorphic conditions effects on Raman spectra f poorly ordered carbonaceous
4612 matter in chondrites and coals. Earth Planet. Sci. Lett. 287, 185–193.

4613 Quirico, E., Bourot-denise, M., Robin, C., Montagnac, G., Beck, P., 2011. A reappraisal of the
4614 metamorphic history of EH3 and EL3 enstatite chondrites. Geochim. Cosmochim. Acta. 75, 3088–
4615 3102.

4616 Rahl, J.M., Anderson, K.M., Brandon, M., Fassoulas, C., 2005. Raman spectroscopic carbonaceous
4617 material thermometry of low-grade metamorphic rocks: Calibration and application to tectonic
4618 exhumation in Crete, Greece. Earth Planet. Sci. Lett. 240, 339–354.

4619 Raman, C.V., Krishnan, K.S., 1928. A new type of secondary radiation. Nature. 121, 501-502.

4620 Rantitsch, G., Grogger, W., Teichert, C., Ebner, F., Hofer, C., Maurer, E.M., Schaffer, B., Toth, M., 2004.
4621 Conversion of carbonaceous material to graphite within the Greywacke Zone of the Eastern Alps.
4622 Int. J. Earth Sci. 93, 959– 973

Rantitsch, G., Lämmerer, W., Fisslthaler, E., Mitsche, S., Kaltenböck, H., 2016. On the discrimination of semi-graphite and graphite by Raman spectroscopy. Int. J. Coal Geol. 159, 49–56.

Rantitsch, G., Bhattacharyya, A., Schenk, J., 2019. Microstructural evolution of blast furnace coke during experimental heating – The IFORS approach. Berg–Huettenmaenn. Monatsh. 164, 257–260.

Ravenhurst, C.E., Donelick, R.A., 1992. Fission Track Thermochronology. In Short Course. Handbook on Low Temperature Thermochronology, ed. Zentilli, M., Reynolds, P.H., pp. 21-42.

Rawson, P.F., Riley, L.A., 1982. Latest Jurassic-Early Cretaceous events and the "late Cimmerian unconformity" in North Sea area. AAPG Bulletin. 66, 2628–2648.

Raymond, A.C., 1991. Carboniferous rocks of the Eastern and Central Midland Valley of Scotland: organic petrology, organic geochemistry and effects of igneous activity. Unpublished PhD Thesis, University of Newcastle upon Tyne.

Reynolds, T., 1994. Quantitative analysis of submarine fans in the Tertiary of the North Sea Basin. Marine and Petroleum Geology. 11, 202–207.

Richardson, J.B., 1996. Lower and Middle Palaeozoic records of terrestrial palynomorphs. In: Jansonius, J., McGregor, D.C. (Eds.), Palynology: Principles and Applications. American Association of Stratigraphic Palynologists Foundation, Dallas, 555–574

Roberts, S., Tricker, P.M., Marshall, J.E.A., 1995. Raman spectroscopy of chitinozoans as a maturation indicator. Org. Geochem. 23, 223–228.

Romankevich, E.A. (1984) Geochemistry of Organic Matter in the Ocean, Springer-Verlag, Berlin, 334pp.

Romero-Sarmiento, M.F., Rouzaud, J.N., Bernard, S., Deldicque, D., Thomas, M., Littke, R., 2014. Evolution of Barnett Shale organic carbon structure and nanostructure with increasing maturation. Org. Geochem. 71, 7–16

Sauerer, B., Craddock, P.R., Aljohani, M.D., Alsamadony, K. L. Abdallah, W., 2017. Fast and accurate shale maturity determination by Raman spectroscopy measurement with minimal sample preparation. Int. J. Coal Geol. 173, 150–157.

4650 Scharf, A., Handy, M.R., Ziemann, M.A., Schmid, S.M., 2013. Peak-temperature patterns of polyphase
4651 metamorphism resulting from accretion, subduction and collision (eastern Tauern window,
4652 European alps) – A study with Raman microspectroscopy on carbonaceous material (RSCM). J.
4653 Metamorph. Geol. 31, 863–880.

4654 Schiffbauer, J.D., Wallace, A.F., Hunter, J.L.-Jr, Kowalewski, M., Bodnar, R.J., Xiao, S., 2012. Thermally-
4655 induced structural and chemical alteration of organic-walled microfossils: An experimental
4656 approach to understanding fossil preservation in metasediments. Geobiol. 10, 402–423.

4657 Schito, A., Romano, C., Corrado, S., Grigo, D., Poe, B., 2017. Diagenetic thermal evolution of organic
4658 matter by Raman spectroscopy. Org. Geochem. 106, 57–67.

4659 Schito, A., Spina, A., Corrado, S., Cirilli, S., Romano, C., 2019. Comparing optical and Raman
4660 spectroscopic investigations of phytoclasts and sporomorphs for thermal maturity assessment:
4661 The case study of Hettangian continental facies in the Holy cross Mts. (central Poland). Marine
4662 Petrol. Geol. 104, 331–345.

4663 Schito, A., Corrado, S., 2018. An automatic approach for characterization of the thermal maturity of
4664 dispersed organic matter Raman spectra at low diagenetic stages. In: Dowey, P., Osborne, M.,
4665 Volk, H. (Eds.) Application of Analytical Techniques to Petroleum Systems. Geol. Soc. London Spec.
4666 Publ. 484 doi: 10.1144/SP484.5.

4667 Schmidt, J.L., Hinrichs, R., Araujo, C.V., 2017. Maturity estimation of phytoclasts in strew mounts by
4668 micro-Raman spectroscopy. Int. J. Coal Geol. 173, 1–8.

4669 Schopf, J.W., Kudryavtsev, A.B., Agresti, D.G., Czaja, A.D., Wdowiak, T.J., 2005. Raman imagery: A new
4670 approach to assess the geochemical maturity and biogenicity of permineralized Precambrian
4671 fossils. Astrobiol. 5, 333–371.

4672 Sigman, D.M., Hain, M.P. 2012. The biological productivity of the ocean. Nature Edu. Knowledge, 3, 1–
4673 16.

4674 Słowakiewicz, M., Tucker, M.E., Vane, C.H., Harding, R., Collins, A., Pancost, R.D., 2014. Shale-gas
4675 potential of the Mid-Carboniferous Bowland-Hodder Unit in the Cleveland Basin (Yorkshire),
4676 Central Britain. J. Petrol. Geol. 38, 59-75.

4677 Smekal, A., 1923. Zur Quantentheorie der Dispersion. Naturwissenschafter, 11, 873-875.

4678 Smelror, M., Petrov, O.V., Larssen, G.B., Werner, S., 2009. Atlas – Geological History of the Barents
4679 Sea. Norges Geologiske Undersøkelse, Trondheim.

4680 Smith, E., Dent, G., 2005. Modern Raman spectroscopy – a practical approach. John Wiley and Sons,
4681 Ltd. pp. 210.

4682 Smith, N., Turner, P., Williams, G., 2011. UK data and analysis for shale gas prospectivity. In: Vining,
4683 B.A. and Pickering, S.C. (Eds) Petroleum Geology: From Mature Basins to New Frontiers.
4684 Petroleum Geology Conference Series 7, Geol. Soc. London. 1087–1098.

4685 Song, Y., Jiang, C., Qu, M., 2019. Macromolecular evolution and structural defects in tectonically
4686 deformed coals. Fuel 236, 1432–1445.

4687 Spötl, C., Houseknecht, D.W., Jaques, R.C., 1998. Kerogen maturation and incipient graphitization of
4688 hydrocarbon source rocks in the Arkoma Basin, Oklahoma and Arkansas: A combined
4689 petrographic and Raman spectrometric study. Org. Geochem. 28, 535–542.

4690 Stanev, E.V., Poulain, P.M., Grayek, S., Johnson, K.S., Claustre, H., Murray, J.W., 2018. Understanding
4691 the dynamics of the oxic-anoxic interface in the Black Sea. Geophysical Research Letters, 45.

4692 Starkey, N.A., Franchi, I.A., Alexander, C.M.O'D., 2013. A Raman spectroscopic study of organic matter
4693 in interplanetary dust particles and meteorites using multiple wavelength laser excitation.
4694 Meteor. Planet. Sci. 48, 1800–1822.

4695 Suárez-Ruiz, I., Flores, D., Mendonça Filho, J.G., Hackley, P.C., 2012. Review and update of the
4696 applications of organic petrology: Part 1, geological applications. Int. J. Coal Geol. 99, 54–112.

4697 Suess, E., 1980. Particulate organic carbon flux in the oceans – surface productivity and oxygen
4698 utilization. Nature, 228, 260–263.

4699 Surlyk, F., Donds, T., Clausen, C.K., Higham, J., 2003. Upper Cretaceous. In: Evans, D., Graham, C.,
4700 Armour, A., Bathurst, P., (Eds.). The Millennium Atlas: petroleum geology of the central and
4701 northern North Sea. 213–233.

4702 Susanne, G., Worden, R.H., Johns, W.D., Kurzweil, H., 2008. Diagenesis and reservoir quality of
4703 Miocene sandstones in the Vienna Basin, Austria. Mar. Petrol. Geol. 25, 681–695.

Taylor, T.R., Kittridge, M.G., Winefield, P., Bryndzia, L.T., Bonnell, L.M., 2015. Reservoir quality and rock properties modelling – Triassic and Jurassic sandstones, greater Shearwater area, UK Central North Sea. Mar. Petrol. Geol. 65, 1–21.

Teichmüller, M., 1974. Entstehung und Veränderung bituminöser substanzen in Kohlen in Beziehung zur Enstenhung und Umwandlung des Erdols-Fortschr. Geoloigische Rheinld. U. Westf. 24, 65–112.

Teichmüller, M., 1987. Organic material and very low- grade metamorphism. In: Low Temperature Metamorphism, ed. M. Frey, Blackie, Glasgow. 114-161.

Tissot, B.P., Welte, D.H., 1984. Petroleum Formation and Occurrence (2nd Ed.). Berlin, Springer-Verlag, 699 p.

Tissot, B., Espitalié, J., 1975. L'évolution thermique des sédiments : applications d'une simulation mathématique. Oil & Gas Science and Technology - Rev. IFP, 30, 743-777.

Tissot, B.P., Pelet, R., Ungerer, P., 1987. Thermal history of sedimentary basins, maturation indices, and kinetics of oil and gas generation. Am. Assoc. Petrol. Geol. Bull. 71, 1445–1466.

Thiel, J., Byrne, J.M., Kappler, A., Schink, B., Pester, M., 2019. Pyrite formation from FeS and H2S is mediated through microbial redox activity. PNAS, 116, 6897–6902.

Toxopeus, J.M.A.B., 1983. Selection Criteria for the use of vitrinite reflectance as a maturity tool. Geological Society, London, Special Publications. 12, 295–307.

Trabucho-Alexandre, J., 2015. Organic matter-rich shale deposition environments. In: Rezaee, R., (Eds.) Fundamentals of gas shale reservoirs. John Wiley and Sons. pp. 21–39.

Traverse, A., 1988. Paleopalynology. Unwin Hyman, Boston, 600 p.

Tunistra, F., Koenig, J.L., 1970. Raman spectrum of graphite. J. Chem. Phys. 53, 1126.

Turner, H.E., 2018. Integrated correlation of the Kimmeridge Clay Formation (Late Jurassic–Early Cretaceous): A Boreal–Tethyan transect. Unpublished PhD Thesis, University of Portsmouth, UK.

Ulyanova, E.V., Molchanov, A.N., Prokhorov, I.Y., Grinyov, V.G., 2014. Fine structure of Raman spectra in coals of different rank. Int. J. Coal Geol. 121, 37–43.

Underhill, J.R., Partington, M.A., 1993. Jurassic thermal doming and deflation in the North Sea: implications of the sequence stratigraphic evidence. Geological Society, London, Petroleum Geology Conference series, 4, 337–345

Vandenbroucke, M., 2003. Kerogen: from types to models of chemical structure. Oil & Gas Science and Technology – Rev. IFP. 58, 243–270.

Verdel, C., Niemi, N., Van der Pluijm, B.A., 2011. Variations in the illite-muscovite transition related to metamorphic conditions and detrital muscovite content: insight from the Paleozoic passive margin of the S.W. US. J Geol. 119, 419–437.

Vidano, R.P., Fischbach, D.B., Willis, L.J., Loehr T.M., 1981. Observation of Raman band shifting with excitation wavelength for carbons and graphites. Solid State Comm. 39, 341–344.

Villanueva, U., Raposo, J.C., Castro, K., de Diego A., Arana, G., Madariaga J.M., 2008. Raman spectroscopy speciation of natural and anthropogenic solid phases in river and estuarine sediments with appreciable amount of clay and organic matter. J. Raman Spectrosc. 39, 1195–1203.

Volk, H., Horsfield, B., Mann, U., Suchy, V., 2002. Variability of petroleum inclusions in vein, fossil and vug cements – a geochemical study in the Barrandian Basin (Lower Palaeozoic, Czech Republic). Org. Geochem. 33, 1319–1341.

Wang, Y., Qiu, N., Borjigin, T., Shen, B., Xie, X., Ma, Z., Lu, C., Yang, Y., Yang, L., Cheng, L., Fang, G., Cui, Y., 2018. Integrated assessment of thermal maturity of the Upper Ordovician–Lower Silurian Wufeng–Longmaxi shale in Sichuan Basin, China. Marine Petrol. Geol. 100, 447–465.

Waples, D. W., 1985. Geochemistry in Petroleum Exploration. Boston, International Human Resources Development, 232 p.

Warr, L.N., Rice, A.H.N., 1994. Interlaboratory standardization and calibration of clay mineral crystallinity and crystallite size data. J. Metamorph. Geol. 12, 141-152.

Waters, C.N., Waters, R.A., Barclay, W.J., Davies J.R., 2009. A lithostratigraphic framework for Carboniferous successions of southern Great Britain (onshore) British Geological Survey, Research Report (2009) (RR/09/01). http://nora.nerc.ac.uk/id/eprint/8281/1/RR09001.pdf.

4757 Wilkins, R.W.T., Wilmshurst, J. R., Hladky, G., Ellacott, M. V., Buckingham, C.P., 1995. Should
4758 fluorescence alteration replace vitrinite reflectance as a major tool for thermal maturity
4759 determination in oil exploration? Org. Geochem. 22, 191-209.

4760 Wilkins, R.W.T., 1999. The problem of inconsistency between thermal maturity indicators used for
4761 petroleum exploration in Australian basins. J. Austral. Geol. Geophys. 17, 67–76.

4762 Wilkins, R.W.T., Boudou, R., Sherwood, N., Xiao, X., 2014. Thermal maturity evaluation from inertinites
4763 by Raman spectroscopy: The 'RaMM' technique. Int. J. Coal Geol. 128, 143–152.

4764 Wilkins, R.W.T., Wang, M., Gan, H., Li, Z., 2015. A RaMM study of thermal maturity of dispersed organic
4765 matter in marine source rocks. Int. J. Coal Geol. 150–151, 252–264.

4766 Wilkins, R.W.T., Sherwood, N., Li, Z., 2018. RaMM (Raman maturity method) study of samples used in
4767 an interlaboratory exercise on a standard test method for determination of vitrinite reflectance
4768 on dispersed organic matter in rocks. Marine Petrol. Geol. 91, 236–250.

4769 Wood, R.J., Edrich, S.P. Hutchison, I., 1989: Influence of North Atlantic Tectonics on the Large-Scale
4770 Uplift of the Stappen high and Loppa High, western Barents Shelf. In: Tankard, A. J. and Balkwill,
4771 H. R. (eds) Extensional tectonics and stratigraphy of the North Atlantic margins. Am. Ass. Petrol.
4772 Geol. Memoirs. 46, 559–566.

4773 Wopenka, B., Pasteris, J.D., 1993. Structural characterization of kerogens to granulite-facies graphite:
4774 Applicability of Raman microprobe spectroscopy. Am. Mineral. 78, 533–577.

4775 Worsley, D., 2006: The post-Caledonian geological development of Svalbard and the Barents Sea.
4776 Norsk Geologisk Forening. Abstracts and Proceedings. 3, 5–21.

4777 Wu, L.M., Zhou, C.H., Keeling, J., Tong, D.S., Yu, W.H., 2012. Towards an understanding of the role of
4778 clay minerals in crude oil formation, migration and accumulation. Earth Sci. Rev. 115, 373–386.

4779 Yan, Q., Peng, P., Yu, C., Liu, J., 2004. The role of sulfur in the pyrolysis of kerogen. Chinese Science
4780 Bulletin, 49, 10-18.

4781 Yoshida, A., Kaburagi, Y., Hishiyama, Y., 2006. Full width at half maximum intensity of the G band in
4782 the first order Raman spectrum of carbon material as a parameter for graphitization. Carbon 44,
4783 2330–2356.

Yu, W., Polgari, M., Gyollai, I., Fintor, K., Szabo, M., Kovács, I., Fekete, J., Du, Y., Zhou, Q., 2019. Microbial metallogenesis of Cryogenian manganese ore deposits in South China. Precamb. Res. 322, 122–135.

Yuman, W., Xinjing, L., Bo, C., Wei, W., Dazhong, D., Jian, Z., Jing, H., Jie, M., Bing, D., Hao, W., Shan, J., 2018. Lower limit of thermal maturity for the carbonization of organic matter in marine shale and its exploration risk. Petrol. Explor. Develop. 45, 402–411.

Zeng, Y., Wu, C., 2007 Raman and infrared spectroscopic study of kerogen treated at elevated temperatures and pressures. Fuel 86, 1192–1200.

Zhang, Y., Li, Z., 2019. Raman spectroscopic study of chemical structure and thermal maturity of vitrinite from a suite of Australia coals. Fuel 241, 188–198.

Zhang, C., Santosh, M., 2019. Coupled laser Raman spectroscopy and carbon stable isotopes of graphite from the khondalite belt of Kerala, southern India. Lithos 334–335, 245–253.

Zhou, Q., Xiao, X., Pan, L., Tian, H., 2014. The relationship between micro-Raman spectral parameters and reflectance of solid bitumen. Int. J. Coal Geol. 121,19–25.

Ziegler, P.A., von Hoorn, B., 1989. Evolution of North Sea rift system Extensional tectonics and stratigraphy of the North Atlantic margins. In: Tankard, A.J., Balkwill, H.R. (Eds.): AAPG Memoir. 471–500.

# Appendices

## Appendix A Summary of Raman instrumentation and methods reported in the literature.

Electronic Excel file.

# Appendix B Automated Raman processing method.

## Appendix B1. Original Raman processing method from Henry et al. (2018).

Electronic Excel file. This method was used in Chapter 4.

## Appendix B2. Raman processing method V2.

Electronic Excel file. This method was used in Chapter 5, 6, 7 and 8.

## Appendix B3. MATLAB code of the Raman processing method.

**Steps**

1. Load Spectra
2. Plot Spectra
3. Perform a Savitzky-Golay smoothing filter using a 21-pointquadratic polynomial algorithm
4. Perform a 3rd-order polynomial baseline correction
5. Normalize the spectra to have a G band height with an intensity of 2000 au.
6. Calculate the G-FWHM Raman parameter

```
%PROCESSING THE SPECTRA

% Load and plot the Raw spectra

load test_matlab.txt

wavenumber = test_matlab(:,1);

height = test_matlab(:,2);

subplot(3,2,1)

plot(wavenumber, height, 'black')

title('Raw Spectrum'), xlabel('Wavenumber (cm^{-1})'), ylabel('Intensity
(au)')



% Perform Savitzky-Goal Filtering

height_sgf = sgolayfilt(height, 4, 21);
```

```
subplot(3,2,2)

plot(wavenumber, height_sgf, 'black')

title('Smoothed Spectrum'), xlabel('Wavenumber (cm^{-1})'),
ylabel('Intensity (au)')


% Background Correction

background = [wavenumber([1 109 636 726]), height_sgf([1 109 636 726])];

background_x = background(:,1);

background_y = background(:,2);

p = polyfit(background_x, background_y, 3)

background_2y = (p(1) * wavenumber.^3.) + (p(2) * wavenumber.^2.) + (p(3) *
wavenumber) + p(4)

subplot(3,2,3)

plot(wavenumber, background_2y, 'black')

title('Background'), xlabel('Wavenumber (cm^{-1})'), ylabel('Intensity
(au)')

height_cor = height_sgf - background_2y;

subplot(3,2,4)

plot(wavenumber, height_sgf, 'black')

hold on

plot(wavenumber, background_2y, 'black')

title('Spectrum and Background'), xlabel('Wavenumber (cm^{-1})'),
ylabel('Intensity (au)')

subplot(3,2,5)

plot(wavenumber, height_cor, 'black')

title('Background'), xlabel('Wavenumber (cm^{-1})'), ylabel('Intensity
(au)')
```

```
% Normalize the Spectrum

scale = max/2000;

height_final = height_cor / scale;

subplot(3,2,6)

plot(wavenumber, height_final, 'black')

title('Final Spectrum'), xlabel('Wavenumber (cm^{-1})'), ylabel('Intensity
(au)')
```

## %Calculating and Plotting G-FWHM

```
% Calculating the G-FHWM

half_height = 1000;

above_half_max = height_final >= 990.5;

first_index = find(above_half_max, 1, 'first');

last_index = find(above_half_max, 1, 'last');

position_1 = test_matlab(257, 1);

position_2 = test_matlab(295, 1);

G_FWHM = position_1 - position_2


% Plotting the G-FWHM

G_FWHM_2 = [wavenumber([first_index last_index]), height_final([last_index
last_index])];

G_FWHM_x = G_FWHM_2(:,1);

G_FWHM_y = G_FWHM_2(:,2);
```

```
subplot(3,2,6)

hold on

plot(G_FWHM_x, G_FWHM_y, 'r')


G_FWHM_1 = [wavenumber([first_index last_index]), height_final([first_index
first_index])];

G_FWHM_x1 = G_FWHM_1(:,1);

G_FWHM_y1 = G_FWHM_1(:,2);

subplot(3,2,6)

hold on

plot(G_FWHM_x1, G_FWHM_y1, 'r')


% Making sure the axes are correct

subplot(3,2,5)

axis([900 2000 0 inf])


subplot(3,2,6)

axis([900 2000 0 2000])
```

## Audit trail of the processing of the Raman spectra

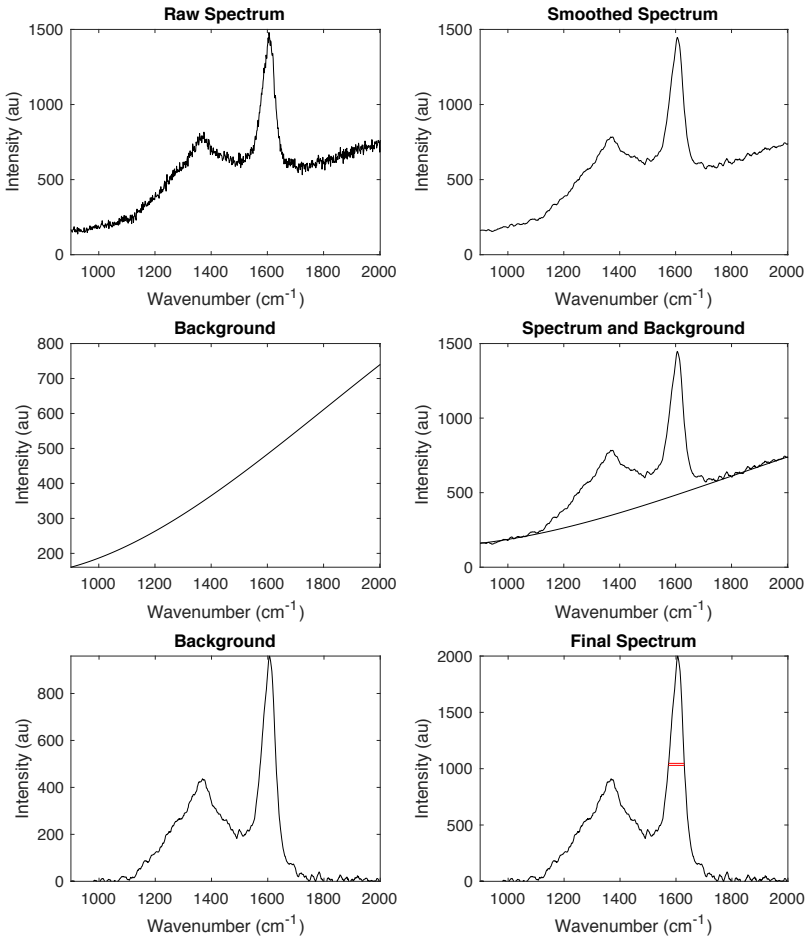

# Appendix C Representative images of organic matter macerals taken from strew slides

## Appendix C1. Translucent phytoclasts.

**Appendix B1.** Translucent phytoclasts.

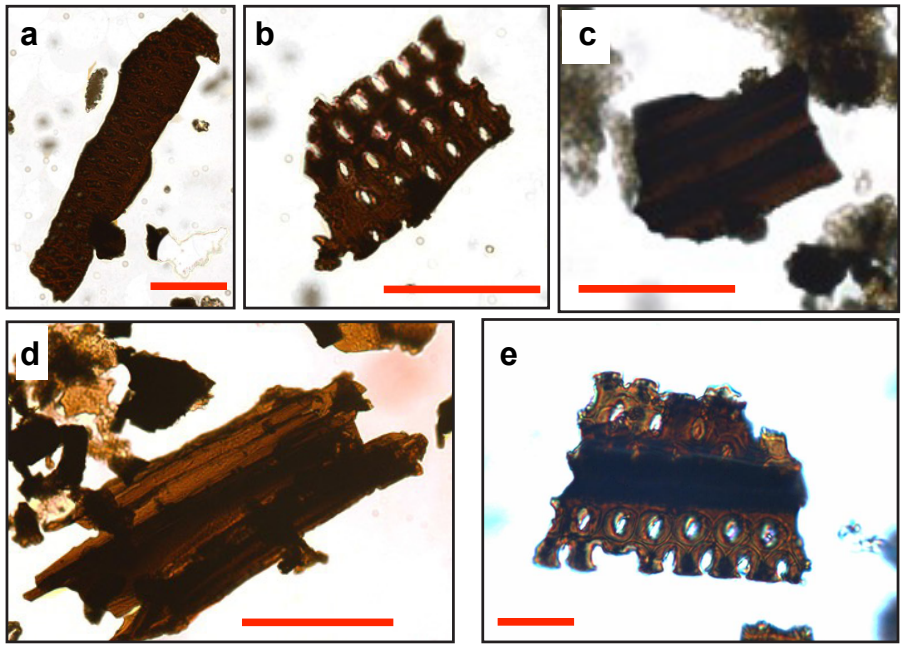


50 µm

**a** Lath shaped pitted phytoclast (SSK 4522).
**b** Equidimensional pitted phytoclast (SSK 4471).
**c** Equidimensional banded phytoclast (SSK 4522).
**d** Fibrous/striped phytoclast (SSK 4471).
**e** Equidimensional pitted phytoclast (SSK 4471).

## Appendix C2. Opaque phytoclasts.

**Appendix B2.** Opaque phytoclasts — 50 µm

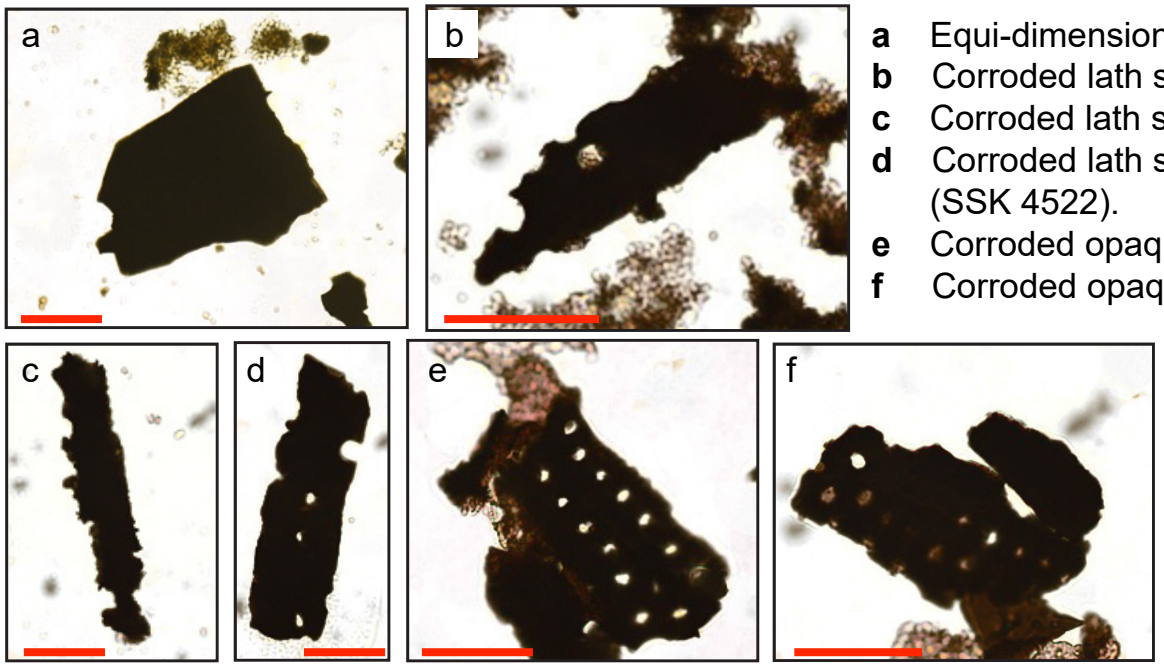


**a** Equi-dimensional opaque phytoclast (SSK 4471)
**b** Corroded lath shaped opaque phytoclast (SSK 4522).
**c** Corroded lath shaped opaque phytoclast (SSK 4522).
**d** Corroded lath shaped opaque phytoclast with remnant pits (SSK 4522).
**e** Corroded opaque phytoclast with remnant pits (SSK 4471).
**f** Corroded opaque phytoclast with remnant pits (SSK 4471).

## Appendix C3. Psuedo-amorphous phytoclasts.

**Appendix B3.** Psuedo-amorphous phytoclast

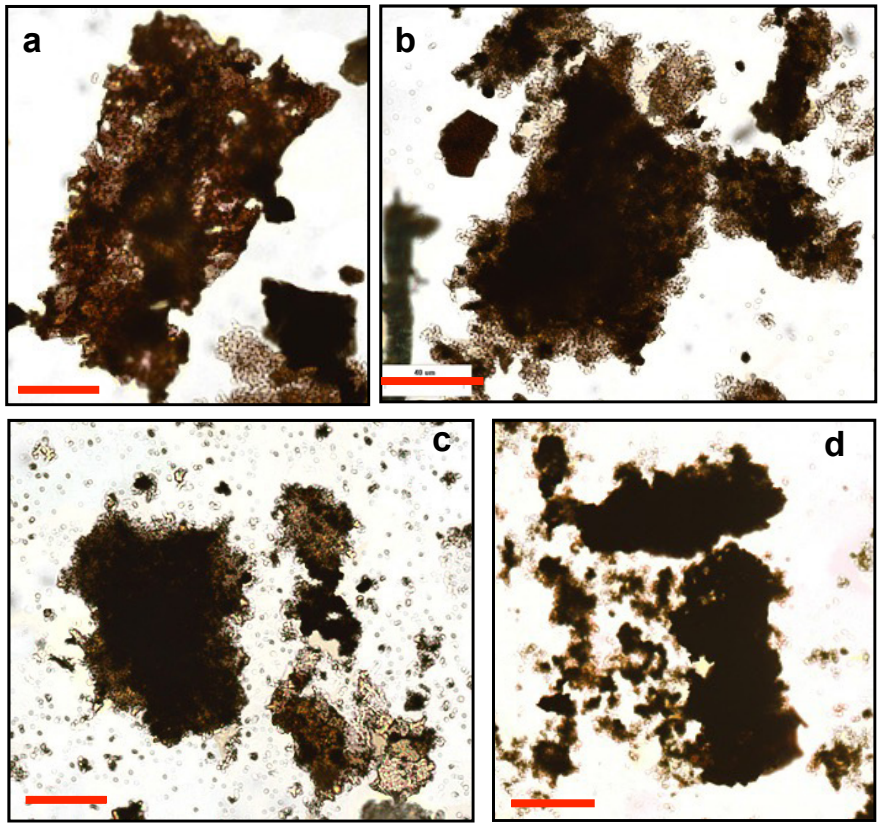


50 µm

**a** Biodegraded phytoclast, with possible pitted remnants (SSK 4522).
**b** Biodegraded phytoclasts with a relict rectangular appearance (SSK 4471).
**c** Biodegraded phytoclasts with a relict rectangular appearance (HC02-73).
**d** Biodegraded and corroded phytoclasts with a relict rectangular appearance (MPA 61616).

## Appendix C4. Amorphous organic matter (AOM).

**Appendix B4.** Amorphous organic matter (AOM)

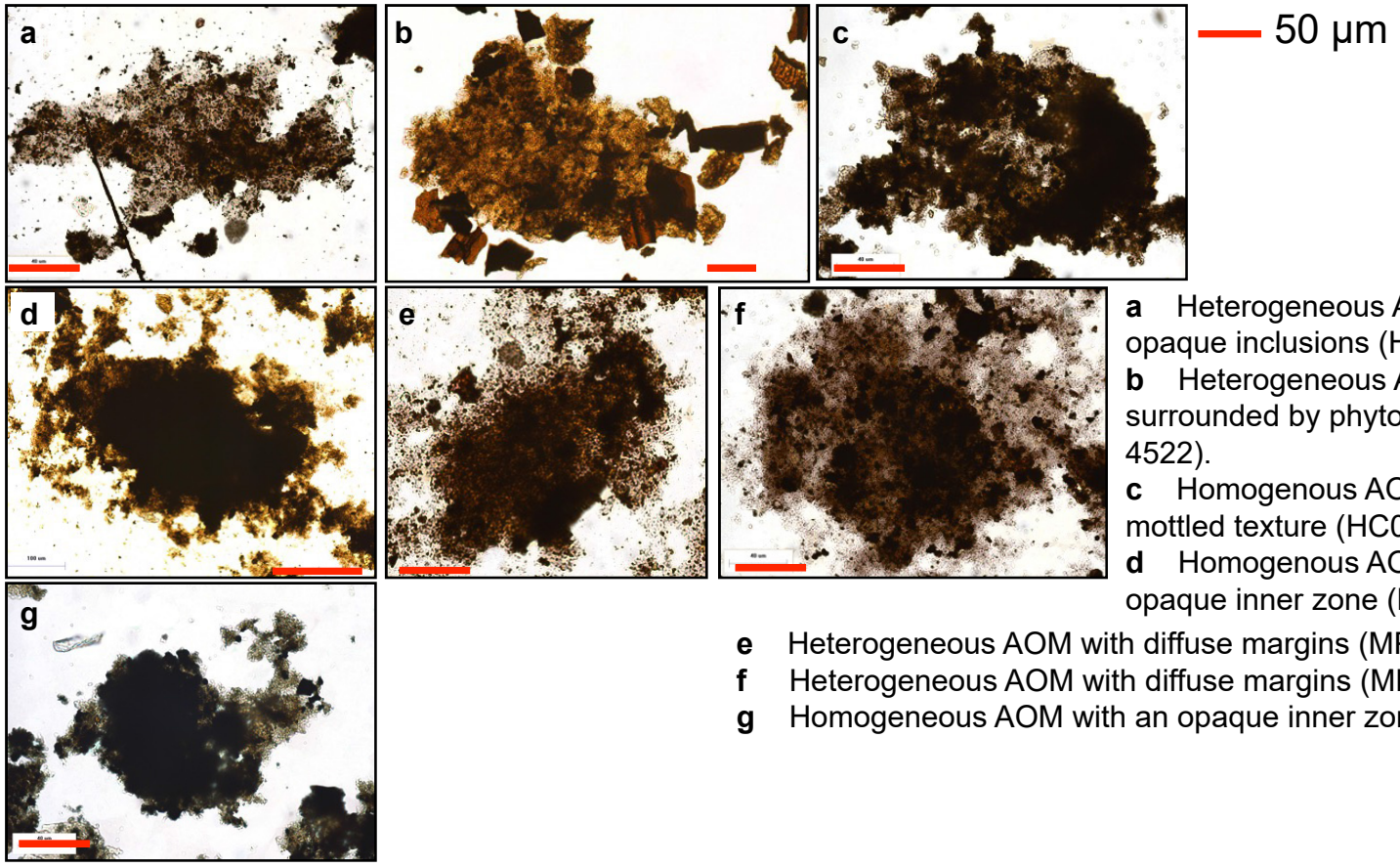


**a** Heterogeneous AOM with opaque inclusions (HC02-73).
**b** Heterogeneous AOM surrounded by phytoclasts (SSK 4522).
**c** Homogenous AOM with a mottled texture (HC02-73).
**d** Homogenous AOM with an opaque inner zone (MPA 61616).
**e** Heterogeneous AOM with diffuse margins (MPA 61619).
**f** Heterogeneous AOM with diffuse margins (MPA 61619).
**g** Homogeneous AOM with an opaque inner zone (HC02-73).

# Appendix D Vitrinite reflectance methodology

## 1 Objective

Vitrinite reflectance was performed to verify VR measurements acquired from other sources and where VR measurements were missing. The VR measurements are then compared to Raman, Rock-Eval and illite crystallinity results.

## 2 Sample preparation

**Shale:** the organic matter was isolated using the technique discussed in section 2.1.

**Coals:** whole rock coal samples were used.

### 2.1 Organic matter separation method for shale samples

Gently crush the rock to c. 2mm, in order to facilitate a faster reaction with HCl and HF acid.

1. Add 100 ml of 37 % concentrated HCL in a 500 ml beaker with the sample in a fume cupboard. Keep a wash bottle topped up with distilled nearby, in case the reaction is too strong. Leave for 18 hours.
    a. After 18 hours, add 400 ml of water in the container. Wait until the rock particles have settled and decant. Repeat the procedure three times. Then wash the sample using a 15-µm polyester mesh.
2. Add the cleaned rock residue to another 500 ml beaker (make sure it is polyphenylene ether plastic). Then add 100 ml of 40 % concentrated HF into the beaker. Leave for 24 hours. If the rock is not fully disaggregated after 24 hours, facilitate the reaction by stirring and/or leave the sample in acid for additional days.
3. Once completely disaggregated, add 400 ml of water into the 500 ml beaker and decant. Repeat the process three times and then wash the residual kerogen using a 15-µm polyester mesh.
4. Transfer the isolated kerogen into a vial.

### 2.2 Polishing

For the polishing stage, 2.5 cm wide epoxy moulds were made. Then a 1 cm hole was drilled into the epoxy mould.

Use a pipette to transfer the isolate kerogen from the vial into the hole that was drilled in the epoxy mould, the sample was then left to dry on a hot play at 40 $^{o}$C, until the kerogen is completely dry. In the case of coal fragments, these where transferred and positioned using tweezers. Once the sample is placed in the hole, the hole was filled with a mixture of epoxy and hardener and then placed on a hot plate at 40 $^{o}$C for 24–48 hours, in order to facilitate the solidification of the resin mixture.

Once the resin in the samples has solidified, they are evenly placed in a sample holder ready for grinding. Each sample holder had space for six samples. When there were not enough samples to balance the sample holder, blank moulds were inserted. At each grinding stage the machine was rotating at c. 150 RPM at a low pressure of approximately 0.02 MPa, to not damage the organic matter, and 8–10 drips per second of water was used as a lubricant. Each grinding stage lasted approximately 30 seconds and was examined using a microscope. A P400 silicon carbide paper was firstly used to grind the sample until the organic matter was exposed at the surface for each sample. Then P600, P800, P1200 and P2500 silicon carbide papers were used.

Every polishing stage was performed on separate lap cloths for each polishing stage. The sample holder was set to rotate at c. 150 RPM at a pressure of c. 0.02 MPa, for two minutes. After each polishing stage, the samples were analysed using a reflected light microscope to monitor the relief and scratches, making sure that the scratches systematically reduce in width after each successive polishing stage. If the scratch widths were not a ubiquitous size, the samples were re-polished using the same polishing grade. The samples were first polished using a diamond liquid suspension of 9 µm, 6 µm, 3 µm, 1 µm and were finished off with a 0.04 µm colloidal silica suspension.

Once the samples have been checked and the quality is acceptable (no relief and minimal scratches), the samples were stored in an air tight plastic container.

# 3 Performing vitrinite reflectance

## 3.1 Vitrinite reflectance: calibration and measurements

Wait 30 minutes after switching the microscope and light source on, to allow the bulbs to stabilise.

- **Microscope instrument:** Carl Zeiss Axio Imager.A2
- **Calibration samples:** GGG (1.722 %) and spinel standard (0.420 %)
- **Oil:** Refractive index 1.518
- **Method:** Random reflectance
- **Light Source:** monochromatic light 546 nm
- **Software:** Axiovision 4.8

### 3.1.1 Calibration

1. A drop of immersion oil was applied on the gadolinium gallium garnet (GGG) (1.722 %) standard sample and was then placed under the oil immersion lens. The sample was then focused by firstly reducing the field diaphragm and then by moving focus knob until the field diaphragm edges become clear, whilst also making sure that the field diaphragm is aligned.
2. When the standard sample is focused and aligned, collect five "*mean grey values*" from several different areas across the sample. Once complete, the "*mean grey value*" is calibrated with the reflectance. See the Red "+" sign in the Figure AD3.1.

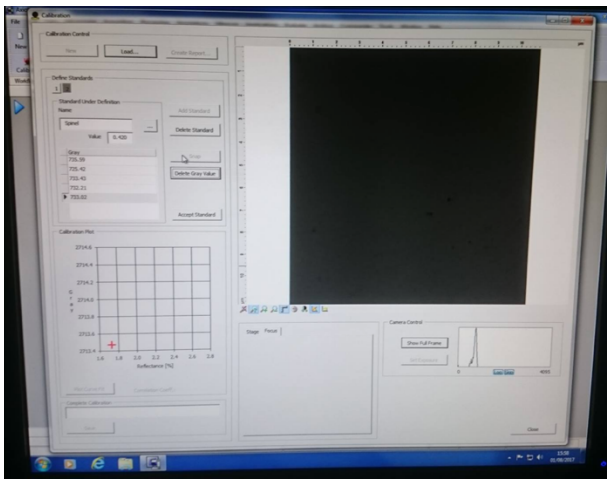

**Figure AD3.1.** Screenshot of the calibration panel using the Axiovision 4.8 software. The red plus sign is the calibration for the GGG (1.722 %) standard against the mean grey value.

3. The same is done for the lower reflectance spinel standard (0.420%). Once complete, two red "**+**" points will be displayed on the calibration curve (Figure AD3.2).

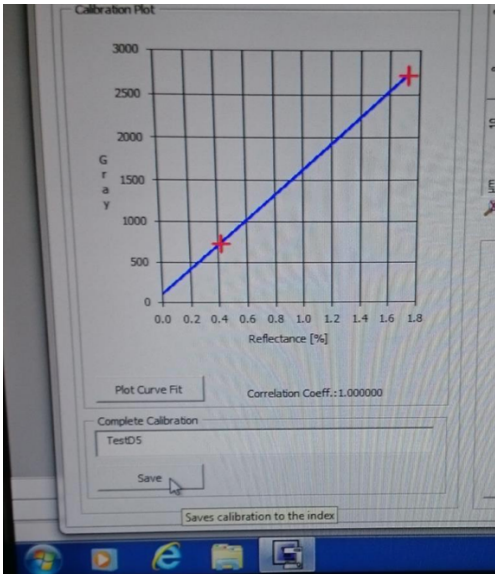


**Figure AD3.2.** Screenshot of the calibration panel for both the GGG (1.722 %) and Spinel (0.420 %) standard against the mean grey value.

### 3.1.2 Performing vitrinite reflectance measurements

1. Apply a drop of immersion oil on the sample prior to vitrinite reflectance analysis.
2. Put the sample under the oil immersion lens and focus on the sample.

3. The field of view was divided into quadrants, to make sure that the same vitrinite particle was not measured twice.
4. Aim to perform 30 to 50 measurements for each sample when possible. Ideally 50 measurements were determined, as some measurements will be disregarded and not used to calculate the mean random reflectance.
5. The instrument was re-calibrated every 30 minutes.
6. When possible, large vitrinite particles with unscratched surfaces were targeted for analysis. Small vitrinite particles and vitrinite particles that were close to bright pyrite grains, were avoided.
7. Due to the limited range of the standards (0.420 – 1.722 %), samples with previous VR measurements > 2 %$VR_o$ were not measured.

## 3.2 Vitrinite reflectance: processing the results

Before calculating the mean random reflectance, standard deviation and number of measurements, histograms were constructed showing the VR measurements, to see whether different VR populations were present. Anomalously outliers were disregarded. What was perceived to be cavings and VR values from inertinite particles were also rejected.

However, it should be noted that due to the igneous intrusions, cavings were treated differently whether the samples were above or below the intrusion. Typically, when studying cavings in normal burial conditions, the lower maturity population may be treated as cavings. However, for samples below an igneous intrusion, the higher maturity population may also be from cavings.

Therefore, Below the igneous intrusion, the populations with higher than expected VR measurements were treated as cavings and the population with lower VR measurements were used to calculate the mean random reflectance and standard deviation. For samples above the igneous intrusion, the populations with lower than expected VR measurements were treated as cavings and spuriously high VR measurements were treated as inertinite particles.

# Appendix E Spreadsheet containing all the numerical data and additional information

Electronic Excel file.

# Appendix F Calibration curves constructed in Chapter 7.

**Table 1.** The calibration rock-chip samples used in Chapter 7. (a) National Physical Library (NPL) Raman instrument calibration samples. (b) The newly installed Kingston University instrument calibration samples.

(a) NPL Calibration (532 nm)

| Well | Sample (SSK) | Depth (m) |
|---|---|---|
| MoB-1 | 80037 | 305 |
| MoB-1 | 80251 | 582 |
| MoB-1 | 80254 | 762 |
| MoB-1 | 80255 | 777 |
| MoB-1 | 80263 | 1125 |
| MoB-1 | 80264 | 1137 |
| MoB-1 | 80265 | 1195 |
| MoB-1 | 80266 | 1210 |
| MoB-1 | 80269 | 1484 |
| MoB-1 | 80273 | 805 |

(b) Kingston Calibration (532 nm)

| Well | Sample (SSK) | Depth (m) |
|---|---|---|
| MoB-1 | 80251 | 582 |
| MoB-1 | 80254 | 762 |
| MoB-1 | 80273 | 805 |
| MoB-1 | 80274 | 832 |
| MoB-1 | 80258 | 847 |
| MoB-1 | 80263 | 1125 |
| MoB-1 | 80264 | 1137 |
| MoB-1 | 80265 | 1195 |
| MoB-1 | 80266 | 1210 |

MoB-1: Milton of Balgonie-1 well.

**Table 2.** The calibration curve equations for several Raman parameters vs. vitrinite reflectance for the NPL (532 nm) and the newly installed Kingston University Raman instruments (532 nm), as well as the previous Kingston Raman instrument (514 nm) for comparison purposes.

**National Physical Laboratory (532 nm) – Carboniferous rock-chips**

G-FWHM $\%_{eq}VR = 31.05769*\exp^{(-0.04120*G\text{-}FWHM)}$

SSA $\%_{eq}VR = 448.40817*\exp^{(-0.01321*SSA)}$

RBS $\%_{eq}VR = 0.09432*RBS - 20.46853$

R1 $\%_{eq}VR = 7899.20967*\exp^{(-15.00801*R1)}$

**Kingston University (532 nm) – Carboniferous rock-chips**

G-FWHM $\%_{eq}VR = 22.13800*\exp^{(-0.03881*G\text{-}FWHM)}$

SSA $\%_{eq}VR = -73.48994*\ln(SSA) + 440.65274$

RBS $\%_{eq}VR = 0.05349*RBS - 11.37781$

R1 $\%_{eq}VR = 43441.89092\exp^{(-17.57710*R1)}$

**Kingston University (532 nm) – United States Geological Survey (USGS) strew-slides**

G-FWHM $\%_{eq}VR = 6594.03336*G\text{-}FWHM^{(-2.14604)}$

SSA $\%_{eq}VR = 143.97780*\exp^{(-0.01190*SSA)}$

RBS $\%_{eq}VR = 0.02052*RBS - 4.38501$

R1 $\%_{eq}VR = 274.91395*\exp^{(-9.46423*R1)}$

**Kingston University (514 nm) – Carboniferous rock-chips**

G-FWHM $\%_{eq}VR = 35.32431*\exp^{(-0.04554*G\text{-}FWHM)}$

SSA $\%_{eq}VR = 489.80048*\exp^{(-0.01431*SSA)}$

RBS $\%_{eq}VR = 0.15129*RBS - 34.45176$

R1 $\%_{eq}VR = 475531.13999*\exp^{(-22.72431*R1)}$

# Appendix G Conference paper abstracts

**Faculty of Science, Engineering and Computing (SEC) Conference, Kingston University, 2017.**

April 5, 2017 at Penrhyn Road, Kingston University

## Assessing Organic Carbon Maturity using laser Raman spectroscopy

**Delano Henry** (1), Ian Jarvis (1), Gavin Gilmore (1) and Michael Stephenson (2).

(1) Department of Geography and Geology, Kingston University London, Kingston upon Thames KT1 2EE, UK (d.henry@kingston.ac.uk), (2) British Geological Society, Keyworth, Nottingham, NG12 5GG, UK

When exploring for oil and gas, basin models are constructed by geoscientists to help predict the timing of hydrocarbon generation and expulsion; as well as quantifying diagenesis, fluid flow and tectonics and missing stratigraphic units in a sedimentary basin. The basin models need to be calibrated with thermal maturity values derived from optical and geochemical analysis, in order to understand the thermal evolution of a basin through geological time. Vitrinite reflectance (VR) is considered the "gold standard" for assessing the maturity of source rocks, however it has long been recognized that it can often produce unreliable results in dispersed organic matter (DOM) in shales; due to misidentification of primary vitrinite and the suppression and/or retardation effect, caused by macerals with high hydrogen concentration (e.g. liptinites, amorphous organic matter (AOM) and hydrogen rich vitrinites), different lithologies and overpressurized basins. Therefore, in order to get reliable results several methods need to be implemented together in order to crosscheck the results.

In this study, I will investigate the application of Laser Raman spectroscopy as a tool for quantitatively measuring the maturity of various organic materials, as well as assessing the potential to constrain the origins of organic matter in sedimentary rocks. A multidisciplinary approach will be implemented in order to achieve this aim, by comparing the Laser Raman spectra and parameters with petrographic data (vitrinite reflectance, thermal alteration index, fluorescence, palynology), organic and inorganic geochemistry, and the sedimentology of core and outcrop samples. The study will focus on Bowland-Hodder shale successions, an important target for shale gas exploration in the UK. Ultimately, laser Raman spectroscopy has the potential to be an important tool that can be used to rapidly quantify the maturity of

OM early in a field's lifecycle and to characterize and distinguish between different palaeoenvironments.

**Faculty of Science, Engineering and Computing (SEC) Conference, Kingston University, 2018.**

April 16, 2018 at Penrhyn Road, Kingston University

## Calibrating a simple-rapid method for determining organic matter maturity using laser Raman spectroscopy: A case study on UK Carboniferous organic rich mudstones

**Delano Henry** (1), Ian Jarvis (1), Gavin Gilmore (1) and Michael Stephenson (2)

(1) Department of Geography and Geology, Kingston University London, Kingston upon Thames KT1 2EE, UK (d.henry@kingston.ac.uk), (2) British Geological Society, Keyworth, Nottingham, NG12 5GG, UK

Laser Raman spectroscopy is used as a thermal maturity tool, however previous studies have variable methodologies and results. In this study, a simple-rapid automated Raman maturity method is calibrated on a suite of Carboniferous organic rich mudstones from the Inch of Ferryton–1 well in Scotland that has been thermally matured by a quartz dolerite sill, with vitrinite reflectance (VR) values ranging from 0.5-6.01 $\%VR_o$. The calibration curve is then tested on several other wells in the UK on Carboniferous shales and coals. The G–band full width half maximum (G-FWHM) is the best Raman parameter to estimate the thermal maturity of organic matter (OM) in the oil and gas window (0.5-3 %VR) and has a very strong relationship with VR. The method is applied on washed rock cuttings that allow for rapid results, without the need for isolating or polishing OM, significantly reducing the preparation time and costs.

**European Geoscience Union (EGU) Conference, Vienna (Austria), 2018.**

Session ERE4.2 – Unconventional Hydrocarbon Resources

10 April 2019. 17:30–19:00 in Hall X4, Poster board X4.266

Vol. 20, EGU2018-1169-3-2

## Assessing Kerogen Maturity using laser Raman spectroscopy

**Delano Henry** (1), Ian Jarvis (1), Gavin Gilmore (1) and Michael Stephenson (2)

(1) Department of Geography and Geology, Kingston University London, Kingston upon Thames KT1 2EE, UK (d.henry@kingston.ac.uk), (2) British Geological Society, Keyworth, Nottingham, NG12 5GG, UK

Vitrinite reflectance (VR) is considered to be the "gold standard" for assessing the maturity of petroleum source rocks, but it has long been recognized that it may produce unreliable results for dispersed organic matter in mudrocks, due to poor sample preparation, misidentification of primary vitrinite, and due to the suppression and/or retardation effect, caused by macerals with high hydrogen concentration (e.g. liptinites, amorphous organic matter and hydrogen-rich vitrinites), different lithologies, and overpressured basins. This project assesses the application of Raman spectroscopy to determine the maturity of organic-rich mudrocks by implementing a multidisciplinary approach combining VR, other petrographic thermal alteration indices, Rock-Eval pyrolysis and sedimentology. The novelty of the Raman method is that it can be used on all kerogen types and can be applied to pre-Devonian and deep-buried mudrocks with rare or absent vitrinite; analyses can also be performed on unprepared rock chips and drill cuttings. Our results show that several Raman parameters have great promise in determining the maturity of organic matter, and correlate extremely well with VR. Calibration curves constructed using well-characterised samples of Carboniferous shales from northern England and the Midland Valley of Scotland (the main targets for shale gas exploration in the UK), and old Torridonian shales from Scotland, have been successfully applied to determine the maturity of wells elsewhere in the areas, demonstrating the applicability of the tool. A fast and easy, automated method for Raman analysis will be presented that enables the acquisition of large data sets very quickly. Calibration curves are currently being refined and implemented on a wide range of sample sets of different ages in different basins. Overall, Raman spectroscopy provides a powerful additional technique in the geologist's tool kit to quantify the maturity of organic matter early in a field's lifecycle in order

to help determine sweet spots. Analysis can be performed on-site or potentially even downhole during drilling, offering great potential for the rapid characterization and development of non-conventional petroleum reservoirs.

**Faculty of Science, Engineering and Computing (SEC) Conference, Kingston University, 2019.**

April 3, 2019 at Penrhyn Road, Kingston University

## Raman spectroscopy: a novel method in determining the thermal alteration of organic matter in sedimentary rocks

**Delano Henry** (1), Ian Jarvis (1), Gavin Gilmore (1) and Michael Stephenson (2)

(1) Department of Geography and Geology, Kingston University London, Kingston upon Thames KT1 2EE, UK (d.henry@kingston.ac.uk), (2) British Geological Society, Keyworth, Nottingham, NG12 5GG, UK

Oil and gas exploration require geologists to understand the thermal evolution of organic matter (OM) in sedimentary rocks as it undergoes burial. Once the OM is exposed to temperatures >60 °C, the OM will begin to undergo thermal decomposition and produce oil and gas. Oil is primarily produced at lower temperatures (60–120 °C) and gas is primarily produced at higher temperatures (120–300 °C). At temperatures > 300 °C, the OM becomes exhausted and cannot produce any more hydrocarbons, leaving behind a carbon rich OM that will eventually become graphite with increasing pressure and temperature.

Geologists use a method called vitrinite reflectance (VR) to assess the thermal alteration (maturity) of OM, by recording the reflective properties of vitrinite grains which are particles derived from woody plants found in sedimentary rocks. However, it has long been recognized that VR can often produce unreliable results; due to misidentification of primary vitrinite grains and the suppression and/or retardation of VR values, caused by rocks with high hydrogen concentration, different lithologies (rock types) and overpressurized basins. VR also cannot be used where vitrinite grains are absent.

In this study, we will investigate the application of Raman spectroscopy, which measures the inelastic scattering of photons from a physical substance, as a tool to quantitatively measure the maturity OM by comparing the results with VR. The results have also been compared with Rock-Eval pyrolysis, another commonly used method to estimate the maturity of OM, which involves the progressive heating of OM from 300 to 550 °C in an inert atmosphere, whilst measuring the quantities of hydrocarbons generated.

Calibration curves have been constructed so that the Raman can estimate equivalent VR values. A portable Raman instrument has also been tested and the results show that a portable Raman could potentially be used on-site allowing for near real-time analysis, which could be used to help steer wells in the subsurface to hit sweet spots of high gas production during shale gas exploration, as well as decreasing the time needed to bring an oil and gas field into operation.

**European Geoscience Union (EGU) Conference, Vienna (Austria), 2019.**

Session ERE3.3 – Unconventional hydrocarbon resources: Advances and new technologies

12 April 2019. 10:45–12:30 in Hall X1, Poster board X1.112

Vol. 21, EGU2019-3141-3141-2

## Raman spectroscopy: a novel method for determining the thermal maturity of organic matter in sedimentary rocks

**Delano Henry** (1), Ian Jarvis (1), Gavin Gilmore (1), Michael Stephenson (2) and Christopher Vane (2)

(1) Department of Geography and Geology, Kingston University London, Kingston upon Thames KT1 2EE, UK (d.henry@kingston.ac.uk), (2) British Geological Society, Keyworth, Nottingham, NG12 5GG, UK

Over the last decade, an increasing number of studies have demonstrated the effectiveness of Raman spectroscopy for estimating the thermal maturity of organic matter (OM) in sedimentary rocks. A number of Raman parameters display a strong relationship with maturity proxies commonly used in the oil and gas industry, such as vitrinite reflectance (VR) and Rock-Eval pyrolysis. The benefits of Raman spectroscopy are that it is a low-cost, fast, easy and non-destructive tool, that has potential to be deployed using a portable instrument in the field or at well site.

Nonetheless, there remains no consensus on the best methodology for Raman spectroscopy analysis, as many authors have developed unique techniques and methodologies for specific temperature ranges that are convoluted and create unnecessary bias. Henry et al. (2018) developed a rapid, easy and simple Raman method that does not involve complicated and biased deconvolution of spectra, and successfully applied this to the characterization of OM that had been heated to high enough temperatures to generate oil and gas (c. 60–250 $^{o}$C).

Here, we present a suite of Raman results acquired using a desktop and a portable Raman instrument, employing Henry et al.'s (2018) method. Results are compared to VR and Rock-Eval pyrolysis data from the same or adjacent samples. Out of several Raman parameters tested, the G-band full-width at half-maximum (G-FWHM) is demonstrated to be the best Raman parameter to determine the thermal maturity of OM in the oil and gas windows, and

has a strong correlation with VR and Rock-Eval pyrolysis results. Portable Raman results are more scattered than those generated by the laboratory instrument, but a clear trend is apparent and further work is being undertaken. Discrepancies in the desktop vs. portable Raman spectroscopy results may be due to multiple factors, such as the laser spot size (point vs. bulk analysis) and different instrumental conditions. A reliable portable Raman method will allow geologists to perform analysis on-site during drilling, offering rapid quantitative maturity evaluation, an important parameter for identifying “sweet spots” in shale gas/oil reservoirs.

Henry, D.G., Jarvis, I., Gillmore, G., Stephenson, M., Emmings, J., 2018. Assessing low-maturity organic matter maturity in shales using Raman spectroscopy: Effects of sample preparation and operating procedure methodology. International Journal of Coal Geology, 191, 135-151. doi: 10.1016/j.coal.2018.03.005.

**American Association of Petroleum Geologists (AAPG) Conference, San Antonio, TX. 2019.**

Session 350 – Theme 5: Unconventional Reservoir Technology.

21 May 2019, 9:00–12:00 in Exhibit Hall, Poster 96.

Poster presentation presented by Prof. Ian Jarvis

## A comparison of kerogen maturity analysis in shales using laser Raman spectroscopy, vitrinite reflectance and Rock-Eval pyrolysis

**Delano Henry** (1), Ian Jarvis (1), Gavin Gilmore (1), Michael Stephenson (2) and Christopher Vane (2)

(1) Department of Geography and Geology, Kingston University London, Kingston upon Thames KT1 2EE, UK (d.henry@kingston.ac.uk), (2) British Geological Society, Keyworth, Nottingham, NG12 5GG, UK

Laser Raman spectroscopy (LRS) has proven to be a rapid and cheap, non-destructive technique to determine the maturity of kerogen[e.g.1,2]. Here, LRS results are compared with maturity estimates based on vitrinite reflectance (VR) and Rock-Eval pyrolysis. All three methods have advantages and limitations, and having multiple techniques that can be called on to perform maturity analysis, enables geologists to optimize their analysis based on the composition and age of the sample, maturity grade, equipment availability, and time and money constraints. Independent cross checking of results will also reduce risk. We have applied the three maturity methods to study 86 washed rock cuttings from two potential Carboniferous shale gas plays in the UK[3,4], in the Midland Valley of Scotland (MVS) and southern Pennine Basin, age equivalents of the US Barnett and Fayetteville shales. LRS analysis was performed on hand-picked coal and shale cuttings. VR data were compiled from previous studies, together with in-house VR analysis to validate previous results and to obtain values for samples where VR data were unavailable. Rock-Eval pyrolysis was performed on splits of the same samples.

Our results show that the G-band full-width at half-maximum (G-FWHM) is the best LRS parameter to determine the maturity of kerogen and has a strong correlation with VR values of 0.6 - 5 %$VR_o$. Correlation with Rock-Eval $T_{max}$ is also strong up to 2 %$VR_o$ for both G-FWHM and VR, but this breaks down at higher maturities, with an inconsistent decrease in Rock-Eval

$T_{max}$ values. Samples from the MVS and Pennine Basin generate similar results, despite originating from different basins with contrasting geological histories. The depositional environments and organic matter types differ in the two areas: the MVS has lacustrine Type I/III source rocks, and the Pennine Basin marine Type II/III source rocks. The MVS has been affected by intrusion of the Midland Valley Sill, creating thick thermal aureoles and rapid heating; the Pennine Basin has also been affected by igneous intrusions, but on a much smaller scale. Further experiments with a portable LRS are underway to test the ability to perform maturity analysis on-site during drilling, offering rapid characterization and development of shale gas/oil reservoirs.

1. Henry, D.G. et al. 2018. Int. J. Coal Geol. 83, 415-422.
2. Schito, A., Corrado, S. 2018. Geol. Soc. Spec. Pub. 484.
3. Andrews, I.J. 2013. BGS DECC.
4. Monaghan, A.A. 2014. BGS DECC.

**The International Conference on Energy and Sustainable Futures (ICESF), Nottingham, 2019.**

9–11 September 2019

Accepted Poster Presentation

## Raman spectroscopy: an alternative method for determining the thermal alteration (maturity) of organic matter in sedimentary rocks for shale gas exploration

**Delano Henry** (1), Ian Jarvis (1), Gavin Gilmore (1), Michael Stephenson (2) and Christopher Vane (2)

(1) Department of Geography and Geology, Kingston University London, Kingston upon Thames KT1 2EE, UK (d.henry@kingston.ac.uk), (2) British Geological Society, Keyworth, Nottingham, NG12 5GG, UK

Oil and gas exploration require geologists to understand the thermal evolution of organic matter (OM) in sedimentary rocks as it undergoes burial. Once the OM is exposed to temperatures >60 °C, the OM will begin to undergo thermal decomposition and produce oil and gas. Oil is primarily produced at lower temperatures (60–120°C) and gas is primarily produced at higher temperatures (120–300°C). At temperatures >300°C, the OM becomes exhausted and cannot produce any more hydrocarbons, leaving behind a carbon-rich OM that will eventually become graphite with increasing pressure and temperature.

Geologists need to quantify the thermal alteration (maturity) of OM to determine the type and quantities of hydrocarbons produced. The most commonly used method to track the maturity of OM is vitrinite reflectance (VR), which records the reflective properties of vitrinite particles that are derived from woody plants and are found in sedimentary rocks. However, VR can often produce unreliable results, due to misidentification of primary vitrinite particles and the suppression and/or retardation of VR values (caused by rocks with high hydrogen concentration, different lithologies (rock types) and/or overpressurized basins). VR also cannot be used in deposits where vitrinite particles are absent.

In this study, we investigate the application of Raman spectroscopy (a non-destructive analytical technique that measures the inelastic scattering of photons from a physical substance) as a tool to determine the maturity of OM. Several Raman parameters vs. VR

calibration curves have been constructed, with $R^2$ values ranging from 0.63 to 0.96. These demonstrate that Raman can reliably estimate equivalent VR values. A portable Raman instrument has been tested and results show that this could potentially be used on-site, allowing for near real-time analysis. Data could be used to help steer wells in the subsurface to hit 'sweet spots' of high gas production during shale gas exploration, as well as decreasing the time needed to bring an oil and gas field into operation.